Small-angle X-ray Scattering Studies of Reaction Kinetics During Synthesis of Colloidal Polymer Particles

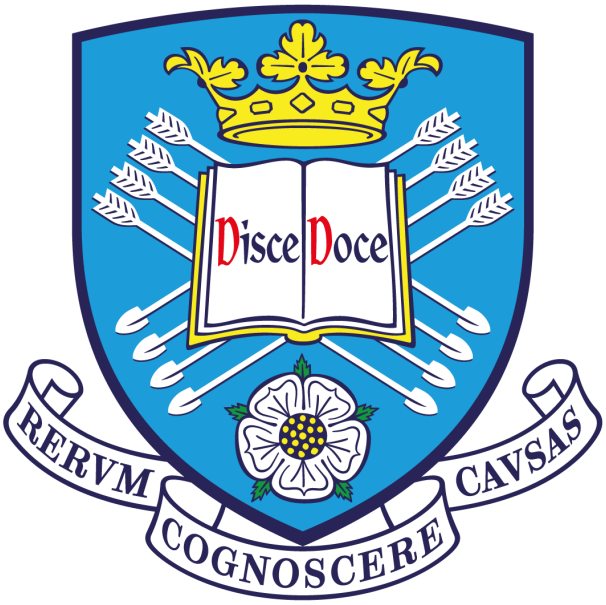

Guoxing Liao

Department of Chemistry

The University of Sheffield

Submitted to the University of Sheffield

In fulfilment of the requirements for the award of

Doctor of Philosophy

April 2022

Declaration

The work described in this Thesis was carried out at the University of Sheffield under the supervision of Dr Oleksandr Mykhaylyk and Professor Steven P. Armes FRS between November 2017 and April 2022 and has not been submitted, either wholly or in part, for this or any other degree. All the work is the original work of the author, except where acknowledged by references.

Signature: _____

Guoxing Liao April 2022

Abstract

This work is focused on the development and application of small-angle x-ray scattering (SAXS) techniques for measuring reaction kinetics during the *in situ* synthesis of polymer nanoparticles. A combination of scattering equations, derived for the various structural morphologies formed during such reactions, and equations that account for mass balance of the reaction components are used to analyse time-resolved SAXS patterns to obtain detailed mechanistic information. Exchange of both reagent and solvent molecules between the self-assembled particles and the surrounding medium occurs during the polymerisation. This causes a continuous change in scattering length density for the system components and enables determination of both the local concentration of the reaction components and various structural parameters for the growing self-assembled particles. The new SAXS approach developed in this work is applied to three different systems: (i) synthesis of poly(stearyl methacrylate)-poly(benzyl methacrylate) (PSMA-PBzMA) diblock copolymer nano-objects via reversible addition-fragmentation chain transfer (RAFT) dispersion polymerisation in a non-polar medium (mineral oil), (ii) synthesis of poly[2-(dimethylamino)ethyl methacrylate]-poly(benzyl methacrylate) (PDMA-PBzMA) diblock copolymer nano-objects via RAFT emulsion polymerisation in a polar medium (80/20 ethanol/water mixture) and (iii) synthesis of poly(2,2,2-trifluoroethyl methacrylate) (PTFEMA)/silica nanocomposite particles via conventional free radical emulsion polymerisation in aqueous media.

For RAFT dispersion polymerisation in mineral oil, SAXS analysis revealed that after micellar nucleation, the rate of polymerisation was proportional to the local monomer concentration within the micelle cores which is consistent with theoretical predictions. It was also found that SAXS could be used to determine Flory-Huggins parameters for pairs of the system components. Moreover, SAXS indicated that the nascent nuclei comprise spherical particles containing a mixture of mineral oil and BzMA monomer within the particle cores stabilised by short PSMA chains.

For RAFT emulsion polymerisation in an 80/20 ethanol/water mixture, SAXS provided detailed information about morphological development in the system from initially dissolved PDMA stabiliser blocks into PDMA-PBzMA deblock copolymers forming spherical micelles at a later stage of the synthesis. The binary solvent composition complicated the SAXS analysis, so two scenarios were considered. According to the most physically realistic scenario, the monomer concentration within the micelle cores was close to zero throughout the reaction, suggesting that the rate of polymerisation was controlled mainly by diffusion of the BzMA monomer through the solvent medium to the spherical micelles and not by the rate of reaction like in the RAFT dispersion polymerisation.

For the free radical aqueous emulsion polymerisation to produce PTFEMA-silica (core-shell) nanocomposite particles, SAXS analysis, apart from measurements of the monomer diffusion coefficient and parameters describing the reaction kinetics, provided information regarding formation of the silica shell and also the silica nanoparticle packing density within this shell.

Overall, *in situ* SAXS measurements combined with a new approach for scattering analysis counting mass balance of reaction components are shown to be more informative than traditional post-mortem characterisation techniques such as electron microscopy or dynamic light scattering.

Publications

Czajka, A., **Liao, G**., Mykhaylyk, O. O., & Armes, S. P. (2021). *In situ* Small-angle X-ray Scattering Studies during the Formation of Polymer/silica Nanocomposite Particles in Aqueous Solution. *Chemical science*, *12*(42), 14288-14300.

Conferences

Sep 2019	Early Career Colloid Meeting, Loughborough, UK
Sep 2021	S4SAS Conference, organised by Diamond Light Source, Sheffield, UK

Acknowledgements

I should first apologise that I am far from finishing the research plan scheduled in the first year, which has been partially discussed in Chapter 5, though now it is clear that the dispersion polymerisation in such ethanol/water mixture might be most difficult part for small angle X-ray scattering (SAXS) analysis in this Thesis. However, I recognised that the procedure I used for SAXS modelling of the monological transition of self-assembled nanoparticles for my master's degree Dissertation, which also was supervised by Dr Oleksandr Mykhaylyk (Sasha) and Prof Steven Armes, was not enough for polymerisation. More fitted variables were involved, and further interpretations of SAXS modelling results always confused me. It was never trivial to produce the result, that the rate of polymerisation was found to be proportional to monomer concentration as the theories predicted, by clicking the modelling button in Igor Pro with Irena Macro. I believe that the SAXS modelling results should justify themselves, at least qualitatively. For SAXS experiments, they record locations of compositions, which is considered to be empirical. Meanwhile, SAXS theories produce sophisticated models (dozens of mathematic equations), and such models can be considered as the synthetic a priori judgments claimed by Immanuel Kant. For the simple case, the mentioned monological transition, some well-known self-assembled nanoparticles SAXS models are fairly enough to our experience. Moreover, for SAXS modelling of polymerisation with more fitted variables, I have to revisit the models by phenomenological reduction invented by Edmund Husserl. He enhanced (of course, my understanding) that the personal intentionality always hinders the whole construction of objects, but we still believe that the objects have been fully described by the sum of the facts observed by particular attitudes. So, sometimes, I wonder whether SAXS can be one of the methods with God's perspective compared with other characterisation techniques? I cannot give any answer, but with such reflections, I see, read, then learn various things in Sheffield provided by Sheffield City Council and in UK, which I cannot access in China. And thanks to Sasha, I can truly synthesize western culture with change my stubborn Chinese mindset. It was not easy, as Husserl said that it was intentionality.

For the experimental contents of this Thesis, Dr Matthew Derry, Dr Elizbeth Jones and Dr Adam Czajka have already provided excellent synchrotron SAXS data. And in Diamond I22, Andy Smith and Tim Snow always stand beside us, and after that, I recognised that good quality of synchrotron data is somehow unpredictable, particularly for polymerisation. It is always a teamwork, including the contributions from Dr Saul Hunter, Dr Oliver Deane, Dr Sarah Byard (Wilson), and Dr Cate O'Brien. And for some other experimental measurement, I very appreciate the help from Dr Tom Neal and Csilla György. For modelling part, I must thank first Sasha's seminars presented in Guangzhou, 2016, which brought me in the SAXS world. And I also appreciate that Prof Steven Armes always brought huge chemistry knowledge for me. The talks with Prof Richard Jones and Prof Anthony Ryan truly inspired me for mass transfer in polymerisation. Also, so many books in the University library promoted my knowledges in SAXS area. Moreover, I have to thank my primary school, middle school and high school math teachers, Li, Guili Lin, and Shiming Chen, who always encouraged me and promoted my math skills.

Besides, studying in Sheffield cannot only conclude as scientific journey. My parents fully supported me, particularly in finance, even though they hardly know nothing about what I am studying. With relatively introvert personality, luckily, I still have some friends with me, including Yu Fu, Zhibin Chen, Juan Gui, Huijuan Chen, and Yiyi Ju, whom I could truly exchange

ideas and deep conversations with. I deeply appreciate Prof Linge Wang, who introduced me to Sasha and brought so many opportunities to me, and I keep good relationships with several current and pervious Lin's group members, including Jinyi Yang, Xueyang Chen, Wenqing Xue, Donghua Dong, and Fangrong Tan. A final special thanks to Yiru Wang, now my wife with two master's degrees at the University of Sheffield, who always supported me in Sheffield. We always share emotions and moments together.

Also, I appreciate everyone who read this Thesis.

Nomenclature

A

A	amplitude of the form factor
A_{ape}	area of an aperture
A_{br}	amplitude of the solvophilic block
$A_{core,micelle}$	amplitude of the core of spherical micelle
$A_{core,worm}$	amplitude of the core of worm-like micelle
$A_{core,vesicle}$	amplitude of the core of vesicle
$A_{corona,micelle}$	amplitude of the corona of spherical micelle
$A_{corona,worm}$	amplitude of the corona of worm-like micelle
$A_{corona,vesicle}$	amplitude of the corona of vesicle
A_{e}	Helmholtz free energy of polymer chain with the excluded volume effect
A_{e_silica}	silica nanoparticle packing efficiency
A_{G}	Helmholtz free energy of the Gaussian chain
A_{GC}	amplitude of ideal polymer chain
A_{int}	interfacial free energy in self-consistent field theory
A_{mix_FH}	Helmholtz free energy of the polymer solution
A_{pApB}	interfacial area between block A and block B in strong segregation theory
a_{phi}	optimal surface area
A_{pc}	amplitude of the solvophobic block
A_{mc}	amplitude of the spherical micelle core
$A_{N_p}^{N_p'}$	N_p-permutation of N_p'
A_{s}	amplitude of the form factor of sphere
$A_{s\text{-}cap}$	spherical cap area coverage by one silica particle on the polymer cores surface
$A_{s\text{-}co}$	total area of the polymer core surface
A_{sh}	amplitude of the form factor of shell with no thickness of membrane
$A_{su\_c\_GC}$	suspension particle core with Gaussian core block chains scattering amplitude
A_{su_GC}	amplitude of the suspension particle with Gaussian core block chains
$A_{su\_s\_cs}$	amplitude of the shell of the suspension particle as core-shell structure
A_{sur}	boundary surface area between the medium and the reaction region
ATRP	atom transfer radical polymerisation

B

$\vec{b}$	end-to-end vector of polymer chain structures
b	length of end-to-end vector of polymer chain structures
b_e	scattering length of electron
BS_{sf}	Boltzmann sigmoidal equation

C

c-ps&silica	core-particulate shell with non-absorbed silica
CCD	charge-coupled device
C_l	product of efficiency, area of an aperture, incident flux, and solid angle
c_{light}	speed of light
$c_{i_{agg}}$	concentration of the aggregates with aggregation number
c_{mon}	monomer concentration
$c_{P\cdot}$	radical concentration
CMC	critical micelle concentration
CMOS	complementary metal-oxide-semiconductor
conv	monomer conversion
cP	primitive cubic
CTA	chain transfer agent

D

D_{agg}	dimension of the aggregates
d_c	parameter for simulation of the nonpenetration of the corona chains in the core
D_f	fractal dimension
D_{lm}	diffusion coefficient of the liquid molecule
D_m	diffusion coefficient of the molecule
d_{silica}	the diagonal of the cube face
DCP	disk centrifuge photosedimentometry
DI	dispersity index
DLS	dynamic light scatterin
DP	repeat unit
DP_{RAFT}	targeted repeat unit of reversible addition-fragmentation chain transfer polymerisation
dq_{HS}	parameter in Boltzmann sigmoidal equation

E

E	spherical excess
E_0	amplitude of the X-ray
E_s	amplitude of scattered x-ray for one particle in medium

F

f_i	initiator efficiency
f_A	fraction of block A of diblock polymer chain in weak segregation theory
f_B	fraction of block B of diblock polymer chain in weak segregation theory
F_{br}	self-correlation term of scattering intensity of the corona block
$F_{c\text{-}ps}$	form factor of the core-particulate shell
f_{fri}	friction
F_{dri}	driving force
F_{int_SST}	interface energy of strong segregation theory
f_{mon}	volume fraction of the monomer in the micelle cores
F_{stA_SST}	stretching energy of block A diblock polymer chain in strong segregation theory
F_{stB_SST}	stretching energy of block B diblock polymer chain in strong segregation theory
f_{pc}	fraction of copolymers disassociated in the solvents
F_{pc}	diblock copolymer form factor
F_{rasp}	raspberry model form factor
F_{rasp_sf}	raspberry model form factor with structure factor
F_{silica}	silica nanoparticle form factor
f_{sm}	fraction of copolymers assembled in spherical micelles
F_{sm}	micelle form factor
F_{SST}	free energy of strong segregation theory
F_{su_cs}	suspension particle as core-shell structure form factor
F_{sm_GC}	suspension particle with Gaussian core block chains form factor
f_{sol}	volume fraction of solvent in the micelle cores
F_{WST}	free energy of weak segregation theory

G

g	number of the segment length of blob
$g\left(\overrightarrow{R_p}\right)$	correlation function of a particle at position $\overrightarrow{R_p}$
GPC	gel permeation chromatography

H

HSP	Hansen solubility parameter

I

I	intensity collected by detector in small angle X-ray scattering experiment
I_2	initiator
$[I_2]$	initiator molar concentration
i_{agg}	is the aggregation number
I_{bg}	solvent background scattering intensity
I_{exp_bg}	solvent background scattering intensity measured by experiments

$I_{c\text{-}ps}$	scattering intensity of the polymer/silica (core-particulate shell) structure
$I_{c\text{-}ps\text{-}silica}$	scattering intensity of the polymer/silica nanocomposite particles
I_{ds}	dimers constructed by spherical micelles scattering intensity
I_i	incident intensity
I_{lsm}	intensity of the relatively large spherical particles
I_{pc}	scattering intensity of the soluble polymer chains
I_{rasp}	scattering intensity of the polymer/silica nanocomposite particles described by the raspberry model
I_S	scattering intensity
I_{SB}	scattering intensity of the background
I_{SB+S}	scattering intensity of the sample and the background
$I_{silica\_c\text{-}ps}$	scattering intensity of the absorbed silica nanoparticles within the particle shell
I_{silica_med}	scattering intensity of the non-absorbed silica nanoparticles in medium phase
I_{sm}	scattering intensity of the spherical micelles
I_{ssm}	intensity of the relatively small spherical particles
I_{tot}	total scattering intensity
IR	infrared spectroscopy

J

J_i	incident flux
J_m	flux of molecule
J_{lm}	flux of the liquid molecule
J_n	Bessel function for integer values of n

K

k	magnitude of wave vector
$\vec{k}$	scattered wave vector
$\vec{k_0}$	incident wave vector
k_B	Boltzmann constant
k_d	initiator decomposition rate constant
k_p	propagation rate coefficient
k_p'	reduced propagation rate coefficient
k_{sf}	coefficient of structure factor
k_{tc}	composite rate constant
k_{td}	disproportionation rate constant
$K\alpha$	wavelength of X-ray for characterisation radiation from K shell

L

L	Distance between sample and detector
l_d	closed distance between the particles of the pearl chains
l_{pho_c}	semiempirical critical length

L_w	length of the core of worm-like micelle

M

[M]	monomer molar concentration
$[M]_0$	initial monomer molar concentration
$[M]_p$	monomer molar concentration in the particle
m_{br}	hydrophilic block mass
M_{br}	peak molecular weight of macro- chain transfer agent measured by nuclear magnetic resonance
M_{co}	molar mass of the solvophobic block repeat unit
m_{ini_mon}	initial monomer mass
M_m	molecular weight of monomer
$M_{molecule}$	molecular weight of the molecule
$\overline{M}_n$	number-mean molecular weight
M_p	molecular weight of homopolymer
$\overline{M}_w$	weight-mean molecular weight
$\overline{M}_z$	z-mean molecular weight
MEHQ	monomethyl ether hydroquinone
MT	morphological transition
MT-I_ds-s	morphology transition including the dimers constructed by spherical micelles and the spherical micelles
MT-II_ls-ds-ss	morphology transition including relatively large spherical micelles, the dimers constructed by spherical micelles and relatively small spherical micelles
MT-III_cs	morphology transition including the relatively large suspension particles as core-shell structure and the relatively small suspension particles as core-shell structure
MT-IV_GC-s	morphology transition including the suspension particles with Gaussian core block chains and spherical micelles

N

N	number of segments in polymer chains
$\bar{n}$	mean number of radicals per particle
n_{agg}	aggregation number
N_{agg}	mean aggregation number
N_A	Avogadro constant
$n_{agg\_su\_ch}$	aggregation number of suspension particle as core-shell structure
$N_{agg\_su\_ch}$	mean aggregation number of suspension particle as core-shell structure
$n_{agg\_su\_GC}$	aggregation number of suspension particle with Gaussian core block chains
$N_{agg\_su\_GC}$	mean aggregation number of suspension particle with Gaussian core block chains
$N_{A\&B}$	total number of segments on the diblock copolymer chain

n_{br}	number of moles of solvophilic block
n_{frame}	total number of recorded frames
Δn_{lm}	monomer amount transferring from the medium to the reaction region
n_p	number of the diblock copolymer chains
N_p	number of the particles
$n_{p/V}$	number density of particles in the system
N_{pearl}	number of the particles of the pearl chains
n_{silica}	number of the silica nanoparticles within the particulate shell
N_{silica_cell}	number of the silica nanoparticles on the polymer cores under the ideal unit cell situation
n_{site}	number of sites in Flory-Huggins mean-field theory
NMP	nitroxide mediated polymerisation
NMR	nuclear magnetic resonance
NNLS	non-negative least squares

P

P·	polymer radical
[P·]	polymer radical concentration
P	form factor
p_{agg}	packing parameter
P_{chains}	form factor of ideal chain
$P_{micelle}$	form factor of spherical micelle
p_p	probability of a propagation reaction
P_{GC}	form factor of Gaussian chain
P_w	form factor of worm-like micelle
$P_{vesicle}$	form factor of vesicle
PDI	polydispersity index
PDDF	pair distance distribution function
PISA	polymerisation-induced self-assembly
PY	Percus–Yevick approximation, or Percus–Yevick equation

Q

$\vec{q}$	scattering vector
q	magnitude of scattering vector
q_e	elementary charge

R

$\vec{r}$	position of the photons
$r_{1_{agg}}$	effective radius of the monomer
ΔR	a half of the shortest distance between core interfaces of the neighbouring micelles
R_A	thickness or radius of block A phase in self-consistent field theory
$r_{c\_c\text{-}ps}$	radius of the polymer core of core-particular shell model

$R_{c\_c\text{-}ps}$	mean radius of the polymer core of core-particular shell model
r_{ds}	radius of spherical micelle constructing dimer structure
R_{ds}	mean radius of spherical micelle constructing dimer structure
r_e	classical radius of the electron
R_{ep_e}	equilibria radius of the particle
R_F	root-mean-square end-to-end distance
R_g	root-mean-square radius of gyration
R_{g_br}	radius of gyration of the solvophilic block
R_{g_co}	radius of gyration of the solvophobic block
$R_{g\_co\_est}$	estimation of radius of gyration of the solvophobic block
R_{HS_silica}	effective radius of the hard sphere for silica particle
R_{in}	inner radius of core of vesicle
R_i	rate of decomposition of the initiators to the primary radical formation
$\overrightarrow{R_j}$	position of the particle *j*
r_{lmc}	radius of relatively large spherical particle
R_{lmc}	mean radius of relatively large spherical particle
R_m	radius of the molecule
r_{mc}	micelle core radius
R_{mc}	mean micelle core radius
r_N	final position of the end of the polymer chain with *N* segments
R_{out}	outer radius of core of vesicle
R_p	rate of the propagation
r_{silica}	radius of silica nanoparticle
R_{silica}	mean radius of silica nanoparticle
R_{sf}	one-half of the inter-micelle distance
r_{smc}	radius of relatively small spherical particle
R_{smc}	mean radius of relatively small spherical particle
r_{su}	radius of the suspension particle
R_{su}	mean radius of the suspension particle
r_{su_c}	core radius of the suspension particle of suspension particle as core-shell structure
R_{su_c}	mean core radius of the suspension particle of suspension particle as core-shell structure
R_t	rate of the termination
R_v	mean shell radius of vesicle
R_w	radius of the core of worm-like micelle
RAFT	reversible addition-fragmentation chain transfer
RDF	radical distribution function
RDRP	reversible-deactivation radical polymerisation

S

$S(q)$	structure factor
S_d	structure factor for dimer structure by spherical particles

S_e	entropy of such excluded volume effect
$\left[S_{hs}\left(\phi_{HS_{silica}}\right)\right]_{MAX}$	hard-sphere Percus-Yevick structure factor peak intensity
S_p	mean surface area of the particle cores
S_{pearl}	structure factor for pearl necklace chains
SAS	small angle scattering
SAW	self-avoiding walk
SAXS	small angle X-ray scattering
SEC	size exclusion chromatography
SEM	scanning electron microscopy
S_G	entropy of the conformations of the polymer chains
S_{mix_FH}	entropy of the polymer solution in Flory-Huggins mean-field theory
$Si(x)$	sine integral
SRMP	stable radical mediated polymerization

T

t	time
T	temperature
$t_{ps\_c\text{-}ps}$	thickness of the particulate shell of core-particular shell model
$T_{ps\_c\text{-}ps}$	mean thickness of the particulate shell of core-particular shell model
T_S	transmission of the sample
t_{sh}	thickness of membrane of vesicle
T_{SB}	transmission of the background
T_{SB+S}	transmission of the background and the sample
Δt_{dri}	mean travelling time for the liquid molecules by driving force as chemical potential gradient
Δt_{sol}	mean travelling time for the liquid molecules via Brownian motion
Δt_{tra}	mean travelling time for the liquid molecules
TEM	transmission electron microscopy
TR SAXS	time-resolved small angle X-ray scattering

U

U_{mix_FH}	interactions of internal energy in Flory-Huggins mean-field theory

V

$\bar{\nu}$	mean kinetic chain length
V_{br}	hydrophilic block total volume
v_{br}	solvophilic block volume
V_{co}	hydrophobic block total volume
V_{core}	volume of the core
V_{corona}	volume of the corona chains
v_e	occupied volume of single segment of one polymer chain
V_{eff}	effective volume for Percus–Yevick approximation

V_{ex_liq}	total volume of external liquid
V_{ex_mon}	total volume of the external monomer
V_{ex_sol}	total volume of solvents outside of the cores
V_{geo}	geometrical volume of the aggregates
V_{in_liq}	total volume of liquid components inside of the micelle cores
V_{in_mon}	total volume of the internal monomer
V_{in_sol}	total volume of solvents in the micelle cores
V_{liq}	total volume of liquid
v_{lm}	liquid molecule volume
v_m	velocity of the molecule
V_m	molar volume of monomer
$V_{mc\text{-}co}$	mean volume of the core of the spherical micelle
V_{mon}	volume of monomer remaining in the system
$V_{molecule}$	volume of the molecule
V_o	occupied volume of one polymer chain
V_p	volume of one polymer chain
v_{p_co}	total volume of particle cores in the system
v_{pho}	solvophobic part with occupied volume
V_{pol}	total volume of polymer components
V_s	molar volume of the solvent
$V_s(r)$	total spherical volume of a radius of r
V_{sf}	effective volume fraction of the interacting micelles
V_{site}	total volume of the latte sites in Flory-Huggins mean-field theory
V_{sol}	solvent volume
V_{tot}	total volume of the materials in the studied system composed of liquid and polymer components
$\bar{\nu}_{tr}$	mean kinetic chain length included termination by chain transfer

W

w_{mon}	mass concentration of monomer
w_{SCFT}	width of the interface in self-consistent field theory
WST	weak segregation theory

X

x_m	position of molecule
Δx_{dri}	mean travelling distance for the liquid molecules by driving force as chemical potential gradient
Δx_{lm}	mean travelling distance during mean travelling time for the liquid molecules
Δx_{sol}	mean travelling distance for the liquid molecules via Brownian motion
xpol	volume fraction of polymer in the core
xmon	volume fraction of monomer in the core
xsol	volume fraction of solvent in the core

Z

Z_{FH}	bond number for each site in Flory-Huggins mean-field theory
2D	two-dimensional

CHEMICALS, MONOMERS AND POLYMERS OR POLYMER-STRUCTURE FRAGMENTS

AIBA	2,2'-Azobis(2-isobutyramidine) dihydrochloride
BzMA	benzyl methacrylate
DMF	N,N-dimethyl formamide
DMSO	dimethyl sulfoxide
PBzMA	poly(benzyl methacrylate)
DMA	2-(dimethylamino)ethyl methacrylate
PDMA	poly(2-(dimethylamino)ethyl methacrylate)
P(MAA–PEOMA)	poly(methacrylic acid-co-poly(ethylene oxide) monomethyl ether methacrylate)
SMA	stearyl methacrylate
PSMA	poly(stearyl methacrylate)
T21s	tert-butyl peroxy-2-ethylhexanoate
THF	tetrahydrofuran
TFEMA	2,2,2-trifluoroethyl methacrylate
PTFEMA	poly(2,2,2-trifluoroethyl methacrylate)
$scCO_2$	supercritical carbon dioxide

Greek Alphabet

α_{agg}	constant characteristic of monomer- monomer interaction
α_{silica}	fraction of the penetration depth of the silica nanoparticles in the polymer cores
β_{br}	excess scattering length of solvophilic blocks
β_{core}	excess scattering length of core
β_{corona}	excess scattering length of corona
β_{pc_co}	excess scattering length of solvophobic blocks
β_{mc}	excess scattering length density of the micelle cores
$\gamma_{1_{agg}}$	interfacial free energy per unit area
γ_{SCFT}	surface tension in self-consistent field theory
$\Gamma(a)$	Gamma Function
$\Gamma(a,x)$	upper incomplete Gamma Function
δ_D	dispersion solubility parameter
δ_H	hydrogen bonding solubility parameter
δ_{p_Hb}	cohesive energy density of the polymer
δ_P	polar solubility parameter

δ_{s_Hb}	cohesive energy density of the solvent
ε_{ij}	interactions of i-j to determine Flory-Huggins parameter
$\xi(0)$	scattering length of the molecule per volume at a small angle
ξ_b	radius of blobs
ξ_{br}	scattering length of the solvophilic blocks
$\xi_{c\_c\text{-}ps}$	scattering length density of the polymer core of core-particular shell model
ξ_{co}	scattering length of the solvophobic blocks
ξ_{core}	scattering length of the core
ξ_{corona}	scattering length of the corona
ξ_{mc}	scattering length density of the micelle core
ξ_{med}	scattering length density of the medium of core-particular shell model
ξ_{mon}	scattering length of the monomer
$\xi_{ps\_c\text{-}ps}$	scattering length density of the particulate shell of core-particular shell model
ξ_{silica}	scattering length density of the silica nanoparticles
ξ_{sol}	scattering length of the solvent
ξ_{su}	scattering length density of the suspension with Gaussian core block chains Model
ξ_{su_s}	scattering length density of the suspension particle as core-shell structure
η	efficiency of small angle X-ray scattering experiment
η_{p_vol}	volume packing efficiency
$\eta_{p\_vol\_avg}$	average volume packing efficiency
$\eta_{p\_vol\_avg\_est}$	estimated average volume packing efficiency
$\eta_{p\_vol\_cell}$	ideal unit cell volume packing efficiency
η_{p_sur}	superficial packing efficiency
η_s	viscosity of the solvent
θ	half of scattering angle
θ_{tp}	angle between two vectors of from polymer core centre to the attached points of two silica nanoparticle on the polymer core centre
θ_w	azimuthal angle defined by spherical coordinate
Λ	mean free path of the radiation
Λ_x	mean free path of X-ray
λ	wavelength
μ	linear attenuation coefficient
$\mu^0_{1_{agg}}$	standard part of the chemical potential of the aggregates with aggregation number of 1
$\mu_{i_{agg}}$	chemical potentials of any other aggregates with different aggregation number of molecules
$\mu^0_{i_{agg}}$	standard part of the chemical potential of the aggregates with aggregation number of molecules

$\mu^{0}_{\infty_{agg}}$	bulk energy of a monomer in infinite aggregates
$\Delta\mu_{m}$	chemical potential of molecule by driving force
$\Delta\mu_{p\_FH}$	chemical potential deference of the polymer chain between solution state and melt state
$\Delta\mu_{s\_FH}$	chemical potential deference of the solvent between solution state and pure solvent state
$\Delta\mu_{ArepB\_FH}$	chemical potential of the situation of the polymer chain B replaced by polymer chain A
$\Delta\mu_{lm}$	chemical potential of liquid molecules by driving force as chemical potential gradient
v	exponent of the number of polymer segments
Π	osmotic pressure
Π_{ρ^*}	osmotic pressure of overlap threshold density of the polymer solution
$\bar{\rho}$	mean density of whole material
$\rho\left(\overrightarrow{R_{p}}\right)$	mean number density of a particle at position $\overrightarrow{R_{p}}$
ρ^*	overlap threshold density of the polymer solution
ρ^{**}	density of concentrated polymer solution
ρ_0	density of the segments of the diblock polymer chain
ρ_{br}	hydrophilic block mass density
ρ_{co}	hydrophobic block mass density
ρ_{p}	density of polymer
$\rho_{molecule}$	density of the molecule
ρ_{mon}	mass density of the monomer
σ	standard deviation
$\Delta\sigma$	area on the detector placed at a distance from the sample at a special angle
$\frac{d\sigma}{d\Omega}$	differential scattering cross-section of the sample per unit solid angle
σ_t	width of the interface between core and corona
$\frac{d\Sigma}{d\Omega}$	differential scattering cross-section of the sample per unit solid angle per unit sample
$\left(\frac{d\sigma}{d\Omega}\right)_{e}$	differential scattering cross-section of the sample per unit solid angle of single electron
Υ	structural parameters tuple
$\phi_{c\text{-}ps}$	volume fraction of the cores-particulate shell population
ϕ_{ds}	dimers constructed by spherical micelles volume fraction
ϕ_{ex}	volume fraction of external liquid
ϕ_{HS_silica}	effective volume fraction of the hard-sphere Percus-Yevick structure factor
$\phi_{HS\_silica\_cor}$	corrected effective volume fraction
$\phi_{HS\_silica\_est}$	estimation of effective volume of the hard-sphere Percus-Yevick structure factor

$\phi_{HS\_silica\_m}$	SAXS modelling result of effective volume of the hard-sphere Percus-Yevick structure factor
ϕ_{lm}	liquid molecule volume fraction
ϕ_{lsm}	relatively large spherical particles volume fraction
ϕ_{m}	number density of molecule
$\phi_{med\_c\text{-}ps}$	volume fraction of the medium molecules within the particulate shell
ϕ_{p}	volume fraction of the polymer in the particles
ϕ_{p_FH}	volume fraction of the polymer in Flory-Huggins mean-field theory
ϕ_{pA_FH}	volume fraction of the polymer A in Flory-Huggins mean-field theory
ϕ_{pB_FH}	volume fraction of the polymer B in Flory-Huggins mean-field theory
ϕ_{pc}	volume fraction of the soluble polymer chain
ϕ_{rasp}	volume fraction of the core-particulate shell particles
ϕ_{silica_med}	volume fraction of the non-absorbed silica nanoparticles in medium phase
ϕ_{su_cs}	suspension particle as core-shell structure volume fraction
ϕ_{su_GC}	suspension particle with Gaussian core block chains volume fraction
ϕ_{ssm}	relatively small spherical particles volume fraction
χ^2	chi-paramter
χ_{pm}	Flory-Huggins interaction parameter of polymer-monomer
χ_{ps}	Flory-Huggins parameter of polymer-solvent
χ_{pApB}	Flory-Huggins parameter of polymer A-polymer B
$\chi_{ps\_H\_Hb}$	estimation of the enthalpic contribution to Flory-Huggins parameter of polymer-solvent by Hildebrand solubility parameters
$\chi_{ps\_H\_Han}$	enthalpic contribution to Flory-Huggins parameter of polymer-solvent by Hansen solubility parameters
χ_{ps_Han}	Flory-Huggins parameter of polymer-solvent estimated by Hansen solubility parameters
χ_{ps_S}	entropic contribution to Flory-Huggins parameter of polymer-solvent
Ψ	multivariate normalised distribution function
$\Delta\Omega$	solid angle
ω	frequency

Table of Contents

Chapter 1: Introduction

Chapter 1

Introduction

Monitoring polymerisation can basically track numerous polymer characteristics, such as polymer molecular weight and particle size, which may reveal chemical kinetics and mechanisms. From the practical opinions, monitoring polymerisation for industrial reactors with the additional feedback improves reaction efficiency to optimise the reaction conditions, reduces production cost, and achieves green manufacturing, Therefore, basic polymer physical and chemical properties will be presented in this Chapter. After introducing advantages and disadvantages of various characteristic techniques for monitoring polymerisation, small angle X-ray scattering will be invited to overcome the difficulties of monitoring polymerisation.

1.1 Polymer Chemistry

Hermann Staudinger's idea that polymers comprised long-chain molecules was controversial when first conceived in 1920 but became widely accepted within a decade or so.[1] Nowadays, polymers (or 'macromolecules') are defined as molecules with high relative molecular mass.[2] Polymer chains are composed of many low relative molecular mass units (monomers) connected together by covalent bonds.[2] Naturally-occurring polymers such as rubber, starch and cellulose were extensively studied in the 19th century and chemical modification produced important materials such as vulcanised rubber and cellulose nitrate (celluloid).[3] The first truly synthetic polymer was Bakelite, which was prepared from the reaction between phenol and formaldehyde in 1909.[3] Polymer architectures can be subdivided into linear, branched, comb-like, crosslinked, and dendritic structures.[4]

Linear polymer chains containing only one type of monomer repeat unit are called homopolymers.[2] Linear copolymers can be subdivided into statistical, alternating, block or graft structures.[3,4] For a homopolymer, its molecular weight[3] is given by:

$$M_{\mathrm{p}} = \mathrm{DP} \cdot M_{\mathrm{m}}, \tag{1.1}$$

where M_{p} and M_{m} are the molecular weights of the homopolymer and the monomer repeat unit respectively, and DP is the mean degree of polymerisation. Unlike small molecules, polymers do not possess a unique molecular weight. Instead, they exhibit a molecular weight distribution (MWD).[3] To describe such MWDs, various moments or average molecular weights, $\overline{M}$, are introduced such as:[4]

$$\overline{M} = \frac{\sum N_i \cdot M_{\mathrm{p}\text{-}i}^{j+1}}{\sum N_i \cdot M_{\mathrm{p}\text{-}i}^{j}}, \tag{1.2}$$

where $M_{\mathrm{p}\text{-}i}$ is the molecular weight of the i^{th} polymer, and the corresponding N_{i} is the number of polymer chains. An exponent, j, is used to determine the type of average molecular

weight. When *j* = 1, eq 1.2 becomes $\sum\left(\frac{N_i}{\sum N_i}\cdot M_{\text{p-}i}\right)$, which is defined as the number-average molecular weight, $\overline{M}_{\text{n}}$. When *j* = 2, eq 1.2 becomes $\sum\left[\frac{\left(N_i M_{\text{p-}i}\right)}{\sum\left(N_i M_{\text{p-}i}\right)}\cdot M_{\text{p-}i}\right]$, which is defined as the weight-average molecular weight, $\overline{M}_{\text{w}}$. When *j* = 3, eq 1.2 becomes $\sum\left[\frac{\left(N_i M_{\text{p-}i}^2\right)}{\sum\left(N_i M_{\text{p-}i}^2\right)}\cdot M_{\text{p-}i}\right]$, which is defined as the z-average molecular weight, $\overline{M}_{\text{z}}$. The dispersity index (DI) is a crude measure of the width of the MWD, as defined by the following equation:[3]

$$\text{DI} = \frac{\overline{M}_{\text{w}}}{\overline{M}_{\text{n}}}. \qquad (1.3)$$

For certain natural proteins, the PDI can be equal to unity, indicating that all chains possess precisely the same molecular weight. For a well-controlled anionic polymerisation, the PDI can be as low as 1.01, while for certain types of polyethylene the PDI can exceed 30.[5]

1.1.1 Polymer Synthesis

Polymerisation mechanisms can be divided into step growth polymerisation and chain growth polymerisation.[6, 7] Chain growth polymerisation includes free radical polymerisation, ionic polymerisation, and metal-catalysed polymerisation.[6] Various techniques are required depending on the polymerisation mechanism. For step growth polymerisation, these include bulk, solution or interfacial polymerization.[6] For ionic polymerisation, techniques include solution, slurry, and gas-phase polymerization.[6] Free radical polymerisations can be conducted under bulk, solution, suspension, emulsion or dispersion conditions.[6, 8] As discussed below, free radical polymerisation provides up to 45% of all synthetic polymers and is applicable to a wide range of vinyl monomers.[9-11] It is also the basis for the polymerisation considered in this Thesis.

1.1.1.1 Free Radical Polymerisation

In free radical polymerisation, initiators undergo slow thermal decomposition to generate radicals, which then react rapidly with a single monomer unit in the initiation step.[7] During propagation, the resulting monomer-radical adducts each react with many monomers to produce fast-growing polymer chains. Such polymer radicals undergo termination by either combination or disproportionation.[7] In addition, polymer radicals can undergo chain transfer side-reactions via reaction with monomer, solvent or non-propagating polymer chains.[12]

The kinetics of free radical polymerisation has been well-studied.[7, 12] The rate of decomposition of the initiator to form primary radicals is given by:

$$R_i = 2f_i \cdot k_d \cdot [I_2], \tag{1.4}$$

where k_d is the initiator decomposition rate constant, $[I_2]$ is the initiator concentration, and f_i is the initiator efficiency. The rate of propagation is given by:

$$R_p = k_p \cdot [M] \cdot [P\cdot], \tag{1.5}$$

where k_p is the propagation rate constant, [M] is the monomer concentration, and [P·] is the polymer radical concentration. The overall rate of termination, which includes both combination and disproportionation mechanisms, can be written as:

$$R_t = 2(k_{tc} + k_{td}) \cdot [P\cdot]^2 = 2k_t \cdot [P\cdot]^2, \tag{1.6}$$

where k_{tc} is the combination rate constant, k_{td} is the disproportionation rate constant, and k_t is the composite termination rate constant. Invoking the steady-state approximation, whereby $R_i = R_t$, equations 1.4 and 1.5 can be combined to give:

$$[P\cdot] = \sqrt{f_i \cdot \frac{k_d}{k_t}} \cdot [I_2]^{0.5}. \tag{1.7}$$

Thus, the rate of propagation for a free radical polymerisation, eq 1.5, can be written as:

$$R_p = k_p \cdot \sqrt{f_i \cdot \frac{k_d}{k_t}} \cdot [I_2]^{0.5} \cdot [M]. \tag{1.8}$$

Given that the rate of propagation, $R_p = -\frac{d[M]}{dt}$ and $[I_2]$ is relatively constant, the monomer concentration can be given as:

$$[M] = [M]_0 \cdot e^{-k_p \cdot \sqrt{f_i \cdot \frac{k_d}{k_t}} \cdot [I_2]^{0.5} \cdot t}, \tag{1.9}$$

where $[M]_0$ is the initial monomer concentration, and t is the reaction time. This eq 1.9 indicates that $\ln([M]_0/[M])$ should be proportional to t.

In the absence of any chain transfer side-reactions, the average kinetic chain length, $\bar{\nu}$, is defined as the average number of monomers that react with each primary radical:

$$\bar{\nu} = \frac{R_p}{R_i} = \frac{R_p}{R_t} = \frac{k_p \cdot [M]}{2k_t \cdot [P\cdot]} = \frac{k_p}{2\sqrt{f_i \cdot k_d \cdot k_t}} \cdot [M] \cdot [I_2]^{-0.5}. \tag{1.10}$$

For termination by combination, $\overline{M}_n$ is equal to $2\bar{\nu}$, while for termination by disproportionation, $\overline{M}_n$ is simply equal to $\bar{\nu}$. However, if chain transfer occurs then the modified kinetic chain length, $\bar{\nu}_{tr}$, is given by:

$$\bar{\nu}_{tr} = \frac{R_p}{R_t + R_{tr}}, \quad (1.11)$$

where R_{tr} is the rate of chain transfer.

Therefore, the molecular weight distributions differ for polymer chains terminated by combination and those terminated by disproportionation. If the probability of propagation is given by $p_p = R_p / \left(R_p + R_t + R_{tr}\right)$,[1] for termination by combination with corresponding $\overline{M}_{n\_c} = \frac{1}{1-p_p}$ and $\overline{M}_{w\_c} = \frac{1+p_p}{1-p_p}$, the $\overline{M}_{w\_c} / \overline{M}_{n\_c}$ is given by 1 + p_p, while for termination by disproportionation with corresponding $\overline{M}_{n\_c} = \frac{2}{1-p_p}$ and $\overline{M}_{w\_c} = \frac{2+p_p}{1-p_p}$, the $\overline{M}_{w\_c} / \overline{M}_{n\_c}$ is given by 1 + p_p/2. As p_p approaches unity and if R_t and R_{tr} are smaller than R_p, then the $\overline{M}_{w\_c} / \overline{M}_{n\_c}$ for a free radical polymerisation should lie between 1.5 and 2.0.[7] The development of controlled/living free radical polymerisation techniques (see following section) over the past thirty years provides better control over the target DP and ensures significantly lower $\overline{M}_{w\_c} / \overline{M}_{n\_c}$ values.[7, 12-15]

1.1.1.2 Controlled/Living Free Radical Polymerisation

Controlled/living free radical polymerisation, or reversible-deactivation radical polymerisation (RDRP)[2] requires a dynamic equilibrium between the active polymer radicals and the dormant species in order to lower the radical concentration and suppress the rate of termination relative to that of propagation. Atom transfer radical polymerization (ATRP) and nitroxide-mediated polymerisation (NMP) involve reversible deactivation,[13-18] whereas reversible addition-fragmentation chain transfer (RAFT) polymerisation is based on the principle of rapid reversible chain transfer.[13] In principle, living anionic polymerisation can provide excellent control over the polymer MWD and target DP.[13, 15, 17, 19] However, in practice this technique is only applicable to a rather narrow range of vinyl and cyclic monomers and is highly intolerant of both monomer functionality and the presence of protic sources (e.g. water).[13] On the other hand, RAFT polymerisation involves a malodorous organosulfur-based RAFT agent, which is located on every polymer chain-end and confers intrinsic colouration.[14, 15, 20-22]

1.1.1.3 Reversible Addition-Fragmentation chain Transfer (RAFT) Polymerisation

RAFT polymerisation utilises a thiocarbonylthio chain transfer agent (CTA) to create a dynamic equilibrium between the polymer radicals and the dormant polymer chains.[15, 21] The initiation and propagation stages follow the same mechanism as that for a conventional free radical polymerisation (Figure 1.1 i and ii).[15, 21] However, the polymer radicals then react reversibly with the CTA to produce dormant chains plus new primary radicals that are capable of further propagation (Figure 1.1 iii, iv and v).[15, 21] In a RAFT polymerisation for

which 100% monomer conversion is achieved, the target DP simply depends on the initial monomer concentration divided by the CTA concentration, as indicated by eq. (1.12):[15, 21]

$$DP_{RAFT} = \frac{[M]_0}{[CTA]}, \quad (1.12)$$

For a well-controlled RAFT polymerisation, an appropriate CTA for a given monomer should be selected and the [CTA]/[I] molar ratio should be optimised to achieve a relatively narrow MWD (e.g. $M_w/M_n < 1.20$).[16] This is much better control than that achieved via conventional free radical polymerisation.[21-23] Moreover, because RAFT polymerisation involves radical chemistry it is much more tolerant of monomer functionality and protic solvents than living anionic polymerisation.[21-23]

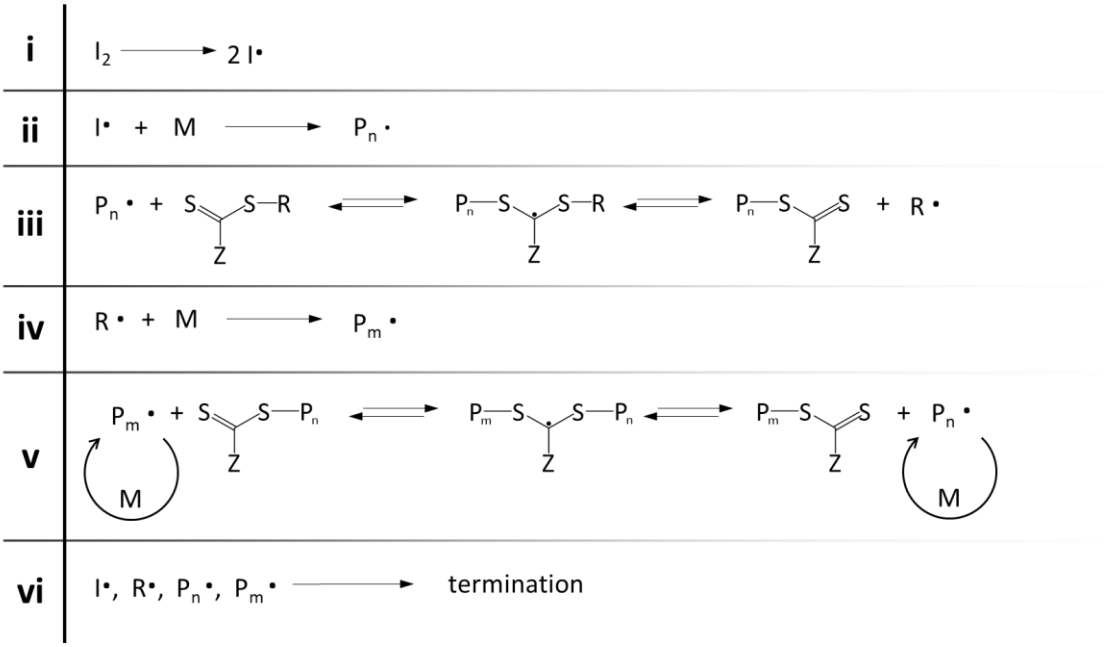

Figure 1.1. A schematic presentation of reversible addition-fragmentation chain transfer (RAFT) polymerisation.

1.1.1.4 Emulsion Polymerisation

Aqueous emulsion polymerisation requires a water-immiscible monomer, a water-soluble initiator, a suitable surfactant and water.[24, 25] Compared to free radical solution polymerisation, emulsion polymerisation can produce high molecular weight polymers at a relatively fast rate of polymerisation while achieving efficient heat transfer.[24] Moreover, very high monomer conversions (> 99%) can be achieved and water is a cheap, non-toxic, non-flammable solvent. Thus, aqueous emulsion polymerisation is considered to be an environmentally-friendly process.

The classical mechanism for emulsion polymerisation can be subdivided into three intervals. Interval I involves particle nucleation (Figure 1.2).[24, 25] There are three possible processes: homogeneous nucleation, micellar nucleation or monomer droplet nucleation.[24, 25] For

homogeneous nucleation, there are no micelles present prior to the polymerisation. Homogeneous nucleation typically occurs when the monomer solubility is relatively high.[26] Once surface-active oligomers are formed within the aqueous continuous phase, self-assembly occurs *in situ* to produce micelles. This is also known as 'surfactant-free' emulsion polymerisation.[27] In the case of micellar nucleation, the added surfactant forms micelles and monomer becomes partitioned within the micelle cores. In both cases, the water-soluble radicals generated via thermal decomposition of the initiator (e.g. ammonium persulfate) enter such micelles, which become the locus for the ensuing polymerisation. For monomer droplet nucleation, the monomer droplets must be relatively fine. Normally, the monomer droplets are µm-sized and their number concentration is relatively low. However, if the monomer droplet diameter is reduced to around 80 – 300 nm, then such droplets can efficiently capture oligomeric radicals from the aqueous continuous phase. This formulation is sometimes known as 'miniemulsion polymerisation'.[28]

Interval II involves particle growth with the continued presence of monomer droplets (Figure 1.2).[24] Because the polymerisation occurs exclusively within the particles, the rate of polymerisation of free radical polymerisation, eq 1.5, can be rewritten as:[25, 29]

$$R_p = k_p \cdot [M]_p \cdot \left(\bar{n} \cdot \frac{N_p}{N_A} \right), \tag{1.13}$$

where $[M]_p$ is the monomer concentration within the particles, $\bar{n}$ is the average number of radicals per particle, N_p is the number of particles and N_A is Avogadro's constant. Smith-Ewart theory provides estimates for $\bar{n}$ and N_p.[29, 30] The balance of $\bar{n}$ can be described as the sum of the rate of radical entry into particles, the rate of radical exit from particles, and the rate of termination within the particles. The ideal zero-one kinetic condition when $\bar{n}$ is approximately equal to 0.5 is a prerequisite for eq 1.13: this ideal condition also predicts that N_p remains constant during Interval II. At equilibrium, monomer-swollen particles can be described by the Morton-Kaizerman-Altier equation:[31]

$$\frac{2 \cdot V_m \cdot \gamma_{ps}}{k_B \cdot T \cdot R_{ep\_e}} = -\ln(1-\phi_p) - \left(1 - \frac{1}{\overline{M}_n}\right) \cdot \phi_p - \chi_{pm} \cdot \phi_p^{\,2}, \tag{1.14}$$

where V_m is the molar volume of monomer, R_{ep_e} is the equilibrium particle radius, k_B is the Boltzmann constant, T is the reaction temperature (in K), ϕ_p is the polymer volume fraction within the particles, and χ_{pm} is the Flory-Huggins interaction parameter for the polymer and the monomer. The left-hand side of eq 1.14 represents the chemical potential of the interfacial energy, and the right-hand side is based on Flory-Huggins mean-field theory[1, 32, 33], which will be discussed in section 1.2.2.

Interval III involves particle growth in the absence of any monomer droplets (Figure 1.2 Interval III).[24, 25] During this interval, the rate of termination may be reduced by the high viscosity conferred by the high molecular weight polymer chains within the particles. Under such conditions, R_p may increase significantly, which is known as the autoacceleration effect.[25]

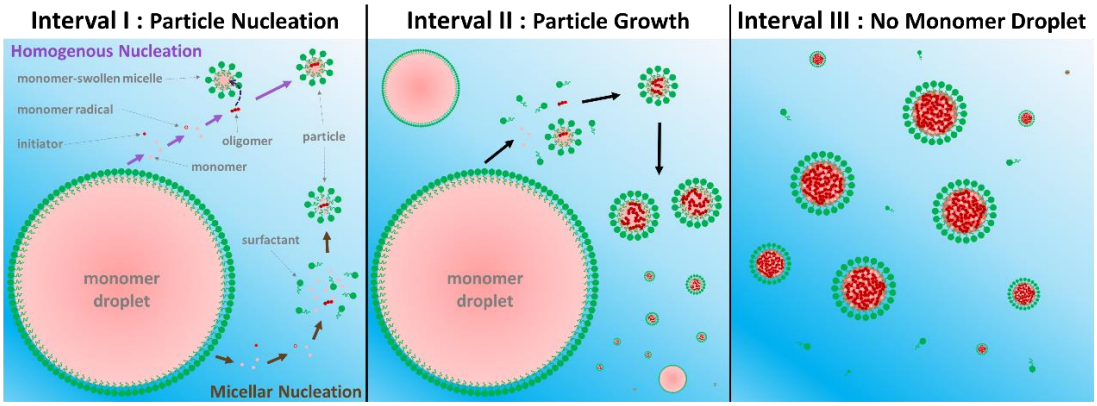

Figure 1.2. Schematic representation of the three main intervals for emulsion polymerisation.[24, 25] Particle formation via either homogeneous nucleation (purple arrows) or micellar nucleation (brown arrows) occurs during Interval I. Particle growth occurs during Interval II via polymerisation within the monomer-swollen particles stablished by surfactants (green symbols). There are no remaining monomer droplets (pink circle stabilised by surfactants as green symbols) during Interval III: particle growth occurs more slowly in this case because no monomer replenishment occurs as the polymerisation occurs within the particles.

1.1.1.5 Dispersion Polymerisation

To provide micron-size monodisperse particles, dispersion polymerisation defined as a type of precipitation polymerisation could produce polymer particles of 0.1 - 15 µm in diameter[34] with various monomers, including methyl methacrylate[35], styrene[36-41], n-butyl acrylate[42, 43], and n-vinyl pyrrolidone[44]. Dispersion polymerisation involves a suitable solvent, a soluble monomer in such solvent, a soluble initiator, and a soluble polymeric stabiliser (Figure 1.3 i).[2, 34] After initiation, the polymer radicals grow in size (Figure 1.3 ii) and eventually become insoluble (Figure 1.3 iii). After the formation of colloidally unstable nuclei (Figure 1.3 iii), aggregation of these nascent particles occurs with the concomitant adsorption of stabiliser chains to confer colloidal stability (Figure 1.3 iv and v).[34, 45] Thereafter, the number of particles, which are potentially monomer-swollen, remain relatively constant but particle growth continues until all the monomer is consumed (Figure 1.3 vi).[34]

Particle stabilisation (Figure 1.3 iv) has been commented as the more critical process to determine particle size rather the precipitation or nucleation of the particles (Figure 1.3 iii).[36] This argument is also confirmed by the formula of the radius of particle of dispersion polymerisation, R_D.[38] And R_D can be given with a relation of the molecular weight of polymeric stabiliser, M_{PS}, the weight of polymeric stabiliser in feed, W_{PS}, the critical area of particle surface covered by a single polymeric stabiliser, S_{crit}, the diffusion-controlled rate constant for particle coagulation, k_C, and the other constants related to radical imitation as:[38]

$$R_D \sim \left(\frac{M_{PS}}{W_{PS} S_{crit}}\right)^{\frac{1}{2}} \cdot k_C^{\frac{1}{6}} \cdot \left(\frac{k_t}{f_i \cdot k_d \cdot [I_2]}\right)^{\frac{1}{12}}, \qquad (1.15)$$

And this relation has been tested by a few experiments.[46-51] Therefore, it is significant to study the mechanism of particle stabilisation. In non-polar medium, it requires the absorbed polymeric stabilisers to create a steric barrier to stabilise the particles, which named as steric stabilisation mechanism.[52] For the polymeric stabiliser criteria of non-polar system, it

requires high surface coverage and strong adsorption on particles for the well-soluble polymeric stabilisers in low free polymeric stabiliser concentration.[45] Several typical polymeric architectures are acceptable for dispersion polymerisation in non-polar medium: random copolymers P_{an}-P_{sol} (e.g. polydimethylsiloxane-poly(glycidyl methacrylate) (PDMS-PMMA) in hexanes[53] and heptane[54]), block copolymers P_{an}-P_{sol} or P_{an}-P_{sol}-P_{an} (e.g. polydimethylsiloxane-polystyrene (PDMS-PS) in n-heptane[55]), graft copolymers P_{an}-P_{sol} (e.g. poly(12-hydroxystearic acid)-poly(glycidyl methacrylate) (PHSA-PMMA) in n-alkanes[56, 57]), and reactive homopolymers P_{sol} (e.g. poly(lauryl methacrylate) (PLMA) in n-alkanes[58]). P_{an} and P_{sol} are represented anchoring polymer block on the particle surface and soluble polymer block. In polar medium (e.g. water), the particles can be also stabilised by polyelectrolyte or polyampholyte brushes to not only create a steric barrier but also electrical double layers.[59, 60] The mechanism of particle stabilisation involves electrical double layers is named as electrostatic stabilisation.[59, 60] Poly(methacrylic acid) (PMAA) has been reported by Fritz[59] as one of the polymeric stabilisers for dispersion polymerisation of polystyrene−poly(butyl acrylate). And in this research, Derjaguin-Landau-Verwey-Overbeek (DLVO) theory has been applied and relatively successfully interpret the particle stabilisation. Since the coating process by dispersion polymerisation in 1960s,[45] more research targeted to prepare polymer colloids by dispersion polymerisation. Dispersion polymerisation of PMMA stabilised by PHSA in hexane provide particle to embed fluorescent dyes (e.g. rhodamine isothiocyanate) for further coating and printing applications.[61] To reduce the cost and promote environmental-friendly synthesis of polyacrylonitrile (PAN), dispersion polymerisation of PAN stabilised by PDMS-PS-PDMS triblock copolymeric stabiliser in alkanes have been reported.[62] To produce around 1 - 18 µm monodisperse particle, polystyrene has been prepared dispersion polymerisation by methanol, ethanol, and 2-methoxyethanol/ethanol mixture.[36-41] Very few studies in pure ethanol solvent have been reported[63], and more aqueous dispersion polymerisation via RAFT synthesis will be discussed in Polymerisation-Induced Self-Assembly Section.

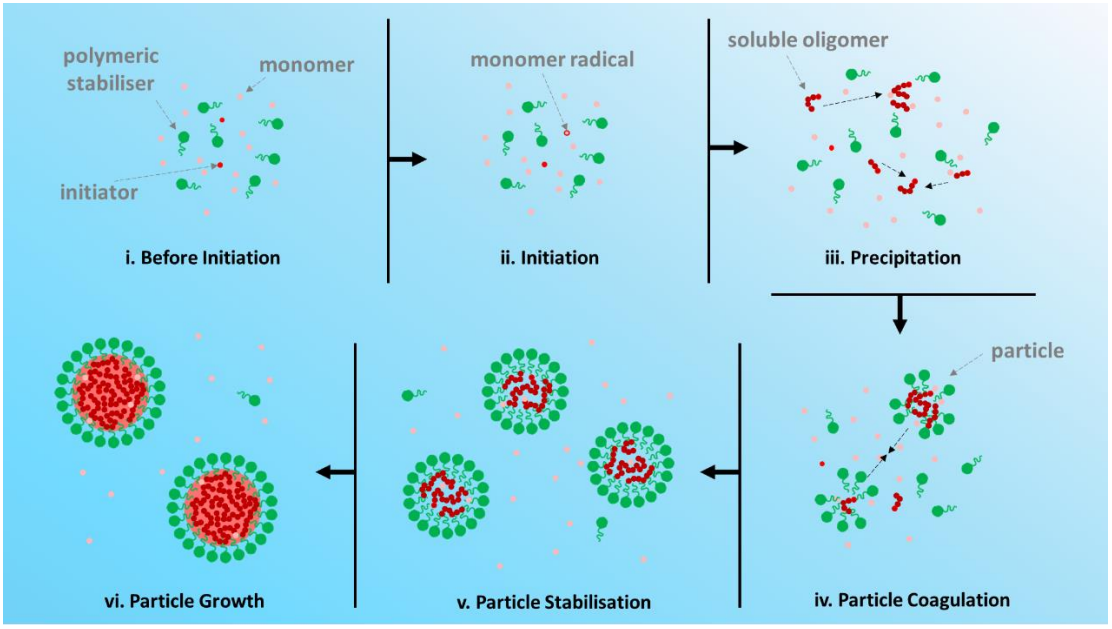

Figure 1.3. Schematic representation of the mechanism of dispersion polymerisation.[34, 45, 64] Dispersion polymerisation involves initiator (red circle), soluble monomer (pink circle), and polymeric stabiliser (green symbol) (i). After initiation, the monomer radicals generate soluble oligomers (ii), and then, when the repeat unit of soluble oligomers increase to a critical point, such oligomers can be considered as insoluble polymers. And such polymers precipitate into particles stabilised by polymeric stabilisers (iii). The unstable particles then coagulate (iv) and form stable particles (v). The particles grow until monomers are all consumed (vi).

1.2 Polymer Physics

Linear polymers can be obtained by homopolymerisation of various vinyl monomers.[4, 65] However, for branched, comb-like or crosslinked copolymer architectures, at least two comonomers are usually employed.[4] Polymer chains can be represented by an end-to-end vector, $\vec{b}$, which represents segments comprising either just one or multiple repeat units. Such vectors are named Kuhn segments (Figure 1.4).[3, 4, 65] Chain conformations can be characterised in terms of such end-to-end vectors or segments. If segment motion is independent of the rest of the chain, the chain conformation can be described by an ideal chain model.[3] Clearly, the segments of the polymer chains cannot share the same space as other segments.[3] Thus, excluded volume effects influence the chain conformation.[3]

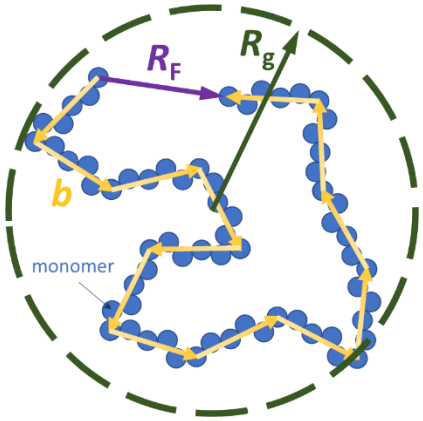

Figure 1.4. A schematic presentation of polymer chain constructed by monomers (blue circles). Kuhn Segments of length as *b* are constructed by serval monomers (5 monomers in the case in the figure). R_F is the root-mean-square end-to-end distance, and R_g is the root-mean-square radius of gyration.

1.2.1 Ideal Chain Models and Real Chain Models

For a single ideal polymer chain, the segments of such polymer chains can be described by random walk model.[3, 66] Because this random walk is in 3D space, the movement of the segments can be described by a Cartesian coordinate system via a Markovian process. Thus, each segment can only choose one dimension, and the probability of this choice is always 1/6. Moreover, because the number of segments, *N*, is relatively large, the probability density function, $P(r_N)$, of the final position of the chain-end r_N for a polymer with *N* segments is given by:[3, 66]

$$P(r_N) = \frac{1}{\left(2\pi \cdot \frac{Nb^2}{3}\right)^{\frac{3}{2}}} e^{-\frac{1}{2} \cdot \frac{r_N^2}{\frac{Nb^2}{3}}} . \quad (1.16)$$

The standard deviation for such a distribution of r_N, $< (r_N - r_0)^2 >$, is given by $b \cdot N^{0.5}$, which is defined as the root-mean-square end-to-end distance, R_F. Unfortunately, there is no suitable measurement technique for R_F. Thus, the root-mean-square radius of gyration, R_g, is introduced, as given by:[4]

$$R_g = \sqrt{\left\langle \frac{1}{N+1} \sum_{i=0}^{N} \left(r_i - \frac{1}{N+1} \sum_{j=0}^{N} r_j \right) \right\rangle} . \quad (1.17)$$

R_g is calculated to be $b \cdot N^{0.5}/6^{0.5}$. If all the probabilities between segments of the polymer chains follow a Gaussian distribution, this corresponds to a Gaussian chain model. For such an ideal polymer chain, the change in free energy is given by the change in entropy for the polymer chain conformations, ΔS_G. For any part of a Gaussian chain with n segments, minimisation of its Helmholtz free energy, ΔA_G, gives:[4]

$$\Delta A_G = -T \Delta S_G = \frac{3k_B T}{2nb^2} \cdot r_n^2 , \quad (1.18)$$

where T is the absolute temperature. The condition for the Gaussian chain to approach equilibrium is:[4]

$$\frac{\partial \Delta A}{\partial r_n} = \frac{3k_B T}{nb^2} \cdot r_n . \quad (1.19)$$

For Hooke's law, the force constant is equal to $\left(3k_B T\right) / \left(nb^2\right)$, so the elastic potential energy as given by eq 1.19 stretches the end-to-end distance of the Gaussian chain, which indicates that the entropic elasticity is a property of the ideal chain model.[4]

For such an ideal chain model, there is no memory of the segmental positions. However, for real chains, any given segment cannot overlap with other segments. To describe real chains by mathematical models, one of the options is the self-avoiding walk (SAW) model[66, 67], and this model provides an opportunity to study the polymer chain properties by simulations[4]. When a single segment occupies a volume v_e, the entropy change for such an excluded volume effect, ΔS_e, is given as:[4, 68]

$$\Delta S_e = k_B \ln \frac{V_o - v_e}{V_o} \approx -k_B \frac{v_e}{V_o} , \quad (1.20)$$

where V_o is the volume occupied by a single polymer chain. For the pair excluded volume interactions, combined with ΔS_G, the Helmholtz free energy of a polymer chain accounting for the effect of excluded volume, ΔA_e, is given as:[4, 68-70]

$$\Delta A_e = -T\left(\Delta S_e + \Delta S_G\right) = k_B T \cdot \frac{N^2}{2} \cdot \frac{b^3}{R_F^3} + \frac{3k_B T}{2Nb^2} \cdot R_F^2 . \quad (1.21)$$

To minimise ΔA_e as function of R_F, R_F is proportional to $N^{3/5}$. For only three-body interactions (which implies weaker interactions between the segments), the Helmholtz free energy of a polymer chain accounting for the effect of excluded volume, ΔA_e, is given as:[4, 68-70]

$$\Delta A_e = -T\left(\Delta S_e + \Delta S_G\right) = k_B T \cdot \frac{N^3}{3} \cdot \left(\frac{b^3}{R_F^3}\right)^2 + \frac{3k_B T}{2Nb^2} \cdot R_F^2 , \quad (1.22)$$

To minimise ΔA_e as function of R_F, R_F is proportional to $N^{0.5}$, which matches the R_F indicated above for an ideal chain model. However, V_o ideally describes the polymer chains as solid cubes (eq 1.21). A fractal dimension, D_f, is required for the polymer chains, so V_o is now expressed as R_F^d.[69, 70] Consequently, eq 1.21 can be rewritten as:[69, 70]

$$\Delta A_{e\_d} = -T\left(\Delta S_e + \Delta S_G\right) = k_B T \cdot \frac{N^2}{2} \cdot \frac{v_e}{R_F^d} + \frac{3k_B T}{2Nb^2} \cdot R_F^2 . \quad (1.23)$$

To minimise ΔA_{e_d} of R_F, R_F is proportional to $N^{3/(d+2)}$. Moreover, R_F is proportional to N^v, which indicates that the exponent v is equal to $3/(d+2)$.[69, 70] For fractal dimensions 1, 2, 3 and 4, v = 1, 3/4, 3/5 or 0.5, respectively. If the fractal dimension exceeds 4, the contribution of elastic energy potential, ΔS_G, is stronger than the repulsive effect arising from the excluded volume, ΔS_e.[69, 70]

1.2.2 Polymer Solutions and Flory-Huggins Mean-field Theory

Most linear polymers can be dissolved in a suitable solvent to form a polymer solution.[71] The Flory-Huggins mean-field theory was developed to describe the thermodynamics of such a system.[1, 32, 33] This is a lattice theory with a number of sites, n_{site}. The entropy of the polymer solution per site, $\Delta S_{mix\_FH}/(k_B \cdot n_{site})$, is given by:[4]

$$-\frac{\Delta S_{mix\_FH}}{k_B \cdot n_{site}} = \frac{\phi_{p\_FH}}{N} \ln \phi_{p\_FH} + \left(1-\phi_{p\_FH}\right) \ln\left(1-\phi_{p\_FH}\right), \quad (1.24)$$

where ϕ_{p_FH} is the volume fraction of the polymer. The internal energy can be described as the change in interactions per site, $\Delta U_{mix\_FH}/(k_B T \cdot n_{site})$:[4]

$$\frac{\Delta U_{mix\_FH}}{k_B T \cdot n_{site}} = \chi_{ps} \cdot \phi_{p\_FH} \cdot \left(1-\phi_{p\_FH}\right), \quad (1.25)$$

where χ_{ps} is the Flory-Huggins parameter for the polymer-solvent interaction. This parameter is defined as:[4]

$$\chi_{ps} = \frac{Z_{FH}\left(\varepsilon_{PS} - \frac{\varepsilon_{PP} + \varepsilon_{SS}}{2}\right)}{k_B T}, \tag{1.26}$$

where Z_{FH} is the bond number for each site, and ε_{PS}, ε_{PP}, and ε_{SS} are the polymer-solvent, polymer-polymer, and solvent-solvent interactions, respectively. Therefore, the Helmholtz free energy of the polymer solution per site, $\Delta A_{mix\_FH}/(k_B T \cdot n_{site})$, is given by:[4]

$$\frac{\Delta A_{mix\_FH}}{k_B T \cdot n_{site}} = \frac{\phi_{p\_FH}}{N}\ln\phi_{p\_FH} + \left(1-\phi_{p\_FH}\right)\ln\left(1-\phi_{p\_FH}\right) + \chi_{ps}\cdot\phi_{p\_FH}\cdot\left(1-\phi_{p\_FH}\right). \tag{1.27}$$

Eq 1.27 also indicates that the chemical potential difference for the polymer chain in solution and in its melt, $\Delta\mu_{p\_FH}/(k_B T)$, is given by:[4]

$$\frac{\Delta\mu_{p\_FH}}{k_B T} = \ln\phi_{p\_FH} - (N-1)\left(1-\phi_{p\_FH}\right) + \chi_{ps\_FH}\cdot N\cdot\left(1-\phi_{p\_FH}\right)^2. \tag{1.28}$$

while the chemical potential difference between the solution and the pure solvent, $\Delta\mu_{s\_FH}/(k_B T)$, is given by:[4]

$$\frac{\Delta\mu_{s\_FH}}{k_B T} = \ln\left(1-\phi_{p\_FH}\right) + \left(1-\frac{1}{N}\right) + \chi_{ps}\cdot{\phi_{p\_FH}}^2. \tag{1.29}$$

The corresponding osmotic pressure, Π, is given by:[4]

$$\frac{V_{site}\cdot\Pi}{k_B T\cdot n_{site}} = \frac{\phi_{p\_FH}}{N} - \ln\left(1-\phi_{p\_FH}\right) - \phi_{p\_FH} - \chi_{ps}\cdot{\phi_{p\_FH}}^2, \tag{1.30}$$

where V_{site} is the total volume occupied by the lattice sites.

1.2.3 Polymers in Dilute Solution

For a dilute solution of a polymer, eq 1.27 can be rewritten as:[4, 70]

$$\frac{\Delta A_{mix\_FH}}{k_B T\cdot n_{site}} = \frac{\phi_{p\_FH}}{N}\ln\phi_{p\_FH} + \frac{1}{2}{\phi_{p\_FH}}^2\left(1-2\chi_{ps\_FH}\right) + \frac{1}{6}{\phi_{p\_FH}}^3 + O\left({\phi_{p\_FH}}^4\right), \tag{1.31}$$

In this equation, the second term with ${\phi_{p\_FH}}^2$ represents the pair interaction between segments. The coefficient, $(1 - 2\chi_{ps\_FH})$, represents the repulsions between repeat units normalised with respect to the interactions between the adjacent sites. This coefficient is the excluded volume parameter for pair interactions, which indicates that the interactions within the real chain are based on changes in the polymer-solvent interaction on mixing.[70] For the third ${\phi_{p\_FH}}^3$ term (with no coefficient related to χ), this indicated that the three-body

interactions of the segments are not accounted for by the excluded volume effect.[70] Compared with eq 1.22 by considering solely three-body interactions of a result that R_F is proportional to $N^{0.5}$, the third $\phi_{p\_FH}^3$ term indicates that polymer chains subjected to only three-body interactions can be regarded as ideal chains.[70]

1.2.4 Semidilute Polymer Solution and Concentrated Polymer Solution

When the polymer solution concentration increases, and the polymer chains start to overlap with each other (Figure 1.5), this overlap threshold density, ρ^*, is defined as:[4]

$$\rho^* = \frac{1}{N_A}\frac{M_b N}{R_F^3}, \tag{1.32}$$

When R_F is given as $b \cdot N^{\nu}$, the overlap threshold density can be rewritten as:[4]

$$\rho^* = \frac{1}{N_A}\frac{M_b N}{b^3 N^{3\nu}} = \frac{1}{N_A}\frac{M_b}{b^3 N^{3\nu-1}}, \tag{1.33}$$

It follows that, for a real chain with $\nu = 3/5$, ρ^* is proportional to $b^{-3} \cdot N^{-4/5}$.[4] Above such an overlap threshold density, the density of the polymer solution is equal to the density of the segments of the polymer chains, which indicates that the conformations of the polymer chains are equivalent to the conformations of the segments. In such a polymer solution, the segments may be considered to be blobs that exhibit similar geometrical properties to the polymer chains. Therefore, the blob size, ξ_b, can be described with the number of segments, g, of length b, as:[4]

$$\xi_b = b \cdot g^{\nu}. \tag{1.34}$$

Above ρ^*, the density of the polymer solution is given by:[4]

$$\rho_{\geq\rho^*} = \frac{1}{N_A}\frac{M_b g}{\xi_b^3}, \tag{1.35}$$

and, according to equations 1.34 and 1.35, the blob size is given by:[4]

$$\xi_b = \left(\frac{N_A}{M_b}\right)^{\nu} \cdot \left(\rho_{\geq\rho^*}^{\frac{\nu}{1-3\nu}}\right) \cdot \left(b^{\frac{1}{1-3\nu}}\right). \tag{1.36}$$

For a real chain, ξ_b is proportional to $\left(\rho_{\geq\rho^*}^{-\frac{3}{4}}\right) \cdot \left(b^{-\frac{5}{4}}\right)$. When the density continuously increases up to a density ρ^{**}, the blob size is simply equal to the segment length, or:[4]

$$\xi_{b\_\rho^{**}} = b. \tag{1.37}$$

This condition corresponds to a concentrated polymer solution, for which ρ^{**} is given by:[4]

$$\rho_{\geq\rho^*} = \left(\frac{N_A}{M_b}\right)^{3\nu-1} \cdot \left(b^{-3}\right). \tag{1.38}$$

When the density of the polymer solution exceeds ρ^*, the osmotic pressure, Π_{ρ^*}, is equal to $\Pi \cdot \left(\frac{\rho}{\rho^*}\right)^{\frac{1}{3\nu-1}}$, which indicates that the osmotic pressure of the semidilute polymer solution depends on the density, rather than the degree of polymerisation.[4]

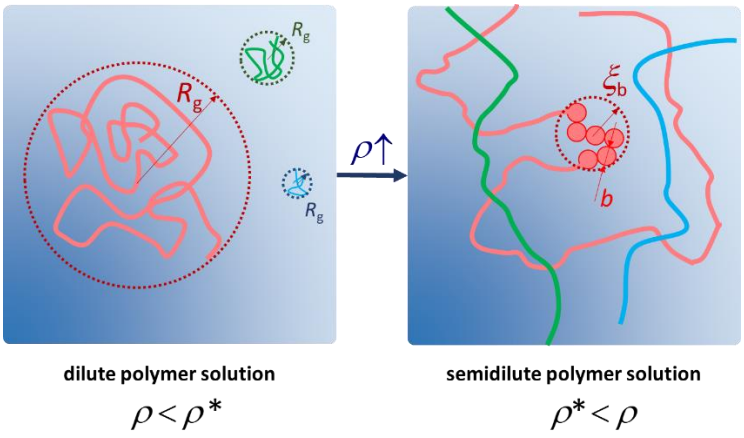

Figure 1.5. Schematic presentation of dilute polymer solution and semidilute polymer solution. In dilute polymer solution, polymer chains are independent to each other (left). Radius of gyration, R_g, can describe the conformation of the polymer chains. When the concentration of the polymer chain, ρ, increases to the point that polymer chains entangle with each other, it requires blob model to describe polymer conformations (right). The radius of the blob is ξ_b, and the length of the segment of the blob is b.

1.2.5 Phase Separation of a Polymer Solution

For a more universal situation, the solvent molecules can be replaced by a polymer B which dissolves polymer A. With this modification, eq 1.27 can be rewritten as:[4]

$$\frac{\Delta A_{mix\_FH}}{k_B T \cdot n_{site}} = \frac{\phi_{pA\_FH}}{N_A} \ln\phi_{pA\_FH} + \frac{\phi_{pB\_FH}}{N_B} \ln\phi_{pB\_FH} + \chi_{pApB} \cdot \phi_{pA\_FH} \cdot \phi_{pB\_FH}, \tag{1.39}$$

where ϕ_{pA_FH} and ϕ_{pB_FH} are the volume fractions of polymer A and polymer B, respectively, N_{pA} and N_{pB} are the mean degrees of polymerisation of polymer A and polymer B, respectively, and χ_{pApB} is the Flory-Huggins parameter for polymer A-polymer B interactions.[1,

[4, 32, 33] To consider the situation where polymer chain B is replaced by polymer chain A, the change in chemical potential per site, $\Delta\mu_{ArepB\_FH}/(k_BT\cdot n_{site})$, is given by:[4]

$$\frac{\Delta\mu_{ArepB\_FH}}{k_BT\cdot n_{site}} = \ln\phi_{pA\_FH} - \frac{N_{pA}}{N_{pB}}\ln\phi_{pB\_FH} + 1 - \frac{N_{pA}}{N_{pB}} + \chi_{pApB}\cdot N_{pA}\cdot N_{pB}\cdot\left(\phi_{pB\_FH} - \phi_{pA\_FH}\right), \tag{1.40}$$

and therefore, for $\Delta\mu_{ArepB\_FH} = 0$, χ_{pApB} is given by:[4]

$$\chi_{pApB} = \frac{1}{N_{pB}}\frac{\ln\frac{\phi_{pA\_FH}^{\frac{1}{N_A}}}{\phi_{pB\_FH}^{\frac{1}{N_B}}} + \frac{1}{N_{pA}} - \frac{1}{N_{pB}}}{\phi_{pA\_FH} - \phi_{pB\_FH}}. \tag{1.41}$$

When $\partial\Delta\mu_{ArepB\_FH}/\partial\phi_{pA\_FH} < 0$, this means that:[4]

$$\chi_{pApB} > \frac{1}{2N_{pA}\cdot\phi_{pA\_FH}} + \frac{1}{2N_{pB}\cdot\phi_{pB\_FH}}, \tag{1.42}$$

so there is phase separation between the two polymers. This also indicates that the condition for a critical Flory-Huggins parameter, χ_{pApB_c}, for no phase separation of any ϕ_{pA_FH} is given by:[4]

$$\chi_{pApB} < \frac{N_{pB}^{\ 0.5}}{N_{pA}^{\ 0.5} + N_{pB}^{\ 0.5}} = \chi_{pApB\_c}. \tag{1.43}$$

1.2.6 Theories of Block Copolymer Phase Separation

For block copolymers, their phase separation has been studied by weak segregation theory (WST), strong segregation theory (SST), and self-consistent field theory (SCFT).[72-82] For WST, it indicates that the relatively small changes in energy between blocks produce the lamellar phase, cylindrical phase, and spherical phase in the context of diblock copolymer phase separation.[76] In principle, the critical point for the $[\chi_{pApB}\cdot N_{pA\&pB}]$, otherwise known as the diblock copolymer order-disorder transition at a given temperature, $[\chi_{pApB}\cdot N_{pA\&pB}]_{ODT\_WST\_c}$, should be equal to 10.5. For the SST model, it also produced the three main classical phases. In this case, $[\chi_{pApB}\cdot N_{pA\&pB}]_{ODT\_SST\_c}$ was predicted to be 9.5, which is close to the WST result. Moreover, SST also predicts the complex gyroid , perforated-lamellar and double-diamond phases, which have been experimentally observed.[83] However, neither SST nor WST can describe more complex structures. Thus, SCFT has been developed to provide more subtle details of phase separation.[84] In this model, the polymer chains are described as coarse-grained paths. Assuming that the volume densities of the segments of block A and block B are the same as ρ_0, the width of the interface for SCFT (Figure 1.6) is given as:[84]

$$w_{SCFT} = b \cdot \left(6\chi_{pApB}\right)^{-0.5} . \tag{1.44}$$

and the surface tension as:[84]

$$\frac{\gamma_{SCFT}}{k_B T} = \rho_0 b \left(\frac{\chi_{pApB}}{6}\right)^{0.5} . \tag{1.45}$$

The radius (or thickness), R_A, of the phase occupied by block A (Figure 1.6) can be determined by minimising the sum of the change in Helmholtz free energy for the polymer chain conformations by using eq 1.18,[84]

$$\Delta A_{G\_A} = \frac{3k_B T}{2N_{pA}{}^{2\nu} b^2} \cdot R_A{}^2 , \tag{1.46}$$

and the interfacial tension between the interface of block A and block B

$$\Delta A_{int} = \frac{\gamma_{SCFT} N_{pA} b^3}{R_A} , \tag{1.47}$$

as the function of R_A.[84] Therefore, R_A is determined to be $\frac{b^{\frac{5}{3}}}{\left(3k_B T\right)^{\frac{1}{3}}} \cdot \gamma_{SCFT}{}^{\frac{1}{3}} \cdot N_{pA}{}^{\frac{2\nu+1}{3}}$. Thus, with eq 1.45 for SCFT or SST, R_A is given by:[84]

$$R_A = b^2 \cdot \left(\frac{\rho_0}{3}\right)^{\frac{1}{3}} \cdot \left(\frac{\chi_{pApB}}{6}\right)^{\frac{1}{6}} \cdot N_{pA}{}^{\frac{2\nu+1}{3}} . \tag{1.48}$$

When $\nu = 1$, R_A is proportional to N_{pA}. Alternatively, if $\nu = 0.50$, then R_A is proportional to $N_{pA}{}^{2/3}$.

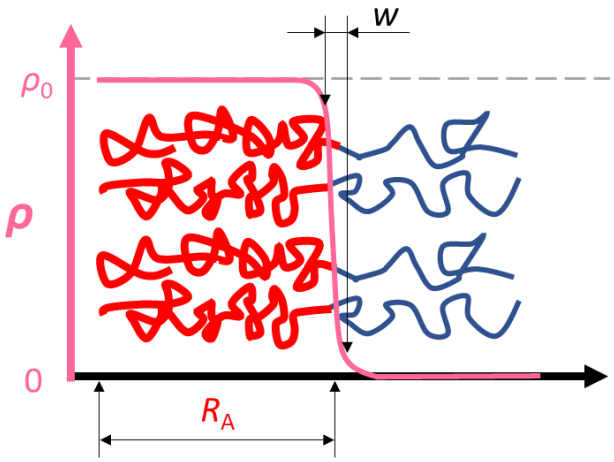

Figure 1.6. Schematic representation of relatively shape diblock copolymer phase separation between block A (red) and block B (blue). The volume density of block red (pink) decreases from ρ_0 to 0. The radius or thickness of block A is R_A. The width between block A and block B is w.

For more realistic situation, the densities of the segments of block A and block B are ρ_{pA} and ρ_{pB}, respectively, and the lengths of the segments of block A and block B are b_{pA} and b_{pB}, respectively. For such realistic situation, the width of the interface for SCFT is given as:[85]

$$w_{SCFT} = \left(\frac{6\chi_{pApB}\left(\rho_{pA}\rho_{pB}\right)^{0.5}}{\left(\beta_{pA}+\beta_{pB}\right)^{2}} \right)^{-0.5} . \tag{1.49}$$

and the surface tension as:[85]

$$\frac{\gamma_{SCFT}}{k_B T} = \left[\left(\rho_{pA}\rho_{pB}\right)^{0.5} \chi_{pApB} \right]^{0.5} \left[\frac{\beta_{pA}+\beta_{pB}}{2} + \frac{\left(\beta_{pA}-\beta_{pB}\right)^{2}}{6\left(\beta_{pA}+\beta_{pB}\right)} \right], \tag{1.50}$$

where parameters β_{pA} and β_{pB} are given as $(\rho_{pA}\cdot b_{pA}^2/6)^{0.5}$ and $(\rho_{pB}\cdot b_{pB}^2/6)^{0.5}$, respectively.

1.2.7 Estimation of the Flory-Huggins Parameter using Hansen Solubility Parameters (HSPs)

Both classical mean-field theory and the more refined WST, SST, and SCFT approaches all involve the Flory-Huggins parameter. To estimate the latter parameter, solubility parameters can be utilised. Thus, Hildebrand solubility parameters[86, 87] were introduced to estimate the enthalpic contribution to the Flory- Huggins parameter using the following expression:

$$\chi_{ps\_H\_Hb} = -T\frac{\partial \chi_{ps}}{\partial T} = \frac{V_s}{N_A k_B T}\left(\delta_{s\_Hb} - \delta_{p\_Hb}\right)^2, \tag{1.51}$$

where V_s is the molar volume of the solvent, and δ_{s_Hb} and δ_{p_Hb} are the cohesive energy densities of the solvent and polymer, respectively. Such Hildebrand solubility parameters are limited to regular solutions and do not consider associations between segments and solvents. For more detailed descriptions of these associations, Hansen introduced three-dimensional cohesive energy densities, a dispersion solubility parameter, δ_D, a polar solubility parameter, δ_P, and a hydrogen bonding solubility parameter, δ_H. Normally, the unit of solubility parameter is $MPa^{0.5}$. These three Hansen solubility parameters are normally presented as [δ_D, δ_P, δ_H]. The enthalpic contribution to the Flory- Huggins parameter by HSP is given by:[88, 89]

$$\chi_{ps\_H\_Han} = \frac{V_s}{N_A k_B T} \frac{4\left(\delta_{D\_s} - \delta_{D\_p}\right)^2 + \left(\delta_{P\_s} - \delta_{P\_p}\right)^2 + \left(\delta_{H\_s} - \delta_{H\_p}\right)^2}{4}, \quad (1.52)$$

where δ_{D_s} and δ_{D_p} are the dispersion solubility parameters for the solvent and polymer, respectively, δ_{P_s} and δ_{P_p} are the polar solubility parameters for the solvent and polymer, respectively, and δ_{H_s} and δ_{H_p} are the hydrogen bonding solubility parameters for the solvent and polymer, respectively. When combined with the entropic contribution[90],

$$\chi_{ps\_S} = \frac{\partial\left(T \cdot \chi_{ps}\right)}{\partial T} = \frac{1}{Z_{FH}}\left(1 - \frac{1}{N}\right)^2, \quad (1.53)$$

the Flory-Huggins parameter is estimated by HSP to be:[89, 91]

$$\begin{aligned} \chi_{ps\_Han} &= \chi_{ps\_H\_Han} + \chi_{ps\_S} \\ &= \frac{V_s}{N_A k_B T} \frac{4\left(\delta_{D\_s} - \delta_{D\_p}\right)^2 + \left(\delta_{P\_s} - \delta_{P\_p}\right)^2 + \left(\delta_{H\_s} - \delta_{H\_p}\right)^2}{4} \\ &\quad + \frac{1}{Z_{FH}}\left(1 - \frac{1}{N}\right)^2 \end{aligned}. \quad (1.54)$$

Normally, Z_{FH} can be chosen to be 2 or 3, and when N is huge, χ_{ps_S} is either 0.5 or 0.33. The research of estimation of Flory-Huggins parameters by Hansen solubility parameters successfully interpret the solubilities of poly(methyl methacrylate), poly(ethyl methacrylate), poly(ethyl methacrylate) and poly(butyl methacrylate) in various solvents.[92]

1.2.8 Thermodynamics of Self-assembly and Morphologies of Self-assembled Structures

Amphiphilic molecules in solution typically prefer to form aggregates.[93] To estimate the thermodynamics of such aggregates, the chemical potential of any given aggregate, $\mu_{i_{agg}}$, is given by:[93]

$$\mu_{agg} = \mu_{i_{agg}} = \mu_{i_{agg}}^0 + \frac{k_B T}{i_{agg}} \ln\left(\frac{c_{i_{agg}}}{i_{agg}}\right), \quad (1.55)$$

where $\mu_{i_{agg}}$ is the chemical potential equal to the chemical potential of any other aggregates with a differing aggregation number, i_{agg} is the aggregation number, $\mu_{i_{agg}}^0$ is the standard part of the chemical potential of the aggregates with an aggregation number of i_{agg}, and $c_{i_{agg}}$ is the

concentration of aggregates possessing an aggregation number of i_{agg}. To form aggregates with an aggregation number of i_{agg}, $\mu^0_{i_{agg}}$ should be less than $\mu^0_{1_{agg}}$. At equilibrium of a single amphiphilic molecule association and dissociation of the aggregates with an aggregation number of i_{agg}, the concentration of aggregates with an aggregation number of i_{agg} is given as:[93]

$$c_{i_{agg}} = i_{agg} \cdot \left(c_{1_{agg}} \cdot e^{\frac{\mu^0_{1_{agg}} - \mu^0_{i_{agg}}}{k_B T}} \right)^{i_{agg}} . \tag{1.56}$$

Given an aggregate of the dimensionality as D_{agg} with an amphiphilic molecule-amphiphilic molecule bond energy of $-\alpha_{agg} k_B T$, $\mu^0_{i_{agg}}$ is given as:[93]

$$\mu^0_{i_{agg}} = \mu^0_{\infty_{agg}} + \frac{\alpha_{agg} k_B T}{i_{agg}^{D_{agg}}}, \tag{1.57}$$

where $\mu^0_{\infty_{agg}}$ is the bulk energy per amphiphilic molecule, and α_{agg} is positive constant dependent on the strength of intermolecular interactions. When $D_{agg} = 1$, the aggregate is in rod-like structure (e.g. cylinder micelle). When $D_{agg} = 2$, the aggregate is in disk structure. When $D_{agg} = 3$, the aggregate is in spherical structure (e.g. spherical micelle). Combined equations 1.56 and 1.57, $c_{i_{agg}}$ can be rewritten as:[93]

$$c_{i_{agg}} = i_{agg} \cdot \left[c_{1_{agg}} \cdot e^{\alpha_{agg}\left(1 - \frac{1}{i_{agg}^{D_{agg}}}\right)} \right]^{i_{agg}}, \tag{1.58}$$

which indicates that

$$c_{1_{agg}} \le e^{-\alpha_{agg}\left(1 - \frac{1}{i_{agg}^{D_{agg}}}\right)}, \tag{1.59}$$

and thus, the critical micelle concentration, CMC, is given as the maximum of $c_{1_{agg}}$:

$$\mathrm{CMC} = e^{-\alpha_{agg}\left(1 - \frac{1}{i_{agg}^{D_{agg}}}\right)}. \tag{1.60}$$

For the micelles with

$$\alpha_{agg} = \frac{4\pi \cdot r^2_{1_{agg}} \cdot \gamma_{1_{agg}}}{k_B T}, \tag{1.61}$$

where $r_{1_{agg}}$ is the effective radius of the monomer, and $\gamma_{1_{agg}}$ is the interfacial free energy per unit area, CMC can be rewritten as:[93]

$$CMC_{micelle} \approx e^{-\frac{4\pi \cdot r_{1_{agg}}^2 \cdot \gamma_{1_{agg}}}{k_B T}}, \quad (1.62)$$

when i_{agg} is relatively large.

For aggregates formed by amphiphilic molecules, v_{pho} is the volume of the solvophobic component, a_{phi} is the optimal interfacial surface area occupied by the solvophilic component, and l_{pho_c} is the semi-empirical critical length of the solvophobic component. For aggregates with an aggregation number of i_{agg}, $i_{agg} \cdot a_{phi}$ is proportional $l_{pho\_c}^2$, and $i_{agg} \cdot v_{pho}$ is proportional $l_{pho\_c}^3$, which indicates that $a_{phi} \cdot l_{pho\_c}$ is proportional to v_{pho} with a coefficient equal to p_{agg}. This coefficient p_{agg} is known as the geometric packing parameter (Figure 1.7).[93] Its numerical value dictates the aggregate morphology. For $p_{agg} < 1/3$, the aggregates are spheres. For $1/3 < p_{agg} < 1/2$, the aggregates prefer to form cylinders. For $1/2 < p_{agg} < 1$, the aggregates form bilayers (i.e. vesicles). For $p_{agg} = 1$, the aggregates are likely to be planar bilayers (i.e. lamellae). To actually achieve different morphologies, sodium dodecyl sulfate (SDS) has been reported forming spherical micelle and cylinders in various concentration NaCl solution.[94-96] To achieve vesicle morphology, phosphatidyl choline (lecithin)[97], phosphatidyl serine[98], and phosphatidyl glycerol[99, 100] have been involved.

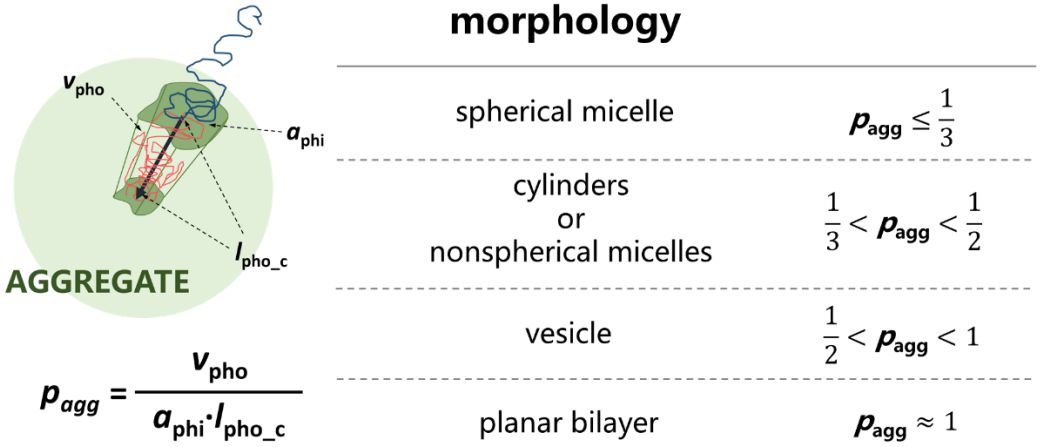

Figure 1.7. Schematic representation of the packing parameter, p_{agg}, which is given as $v_{pho}/(a_{phi} \cdot l_{pho\_c})$, where v_{pho} is the volume of the solvophobic component, a_{phi} is the optimal interfacial surface area occupied by the solvophilic component, and l_{pho_c} is the semi-empirical critical length of the solvophobic component. Different fractional values of p_{agg} correspond to differing morphologies.

1.3 Polymerisation-Induced Self-Assembly (PISA)

Polymerisation-induced self-assembly (PISA) is a highly convenient technique for the *in situ*

self-assembly of diblock copolymer nanoparticles. In contrast to traditional post-polymerisation processing techniques such as a solvent switch or thin film hydration,[101, 102] PISA can be used to prepare colloidal dispersions of nano-objects at up to 50% w/w solids.[103] RAFT polymerisation is the most common method used for PISA formulations.[104-106] RAFT aqueous emulsion polymerisation can be used to access the three most common copolymer morphologies (spherical micelles[107-112], worm-like micelles[108, 110-112], or vesicles[108, 111, 112]). However, in practice kinetically-trapped spheres are often encountered[109, 113-118], and unusual "monkey nut" morphology has been observed[119]. In contrast, since the first report of RAFT dispersion of 4-vinylpyridine (4VP) in tetrahydrofuran (THF) with macro-chain transfer agent (macro-CTA) dithiobenzoate-terminated polystyrene (PS−SC(S)Ph)[120], RAFT dispersion polymerisation can be conducted in various medium. [58, 104, 105, 121-130] RAFT dispersion polymerisation of *N*-isopropylmethacrylamide with poly(dimethylacrylamide)s macro-CTAs[121], 2-hydroxypropyl methacrylate (HPMA) with poly(2-(methacryloyloxy) ethylphosphorylcholine) (PMPC) macro-CTA[122], HPMA with poly(glycerol monomethacrylate) (PGMA) macro-CTA[123], and MMA or benzyl methacrylate (BzMA) with PGMA-PHPMA macro-CTA[124] have been reported in water. Such dispersions can be biological area.[131, 132] PISA via RAFT alcoholic dispersion polymerisation has been involved of the synthesis of PS with poly(2-dimethylaminoethyl methacrylate) (PDMAEMA) macro-CTA in ethanol to establish hexagonally packed hollow hoop structure in particle[125]. PISA synthesis of PS with PVP macro-CTA in methanol [126] and polyacrylamide (PAM) in methanol/water mixture[127] have also been studied. Also, PISA synthesis of PBzMA with poly(lauryl methacrylate) (PLMA) macro-CTA conducted in *n*-heptane as an example of non-polar solvents also provided spherical micelle, worm-like micelle, and vesicle morphologies.[58] Another example PISA synthesis conducted in non-polar medium was synthesis of PBzMA with poly(stearyl methacrylate) (PSMA) macro-CTA in mineral oil [128]. Typically, a solvophobic block is grow from one end of a soluble precursor block (Figure 1.8 i) to produce diblock copolymer chains (Figure 1.8 ii). The solvophobic block becomes insoluble at some critical degree of polymerisation (Figure 1.8 iii), which leads to micellar nucleation via self-assembly (Figure 1.8 iii) and eventually to the formation of sterically-stabilised diblock copolymer nanoparticles (Figure 1.8 iv). The initial micellar nuclei are spherical but p_{agg} increases as the solvophobic blocks grows (Figure 1.8 iv). If a sufficiently asymmetric diblock copolymer is targeted, this can lead to an evolution in copolymer morphology from spheres to worms to vesicles during the polymerisation.[123] Transient intermediate structures such as jellyfish have also been observed by TEM during PISA syntheses (Figure 1.8).[123]

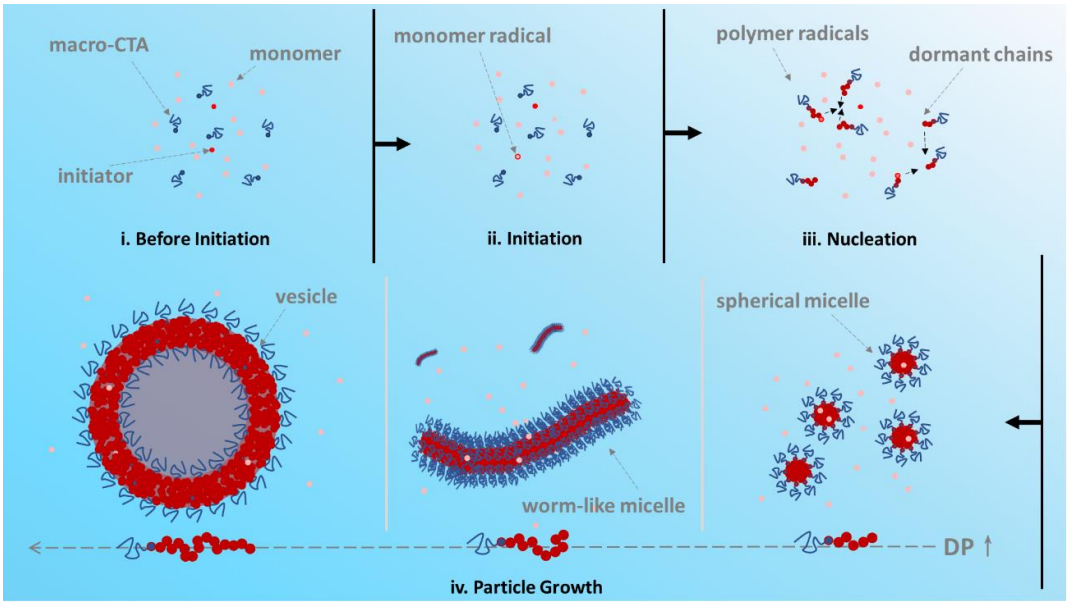

Figure 1.8. Schematic representation of the evolution in copolymer morphology during polymerisation-induced self-assembly via RAFT dispersion polymerisation from spherical micelles to vesicles.[104, 105]

1.4 Diffusion

The mass transport of monomer during PISA depends on diffusion.[133-137] For a traditional diffusion process, Fick's First law is applicable:[138-143]

$$J_m = D_m \frac{\partial \phi_m}{\partial x_m}, \tag{1.63}$$

where J_m is the molecular flux, D_m is the diffusion coefficient, ϕ_m is the number density, and x_m is the position. However, this is not sufficient to explain the diffusion of molecules across a concentration gradient. To introduce the chemical potential as the driving force, the flux can be rewritten as:[139, 141, 143]

$$J_m = v_m \cdot \phi_m, \tag{1.64}$$

where v_m is the velocity of the molecule. If the molecules have a constant velocity resulting from the balance of the friction, f_{fri}, and the driving force, F_{dri}, then v_m can be defined as:[139, 141, 143]

$$v_m = \frac{F_{dri}}{f_{fri}}. \tag{1.65}$$

The driving force for the molecules is described by their chemical potential, μ_m, such that:[139, 141, 143]

$$F_{dri} = \frac{\partial \mu_m}{\partial x_m} . \quad (1.66)$$

Therefore, Fick's First law can be rewritten as:

$$J_m = \frac{k_B T}{f_{fri}} \frac{\partial \mu_m}{\partial x_m} \phi_m , \quad (1.67)$$

Thus, D_m is equal to $\frac{k_B T}{f_{fri}}$ and, using the Stokes-Einstein equation [139, 141, 143], the friction is given as:

$$f_{fri} = 6\pi\eta_s R_m , \quad (1.68)$$

where η_s is the viscosity of the solvent, and R_m is the mean spherical radius of the molecule.

1.5 Monitoring Polymerisation Reactions *in Situ*

Various characterisation techniques have been used to monitor polymerisations,[144] including transmission electron microscopy (TEM)[145-147] and scanning electron microscopy (SEM)[148-151] for determining the evolution in copolymer morphology, gel permeation chromatography (GPC)[152-154] for assessing changes in the MWD, nuclear magnetic resonance (NMR)[155-157] for calculating the instantaneous monomer conversion and dynamic light scattering (DLS)[158-161] for examining particle size distributions. Unfortunately, most studies have focused on periodic sampling methods to investigate PISA syntheses,[58, 104, 105, 119, 122, 129, 162-166] with relatively few *in situ* studies being undertaken.[128, 144, 167, 168] In principle, various techniques are suitable for *in situ* studies.[144] For example, infrared spectroscopy (IR) can be used to monitor monomer conversion during the polymerisation. This technique was employed to monitor the living anionic polymerisation of either isoprene in THF or styrene in cyclohexane, respectively.[169] Similarly, the bulk polymerisation of methyl methacrylate has been monitored by *in situ* near-IR spectroscopy by measuring the conversion of vinyl groups to methylenic protons at 868 and 922 nm.[170] The synthesis of polyurethanes has also been investigated.[171] In this case, an near-IR band at 1648 nm was employed to monitor the extent reaction of isocyanate during the polymerisation. Furthermore, a series of *in situ* IR studies of various polymerisations conducted in supercritical carbon dioxide ($scCO_2$) have been published.[172-178] However, it is relatively difficult to calibrate the IR band intensity for such *in situ* IR studies.[144, 178] On-line matrix-assisted laser desorption ionization (MALDI) mass spectroscopy (MS) studies have also been applied to monitor the RAFT polymerisation of methyl methacrylate.[179] From peak molecular weight given by MS spectra, it successfully monitored the polymerisation process, but such MALDI MS required narrow MWD polymers to provide accurate polymerisation monitoring analysis.

In situ NMR spectroscopy studies have been widely applied to many chemical reactions, including polymerisations.[180-184] For controlled/living polymerisation, ^{1}H NMR spectroscopy

enables the monomer conversion to be determined during polymerisation.[144] For example, the polymerisation of styrene via ATRP[185] and the polymerisation of methyl methacrylate using a poly(ethylene glycol) macroinitiator via ATRP[19] were each monitored by *in situ* ^{1}H NMR spectroscopy. Similarly, the RAFT aqueous emulsion polymerisation of 2-methoxyethyl methacrylate using a poly(glycerol monomethacrylate) precursor has been examined by *in situ* NMR in D_2O and by *ex situ* NMR after dilution using d_6-DMSO.[167] *In situ* ^{1}H NMR studies also enabled determination of the polymer molecular weight and monomer conversion during the living ring-opening polymerisation of L-lactide.[186] Finally, *in situ* ^{23}Na and ^{13}C solid-state NMR spectroscopy has been used to follow the synthesis of poly(hydroxyaceticacid).[187]

In situ calorimetry has been applied to monitor polymerisations.[188-190] This approach has been employed for the terpolymerisation of styrene with *n*-butyl acrylate and methyl methacrylate via aqueous emulsion polymerization.[190] *In situ* conductivity measurements were also utilized because such terpolymerisations required an ionic surfactant.[144] Indeed, *in situ* conductivity studies of emulsion polymerisations are well-established,[191] and models have been validated for the polymerisation of styrene with various surfactants.[192] Such experiments can reveal the onset of particle nucleation, subsequent particle growth, and changes in the rate emulsion polymerisation.[192] Similarly, the emulsion polymerisation of *n*-butyl methacrylate in the presence of various concentrations of sodium lauryl sulfate has been reported.[193] Online solution densitometry studies have been used to determine the instantaneous monomer conversion during the homopolymerisation of styrene, the homopolymerisation of methyl methacrylate and the statistical copolymerisation of styrene with methyl methacrylate, acrylonitrile with methyl methacrylate, and vinyl acetate with methyl methacrylate.[194, 195] Online viscosity studies during the bulk polymerisation of *N*-vinyl pyrrolidone[196] and the synthesis of polyurethanes[197] enabled the determination of the molecular weight and monomer conversion. Online DLS studies during the synthesis of polystyrene, poly(methyl methacrylate), poly(butadiene-acrylonitrile), poly(styrene-butadiene) and poly(vinyl acetate) latexes has enabled the evolution in particle size to be determined.[198] Online SEC studies was used to assess the living radical polymerisation of methyl acrylate in DMSO[199] and also in toluene in the presence of additives such as alcohols and phenol.[200] *In situ* visible absorption spectroscopy studies during the PISA synthesis of poly(stearyl methacrylate)-poly(2,2,2-trifluoroethyl methacrylate) nanoparticles via RAFT dispersion polymerisation in *n*-tetradecane was reported by Cornel and co-workers.[201] In this case, a relatively weak absorption band at 446 nm assigned to the trithiocarbonate RAFT end-groups enabled the conversion of 2,2,2-trifluoroethyl methacrylate to be determined during the polymerisation. This approach enabled the onset of micellar nucleation to be identified from the corresponding rate enhancement.

Nevertheless, the above techniques typically only provide partial information such as the monomer conversion or the particle size during the polymerisation. A few online studies have involved two or more *in situ* characterisation techniques,[144, 189, 194, 199, 200, 202] but this necessarily involves more complex instrument design. To overcome these difficulties, small angle X-ray scattering (SAXS) has been employed for the *in situ* monitoring of polymerisations.[128, 167, 168, 203-205] This sophisticated approach has been applied to the formation of ordered mesoporous carbons[206], polyethylene[207], polylactide,[208] poly(vinylidene fluoride)[209], the study of morphological transitions of poly(ethylene oxide) and synthetic lithium hectorite nanocomposites.[210] *In situ* SAXS studies of morphological transitions of a polysulfobetaine-based triblock copolymer in 0.5 M NaCl solution have also been reported.[211] Such triblock copolymers formed a core-shell structure at 5 °C but almost all of the triblock copolymer chains became soluble in water on heating to 50 °C. *In situ* SAXS was also used to study the absorption of 20 nm silica nanoparticles onto sterically-stabilised

poly(2-vinylpyridine) latex and the rapid redistribution of these nanoparticles that occurred when introducing further bare latex particles.[212] The thermally-triggered release of silica nanoparticles from within poly(glycerol monomethacrylate)-poly(2-hydroxypropyl methacrylate) diblock copolymer vesicles was also monitored by *in situ* SAXS.[213] These experiments confirmed complete vesicle disintegration and hence silica nanoparticle release occurred within 8 min at 0 °C. The morphological transitions exhibited by poly(glycerol monomethacrylate)-poly(2-hydroxypropyl methacrylate) diblock copolymer vesicles that occurred on addition of 3-aminophenylboronic acid at pH 10.5 was studied by *in situ* SAXS.[214] In this case, the vesicles were gradually transformed into a binary mixture of spheres and worms within 45 min. Such *in situ* SAXS results were also confirmed by ex-situ TEM results. *In situ* SAXS studies of the rheological behaviours of poly(isoprene-ethylene glycol) in dioxane at 20% w/w solids injected in water in SIFEL microfluidic device and capillary interdiffusion.[215] This research observed the self-assembled aggregate formation during the mixture process. And it indicated that *in situ* SAXS studies could observe rapidly morphological transition of diblock copolymers on time scale of milliseconds. Another thermally triggered morphological transition research observed *in situ* SAXS method of poly(stearyl methacrylate)-poly(benzyl methacrylate) in mineral oil at 10% w/w solids presented a transition from vesicle to worm-like micelle.[216]

To monitor polymerisation *in situ*, numerous research of PISA process via RAFT synthesis of self-assembled particles have been reported. [128, 167, 168, 203-205] The PISA process via RAFT synthesis of poly(stearyl methacrylate)-poly(benzyl methacrylate) in mineral oil at 10% w/w solids was recorded by *in situ* SAXS method.[128] This research recorded the morphological transition of poly(stearyl methacrylate)-poly(benzyl methacrylate) from soluble copolymer, spherical micelle, worm-like micelle to vesicle as final product. Meanwhile, it revealed the membrane thickness evolution of the diblock copolymer vesicle. Also, this research indicated a potential acceleration effect of the rate of polymerisation by X-ray compared with *ex situ* ^{1}H NMR results. However, benzyl methacrylate monomer conversion given by SAXS was not directly provided by SAXS modelling. Poly(methyl methacrylate-styrene) via RAFT synthesis in $scCO_2$ has been observed by *in situ* SAXS method, and phase diagram of poly(methyl methacrylate-styrene) have been presented according to *in situ* SAXS patterns and the extra evident as ex-situ TEM results.[203]The PISA process via RAFT synthesis of poly(glycerol monomethacrylate)-poly(2-methoxyethyl methacrylate) in water at 10% w/w solids was recorded by *in situ* SAXS method.[167] At the scattering vector equal to 0.025 $Å^{-1}$, the nucleation of diblock copolymer particles during RAFT synthesis could be observed by the *in situ* SAXS patterns. This research also presented *in situ* ^{1}H NMR results for monomer conversion, but it was lack of comparison between *in situ* SAXS results and *in situ* ^{1}H NMR for chemical kinetic perspective. The PISA process via RAFT synthesis of poly(glycerol monomethacrylate)-poly(2-hydroxypropyl methacrylate) in water at 10% w/w solids was recorded by *in situ* SAXS method.[168] This *in situ* SAXS studies also recorded diblock copolymer morphological transition from soluble copolymer, spherical micelle, worm-like micelle to vesicle. Similarly, it also presented the membrane thickness evolution of the diblock copolymer vesicle, and the mechanism of such evolution was similar with the results of poly(stearyl methacrylate)-poly(benzyl methacrylate) RAFT synthesis. [128] Research targeted to monitor the particle nucleation and particle growth process of PISA process via RAFT synthesis measured by *in situ* SAXS method has been reported.[204] The PISA process via RAFT synthesis of poly(N-acryloylmorpholine-N-acryloylthiomorpholine) in water was observed by *in situ* SAXS. This research presented the changes of particle size, aggregation number during PISA process via RAFT synthesis. Also, it concluded that the rate-limiting process in PISA process via RAFT synthesis should be the rate of polymerisation, and it also revealed the rate of nucleation process was relatively faster than polymerisation. *in situ* SAXS studies of PISA

process via RAFT synthesis of poly(hydrogenated polybutadiene-benzyl methacrylate) in *n*-dodecane at 40 % w/w recorded the morphological transition from body-centred cubic sphere phase to the mixture of hexagonal close-packed sphere phase and hexagonal cylinder phase.[205]

1.6 Small Angle X-ray Scattering (SAXS)

Small angle X-ray scattering (SAXS) has been applied to monitor various PISA syntheses *in situ*.[128, 167, 168, 203-205] Such SAXS data require detailed analysis to fully understand the various molecular and supramolecular processes that occur during PISA. The following sections provide an experimental perspective for SAXS and the various scattering models.

1.6.1 Small Angle X-ray Scattering Experiments

An X-ray scattering instrument consists of a radiation source, a monochromator, a collimator, a sample holder, and a detector.[217] Typically, the X-ray wavelength ranges from 10^{-2} to 10^{2} Å, but it requires a narrow range from 0.5 to 2.5 Å for analysis of most chemical structures.[217] Widely used metals for generating such X-rays include Cu and Mo. For a higher intensity X-ray flux, liquid metals such as Ga, In and Sn have been developed. In each case, an excitation voltage is applied to the metal to eject K shell electrons, and the excess energy triggers the emission of X-rays of the desired wavelength. Typical X-ray wavelengths for Cu*Kα*, Mo*Kα*, Ga*Kα* are 1.5, 0.7, and 1.34 Å, respectively.[217] For more precise measurements and the best possible temporal resolution, a synchrotron X-ray source provides a high intensity beam. In this case, an X-ray beam is generated from electrons accelerated by an intense magnetic field. This produces a much greater flux than traditional laboratory-based instruments. The scattered x-ray photons are collected by the detector.[217] Since the intensity decays rapidly from the beam centre, a detector with a particularly wide range in intensity is desirable. Otherwise, information would be lost either at high intensity close to the centre or at low intensity far away from the centre.[218] Also, the detector should be sufficiently sensitive to detect photons arising only from the X-ray source and enable capture of high-quality frames as quickly as possible. Most detectors either comprise a charge-coupled device (CCD) or utilise a complementary metal-oxide-semiconductor (CMOS).[218] A CCD has a relatively slow response time but CMOS can suffer from low resolution. CCD errors can occur when collecting pixel data from each line. Also, CMOS can accept a higher range of intensity. One of the acceptable CCD detectors is PILATUS 1M,[219] which has been widely used for SAXS data collection.[220] The X-ray intensity recorded by the detector is the total intensity, *I*, from all scattering angles. To identify the intensity at a particular angle, 2θ, the specific corresponding area on a detector that is placed at a distance *L* from the sample, $\Delta\sigma$, is defined by its solid angle, $\Delta\Omega$. Given the incident intensity, I_i, the differential scattering cross-section of the sample per unit solid angle is $\frac{d\sigma}{d\Omega}$ can be generated by $IL^2 d\Omega = I_i d\sigma$ (Figure 1.9), and therefore, this differential scattering cross-section is defined as,

$$\frac{d\sigma}{d\Omega} = L^2 \frac{I}{I_i}, \tag{1.69}$$

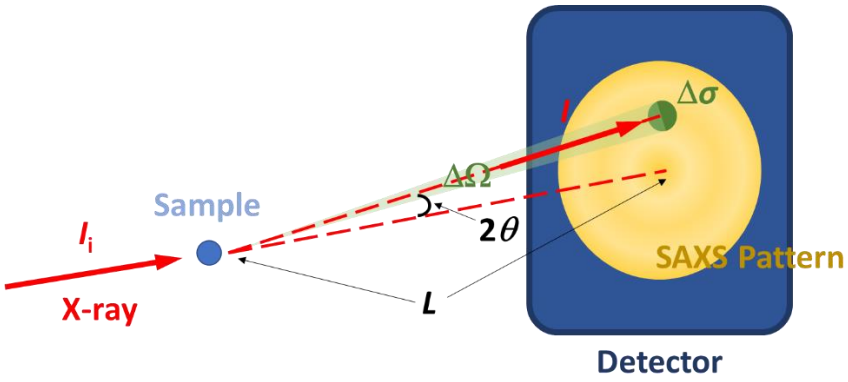

Figure 1.9. Schematic representation of SAXS data (yellow) collection of the sample (light blue) by detector (dark blue) at angle of 2θ. The distance from sample to detector is L. At solid angle $\Delta\Omega$, the specific corresponding area on a detector is $\Delta\sigma$.

The differential scattering cross-section has units of cm^2 and should be normalized by the sample volume, V_{sample},[221]

$$\frac{d\Sigma}{d\Omega} = \frac{1}{V_{sample}} \frac{d\sigma}{d\Omega}, \tag{1.70}$$

The units for the differential scattering cross-section per unit sample is cm^{-1}.

Since the X-ray intensity recorded by the detector includes background signals, this contribution requires subtraction from the sample signal. Background signals include electronic noise, beam tails, and, most critically, scattering from the sample cell and solvent.[221]

In an X-ray scattering experiment, just a few photons meet the electrons and elastic scattering can be assumed, which means that there is no energy transfer between the X-ray and the electrons. Given their low collision probability, each X-ray photon is scattered just once by the sample. Since the X-ray wavelength is much smaller than the size of molecules, the photon scattering obeys Raleigh-Debye-Gans (RDG) theory. For unpolarized X-rays, the differential cross-section of a single electron, $\left(\frac{d\sigma}{d\Omega}\right)_e$, is given by,

$$\left(\frac{d\sigma}{d\Omega}\right)_e = r_e^2 \frac{1+\cos^2 4\theta}{2}. \tag{1.71}$$

Here, r_e is the classical electron radius such that:

$$r_e = \frac{e^2\,(\mathrm{ESU})}{m_e c_{light}^{\ 2}} = 2.82\times10^{-13}\ \mathrm{cm}\,. \tag{1.72}$$

where c_{light} is the speed of light, and e is the elementary charge. As a result, the scattering length, b_e, is given by:

$$\begin{aligned} b_e(\theta) &= r_e\sqrt{\frac{1+\cos^2 4\theta}{2}} \\ \Rightarrow b_e(0) &= r_e\sqrt{\frac{1+\cos^2 0}{2}} = r_e = 2.82\times10^{-13}\ \mathrm{cm} \end{aligned}\,. \tag{1.73}$$

Thus, the scattering length of the molecule (cm^{-2}) at a small scattering angle, ξ, is given by:

$$\begin{aligned} \xi(\theta) \approx \xi(0) = \xi &= \frac{b_e(0)}{V_{molecule}}\sum_i^n n_i z_i \\ &= \frac{b_e(0)\,\rho_{molecule} N_A}{M_{molecule}}\left(\sum_i^n n_i z_i\right)_{molecule} \end{aligned}\,. \tag{1.74}$$

where $V_{molecule}$, $\rho_{molecule}$, and $M_{molecule}$ is the volume, density, and molecular weight of the molecule. Here n is the number of one type of atom with z electrons, and therefore $\left(\sum_i^n n_i z_i\right)_{molecule}$ is the total number of electrons per molecule. To determine the location of molecules in a scattering experiment, the contrast after subtracting backgrounds should reveal the distribution of the objects of study.

When an incident flux, J_i ($cm^{-2}\cdot s^{-1}$), is applied to a sample with thickness of d and scattering length ξ recorded by a detector placed at a distance, L, with an efficiency, η, at an angle 2θ, the incident intensity per second from an aperture of area A_{ape} is given by,

$$I_i = \eta\cdot A_{ape}\cdot J_i\,, \tag{1.75}$$

and the intensity recorded at an angle 2θ is written as,

$$I(\theta) = \eta\cdot A_{ape}\cdot J_i\cdot\Delta\Omega\cdot d\cdot T\cdot\frac{\mathrm{d}\Sigma}{\mathrm{d}\Omega}\,, \tag{1.76}$$

where T represents the transmission of the sample, which is defined as,

$$T = e^{-\mu d} = e^{-\frac{d}{\Lambda}}\,, \tag{1.77}$$

where μ is the linear attenuation coefficient and Λ is the mean free path of the radiation. For X-ray scattering, the mean free path, Λ_x, is around 0.01 to 1 mm. For a given instrument, the product·, $\eta\cdot A_{ape}\cdot J_i\cdot\Delta\Omega$, or $I_i\cdot\Delta\Omega$, is a constant, C_I. Thus, the intensity at θ can be written as,

$$I(\theta) = C_I \cdot d \cdot T \cdot \frac{d\Sigma}{d\Omega}. \tag{1.78}$$

Thus, intensity depends on the thickness of the sample, transmission, and differential cross-section per sample volume. The sample transmission is defined as,

$$T_S = \frac{I(\theta = 0)}{I_i} = e^{-\frac{d}{\Lambda}}. \tag{1.79}$$

Therefore, the intensity of the background, I_{SB}, and the intensity of the sample and the background, I_{SB+S}, is given by the transmissions of the background, T_{SB}, and the sample and the background, T_{SB+S}, respectively, according to the following relation:

$$\frac{T_{SB+S}}{T_{SB}} = \frac{I_{SB+S}(\theta = 0)}{I_{SB}(\theta = 0)}. \tag{1.80}$$

1.6.2 Small Angle X-ray Scattering Theory

Based on the concept of wave-particle duality of photons, X-rays can be defined in terms of a wave model at time *t*,

$$E(\vec{r}, t) = E_0 e^{i(\vec{k}\cdot\vec{r} - \omega t)}. \tag{1.81}$$

where E_0 is the X-ray amplitude, $\vec{r}$ is the position of the photons, ω is the angular frequency, and $\vec{k}$ is the scattered wave vector (Figure 1.10). The magnitude of $\vec{k}$, *k*, is given by,

$$k = |\vec{k}| = \frac{2\pi}{\lambda}. \tag{1.82}$$

When an X-ray with a wave vector $\vec{k_0}$ is scattered by one particle through an angle 2θ, the difference between the scattered wave vector, $\vec{k}$, and the original is,

$$\vec{q} = \vec{k} - \vec{k_0}. \tag{1.83}$$

Here $\vec{q}$ is termed the scattering vector, and its magnitude is given by the following relation:

$$q = |\vec{q}| = \frac{4\pi}{\lambda}\sin\theta. \tag{1.84}$$

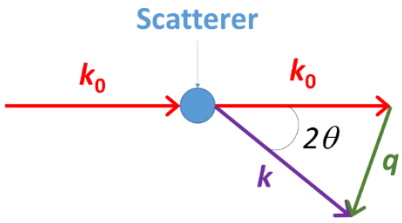

Figure 1.10. Schematic representation of the scattering vector, $\vec{q}$ (green arrow), as defined by the wave vectors $\vec{k}_0$ (red arrow) and $\vec{k}_0$ (purple arrow). The wave vector $\vec{k}_0$ is scattered by the scatterer (denoted by the blue sphere) and hence becomes $\vec{k}$. The angle formed between the wave vectors $\vec{k}$ and $\vec{k}_0$ is 2θ.

The formula for the amplitude of a scattered X-ray for one particle in a medium is given by

$$E_S\left(\vec{q},\vec{r},t\right)=-E_0\frac{e^{i\left(\vec{k}\cdot\vec{L}-\omega t\right)}}{L}\int_{V\left(\vec{r}\right)}\Delta\xi\left(\vec{r},t\right)e^{-i\vec{q}\cdot\vec{r}}\mathrm{d}V\left(\vec{r}\right), \tag{1.85}$$

where L is the distance between the sample and the detector. In a discrete system, the number of this type of particles is N, so the amplitude of such particles in a medium is given by

$$\begin{aligned}E_S\left(\vec{q},\vec{R},\vec{r},t\right)&=\sum_{j=1}^{N}\left(-E_0\frac{e^{i\left(\vec{k}\cdot\vec{L}-\omega t\right)}}{L}\int_{V\left(\vec{r}\right)}\Delta\xi\left(\vec{r},t\right)e^{-i\vec{q}\cdot\vec{r}}\mathrm{d}V\left(\vec{r}\right)\right)e^{-i\vec{q}\cdot\overrightarrow{R_j(t)}}\\&=-E_0\frac{e^{i\left(\vec{k}\cdot\vec{L}-\omega t\right)}}{L}\sum_{j=1}^{N}\left(\int_{V\left(\vec{r}\right)}\Delta\xi\left(\vec{r},t\right)e^{-i\vec{q}\cdot\vec{r}}\mathrm{d}V\left(\vec{r}\right)\right)e^{-i\vec{q}\cdot\overrightarrow{R_j(t)}}\end{aligned}, \tag{1.86}$$

where $\overrightarrow{R_j}$ is the position of the particle j. However, the detector records the X-ray intensity but not its amplitude, and the intensity of this X-ray amplitude is the square of its absolute value:

$$\begin{aligned}I_S\left(\vec{q},\vec{R},\vec{r},t\right)&=E_S\left(\vec{q},\vec{R},\vec{r},t\right)E_S^*\left(\vec{q},\vec{R},\vec{r},t\right)=\left|E_S\left(\vec{q},\vec{R},\vec{r},t\right)\right|^2\\&=\left[\sum_{j=1}^{N}\left(-E_0\frac{e^{i\left(\vec{k}\cdot\vec{L}-\omega t\right)}}{L}\int_{V\left(\vec{r}\right)}\Delta\xi\left(\vec{r},t\right)e^{-i\vec{q}\cdot\vec{r}}\mathrm{d}V\left(\vec{r}\right)\right)e^{-i\vec{q}\cdot\overrightarrow{R_j(t)}}\right]^2\\&=\frac{E_0^2}{L^2}\sum_{k=1}^{N}\sum_{j=1}^{N}\left|\int_{V\left(\vec{r}\right)}\Delta\xi\left(\vec{r},t\right)e^{-i\vec{q}\cdot\vec{r}}\mathrm{d}V\left(\vec{r}\right)\right|^2e^{-i\vec{q}\cdot\left[\overrightarrow{R_j(t)}-\overrightarrow{R_k(t)}\right]}\end{aligned}, \tag{1.87}$$

The X-ray detector provides an ensemble average of the scattered X-ray intensity,

$\left\langle I_S\left(\vec{q},\vec{R},\vec{r},t\right)\right\rangle$. Combined with equations 1.69 and 1.70, and assuming that the particle positions are relatively settled during data acquisition, it gives

$$\frac{\mathrm{d}\sigma}{\mathrm{d}\Omega}=\left\langle\sum_{k=1}^{N}\sum_{j=1}^{N}\left|\int_{V(\vec{r})}\Delta\xi\left(\vec{r}\right)e^{-i\vec{q}\cdot\vec{r}}\mathrm{d}V\left(\vec{r}\right)\right|^2 e^{-i\vec{q}\cdot\left(\vec{R_j}-\vec{R_k}\right)}\right\rangle. \tag{1.88}$$

The expansion of the differential cross-section is given by

$$\begin{aligned}\frac{d\sigma}{d\Omega}&=\sum_{j=1}^{N}\left\langle\left|\int_{V(\vec{r})}\Delta\xi\left(\vec{r}\right)e^{-i\vec{q}\cdot\vec{r}}\mathrm{d}V\left(\vec{r}\right)\right|^2\right\rangle+\sum_{\substack{k=1\\k\neq j}}^{N}\sum_{j=1}^{N}\left[\left\langle\left|\int_{V(\vec{r})}\Delta\xi\left(\vec{r}\right)e^{-i\vec{q}\cdot\vec{r}}\mathrm{d}V\left(\vec{r}\right)\right|^2\right\rangle\left\langle e^{-i\vec{q}\cdot\left(\vec{R_j}-\vec{R_k}\right)}\right\rangle\right]\\&=\sum_{j=1}^{N}\left\langle\left|\int_{V(\vec{r})}\Delta\xi\left(\vec{r}\right)e^{-i\vec{q}\cdot\vec{r}}\mathrm{d}V\left(\vec{r}\right)\right|^2\right\rangle\left\{1+\frac{\sum_{\substack{k=1\\k\neq j}}^{N}\sum_{j=1}^{N}\left[\left\langle\left|\int_{V(\vec{r})}\Delta\xi\left(\vec{r}\right)e^{-i\vec{q}\cdot\vec{r}}\mathrm{d}V\left(\vec{r}\right)\right|^2\right\rangle\left\langle e^{-i\vec{q}\cdot\left(\vec{R_j}-\vec{R_k}\right)}\right\rangle\right]}{\sum_{j=1}^{N}\left\langle\left|\int_{V(\vec{r})}\Delta\xi\left(\vec{r}\right)e^{-i\vec{q}\cdot\vec{r}}\mathrm{d}V\left(\vec{r}\right)\right|^2\right\rangle}\right\}.\end{aligned} \tag{1.89}$$

In particular, we can define the form factor, $P(q)$, and structure factor, $S(q)$, using this formula

$$\begin{cases}P\left(q\right)=\dfrac{\left\langle\left|\int_{V(\vec{r})}\Delta\xi\left(\vec{r}\right)e^{-i\vec{q}\cdot\vec{r}}\mathrm{d}V\left(\vec{r}\right)\right|^2\right\rangle}{\left\langle\left|\int_{V(\vec{r})}\Delta\xi\left(\vec{r}\right)\mathrm{d}V\left(\vec{r}\right)\right|^2\right\rangle}\\[2ex]S\left(q\right)=1+\dfrac{\sum_{\substack{k=1\\k\neq j}}^{N}\sum_{j=1}^{N}\left[\left\langle\left|\int_{V(\vec{r})}\Delta\xi\left(\vec{r}\right)e^{-i\vec{q}\cdot\vec{r}}\mathrm{d}V\left(\vec{r}\right)\right|^2\right\rangle\left\langle e^{-i\vec{q}\cdot\left(\vec{R_j}-\vec{R_k}\right)}\right\rangle\right]}{\sum_{j=1}^{N}\left\langle\left|\int_{V(\vec{r})}\Delta\xi\left(\vec{r}\right)e^{-i\vec{q}\cdot\vec{r}}\mathrm{d}V\left(\vec{r}\right)\right|^2\right\rangle}\\[2ex]\quad=1+\dfrac{\sum_{\substack{k=1\\k\neq j}}^{N}\sum_{j=1}^{N}\left\langle e^{-i\vec{q}\cdot\left(\vec{R_j}-\vec{R_k}\right)}\right\rangle}{N}=\dfrac{\sum_{k=1}^{N}\sum_{j=1}^{N}\left\langle e^{-i\vec{q}\cdot\left(\vec{R_j}-\vec{R_k}\right)}\right\rangle}{N}\end{cases}. \tag{1.90}$$

Therefore, the differential cross-section per volume is given by

$$\frac{\mathrm{d}\Sigma}{\mathrm{d}\Omega}=\frac{1}{V}\frac{\mathrm{d}\sigma}{\mathrm{d}\Omega}=\frac{N_{\mathrm{p}}}{V}\left\langle\left|\int_{V(\vec{r})}\Delta\xi\left(\vec{r}\right)\mathrm{d}V\left(\vec{r}\right)\right|^{2}\right\rangle P(q)S(q)$$
$$=n_{\mathrm{p/V}}\left\langle\left|\int_{V(\vec{r})}\Delta\xi\left(\vec{r}\right)\mathrm{d}V\left(\vec{r}\right)\right|^{2}\right\rangle P(q)S(q) \quad , \tag{1.91}$$

where n_{p}/V is the number density of particles in the system. Since this formula separates the particle structure from the distribution of particles in the medium, it can be simplified in the cases of a dilute system by equating the structure factor to unity. Thus, it directly presents the particle structure in this case.

For an isotropic system, the amplitude of the form factor is given by

$$A(q)=\frac{\left\langle\int_{V(\vec{r})}\Delta\xi\left(\vec{r}\right)e^{-i\vec{q}\cdot\vec{r}}\mathrm{d}V\left(\vec{r}\right)\right\rangle}{\left\langle\int_{V(\vec{r})}\Delta\xi\left(\vec{r}\right)\mathrm{d}V\left(\vec{r}\right)\right\rangle}=\frac{4\pi\int_{0}^{\infty}\Delta\xi\left(\vec{r}\right)\frac{\sin qr}{qr}r^{2}\mathrm{d}r}{\int_{V(\vec{r})}\Delta\xi\left(\vec{r}\right)\mathrm{d}V\left(\vec{r}\right)}. \tag{1.92}$$

For hard spheres (Figure 1.11), this amplitude could be rewritten as

$$A_{\mathrm{s}}\left(q,r\right)=\frac{4\pi\int_{0}^{\infty}\Delta\xi\left(\vec{r}\right)\frac{\sin qr}{qr}r^{2}\mathrm{d}r}{\int_{V(\vec{r})}\Delta\xi\left(\vec{r}\right)dV\left(\vec{r}\right)}=\frac{3\left[\sin\left(qR_{\mathrm{s}}\right)-\left(qR_{\mathrm{s}}\right)\cos\left(qR_{\mathrm{s}}\right)\right]}{\left(qR_{\mathrm{s}}\right)^{3}}. \tag{1.93}$$

For the case of a shell of radius of R_{sh} (Figure 1.11), the amplitude can be rewritten as

$$A_{\mathrm{sh}}\left(q,R_{\mathrm{sh}}\right)=\frac{4\pi\int_{0}^{\infty}\Delta\xi\left(\vec{r}\right)\frac{\sin qr}{qr}r^{2}\mathrm{d}r}{\int_{V(\vec{r})}\Delta\xi\left(\vec{r}\right)\mathrm{d}V\left(\vec{r}\right)}=\frac{\sin qR_{\mathrm{sh}}}{qR_{\mathrm{sh}}}. \tag{1.94}$$

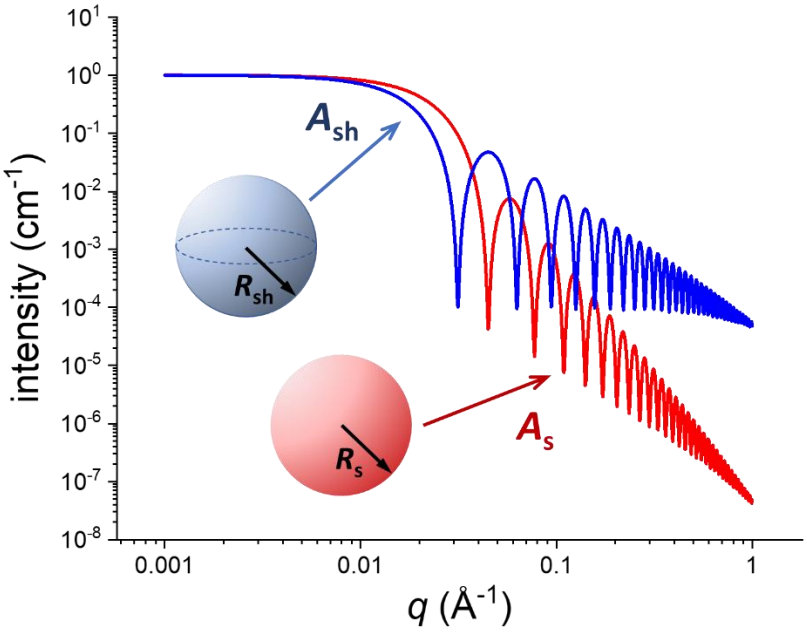

Figure 1.11. Schematic presentation of SAXS patterns of $I(q) = A_s^2(q)$ (red) and $I(q) = A_{sh}^2(q)$ (blue) of the hard shell and shell of both radii, R_s and R_{sh}, of 10 nm.

Structure factor should be introduced to account for scattering from concentrated systems.[222] In a discrete system with N_p particles, consider a particle at a position $\overrightarrow{R_p}$. The average number density in this region, $\rho\left(\overrightarrow{R_p}\right)$, could be given by the product of the average density of whole material, $\bar{\rho}$, and a correlation function, $g\left(\overrightarrow{R_p}\right)$, such that

$$\rho\left(\overrightarrow{R_p}\right) = \bar{\rho} \cdot g\left(\overrightarrow{R_p}\right), \tag{1.95}$$

where the correlation function $g\left(\overrightarrow{R_p}\right)$ is the radius distribution function (RDF) or pair correlation function. This function is a special case of a pair distribution function (PDF) when there is no orientation dependence. However, the last formula is for one-particle density, so more generally for N_p-particle density, $\rho^{(N_p)}\left(\cdots, \overrightarrow{R_{p\text{-}i}}, \cdots\right)$, with position of particles, $\overrightarrow{R_{p\text{-}i}}$, the N_p-order correlation function, $g^{(N_p)}\left(\cdots, \overrightarrow{R_{p\text{-}i}}, \cdots\right)$, is $\rho^{(N_p)}\left(\cdots, \overrightarrow{R_{p\text{-}i}}, \cdots\right) = \bar{\rho}^{N_p} \cdot g^{(N_p)}\left(\cdots, \overrightarrow{R_{p\text{-}i}}, \cdots\right)$.

In particular, when considering the distance between any two particles, the second-order correlation function, $g^{(2)}\left(\overrightarrow{R_{p\text{-}1}}, \overrightarrow{R_{p\text{-}2}}\right)$, or simply $g\left(\overrightarrow{R_p}\right)$, should be introduced to define the interaction or interference between two particles. Meanwhile, $P^{(N_p)}\left(\cdots, \overrightarrow{R_{p\text{-}i}}, \cdots\right)$, for N_p-particle density, the $\rho^{(N_p)}\left(\cdots, \overrightarrow{R_{p\text{-}i}}, \cdots\right)$ in sequence can be rewritten as the product of N_p-permutation of N_p', $A_{N_p}^{N_p'}$, and the probability,[223]

$$\rho^{(N_p)}\left(\cdots, \overrightarrow{R_{p\text{-}i}}, \cdots\right) = A_{N_p}^{N_p'} \cdot P^{(N_p)}\left(\cdots, \overrightarrow{R_{p\text{-}i}}, \cdots\right) = \frac{N_p!}{\left(N_p - N_p'\right)!} \cdot P^{(N_p)}\left(\cdots, \overrightarrow{R_{p\text{-}i}}, \cdots\right) \cdot$$

In the case of a two-particle density, the second-order correlation function, $g\left(\vec{R}\right)$, can be rewritten as,

$$g\left(\vec{R}\right)=\frac{N\left(N-1\right)}{\rho^2}\cdot P^{(2)}\left(\overrightarrow{R_{\text{p-1}}},\overrightarrow{R_{\text{p-2}}}\right)=\frac{N\left(N-1\right)}{\rho^2}\cdot\left[\frac{1}{V}\cdot\frac{\left\langle\sum_{\substack{j=1\\j\neq i}}^{N}\sum_{i=1}^{N}\delta\left[\vec{R}-\left(\overrightarrow{R_i}-\overrightarrow{R_j}\right)\right]\right\rangle}{N\left(N-1\right)}\right] \quad (1.96)$$

$$=\frac{1}{N\rho}\left\langle\sum_{\substack{j=1\\j\neq i}}^{N}\sum_{i=1}^{N}\delta\left[\vec{R}-\left(\vec{r_i}-\vec{r_j}\right)\right]\right\rangle$$

.

By confirming the possibility of configuration for two-particle density, the second-order correlation function can be rewritten as [223]

$$g\left(\vec{R}\right)=\frac{N\left(N-1\right)}{\rho^2}\cdot P^{(2)}\left(\vec{r_1},\vec{r_2}\right)=\frac{N\left(N-1\right)}{\rho^2}\cdot\left[\frac{1}{V}\cdot\frac{\left\langle\sum_{\substack{j=1\\j\neq i}}^{N}\sum_{i=1}^{N}\delta\left[\vec{R}-\left(\vec{r_i}-\vec{r_j}\right)\right]\right\rangle}{N\left(N-1\right)}\right]. \quad (1.97)$$

$$=\frac{1}{N\rho}\left\langle\sum_{\substack{j=1\\j\neq i}}^{N}\sum_{i=1}^{N}\delta\left[\vec{R}-\left(\vec{r_i}-\vec{r_j}\right)\right]\right\rangle$$

Referring to the structure factor given in 1.90, the $\left\langle e^{-i\vec{q}\cdot\left(\vec{R_j}-\vec{R_k}\right)}\right\rangle$ term can be rewritten via Dirac Delta Function as[224]

$$\left\langle e^{-i\vec{q}\cdot\left(\vec{R_j}-\vec{R_k}\right)}\right\rangle=\left\langle\int_{-\infty}^{\infty}e^{-i\vec{q}\cdot\vec{R}}\delta\left[\vec{R}-\left(\overrightarrow{R_j}-\overrightarrow{R_k}\right)\right]\mathrm{d}\vec{R}\right\rangle. \quad (1.98)$$

Thus, the $\sum_{k=1}^{N}\sum_{j=1}^{N}\left\langle e^{-i\vec{q}\cdot\left(\vec{R_j}-\vec{R_k}\right)}\right\rangle$ in 1.90 should be given by

$$\sum_{\substack{k=1\\k\neq j}}^{N}\sum_{j=1}^{N}\left\langle e^{-i\vec{q}\cdot\left(\vec{R_j}-\vec{R_k}\right)}\right\rangle=\sum_{\substack{k=1\\k\neq j}}^{N}\sum_{j=1}^{N}\left\langle\int_{-\infty}^{\infty}e^{-i\vec{q}\cdot\vec{R}}\delta\left[\vec{R}-\left(\overrightarrow{R_j}-\overrightarrow{R_k}\right)\right]\mathrm{d}\vec{R}\right\rangle$$

$$=\left\langle\int_{-\infty}^{\infty}e^{-i\vec{q}\cdot\vec{R}}\sum_{\substack{k=1\\k\neq j}}^{N}\sum_{j=1}^{N}\delta\left[\vec{R}-\left(\overrightarrow{R_j}-\overrightarrow{R_k}\right)\right]\mathrm{d}\vec{R}\right\rangle. \quad (1.99)$$

$$=\int_{-\infty}^{\infty}e^{-i\vec{q}\cdot\vec{R}}\left\langle\sum_{\substack{k=1\\k\neq j}}^{N}\sum_{j=1}^{N}\delta\left[\vec{R}-\left(\overrightarrow{R_j}-\overrightarrow{R_k}\right)\right]\right\rangle\mathrm{d}\vec{R}$$

As a result, the structure factor can be rewritten as [225]

$$S(q) = 1 + \frac{\int_{-\infty}^{\infty} e^{-i\vec{q}\cdot\vec{R}} \left\langle \sum_{k=1}^{N}\sum_{\substack{j=1 \\ k\neq j}}^{N} \delta\left[\vec{R} - \left(\overrightarrow{R_j} - \overrightarrow{R_k}\right)\right] \right\rangle d\vec{R}}{N} = 1 + \rho \int_{V(\vec{R})} e^{-i\vec{q}\cdot\vec{R}} g\left(\vec{R}\right) dV = 1 + 4\pi\rho \int_{\vec{R}} g\left(\vec{R}\right) \frac{\sin qR}{qR} R^2 dR \quad (1.100)$$

However, at q = 0 this structure factor formula fails because there is no information to identify the distance between particles. Hence at q = 0 a modified structure factor, $S_{mod}(q)$, is introduced to eliminate excess counting, [221]

$$S_{mod}(q) = S(q) - \rho\delta(q) = 1 + \rho \int_{V(\vec{R})} e^{-i\vec{q}\cdot\vec{R}} \left[g\left(\vec{R}\right) - 1\right] dV = 1 + 4\pi\rho \int_{\vec{R}} \left[g\left(\vec{R}\right) - 1\right] \frac{\sin qR}{qR} R^2 dR \quad (1.101)$$

Given the correlation between form factor amplitudes, the differential cross-section can be rewritten as, [221]

$$\frac{d\Sigma}{d\Omega} = n \left\langle \left| \int_{V(\vec{r})} \Delta\xi\left(\vec{r}\right) dV\left(\vec{r}\right) \right|^2 \right\rangle \left\{P(q) + \left[S(q) - 1\right] A^2(q)\right\}. \quad (1.102)$$

Since q can be viewed as a way to measure particular regions within particles[66], when $\vec{q}\cdot\vec{R}$ becomes greater, the signal provides information on the particle size, shape and internal structure. This provides a practical method for fitting the data when selecting the specific region for corresponding parameters. This concept can be considered as a fundamental axiom for SAXS. At high q, the intensity is proportional to q^{-4}, which is known as Porod's law[217]. At low q, the intensity, $I(q)$, is proportional to the following term

$$I(q) \propto (\Delta\xi)^2 V^2 e^{-\frac{1}{3}q^2 R_g^2}, \quad (1.103)$$

which indicates that the volume or size dominates the scattering data.

For a dilute system, the scattering intensity given by eq 1.87 can be rewritten as:

$$I_S\left(\vec{R},\vec{r},t\right) = E_S\left(\vec{R},\vec{r},t\right) E_S^*\left(\vec{R},\vec{r}',t\right) = 4\pi \cdot N \cdot \frac{{E_0}^2}{L^2} \int_{\vec{r}} \left[\vec{r}^{\,2} \cdot \int_{V(\vec{r}')} \Delta\xi\left(\vec{r}'-\vec{r},t\right) \Delta\xi\left(\vec{r}',t\right) dV\left(\vec{r}'\right) \right] e^{-i\vec{q}\cdot\vec{r}} d\vec{r}. \quad (1.104)$$

The term, $\vec{r}^{\,2} \cdot \int_{V(\vec{r}')} \Delta\xi\left(\vec{r}'-\vec{r},t\right) \Delta\xi\left(\vec{r}',t\right) dV\left(\vec{r}'\right)$, in eq 1.104, is defined as the pair distance distribution function (PDDF) or $p(r)$, which can be also given as:

$$p\left(\vec{r}\right)=\frac{1}{2\pi^2}\int_{\vec{q}}\left(\frac{1}{N}\frac{d\sigma}{d\Omega}\right)\cdot\left(\vec{q}\cdot\vec{r}\right)\cdot\sin\left(\vec{q}\cdot\vec{r}\right)d\vec{q}\,. \tag{1.105}$$

In principle, PDDF analysis can provide valuable information on the size and structure of monodisperse particles. Different particle shapes can be characterised by particular PDDF results (Figure 1.12). A few research have invited PDDF analysis for self-assembled particles.[226-233] However, in practice, for polydisperse particles it can be challenging to determine such information. Furthermore, suitable scattering models may be required to fit the SAXS patterns to provide deeper insights. Various models have been developed for the analysis of hard spheres, spherical micelles, cylindrical micelles and vesicles.[234, 235]

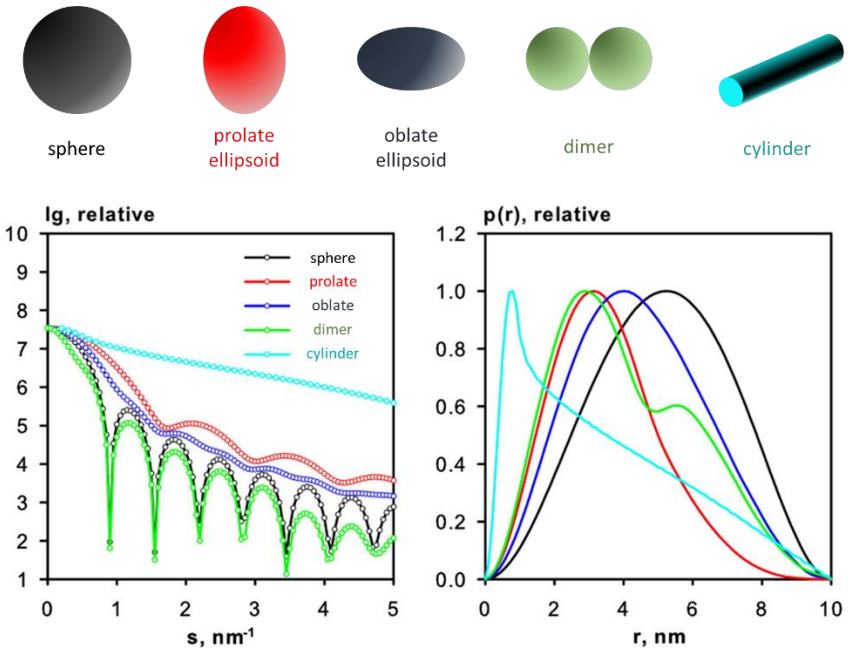

Figure 1.12. Scattering intensities (left) and pair distance distribution functions (PDDF) (right) calculated for solid sphere (black), prolate ellipsoid (red), oblate ellipsoid (blue), dimer (green) and cylinder (cyan) (top cartoons).[236]

1.6.3 Small Angle X-ray Scattering Model for Characterisation of Polymers and Polymer Aggregates

Models for polymer chains can be generally divided into ideal and real chains. The difference between these two concepts is that real chains have no overlap between each polymer segment, whereas this constraint is ignored for ideal chains.[4] The mean repeat unit length for a polymer chain is termed the step motion, *b*. Both models assume a distribution of bond vectors, $\vec{r}_i$, or displacement vectors, $\Delta\vec{r}_i$, between two neighboring units. As for real chains, since the minimum distance between two repeat units is the length of the repeat unit itself,

b, the distance between any two vectors should be never placed closer than *b*. This proprietary zone for each bone vector is called the excluded volume, v_e. For a random walk model, the mean square distance between the m^{th} and n^{th} repeat units can be written as

$$\left\langle \left(\vec{r_m} - \vec{r_n} \right)^2 \right\rangle = b^2 \left| m - n \right|^{2\nu} . \tag{1.106}$$

where exponent *v* has been defined in discussion after the minimising of ΔA_{e_d} of R_F in eq 1.23. For polymer chains with a mean degree of polymerisation, R_g, with *N* Kuhn segments is given by

$$R_g{}^2 = \left\langle \frac{1}{N+1} \sum_{i=0}^{N} \left(\vec{r_i} - \frac{1}{N+1} \sum_{i=0}^{N} \vec{r_i} \right)^2 \right\rangle = \frac{1}{(2\nu+1)(2\nu+2)} b^2 N^{2\nu} . \tag{1.107}$$

In the context of SAXS analysis, the amplitude of polymer chains in a theta solvent is given by the following formula,[237]

$$A_{GC}\left(q, R_g\right) = \left\langle A\left(\vec{q}\right) \right\rangle = \frac{1 - e^{-q^2 R_g{}^2}}{\left(q^2 R_g{}^2\right)^2} . \tag{1.108}$$

Generally, the scattering intensity, $\left\langle \left| F\left(\vec{q}\right) \right|^2 \right\rangle$, is the average of all possible chain configurations and is given by[234]

$$\begin{aligned} \left\langle \left| F\left(\vec{q}\right) \right|^2 \right\rangle &= \sum_{m,n=0}^{N} \left\langle e^{-i\vec{q}\cdot\left(\vec{R_m} - \vec{R_n}\right)} \right\rangle = \sum_{m,n=0}^{N} e^{-\frac{q^2 b^2}{6} \cdot |m-n|^{2\nu}} \\ &= N + 2\sum_{k=1}^{N} (N-k) e^{-\frac{q^2 b^2 k^{2\nu}}{6}} \end{aligned} . \tag{1.109}$$

Thus, the form factor, $P\left(\vec{q}\right)$, of the polymer chains is

$$P_{GC}\left(\vec{q}\right) = \frac{1}{N^2} \left\langle \left| F\left(\vec{q}\right) \right|^2 \right\rangle = \frac{1}{N} \left(1 + 2\sum_{k=1}^{N} \left(1 - \frac{k}{N} \right) e^{-\frac{q^2 b^2 N^{2\nu}}{6} \left(\frac{k}{N}\right)^{2\nu}} \right) . \tag{1.110}$$

Since high molecular weight polymers comprise many repeat units, the summation could be replaced by an integral and certain terms that approach zero can be eliminated. Thus, this form factor can be rewritten as

$$P\left(\vec{q}\right) \approx 2 \cdot \frac{\sum_{k=1}^{N}\left(1-\frac{k}{N}\right) e^{-\frac{q^2 b^2 N^{2\nu}}{6}\left(\frac{k}{N}\right)^{2\nu}}}{N}$$

$$= \nu\left[\left(2\nu+1\right)\left(2\nu+2\right)\frac{q^2 {R_g}^2}{6}\right]^{\frac{1}{\nu}} \left\{\begin{array}{l} \left[\left(2\nu+1\right)\left(2\nu+2\right)\frac{q^2 {R_g}^2}{6}\right]\Gamma\left(\frac{1}{2\nu}\right) \\ -\Gamma\left(\frac{1}{\nu}\right) \\ -\left[\left(2\nu+1\right)\left(2\nu+2\right)\frac{q^2 {R_g}^2}{6}\right]^{\frac{1}{2\nu}} \\ \cdot\Gamma\left(\frac{1}{2\nu}, \left[\left(2\nu+1\right)\left(2\nu+2\right)\frac{q^2 {R_g}^2}{6}\right]\right) \\ +\Gamma\left(\frac{1}{\nu}, \left[\left(2\nu+1\right)\left(2\nu+2\right)\frac{q^2 {R_g}^2}{6}\right]\right) \end{array}\right\}, \quad (1.111)$$

where $\Gamma(a)$ is the Gamma Function and $\Gamma(a,x)$ is the upper incomplete Gamma Function. This form factor suggests that two fitting parameters should be used. However, an ideal chain model with a constant Flory exponent of 0.50 is more concise than real polymer chains and the former is more convenient to model the chain structure.[238] In this case, the form factor is termed the Debye function, , as given by[238, 239] In this case, the form factor is termed the Debye function, $P_{\text{chain}}\left(\vec{q}\right)$, as given by[238, 239]

$$P_{\text{chain}}\left(\vec{q}\right) \overset{N\to\infty}{\cong} \frac{2\left[q^2 R_g^2 - 1 + e^{-q^2 R_g^2}\right]}{\left(q^2 R_g^2\right)^2}. \quad (1.112)$$

The Debye function has only one parameter, R_g, and hence provides a more expedient fit without invoking Gamma Functions.

Although spherical micelles are aggregates of copolymer chains, the high-density cores formed by the hydrophobic blocks can be described by a simple sphere model. Since the hydrophilic blocks extend into the solvent, models for the spherical micelle corona must remain consistent with a polymer chain model. Thus the cross-section of a spherical micelle consists of four components: (i) the self-correlation of the core, (ii) the self-correlation of the corona chains, (iii) the correlation between the core and corona chains, and (iv) the correlation between corona chains.[240] Hence the general form factor of the spherical micelle, $P_{\text{micelle}}(q)$, is given by

$$\begin{aligned} P_{\text{micelle}}\left(q\right) = {} & {N_{\text{agg}}}^2 {\beta_{\text{core}}}^2 {A_{\text{core,micelle}}}^2\left(q\right) \\ & + N_{\text{agg}}\left(N_{\text{agg}}-1\right){\beta_{\text{corona}}}^2 {A_{\text{corona,micelle}}}^2\left(q\right) \\ & + 2{N_{\text{agg}}}^2 \beta_{\text{core}}\beta_{\text{corona}} A_{\text{core,micelle}}\left(q\right) A_{\text{corona,micelle}}\left(q\right) \\ & + N_{\text{agg}}{\beta_{\text{corona}}}^2 P_{\text{chain}}\left(q\right) \end{aligned}. \quad (1.113)$$

where N_{agg} denotes the aggregation number for the spherical micelles and β_{core} and β_{corona}

are excess scattering lengths of the core and the corona, respectively. These latter two parameters are given by

$$\begin{cases} \beta_{\text{core}} = V_{\text{core}}\left(\rho_{\text{core}} - \rho_{\text{sol}}\right) \\ \beta_{\text{corona}} = V_{\text{corona}}\left(\rho_{\text{corona}} - \rho_{\text{sol}}\right) \end{cases}. \tag{1.114}$$

where V_{core} and V_{corona} are the volumes of the core and the corona chains and ρ_{core}, ρ_{corona} and ρ_{sol} are the scattering lengths for the core, corona, and solvent, respectively. Finally, $A_{\text{core,micelle}}$ and $A_{\text{corona,micelle}}$ are the amplitudes of the core and corona. As mentioned above, the core can be modelled using the simple sphere model. However, there may be a concentration gradient for the hydrophilic corona switching to a hydrophobic core, or *vice versa*

$$A_{\text{core,micelle}} = A_{\text{s}}\left(q, R_{\text{c}}\right) e^{-q^2\sigma_{\text{t}}^2}, \tag{1.115}$$

where σ_{t} is the width of the interface between core and corona. Combined with equations 1.94 and 1.108, the spherical micelle corona can be represented as,

$$A_{\text{corona,micelle}} = A_{\text{GC}}\left(q, R_{\text{g}}\right) A_{\text{sh}}\left[q\left(R_{\text{c}} + dR_{\text{g}}\right)\right] e^{-\frac{q^2\sigma_{\text{t}}^2}{2}}, \tag{1.116}$$

where d is a parameter for simulation of the non-penetration of the corona chains within the core, and d lies close to unity.[241]

The primary scattering model for cylinders should combine the form factors for rods and disks. The general form factor is similar as the form factor for a spherical micelle, [241, 242]

$$\begin{aligned} P_{\text{micelle}}\left(q\right) = {} & N_{\text{agg}}{}^2 \beta_{\text{core}}{}^2 \left\langle A_{\text{core,worm}}{}^2\left(q, R_{\text{w}}, L_{\text{w}}, \theta_{\text{w}}\right)\right\rangle \\ & + N_{\text{agg}}\left(N_{\text{agg}} - 1\right)\beta_{corona}{}^2 \left\langle A_{\text{corona,worm}}{}^2\left(q, R_{\text{w}}, L_{\text{w}}, \theta_{\text{w}}\right)\right\rangle \\ & + 2N_{\text{agg}}{}^2 \beta_{\text{core}}\beta_{\text{corona}} \left\langle A_{\text{core,worm}}\left(q, R_{\text{w}}, L_{\text{w}}, \theta_{\text{w}}\right) A_{\text{corona,worm}}\left(q, R_{\text{w}}, L_{\text{w}}, \theta_{\text{w}}\right)\right\rangle \\ & + N_{\text{agg}}\beta_{\text{corona}}{}^2 P_{\text{chain}}\left(q\right) \end{aligned}, \tag{1.117}$$

where $\langle A_{\text{core,worm}}(q, R_{\text{w}}, L_{\text{w}}, \theta_{\text{w}})\rangle$ and $\langle A_{\text{corona,worm}}(q, R_{\text{w}}, L_{\text{w}}, \theta_{\text{w}})\rangle$ are the ensemble-average of the configuration of the worm core radius R_{w} and the length of worm, L_{w}. Here θ_{w} is the azimuthal angle defined by spherical coordinates. These two terms are written as

$$\begin{cases} \left\langle A_{\text{core,worm}}\left(q, R_{\text{w}}, L_{\text{w}}, \theta_{\text{w}}\right)\right\rangle = \left\langle \dfrac{2J_1\left(qR_{\text{w}}\sin\theta_{\text{w}}\right)}{qR_{\text{w}}\sin\theta_{\text{w}}} \cdot \dfrac{\sin\left(\dfrac{qL_{\text{w}}}{2}\cos\theta_{\text{w}}\right)}{\dfrac{qL_{\text{w}}}{2}\cos\theta_{\text{w}}} \right\rangle \\ \left\langle A_{\text{corona,worm}}\left(q, R_{\text{w}}, L_{\text{w}}, \theta_{\text{w}}\right)\right\rangle = \psi\left(qR_{\text{g}}\right) \left\langle \begin{array}{l} \dfrac{L_{\text{w}}}{R_{\text{w}} + L_{\text{w}}} \dfrac{2J_1\left(qR_w\sin\theta_{\text{w}}\right)}{qR_{\text{w}}\sin\theta_{\text{w}}} \cos\left(\dfrac{qL_{\text{w}}}{2}\cos\theta_{\text{w}}\right) + \\ \dfrac{R_{\text{w}}}{R_{\text{w}} + L_{\text{w}}} J_0\left(qR_{\text{w}}\sin\theta_{\text{w}}\right) \dfrac{\sin\left(\dfrac{qL_{\text{w}}}{2}\cos\theta_{\text{w}}\right)}{\dfrac{qL_{\text{w}}}{2}\cos\theta_{\text{w}}} \end{array} \right\rangle \end{cases}, \tag{1.118}$$

where $J_n(x)$ is a Bessel function for integer values of n. Nevertheless, real diblock copolymer

worms do not behave as ideal cylinders, and instead behave more like polymer chains with a much larger radius. Therefore, the concept of Kuhn segment length and contour length should be considered within the model.[243] Such models, with and without excluded volume effects, have been developed to fit SAXS patterns obtained for worm-like micelles.[168, 216, 244]

The vesicle form factor is given by

$$\begin{aligned} P_{\text{vesicle}}(q) = & N_{\text{agg}}{}^2 \beta_{\text{core}}{}^2 A_{\text{core,vesicle}}{}^2(q) \\ & + N_{\text{agg}}\left(N_{\text{agg}}-1\right)\beta_{\text{corona}}{}^2 A_{\text{corona,vesicle}}{}^2(q) \\ & + 2N_{\text{agg}}{}^2 \beta_{\text{core}}\beta_{\text{corona}} A_{\text{core,vesicle}}(q) A_{\text{corona,vesicle}}(q) \\ & + N_{\text{agg}}\beta_{\text{corona}}{}^2 P_{\text{chain}}(q) \end{aligned} . \tag{1.119}$$

The amplitude of the vesicle form factor can be derived from the following formula,

$$A_{\text{core,vesicle}} = \left[V_{\text{s}}(R_{\text{out}})\cdot A_{\text{s}}(q,R_{\text{out}}) - V_{\text{s}}(R_{\text{in}})\cdot A_{\text{s}}(q,R_{\text{in}})\right] e^{-\frac{q^2\sigma_{\text{t}}{}^2}{2}}, \tag{1.120}$$

where R_{out} and R_{in} are the outer and inner vesicle radii, respectively, $V_{\text{s}}(R_{\text{out}})$ is the volume of a sphere of radius R_{out}, and $V_{\text{s}}(R_{\text{in}})$ is the volume of a sphere of radius R_{in}. Taking the membrane thickness to be t_{sh}, the two radii are defined by a mean shell of radius R_{V} such that

$$\begin{cases} R_{\text{out}} = R + \dfrac{t_{\text{sh}}}{2} \\ R_{\text{in}} = R - \dfrac{t_{\text{sh}}}{2} \end{cases} . \tag{1.121}$$

$V_{\text{s}}(r)$ is defined as the volume of a sphere of radius r:

$$V_{\text{s}}(r) = \frac{4}{3}\cdot\pi\cdot r^3 . \tag{1.122}$$

The prior micelle corona treatment can also be applied to vesicles:

$$A_{\text{corona,vesicle}} = A_{\text{GC}}(q,R_{\text{g}})\frac{A_{\text{sh}}\left[q\left(R_{\text{out}}+d_{\text{c}}\cdot R_{\text{g}}\right)\right] + A_{\text{sh}}\left[q\left(R_{\text{in}}-d_{\text{c}}\cdot R_{\text{g}}\right)\right]}{2} e^{-\frac{q^2\sigma_{\text{t}}{}^2}{2}} \tag{1.123}$$

The structure factor should be included, if required.

To calculate the number density of the particles, $n_{\text{p/V}}$, it may require calculating the total core volume of a single copolymer aggregate, V_{agg}, is defined as,

$$V_{\text{agg}} = N_{\text{agg}}\cdot V_{\text{p}} = N_{\text{agg}}\cdot\frac{M_{\text{p}}\cdot\rho_p}{N_A}, \tag{1.124}$$

where ρ_{p} is the polymer density to provide the volume of a single core block chain, V_{p}. Ideally, the geometrical volume occupied by the aggregate is identical to the volume occupied by the self-assembled copolymer chains. However, in practice the insoluble chains

are plasticised by solvent, which leads to swelling. Defining the solvent volume fraction as *xsol*, the aggregation number can be written as

$$N_{agg} = \frac{V_{geo}}{V_{agg,core}}\left(1 - xsol\right), \tag{1.125}$$

where V_{geo} is the geometrical core volume of the aggregates. For spherical micelle, worm-like micelle and vesicle models, these volumes are given by:

$$V_{geo} = \begin{cases} V_{sphere} = V_s\left(R_c\right) = \frac{4}{3}\pi R_c^{\ 3} \\ V_{worm} = \pi R_w^{\ 2} L \\ V_{vesicle} = \left[V_s\left(R_{out}\right) - V_s\left(R_{in}\right)\right] = \frac{4}{3}\pi\left(R_{out}^{\ 3} - R_{in}^{\ 3}\right) \end{cases}. \tag{1.126}$$

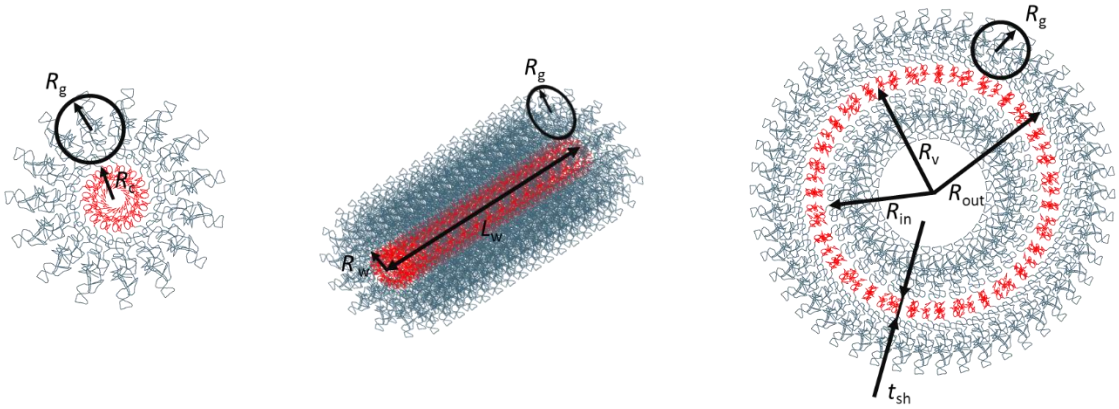

Figure 1.13. A schematic Schematic presentation of spherical micelle, worm-like micelle, vesicle from left to right as aggregates in small angle X-ray scattering research of polymerisation-induced self-assembly process. To describe the aggregates, necessary parameters are required: R_g of each type of aggregate is radius of gyration of corona block of block copolymer. R_c is core radius of spherical micelle structure. R_w is core radius of worm-like micelle structure. L_w is length of worm-like micelle structure. R_v is the centre radius of vesicle structure. R_v is the centre radius of vesicle structure. R_{in} and R_{out} are inner and outer radius of the core of vesicle. t_{sh} is membrane thickness of the vesicle.

For the structure of SAXS modelling of self-assembled nanoparticles, Percus–Yevick approximation or Percus–Yevick equation (PY) is one of the options for hard sphere (excluded volume) interactions.[245] This approximation derives the structure factor for hard spheres to be

$$S\left(q, R_{HS}, n\right) = S\left(A, V_{eff}\right) = \frac{1}{1 + 24V_{eff}\left[\frac{G\left(A\right)}{A}\right]}, \tag{1.127}$$

where R_{HS} is the half closest distance between the centers of the particles, A is equal to $2qR$, and V_{eff} is the effective volume for PY. The effective volume of the structure can be taken to

be the particle volume fraction. The formula, $G(A)$, is given by

$$G(A)=\frac{\alpha}{A^2}(\sin A-A\cos A)+\frac{\beta}{A^3}\left[2A\sin A-\left(2-A^2\right)\cos A-2\right]+\frac{\gamma}{A^5}\left\{-A^4\cos A+4\left[\left(3A^2-6\right)\cos A+\left(A^3-6A\right)\sin A+6\right]\right\}, \quad (1.128)$$

where $\alpha_{V_{\text{eff}}}$, $\beta_{V_{\text{eff}}}$, and $\gamma_{V_{\text{eff}}}$ are defined as

$$\begin{cases}\alpha_{V_{\text{eff}}}=\dfrac{\left(1+2V_{\text{eff}}\right)^2}{\left(1-V_{\text{eff}}\right)^4}\\ \beta_{V_{\text{eff}}}=-\dfrac{6V_{\text{eff}}\left(1+\dfrac{V_{\text{eff}}}{2}\right)^2}{\left(1-V_{\text{eff}}\right)^4}\\ \gamma_{V_{\text{eff}}}=\dfrac{1}{2}V_{\text{eff}}\alpha=\dfrac{1}{2}V_{\text{eff}}\dfrac{\left(1+2V_{\text{eff}}\right)^2}{\left(1-V_{\text{eff}}\right)^4}\end{cases}. \quad (1.129)$$

Thus, the mean distance between neighbouring particles (or spherical micelles) can be determined. and an example of particle distance and determination is shown in Figure 1.14. For the particles carrying charges, Hayter-Penfold Rescaled Mean Spherical Approximation (RMSA) structure factor can be accepted[246, 247], which provides the effective radius of charged spherical particle, volume fraction of spherical particle, the number of charges on sphere (in electrons).

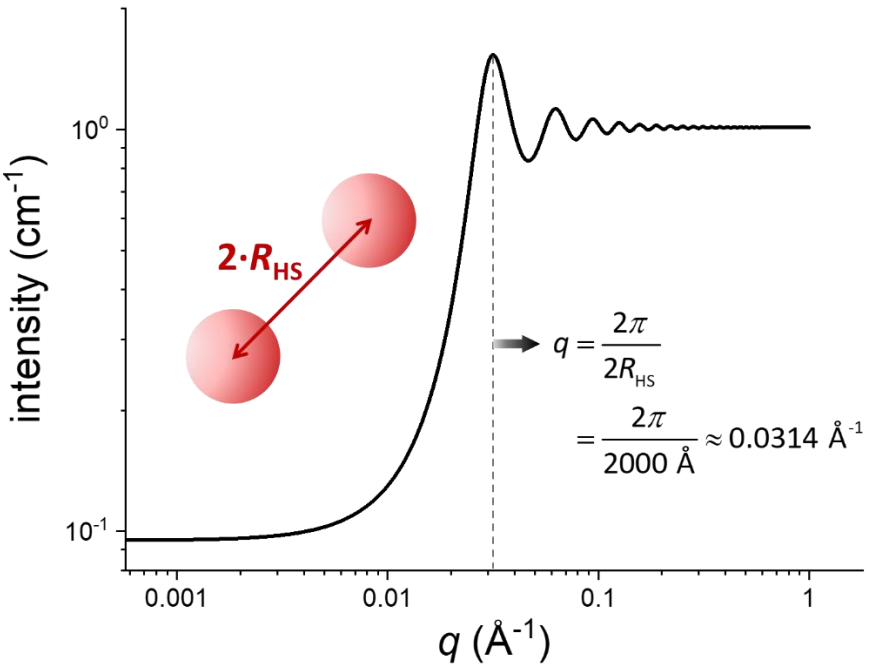

Figure 1.14. SAXS patterns of $S(q)$ as Percus–Yevick approximation when the half closest distance between the particle (red) centres R_{HS} = 100 Å and the effective volume V_{eff} = 0.3. The first peak is located at q = 0.0314 Å^{-1}.

1.7 Thesis Outline

The law of conservation of mass is combined with a population balance model to improve SAXS scattering models to study the self-assembly of diblock copolymer nanoparticles via PISA in Chapter 2. This enabled both chemical kinetics and mass transfer to be considered during such syntheses. In Chapter 3, *in situ* SAXS data acquired during the PISA synthesis of poly(stearyl methacrylate)-poly(benzyl methacrylate) ($PSMA_{31}$–$PBzMA_{2000}$) spherical nanoparticles in mineral oil are analysed to validate this new analytical approach. In the following Chapter, the very early (pre-micellar nucleation) stages of this PISA formulation are considered in detail. In Chapter 5, the PISA synthesis of poly(2-(dimethylamino)ethyl methacrylate)-poly(benzyl methacrylate) ($PDMA_{43}$-$PBzMA_{200}$) nano-objects in an 80/20 w/w ethanol/water mixture is analysed using the same methodology. Finally, the population balance concept is also applied to the formation of poly(2,2,2-trifluoroethyl methacrylate)/silica nanocomposite particles via conventional free radical polymerisation in Chapter 6. Finally, overall conclusions and prospects for future work are discussed in Chapter 7.

1.8 References

1. Flory, P. J., *Principles of Polymer Chemistry*. Cornell University Press: ITHACA, New York, 1953.
2. McNaught, A. D.; Wilkinson, A.; Pure, I. U. o.; Chemistry, A., *Compendium of Chemical Terminology: IUPAC Recommendations*. Blackwell Science: Oxford, 1997.
3. Young, R. J.; Lovell, P. A., *Introduction to polymers*. CRC press: Boca Raton, FL, USA, 2011.
4. Teraoka, I., *Polymer Solutions: An Introduction to Physical Properties*. Wiley: New York, 2002.
5. Braun, D.; Cherdron, H.; Rehahn, M.; Ritter, H.; Voit, B., *Polymer Synthesis: Theory and Practice: Fundamentals, Methods, Experiments*. Springer: Berlin Heidelberg, 2005.
6. Odian, G., *Principles of Polymerization*. Wiley: Hoboken, New Jersey, 2004.
7. Moad, G.; Solomon, D. H., *The Chemistry of Radical Polymerization*. Elsevier Science: Oxford, 2006.
8. Buback, M.; van Herk, A. M., *Radical Polymerization: Kinetics and Mechanism*. John Wiley & Sons: Berlin Heidelberg, 2007.
9. Chatgilialoglu, C.; Studer, A., *Encyclopedia of Radicals in Chemistry, Biology and Materials*. Wiley: Berlin Heidelberg, 2012.
10. Braun, D., Origins and development of initiation of free radical polymerization processes. *International Journal of Polymer Science* **2009,** *2009*.
11. Nesvadba, P., Radical Polymerization in Industry. In *Encyclopedia of Radicals in Chemistry, Biology and Materials*, 2012.
12. Mishra, M.; Yagci, Y., *Handbook of Vinyl Polymers: Radical Polymerization, Process, and Technology, Second Edition*. CRC Press: Boca Raton, 2016.

13. Braunecker, W. A.; Matyjaszewski, K., Controlled/living radical polymerization: Features, developments, and perspectives. *Progress in Polymer Science* **2007,** *32* (1), 93-146.
14. Moad, G.; Rizzardo, E.; Thang, S. H., Living Radical Polymerization by the RAFT Process. *Australian Journal of Chemistry* **2005,** *58* (6), 379-410.
15. Moad, G.; Rizzardo, E.; Thang, S. H., Living radical polymerization by the RAFT process–a third update. *Australian Journal of Chemistry* **2012,** *65* (8), 985-1076.
16. Keddie, D. J., A guide to the synthesis of block copolymers using reversible-addition fragmentation chain transfer (RAFT) polymerization. *Chemical Society Reviews* **2014,** *43* (2), 496-505.
17. Chiefari, J.; Chong, Y. K.; Ercole, F.; Krstina, J.; Jeffery, J.; Le, T. P. T.; Mayadunne, R. T. A.; Meijs, G. F.; Moad, C. L.; Moad, G.; Rizzardo, E.; Thang, S. H., Living Free-Radical Polymerization by Reversible Addition−Fragmentation Chain Transfer: The RAFT Process. *Macromolecules* **1998,** *31* (16), 5559-5562.
18. Mukherjee, S.; Boudouris, B. W., *Organic Radical Polymers: New Avenues in Organic Electronics*. Springer International Publishing: Switzerland, 2017.
19. Perrier, S.; Haddleton, D. M., In Situ NMR Monitoring of Living Radical Polymerization. In *In Situ Spectroscopy of Monomer and Polymer Synthesis*, Puskas, J. E.; Long, T. E.; Storey, R. F.; Shaikh, S.; Simmons, C. L., Eds. Springer US: Boston, MA, 2003; pp 125-146.
20. Barner-Kowollik, C., *Handbook of RAFT Polymerization*. Wiley: Germany, 2008.
21. Perrier, S., 50th Anniversary Perspective: RAFT Polymerization—A User Guide. *Macromolecules* **2017,** *50* (19), 7433-7447.
22. Moad, G.; Rizzardo, E., *RAFT Polymerization: Methods, Synthesis, and Applications*. Wiley: Weinheim, 2021.
23. Konkolewicz, D.; Hawkett, B. S.; Gray-Weale, A.; Perrier, S., RAFT Polymerization Kinetics: Combination of Apparently Conflicting Models. *Macromolecules* **2008,** *41* (17), 6400-6412.
24. Lovell, P. A.; El-Aasser, M. S., *Emulsion Polymerization and Emulsion Polymers*. John Wiley and Sons: Chichester, 1997.
25. Lovell, P. A.; Schork, F. J., Fundamentals of Emulsion Polymerization. *Biomacromolecules* **2020,** *21* (11), 4396-4441.
26. Hansen, F.; Ugelstad, J., Particle nucleation in emulsion polymerization. I. A theory for homogeneous nucleation. *Journal of Polymer Science: Polymer Chemistry Edition* **1978,** *16* (8), 1953-1979.
27. Zhou, J.; Yao, H.; Ma, J., Recent advances in RAFT-mediated surfactant-free emulsion polymerization. *Polymer Chemistry* **2018,** *9* (19), 2532-2561.
28. Asua, J. M., Miniemulsion polymerization. *Progress in Polymer Science* **2002,** *27* (7), 1283-1346.
29. Smith, W. V.; Ewart, R. H., Kinetics of emulsion polymerization. *The journal of chemical physics* **1948,** *16* (6), 592-599.
30. Smith, W. V., Chain initiation in styrene emulsion polymerization. *Journal of the American Chemical Society* **1949,** *71* (12), 4077-4082.
31. Morton, M.; Kaizerman, S.; Altier, M. W., Swelling of latex particles. *Journal of Colloid Science* **1954,** *9* (4), 300-312.
32. Flory, P. J., Thermodynamics of high polymer solutions. *The Journal of chemical physics* **1942,** *10* (1), 51-61.
33. Huggins, M. L., A revised theory of high polymer solutions. *Journal of the American Chemical Society* **1964,** *86* (17), 3535-3540.
34. Kawaguchi, S.; Ito, K., Dispersion polymerization. In *Polymer particles*, Springer: 2005; pp 299-328.
35. Walbridge, D.; Waters, J., Rheology of sterically stabilized dispersions of poly (methyl methacrylate) in aliphatic hydrocarbons. *Discussions of the Faraday Society* **1966,** *42*, 294-300.

36. Paine, A. J., Dispersion polymerization of styrene in polar solvents: I. Grafting mechanism of stabilization by hydroxypropyl cellulose. *Journal of Colloid and Interface Science* **1990,** *138* (1), 157-169.
37. Paine, A. J.; Deslandes, Y.; Gerroir, P.; Henrissat, B., Dispersion polymerization of styrene in polar solvents: II. Visualization of surface layers of steric stabilizer on dispersion-polymerized and precipitated polystyrene latex particles by transmission electron microscopy. *Journal of Colloid and Interface Science* **1990,** *138* (1), 170-181.
38. Paine, A. J.; Luymes, W.; McNulty, J., Dispersion polymerization of styrene in polar solvents. 6. Influence of reaction parameters on particle size and molecular weight in poly (N-vinylpyrrolidone)-stabilized reactions. *Macromolecules* **1990,** *23* (12), 3104-3109.
39. Paine, A. J., Dispersion polymerization of styrene in polar solvents. 7. A simple mechanistic model to predict particle size. *macromolecules* **1990,** *23* (12), 3109-3117.
40. Winnik, F. M.; Paine, A. J., Dispersion polymerization of styrene in polar solvents. Characterization of stabilizer in ordinary and precipitated particles by fluorescence quenching. *Langmuir* **1989,** *5* (4), 903-910.
41. Paine, A. J., Dispersion polymerization of styrene in polar solvents. IV. Solvency control of particle size from hydroxypropyl cellulose stabilized polymerizations. *Journal of Polymer Science Part A: Polymer Chemistry* **1990,** *28* (9), 2485-2500.
42. Wang, D.; Dimonie, V. L.; Sudol, E. D.; El-Aasser, M. S., Dispersion polymerization of n-butyl acrylate. *Journal of Applied Polymer Science* **2002,** *84* (14), 2692-2709.
43. Lee, K.-C.; Her, J.-H.; Kim, K.-J., Effects of Reaction Parameters on Particle Size, Molecular Weight, and Kinetics for Dispersion Polymerization of n-Butyl Acrylate. *International Journal of Polymer Analysis and Characterization* **2009,** *14* (7), 600-616.
44. Lee, H.; Terry, E.; Zong, M.; Arrowsmith, N.; Perrier, S.; Thurecht, K. J.; Howdle, S. M., Successful dispersion polymerization in supercritical CO2 using polyvinylalkylate hydrocarbon surfactants synthesized and anchored via RAFT. *Journal of the American Chemical Society* **2008,** *130* (37), 12242-12243.
45. Richez, A. P.; Yow, H. N.; Biggs, S.; Cayre, O. J., Dispersion polymerization in non-polar solvent: Evolution toward emerging applications. *Progress in Polymer Science* **2013,** *38* (6), 897-931.
46. Nugroho, M.; Kawaguchi, S.; Ito, K.; Winnik, M., Control of particle size in dispersion polymerization using poly (ethylene oxide) macromonomers. *Journal of Macromolecular Science, Part A* **1995,** *32* (sup1), 593-601.
47. Kawaguchi, S.; Winnik, M. A.; Ito, K., Dispersion copolymerization of n-butyl methacrylate with poly (ethylene oxide) macromonomers in methanol-water. Comparison of experiment with theory. *Macromolecules* **1995,** *28* (4), 1159-1166.
48. Ito, K.; Kawaguchi, S., Poly (macromonomers): homo-and copolymerization. In *Branched Polymers I*, Springer: 1999; pp 129-178.
49. Liu, J.; Gan, L.; Chew, C.; Quek, C.; Gong, H.; Gan, L., The particle size of latexes from dispersion polymerization of styrene using poly (ethylene oxide) macromonomer as a polymerizable stabilizer. *Journal of Polymer Science Part A: Polymer Chemistry* **1997,** *35* (16), 3575-3583.
50. Liu, J.; Chew, C.; Wong, S.; Gan, L.; Lin, J.; Tan, K., Dispersion polymerization of styrene in aqueous ethanol media using poly (ethylene oxide) macromonomer as a polymerizable stabilizer. *Polymer* **1998,** *39* (2), 283-289.
51. Imai, H.; Kawaguchi, S.; Ito, K., Syntheses of Poly (ethylene oxide-b-styrene oxide) Macromonomers and Their Application to Emulsion and Dispersion Copolymerizations with Styrene. *Polymer journal* **2003,** *35* (6), 528-534.
52. Vincent, B., The effect of adsorbed polymers on dispersion stability. *Advances in Colloid and Interface Science* **1974,** *4* (2-3), 193-277.
53. Klein, S. M.; Manoharan, V. N.; Pine, D. J.; Lange, F. F., Preparation of monodisperse

PMMA microspheres in nonpolar solvents by dispersion polymerization with a macromonomeric stabilizer. *Colloid and Polymer Science* **2003,** *282* (1), 7-13.
54. Pelton, R. H.; Osterroth, A.; Brook, M. A., Silicone stabilized poly(methyl methacrylate) nonaqueous latexes: I. Preparation and characterization. *Journal of Colloid and Interface Science* **1990,** *137* (1), 120-127.
55. Dawkins, J.; Taylor, G., Nonaqueous polystyrene dispersions: Radical dispersion polymerization in the presence of AB block copolymers of polystyrene and poly (dimethyl siloxane). *European Polymer Journal* **1979,** *15* (5), 453-457.
56. Hu, H.; Larson, R. G., Preparation of fluorescent particles with long excitation and emission wavelengths dispersible in organic solvents. *Langmuir* **2004,** *20* (18), 7436-7443.
57. Hu, H.; Larson, R. G., One-step preparation of highly monodisperse micron-size particles in organic solvents. *Journal of the American Chemical Society* **2004,** *126* (43), 13894-13895.
58. Fielding, L. A.; Derry, M. J.; Ladmiral, V.; Rosselgong, J.; Rodrigues, A. M.; Ratcliffe, L. P. D.; Sugihara, S.; Armes, S. P., RAFT dispersion polymerization in non-polar solvents: facile production of block copolymer spheres, worms and vesicles in n-alkanes. *Chemical Science* **2013,** *4* (5), 2081-2087.
59. Fritz, G.; Schädler, V.; Willenbacher, N.; Wagner, N. J., Electrosteric stabilization of colloidal dispersions. *Langmuir* **2002,** *18* (16), 6381-6390.
60. Tadros, T. F., *Colloid Stability: The Role of Surface Forces - Part I*. Wiley: Weinheim, 2006.
61. Bosma, G.; Pathmamanoharan, C.; de Hoog, E. H. A.; Kegel, W. K.; van Blaaderen, A.; Lekkerkerker, H. N. W., Preparation of Monodisperse, Fluorescent PMMA–Latex Colloids by Dispersion Polymerization. *Journal of Colloid and Interface Science* **2002,** *245* (2), 292-300.
62. Everett, D. H.; Stageman, J. F., Preparation and stability of novel polymer colloids in a range of simple liquids. *Faraday Discussions of the Chemical Society* **1978,** *65*, 230-241.
63. Charleux, B.; Cunningham, M.; Leiza, J. R., 3.14 - Vinyl Polymerization in Heterogeneous Systems. In *Polymer Science: A Comprehensive Reference*, Matyjaszewski, K.; Möller, M., Eds. Elsevier: Amsterdam, 2012; pp 463-499.
64. Sudol, E. D., Dispersion polymerization. In *Polymeric dispersions: principles and applications*, Springer: 1997; pp 141-153.
65. Rubinstein, M.; Colby, R. H., *Polymer Physics*. OUP Oxford: Oxford, 2003.
66. Cloizeaux, J.; Jannink, G., *Polymers in Solution: Their Modelling and Structure*. OUP Oxford: Oxford, 2010.
67. Yamakawa, H., *Modern Theory of Polymer Solutions*. Harper & Row: New York, 1971.
68. Schäfer, L., *Excluded Volume Effects in Polymer Solutions: as Explained by the Renormalization Group*. Springer: Berlin Heidelberg, 2011.
69. de Gennes, P. G., *Introduction to Polymer Dynamics*. Cambridge University Press: New York, 1990.
70. de Gennes, P. G.; Gennes, P. P. G.; Press, C. U., *Scaling Concepts in Polymer Physics*. Cornell University Press: ITHACA, New York, 1979.
71. Brandrup, J.; Immergut, E. H.; Grulke, E. A.; Abe, A.; Bloch, D. R., *Polymer handbook*. Wiley: New York, 1999; Vol. 89.
72. Matsen, M. W.; Bates, F. S., Block copolymer microstructures in the intermediate-segregation regime. *The Journal of Chemical Physics* **1997,** *106* (6), 2436-2448.
73. Bates, F. S.; Fredrickson, G. H., Block Copolymer Thermodynamics: Theory and Experiment. *Annual Review of Physical Chemistry* **1990,** *41* (1), 525-557.
74. Bates, F. S.; Fredrickson, G. H., Block copolymers-designer soft materials. *Physics today* **2000,** *52*.
75. G H Fredrickson, a.; Bates, F. S., Dynamics of Block Copolymers: Theory and Experiment. *Annual Review of Materials Science* **1996,** *26* (1), 501-550.
76. Matsen, M. W.; Bates, F. S., Unifying weak-and strong-segregation block copolymer

theories. *Macromolecules* **1996,** *29* (4), 1091-1098.
77. Jones, R. A. L.; Richards, R. W., *Polymers at Surfaces and Interfaces*. Cambridge University Press: New York, 1999.
78. Helfand, E.; Wasserman, Z. R., Block Copolymer Theory. 4. Narrow Interphase Approximation. *Macromolecules* **1976,** *9* (6), 879-888.
79. Helfand, E.; Wasserman, Z. R., Block Copolymer Theory. 5. Spherical Domains. *Macromolecules* **1978,** *11* (5), 960-966.
80. Helfand, E.; Wasserman, Z., Block Copolymer Theory. 6. Cylindrical Domains. *Macromolecules* **1980,** *13* (4), 994-998.
81. Helfand, E., Block Copolymer Theory. II. Statistical Thermodynamics of the Microphases. In *Recent Advances in Polymer Blends, Grafts, and Blocks*, Springer: 1974; pp 141-156.
82. Helfand, E., Block Copolymer Theory. III. Statistical Mechanics of the Microdomain Structure. *Macromolecules* **1975,** *8* (4), 552-556.
83. Matsen, M. W.; Bates, F. S., Origins of complex self-assembly in block copolymers. *Macromolecules* **1996,** *29* (23), 7641-7644.
84. Matsen, M. W., Self-consistent field theory and its applications. *Soft Matter* **2006,** *1*.
85. Helfand, E.; Sapse, A. M., Theory of unsymmetric polymer–polymer interfaces. *The Journal of Chemical Physics* **1975,** *62* (4), 1327-1331.
86. Hildebrand, J. H.; Scott, R. L., *Regular Solutions*. Prentice-Hall: Englewood Cliffs, 1962.
87. Hildebrand, J. H.; Scott, R. L., *The Solubility of Nonelectrolytes*. Dover Publications: New York, 1964.
88. Abbott, S.; Hansen, C. M., *Hansen solubility parameters in practice*. Hansen-Solubility: 2008.
89. Hansen, C. M., *Hansen solubility parameters: a user's handbook*. CRC press: New York, 2007.
90. Van Dijk, M.; Wakker, A., Some observations on the behaviour of the thermodynamic interaction parameter in dilute polymer solutions. *Polymer* **1993,** *34* (1), 132-137.
91. Barton, A. F., *CRC handbook of solubility parameters and other cohesion parameters*. Routledge: Boca Raton, 2017.
92. Lindvig, T.; Michelsen, M. L.; Kontogeorgis, G. M., A Flory–Huggins model based on the Hansen solubility parameters. *Fluid Phase Equilibria* **2002,** *203* (1-2), 247-260.
93. Israelachvili, J. N., *Intermolecular and Surface Forces*. Elsevier Science: United States, 2015.
94. Zhao, J.; Fung, B., NMR study of the transformation of sodium dodecyl sulfate micelles. *Langmuir* **1993,** *9* (5), 1228-1231.
95. Gradzielski, M., Kinetics of morphological changes in surfactant systems. *Current opinion in colloid & interface science* **2003,** *8* (4-5), 337-345.
96. Varade, D.; Joshi, T.; Aswal, V. K.; Goyal, P. S.; Hassan, P. A.; Bahadur, P., Micellar behavior of mixtures of sodium dodecyl sulfate and dodecyldimethylamine oxide in aqueous solutions. *Colloids and Surfaces A: Physicochemical and Engineering Aspects* **2005,** *259* (1), 103-109.
97. Huang, C.-h., Phosphatidylcholine vesicles. Formation and physical characteristics. *Biochemistry* **1969,** *8* (1), 344-352.
98. Peress, N. S.; Anderson, H. C.; Sajdera, S. W., The lipids of matrix vesicles from bovine fetal epiphyseal cartilage. *Calcified tissue research* **1974,** *14* (1), 275-281.
99. Szoka Jr, F.; Papahadjopoulos, D., Comparative properties and methods of preparation of lipid vesicles (liposomes). *Annual review of biophysics and bioengineering* **1980,** *9* (1), 467-508.
100. Lentz, B. R.; Alford, D. R.; Dombrose, F. A., Determination of phosphatidylglycerol asymmetry in small, unilamellar vesicles by chemical modification. *Biochemistry* **1980,** *19* (12),

2555-2559.
101. Fetsch, C.; Gaitzsch, J.; Messager, L.; Battaglia, G.; Luxenhofer, R., Self-Assembly of Amphiphilic Block Copolypeptoids – Micelles, Worms and Polymersomes. *Scientific Reports* **2016,** *6* (1), 33491.
102. Mai, Y.; Eisenberg, A., Self-assembly of block copolymers. *Chemical Society Reviews* **2012,** *41* (18), 5969-5985.
103. Canning, S. L.; Smith, G. N.; Armes, S. P., A Critical Appraisal of RAFT-Mediated Polymerization-Induced Self-Assembly. *Macromolecules* **2016,** *49* (6), 1985-2001.
104. Warren, N. J.; Armes, S. P., Polymerization-Induced Self-Assembly of Block Copolymer Nano-objects via RAFT Aqueous Dispersion Polymerization. *Journal of the American Chemical Society* **2014,** *136* (29), 10174-10185.
105. Derry, M. J.; Fielding, L. A.; Armes, S. P., Polymerization-induced self-assembly of block copolymer nanoparticles via RAFT non-aqueous dispersion polymerization. *Progress in Polymer Science* **2016,** *52*, 1-18.
106. Lowe, A. B., RAFT alcoholic dispersion polymerization with polymerization-induced self-assembly. *Polymer* **2016,** *106*, 161-181.
107. Ferguson, C. J.; Hughes, R. J.; Pham, B. T. T.; Hawkett, B. S.; Gilbert, R. G.; Serelis, A. K.; Such, C. H., Effective ab Initio Emulsion Polymerization under RAFT Control. *Macromolecules* **2002,** *35* (25), 9243-9245.
108. Zhang, X.; Boissé, S.; Zhang, W.; Beaunier, P.; D'Agosto, F.; Rieger, J.; Charleux, B., Well-Defined Amphiphilic Block Copolymers and Nano-objects Formed in Situ via RAFT-Mediated Aqueous Emulsion Polymerization. *Macromolecules* **2011,** *44* (11), 4149-4158.
109. Cunningham, V. J.; Alswieleh, A. M.; Thompson, K. L.; Williams, M.; Leggett, G. J.; Armes, S. P.; Musa, O. M., Poly(glycerol monomethacrylate)–Poly(benzyl methacrylate) Diblock Copolymer Nanoparticles via RAFT Emulsion Polymerization: Synthesis, Characterization, and Interfacial Activity. *Macromolecules* **2014,** *47* (16), 5613-5623.
110. Boissé, S.; Rieger, J.; Belal, K.; Di-Cicco, A.; Beaunier, P.; Li, M.-H.; Charleux, B., Amphiphilic block copolymer nano-fibers via RAFT-mediated polymerization in aqueous dispersed system. *Chemical Communications* **2010,** *46* (11), 1950-1952.
111. Zhang, W.; D'Agosto, F.; Boyron, O.; Rieger, J.; Charleux, B., Toward a Better Understanding of the Parameters that Lead to the Formation of Nonspherical Polystyrene Particles via RAFT-Mediated One-Pot Aqueous Emulsion Polymerization. *Macromolecules* **2012,** *45* (10), 4075-4084.
112. Zhang, W.; D'Agosto, F.; Dugas, P.-Y.; Rieger, J.; Charleux, B., RAFT-mediated one-pot aqueous emulsion polymerization of methyl methacrylate in presence of poly(methacrylic acid-co-poly(ethylene oxide) methacrylate) trithiocarbonate macromolecular chain transfer agent. *Polymer* **2013,** *54* (8), 2011-2019.
113. Rieger, J.; Zhang, W.; Stoffelbach, F.; Charleux, B., Surfactant-free RAFT emulsion polymerization using poly (N, N-dimethylacrylamide) trithiocarbonate macromolecular chain transfer agents. *Macromolecules* **2010,** *43* (15), 6302-6310.
114. Truong, N. P.; Dussert, M. V.; Whittaker, M. R.; Quinn, J. F.; Davis, T. P., Rapid synthesis of ultrahigh molecular weight and low polydispersity polystyrene diblock copolymers by RAFT-mediated emulsion polymerization. *Polymer Chemistry* **2015,** *6* (20), 3865-3874.
115. Rieger, J.; Stoffelbach, F.; Bui, C.; Alaimo, D.; Jérôme, C.; Charleux, B., Amphiphilic poly (ethylene oxide) macromolecular RAFT agent as a stabilizer and control agent in ab initio batch emulsion polymerization. *Macromolecules* **2008,** *41* (12), 4065-4068.
116. Zhang, W.; D'Agosto, F.; Boyron, O.; Rieger, J.; Charleux, B., One-pot synthesis of poly (methacrylic acid-co-poly (ethylene oxide) methyl ether methacrylate)-b-polystyrene amphiphilic block copolymers and their self-assemblies in water via RAFT-mediated radical emulsion polymerization. A kinetic study. *Macromolecules* **2011,** *44* (19), 7584-7593.
117. Chaduc, I.; Zhang, W.; Rieger, J.; Lansalot, M.; d'Agosto, F.; Charleux, B., Amphiphilic

Block Copolymers from a Direct and One‐pot RAFT Synthesis in Water. *Macromolecular rapid communications* **2011,** *32* (16), 1270-1276.
118. Chaduc, I.; Girod, M.; Antoine, R.; Charleux, B.; D'Agosto, F.; Lansalot, M., Batch emulsion polymerization mediated by poly (methacrylic acid) macroRAFT agents: One-pot synthesis of self-stabilized particles. *Macromolecules* **2012,** *45* (15), 5881-5893.
119. Cockram, A. A.; Neal, T. J.; Derry, M. J.; Mykhaylyk, O. O.; Williams, N. S. J.; Murray, M. W.; Emmett, S. N.; Armes, S. P., Effect of Monomer Solubility on the Evolution of Copolymer Morphology during Polymerization-Induced Self-Assembly in Aqueous Solution. *Macromolecules* **2017,** *50* (3), 796-802.
120. Zheng, G.; Pan, C., Reversible Addition−Fragmentation Transfer Polymerization in Nanosized Micelles Formed in Situ. *Macromolecules* **2006,** *39* (1), 95-102.
121. An, Z.; Shi, Q.; Tang, W.; Tsung, C.-K.; Hawker, C. J.; Stucky, G. D., Facile RAFT Precipitation Polymerization for the Microwave-Assisted Synthesis of Well-Defined, Double Hydrophilic Block Copolymers and Nanostructured Hydrogels. *Journal of the American Chemical Society* **2007,** *129* (46), 14493-14499.
122. Sugihara, S.; Blanazs, A.; Armes, S. P.; Ryan, A. J.; Lewis, A. L., Aqueous Dispersion Polymerization: A New Paradigm for in Situ Block Copolymer Self-Assembly in Concentrated Solution. *Journal of the American Chemical Society* **2011,** *133* (39), 15707-15713.
123. Blanazs, A.; Madsen, J.; Battaglia, G.; Ryan, A. J.; Armes, S. P., Mechanistic Insights for Block Copolymer Morphologies: How Do Worms Form Vesicles? *Journal of the American Chemical Society* **2011,** *133* (41), 16581-16587.
124. Chambon, P.; Blanazs, A.; Battaglia, G.; Armes, S. P., Facile Synthesis of Methacrylic ABC Triblock Copolymer Vesicles by RAFT Aqueous Dispersion Polymerization. *Macromolecules* **2012,** *45* (12), 5081-5090.
125. Zhang, W.-J.; Hong, C.-Y.; Pan, C.-Y., Formation of Hexagonally Packed Hollow Hoops and Morphology Transition in RAFT Ethanol Dispersion Polymerization. *Macromolecular Rapid Communications* **2015,** *36* (15), 1428-1436.
126. Wan, W.-M.; Pan, C.-Y., One-pot synthesis of polymeric nanomaterials via RAFT dispersion polymerization induced self-assembly and re-organization. *Polymer Chemistry* **2010,** *1* (9), 1475-1484.
127. Lee, K.-C.; Lee, S.-E.; Song, B.-K., Dispersion polymerization of acrylamide in methanol/water media. *Macromolecular Research* **2002,** *10* (3), 140-144.
128. Derry, M. J.; Fielding, L. A.; Warren, N. J.; Mable, C. J.; Smith, A. J.; Mykhaylyk, O. O.; Armes, S. P., In situ small-angle X-ray scattering studies of sterically-stabilized diblock copolymer nanoparticles formed during polymerization-induced self-assembly in non-polar media. *Chemical Science* **2016,** *7* (8), 5078-5090.
129. Jones, E. R.; Semsarilar, M.; Wyman, P.; Boerakker, M.; Armes, S. P., Addition of water to an alcoholic RAFT PISA formulation leads to faster kinetics but limits the evolution of copolymer morphology. *Polymer Chemistry* **2016,** *7* (4), 851-859.
130. Jones, E. R.; Semsarilar, M.; Blanazs, A.; Armes, S. P., Efficient Synthesis of Amine-Functional Diblock Copolymer Nanoparticles via RAFT Dispersion Polymerization of Benzyl Methacrylate in Alcoholic Media. *Macromolecules* **2012,** *45* (12), 5091-5098.
131. Madl, C. M.; Mehta, M.; Duda, G. N.; Heilshorn, S. C.; Mooney, D. J., Presentation of BMP-2 mimicking peptides in 3D hydrogels directs cell fate commitment in osteoblasts and mesenchymal stem cells. *Biomacromolecules* **2014,** *15* (2), 445-455.
132. Engler, A. J.; Sen, S.; Sweeney, H. L.; Discher, D. E., Matrix elasticity directs stem cell lineage specification. *Cell* **2006,** *126* (4), 677-689.
133. Achilias, D. S., A review of modeling of diffusion controlled polymerization reactions. *Macromolecular theory and simulations* **2007,** *16* (4), 319-347.
134. Horie, K.; Mita, I.; Kambe, H., Calorimetric investigation of polymerization reactions. I. Diffusion‐controlled polymerization of methyl methacrylate and styrene. *Journal of*

Polymer Science Part A‐1: Polymer Chemistry **1968,** *6* (9), 2663-2676.
135. Marten, F.; Hamielec, A., High conversion diffusion-controlled polymerization. ACS Publications: WASHINGTON, 1979.
136. Achilias, D.; Kiparissides, C., Development of a general mathematical framework for modeling diffusion-controlled free-radical polymerization reactions. *Macromolecules* **1992,** *25* (14), 3739-3750.
137. Marten, F.; Hamielec, A., High‐conversion diffusion‐controlled polymerization of styrene. I. *Journal of Applied Polymer Science* **1982,** *27* (2), 489-505.
138. Freedman, D., *Brownian Motion and Diffusion*. Springer: New York, 2012.
139. Heitjans, P.; Kärger, J., *Diffusion in Condensed Matter: Methods, Materials, Models*. Springer: Berlin Heidelberg, 2006.
140. Cussler, E. L.; Cussler, E. L., *Diffusion: Mass Transfer in Fluid Systems*. Cambridge University Press: New York, 2009.
141. Banks, R. B., *Growth and Diffusion Phenomena: Mathematical Frameworks and Applications*. Springer Berlin Heidelberg: Berlin, Heidelberg, 2013.
142. Jackson, K. A., *Kinetic Processes: Crystal Growth, Diffusion, and Phase Transitions in Materials*. John Wiley & Sons: Weinheim, 2010.
143. Crank, J., *The mathematics of diffusion*. Oxford university press: Oxford, 1979.
144. Reed, W. F.; Alb, A. M., *Monitoring Polymerization Reactions: From Fundamentals to Applications*. Wiley: Hoboken, New Jersey, 2014.
145. Libera, M. R.; Egerton, R. F., Advances in the Transmission Electron Microscopy of Polymers. *Polymer Reviews* **2010,** *50* (3), 321-339.
146. Bassett, D. C.; Keith, H. D., Electron microscopy and spherulitic organization in polymers. *Critical Reviews in Solid State and Materials Sciences* **1984,** *12* (2), 97-163.
147. Kuei, B.; Aplan, M. P.; Litofsky, J. H.; Gomez, E. D., New opportunities in transmission electron microscopy of polymers. *Materials Science and Engineering: R: Reports* **2020,** *139*, 100516.
148. Golozar, M.; Hovington, P.; Paolella, A.; Bessette, S.; Lagacé, M.; Bouchard, P.; Demers, H.; Gauvin, R.; Zaghib, K., In Situ Scanning Electron Microscopy Detection of Carbide Nature of Dendrites in Li–Polymer Batteries. *Nano Letters* **2018,** *18* (12), 7583-7589.
149. Orekhov, A. S.; Klechkovskaya, V. V.; Kononova, S. V., Low-voltage scanning electron microscopy of multilayer polymer systems. *Crystallography Reports* **2017,** *62* (5), 710-715.
150. Semsarilar, M.; Penfold, N. J. W.; Jones, E. R.; Armes, S. P., Semi-crystalline diblock copolymer nano-objects prepared via RAFT alcoholic dispersion polymerization of stearyl methacrylate. *Polymer Chemistry* **2015,** *6* (10), 1751-1757.
151. Michler, G. H., Electron microscopy in polymer science. *Applied Spectroscopy Reviews* **1993,** *28* (4), 327-384.
152. Liu, Z.; Erhan, S. Z., Ring-opening polymerization of epoxidized soybean oil. *Journal of the American Oil Chemists' Society* **2010,** *87* (4), 437-444.
153. Potthast, A.; Radosta, S.; Saake, B.; Lebioda, S.; Heinze, T.; Henniges, U.; Isogai, A.; Koschella, A.; Kosma, P.; Rosenau, T., Comparison testing of methods for gel permeation chromatography of cellulose: coming closer to a standard protocol. *Cellulose* **2015,** *22* (3), 1591-1613.
154. Tasdelen, M. A.; Uygun, M.; Yagci, Y., Photoinduced controlled radical polymerization. *Macromolecular rapid communications* **2011,** *32* (1), 58-62.
155. Wang, H.; Li, Q.; Dai, J.; Du, F.; Zheng, H.; Bai, R., Real-time and in situ investigation of "living"/controlled photopolymerization in the presence of a trithiocarbonate. *Macromolecules* **2013,** *46* (7), 2576-2582.
156. Wen, J.-L.; Sun, S.-L.; Xue, B.-L.; Sun, R.-C., Recent advances in characterization of lignin polymer by solution-state nuclear magnetic resonance (NMR) methodology. *Materials* **2013,** *6* (1), 359-391.

157. Ren, T.; Liu, Q.; Lu, H.; Liu, H.; Zhang, X.; Du, J., Multifunctional polymer vesicles for ultrasensitive magnetic resonance imaging and drug delivery. *Journal of Materials Chemistry* **2012,** *22* (24), 12329-12338.
158. Csetneki, I.; Faix, M. K.; Szilagyi, A.; Kovacs, A.; Nemeth, Z.; Zrinyi, M., Preparation of magnetic polystyrene latex via the miniemulsion polymerization technique. *Journal of Polymer Science Part A: Polymer Chemistry* **2004,** *42* (19), 4802-4808.
159. Barth, H. G.; Mays, J. W., *Modern Methods of Polymer Characterization*. Wiley: New York, 1991.
160. Karagoz, B.; Esser, L.; Duong, H. T.; Basuki, J. S.; Boyer, C.; Davis, T. P., Polymerization-Induced Self-Assembly (PISA)–control over the morphology of nanoparticles for drug delivery applications. *Polymer Chemistry* **2014,** *5* (2), 350-355.
161. Zhang, W.; Fang, B.; Walther, A.; Müller, A. H., Synthesis via RAFT polymerization of tadpole-shaped organic/inorganic hybrid poly (acrylic acid) containing polyhedral oligomeric silsesquioxane (POSS) and their self-assembly in water. *Macromolecules* **2009,** *42* (7), 2563-2569.
162. Warren, N. J.; Mykhaylyk, O. O.; Mahmood, D.; Ryan, A. J.; Armes, S. P., RAFT Aqueous Dispersion Polymerization Yields Poly(ethylene glycol)-Based Diblock Copolymer Nano-Objects with Predictable Single Phase Morphologies. *Journal of the American Chemical Society* **2014,** *136* (3), 1023-1033.
163. Warren, N. J.; Mykhaylyk, O. O.; Ryan, A. J.; Williams, M.; Doussineau, T.; Dugourd, P.; Antoine, R.; Portale, G.; Armes, S. P., Testing the Vesicular Morphology to Destruction: Birth and Death of Diblock Copolymer Vesicles Prepared via Polymerization-Induced Self-Assembly. *Journal of the American Chemical Society* **2015,** *137* (5), 1929-1937.
164. Derry, M. J.; Smith, T.; O'Hora, P. S.; Armes, S. P., Block Copolymer Nanoparticles Prepared via Polymerization-Induced Self-Assembly Provide Excellent Boundary Lubrication Performance for Next-Generation Ultralow-Viscosity Automotive Engine Oils. *ACS Applied Materials & Interfaces* **2019,** *11* (36), 33364-33369.
165. Semsarilar, M.; Jones, E. R.; Blanazs, A.; Armes, S. P., Efficient Synthesis of Sterically-Stabilized Nano-Objects via RAFT Dispersion Polymerization of Benzyl Methacrylate in Alcoholic Media. *Advanced Materials* **2012,** *24* (25), 3378-3382.
166. Jones, E.; Mykhaylyk, O.; Semsarilar, M.; Boerakker, M.; Wyman, P.; Armes, S., How do spherical diblock copolymer nanoparticles grow during RAFT alcoholic dispersion polymerization? *Macromolecules* **2015,** *49* (1), 172-181.
167. Brotherton, E. E.; Hatton, F. L.; Cockram, A. A.; Derry, M. J.; Czajka, A.; Cornel, E. J.; Topham, P. D.; Mykhaylyk, O. O.; Armes, S. P., In Situ Small-Angle X-ray Scattering Studies During Reversible Addition–Fragmentation Chain Transfer Aqueous Emulsion Polymerization. *Journal of the American Chemical Society* **2019,** *141* (34), 13664-13675.
168. Czajka, A.; Armes, S. P., In situ SAXS studies of a prototypical RAFT aqueous dispersion polymerization formulation: monitoring the evolution in copolymer morphology during polymerization-induced self-assembly. *Chemical Science* **2020,** *11* (42), 11443-11454.
169. Long, T.; Liu, H.; Schell, B.; Teegarden, D. M.; Uerz, D., Determination of solution polymerization kinetics by near-infrared spectroscopy. 1. Living anionic polymerization processes. *Macromolecules* **1993,** *26* (23), 6237-6242.
170. Aldridge, P. K.; Kelly, J. J.; Callis, J. B.; Burns, D. H., Noninvasive monitoring of bulk polymerization using short-wavelength near-infrared spectroscopy. *Analytical Chemistry* **1993,** *65* (24), 3581-3585.
171. DeThomas, F. A.; Hall, J. W.; Monfre, S. L., Real-time monitoring of polyurethane production using near-infrared spectroscopy. *Talanta* **1994,** *41* (3), 425-431.
172. Ollagnier, J.-N.; Tassaing, T.; Harrisson, S.; Destarac, M., Application of online infrared spectroscopy to study the kinetics of precipitation polymerization of acrylic acid in supercritical carbon dioxide. *Reaction Chemistry & Engineering* **2016,** *1* (4), 372-378.

173. Beuermann, S.; Buback, M.; Isemer, C.; Wahl, A., Homogeneous free‐radical polymerization of styrene in supercritical CO2. *Macromolecular rapid communications* **1999,** *20* (1), 26-32.
174. Giles, M.; Hay, J.; Howdle, S.; Winder, R., Macromonomer surfactants for the polymerisation of methyl methacrylate in supercritical CO2. *Polymer* **2000,** *41* (18), 6715-6721.
175. Matsuyama, K.; Mishima, K., Preparation of poly (methyl methacrylate)–TiO2 nanoparticle composites by pseudo-dispersion polymerization of methyl methacrylate in supercritical CO2. *The Journal of Supercritical Fluids* **2009,** *49* (2), 256-264.
176. Du, J.; Zhang, J.; Han, B.; Liu, Z.; Wan, M., Polyaniline microtubes synthesized via supercritical CO2 and aqueous interfacial polymerization. *Synthetic metals* **2005,** *155* (3), 523-526.
177. Hammad, A.; Noby, H.; Elkady, M.; El-Shazly, A. In *In-situ polymerization of polyaniline/polypyrrole copolymer using different techniques*, IOP conference series: materials Science and engineering, IOP Publishing: 2018; p 012001.
178. Kortsen, K.; Pacheco, A. A. C.; Lentz, J. C.; Taresco, V.; Howdle, S. M., On-line polymerisation monitoring in scCO2: a reliable and inexpensive sampling method in high pressure applications. *The Journal of Supercritical Fluids* **2021,** *167*, 105047.
179. Fijten, M. W.; Meier, M. A.; Hoogenboom, R.; Schubert, U. S., Automated parallel investigations/optimizations of the reversible addition‐fragmentation chain transfer polymerization of methyl methacrylate. *Journal of Polymer Science Part A: Polymer Chemistry* **2004,** *42* (22), 5775-5783.
180. Keifer, P. A., NMR tools for biotechnology. *Current Opinion in Biotechnology* **1999,** *10* (1), 34-41.
181. Neudert, R.; Ströfer, E.; Bremser, W., On‐line NMR in process engineering. *Magnetic resonance in chemistry* **1986,** *24* (12), 1089-1092.
182. Woelk, K.; Bargon, J., High‐pressure NMR probes for the in situ investigation of gas/liquid reactions. *Review of scientific instruments* **1992,** *63* (6), 3307-3310.
183. Keifer, P. A., High-resolution NMR techniques for solid-phase synthesis and combinatorial chemistry. *Drug Discovery Today* **1997,** *2* (11), 468-478.
184. McDermott, R.; Trabesinger, A. H.; Muck, M.; Hahn, E. L.; Pines, A.; Clarke, J., Liquid-state NMR and scalar couplings in microtesla magnetic fields. *Science* **2002,** *295* (5563), 2247-2249.
185. Lutz, J.-F.; Matyjaszewski, K., Nuclear magnetic resonance monitoring of chain-end functionality in the atom transfer radical polymerization of styrene. *Journal of Polymer Science Part A: Polymer Chemistry* **2005,** *43* (4), 897-910.
186. Li, H.; Wang, C.; Bai, F.; Yue, J.; Woo, H.-G., Living Ring-Opening Polymerization of l-Lactide Catalyzed by Red-Al. *Organometallics* **2004,** *23* (6), 1411-1415.
187. Aliev, A. E.; Elizabé, L.; Kariuki, B. M.; Kirschnick, H.; Thomas, J. M.; Epple, M.; Harris, K. D., In Situ Monitoring of Solid‐State Polymerization Reactions in Sodium Chloroacetate and Sodium Bromoacetate by 23Na and 13C Solid‐State NMR Spectroscopy. *Chemistry–A European Journal* **2000,** *6* (7), 1120-1126.
188. Vicente, M.; BenAmor, S.; Gugliotta, L. M.; Leiza, J. R.; Asua, J. M., Control of Molecular Weight Distribution in Emulsion Polymerization Using On-Line Reaction Calorimetry. *Industrial & Engineering Chemistry Research* **2001,** *40* (1), 218-227.
189. Elizalde, O.; Azpeitia, M.; Reis, M. M.; Asua, J. M.; Leiza, J. R., Monitoring emulsion polymerization reactors: calorimetry versus Raman spectroscopy. *Industrial & engineering chemistry research* **2005,** *44* (18), 7200-7207.
190. BenAmor, S.; Colombié, D.; McKenna, T., Online reaction calorimetry. Applications to the monitoring of emulsion polymerization without samples or models of the heat-transfer coefficient. *Industrial & engineering chemistry research* **2002,** *41* (17), 4233-4241.
191. Santos, A.; Lima, E.; Pinto, J.; Graillat, C.; McKenna, T., Online monitoring of the

evolution of the number of particles in emulsion polymerization by conductivity measurements. I. Model formulation. *Journal of applied polymer science* **2003,** *90* (5), 1213-1226.
192. Santos, A. F.; Lima, E. L.; Pinto, J. C.; Graillat, C.; McKenna, T. F., On-line monitoring of the evolution of number of particles in emulsion polymerization by conductivity measurements. II. Model validation. *Journal of Applied Polymer Science* **2004,** *91* (2), 941-952.
193. Zhao, F.; Sudol, E. D.; Daniels, E. S.; Klein, A.; El-Aasser, M. S., Online conductivity and stability in the emulsion polymerization of N-butyl methacrylate: Nonreactive versus reactive systems. *Journal of Applied Polymer Science* **2012,** *126* (4), 1267-1276.
194. Canegallo, S.; Storti, G.; Morbidelli, M.; Carrà, S., Densimetry for on-line conversion monitoring in emulsion homo- and copolymerization. *Journal of Applied Polymer Science* **1993,** *47* (6), 961-979.
195. Abbey, K., Polymerization kinetics by precision densimetry. ACS Publications: 1981.
196. Florenzano, F. H.; Strelitzki, R.; Reed, W. F., Absolute, On-Line Monitoring of Molar Mass during Polymerization Reactions. *Macromolecules* **1998,** *31* (21), 7226-7238.
197. Çatalgil-Giz, H.; Giz, A.; Alb, A.; Reed, W. F., Absolute online monitoring of a stepwise polymerization reaction: Polyurethane synthesis. *Journal of Applied Polymer Science* **2001,** *82* (8), 2070-2077.
198. Kourti, T. Polymer latexes: production by homogeneous nucleation and methods for particle size determination. 1989.
199. Levere, M. E.; Willoughby, I.; O'Donohue, S.; de Cuendias, A.; Grice, A. J.; Fidge, C.; Becer, C. R.; Haddleton, D. M., Assessment of SET-LRP in DMSO using online monitoring and Rapid GPC. *Polymer Chemistry* **2010,** *1* (7), 1086-1094.
200. Levere, M. E.; Willoughby, I.; O'Donohue, S.; Wright, P. M.; Grice, A. J.; Fidge, C.; Remzi Becer, C.; Haddleton, D. M., Cu(0) mediated polymerization in toluene using online rapid GPC monitoring. *Journal of Polymer Science Part A: Polymer Chemistry* **2011,** *49* (8), 1753-1763.
201. Cornel, E. J.; van Meurs, S.; Smith, T.; O'Hora, P. S.; Armes, S. P., In Situ Spectroscopic Studies of Highly Transparent Nanoparticle Dispersions Enable Assessment of Trithiocarbonate Chain-End Fidelity during RAFT Dispersion Polymerization in Nonpolar Media. *Journal of the American Chemical Society* **2018,** *140* (40), 12980-12988.
202. Haven, J. J.; Junkers, T., Online Monitoring of Polymerizations: Current Status. *European Journal of Organic Chemistry* **2017,** *2017* (44), 6474-6482.
203. Alauhdin, M.; Bennett, T. M.; He, G.; Bassett, S. P.; Portale, G.; Bras, W.; Hermida-Merino, D.; Howdle, S. M., Monitoring morphology evolution within block copolymer microparticles during dispersion polymerisation in supercritical carbon dioxide: a high pressure SAXS study. *Polymer Chemistry* **2019,** *10* (7), 860-871.
204. Takahashi, R.; Miwa, S.; Sobotta, F. H.; Lee, J. H.; Fujii, S.; Ohta, N.; Brendel, J. C.; Sakurai, K., Unraveling the kinetics of the structural development during polymerization-induced self-assembly: decoupling the polymerization and the micelle structure. *Polymer Chemistry* **2020,** *11* (8), 1514-1524.
205. Rymaruk, M. J.; O'Brien, C. T.; György, C.; Darmau, B.; Jennings, J.; Mykhaylyk, O. O.; Armes, S. P., Small-Angle X-Ray Scattering Studies of Block Copolymer Nano-Objects: Formation of Ordered Phases in Concentrated Solution During Polymerization-Induced Self-Assembly. *Angewandte Chemie International Edition* **2021,** *60* (23), 12955-12963.
206. Schuster, J.; Köhn, R.; Döblinger, M.; Keilbach, A.; Amenitsch, H.; Bein, T., In Situ SAXS Study on a New Mechanism for Mesostructure Formation of Ordered Mesoporous Carbons: Thermally Induced Self-Assembly. *Journal of the American Chemical Society* **2012,** *134* (27), 11136-11145.
207. Humbert, S.; Lame, O.; Chenal, J.-M.; Rochas, C.; Vigier, G., Small strain behavior of polyethylene: In situ SAXS measurements. *Journal of Polymer Science Part B: Polymer Physics* **2010,** *48* (13), 1535-1542.

208. Stoclet, G.; Lefebvre, J. M.; Séguéla, R.; Vanmansart, C., In-situ SAXS study of the plastic deformation behavior of polylactide upon cold-drawing. *Polymer* **2014,** *55* (7), 1817-1828.
209. Defebvin, J.; Barrau, S.; Stoclet, G.; Rochas, C.; Lefebvre, J.-M., In situ SAXS/WAXS investigation of the structural evolution of poly(vinylidene fluoride) upon uniaxial stretching. *Polymer* **2016,** *84*, 148-157.
210. Sandí, G.; Joachin, H.; Kizilel, R.; Seifert, S.; Carrado, K. A., In Situ SAXS Studies of the Structural Changes of Polymer Nanocomposites Used in Battery Applications. *Chemistry of Materials* **2003,** *15* (4), 838-843.
211. Doncom, K. E. B.; Pitto-Barry, A.; Willcock, H.; Lu, A.; McKenzie, B. E.; Kirby, N.; O'Reilly, R. K., Complementary light scattering and synchrotron small-angle X-ray scattering studies of the micelle-to-unimer transition of polysulfobetaines. *Soft Matter* **2015,** *11* (18), 3666-3676.
212. Balmer, J. A.; Mykhaylyk, O. O.; Armes, S. P.; Fairclough, J. P. A.; Ryan, A. J.; Gummel, J.; Murray, M. W.; Murray, K. A.; Williams, N. S. J., Time-Resolved Small-Angle X-ray Scattering Studies of Polymer−Silica Nanocomposite Particles: Initial Formation and Subsequent Silica Redistribution. *Journal of the American Chemical Society* **2011,** *133* (4), 826-837.
213. Mable, C. J.; Gibson, R. R.; Prevost, S.; McKenzie, B. E.; Mykhaylyk, O. O.; Armes, S. P., Loading of Silica Nanoparticles in Block Copolymer Vesicles during Polymerization-Induced Self-Assembly: Encapsulation Efficiency and Thermally Triggered Release. *Journal of the American Chemical Society* **2015,** *137* (51), 16098-16108.
214. Deng, R.; Derry, M. J.; Mable, C. J.; Ning, Y.; Armes, S. P., Using Dynamic Covalent Chemistry To Drive Morphological Transitions: Controlled Release of Encapsulated Nanoparticles from Block Copolymer Vesicles. *Journal of the American Chemical Society* **2017,** *139* (22), 7616-7623.
215. Fürst, C.; Zhang, P.; Roth, S. V.; Drechsler, M.; Förster, S., Self-assembly of block copolymers via micellar intermediate states into vesicles on time scales from milliseconds to days. *Polymer* **2016,** *107*, 434-444.
216. Derry, M. J.; Mykhaylyk, O. O.; Armes, S. P., A vesicle‐to‐worm transition provides a new high‐temperature oil thickening mechanism. *Angewandte Chemie* **2017,** *129* (7), 1772-1776.
217. Roe, R. J., *Methods of X-ray and Neutron Scattering in Polymer Science*. Oxford University Press: New York, 2000.
218. Schnablegger, H.; Singh, Y., The SAXS guide: getting acquainted with the principles. *Austria: Anton Paar GmbH* **2011**.
219. Henrich, B.; Bergamaschi, A.; Broennimann, C.; Dinapoli, R.; Eikenberry, E.; Johnson, I.; Kobas, M.; Kraft, P.; Mozzanica, A.; Schmitt, B., PILATUS: A single photon counting pixel detector for X-ray applications. *Nuclear Instruments and Methods in Physics Research Section A: Accelerators, Spectrometers, Detectors and Associated Equipment* **2009,** *607* (1), 247-249.
220. Neal, T. J.; Beattie, D. L.; Byard, S. J.; Smith, G. N.; Murray, M. W.; Williams, N. S. J.; Emmett, S. N.; Armes, S. P.; Spain, S. G.; Mykhaylyk, O. O., Self-Assembly of Amphiphilic Statistical Copolymers and Their Aqueous Rheological Properties. *Macromolecules* **2018,** *51* (4), 1474-1487.
221. Zemb, T.; Lindner, P., *Neutrons, X-rays and Light: Scattering Methods Applied to Soft Condensed Matter*. Elsevier: North Holland, 2002.
222. McQuarrie, D. A., *Statistical mechanics*. Harper & Row: New York, 1975.
223. Widom, B., *Statistical Mechanics: A Concise Introduction for Chemists*. Cambridge University Press: United Kingdom, 2002.
224. Hartmann, W. M., *Signals, Sound, and Sensation*. American Institute of Physics Melville: New York, 2004.
225. Pedersen, J. S., Analysis of small-angle scattering data from colloids and polymer

solutions: modeling and least-squares fitting. *Advances in Colloid and Interface Science* **1997,** *70*, 171-210.
226. Claridge, S. A.; Mastroianni, A. J.; Au, Y. B.; Liang, H. W.; Micheel, C. M.; Fréchet, J. M. J.; Alivisatos, A. P., Enzymatic Ligation Creates Discrete Multinanoparticle Building Blocks for Self-Assembly. *Journal of the American Chemical Society* **2008,** *130* (29), 9598-9605.
227. Pierleoni, C.; Addison, C.; Hansen, J.-P.; Krakoviack, V., Multiscale Coarse Graining of Diblock Copolymer Self-Assembly: From Monomers to Ordered Micelles. *Physical Review Letters* **2006,** *96* (12), 128302.
228. Adorf, C. S.; Antonaglia, J.; Dshemuchadse, J.; Glotzer, S. C., Inverse design of simple pair potentials for the self-assembly of complex structures. *The Journal of Chemical Physics* **2018,** *149* (20), 204102.
229. Davies, T. S.; Ketner, A. M.; Raghavan, S. R., Self-Assembly of Surfactant Vesicles that Transform into Viscoelastic Wormlike Micelles upon Heating. *Journal of the American Chemical Society* **2006,** *128* (20), 6669-6675.
230. Guilbaud, J.-B.; Saiani, A., Using small angle scattering (SAS) to structurally characterise peptide and protein self-assembled materials. *Chemical Society Reviews* **2011,** *40* (3), 1200-1210.
231. Yin, P.; Li, D.; Liu, T., Solution behaviors and self-assembly of polyoxometalates as models of macroions and amphiphilic polyoxometalate–organic hybrids as novel surfactants. *Chemical Society Reviews* **2012,** *41* (22), 7368-7383.
232. Prévost, S.; Gradzielski, M.; Zemb, T., Self-assembly, phase behaviour and structural behaviour as observed by scattering for classical and non-classical microemulsions. *Advances in Colloid and Interface Science* **2017,** *247*, 374-396.
233. Edler, K. J.; Bowron, D. T., Combining wide-angle and small-angle scattering to study colloids and self-assembly. *Current Opinion in Colloid & Interface Science* **2015,** *20* (4), 227-234.
234. Kohlbrecher, J., SASfit: A program for fitting simple structural models to small angle scattering data. *Paul Scherrer Institut, Laboratory for Neutron Scattering* **2008**.
235. Hammouda, B., The SANS toolbox. *NIST Center for Neutron Research, available at http://tinyurl. com/SANStoolbox* **2008**.
236. Mertens, H. D. T.; Svergun, D. I., Structural characterization of proteins and complexes using small-angle X-ray solution scattering. *Journal of Structural Biology* **2010,** *172* (1), 128-141.
237. Hammouda, B., Structure factor for starburst dendrimers. *Journal of Polymer Science Part B: Polymer Physics* **1992,** *30* (12), 1387-1390.
238. Wei, Y.; Hore, M. J. A., Characterizing polymer structure with small-angle neutron scattering: A Tutorial. *Journal of Applied Physics* **2021,** *129* (17), 171101.
239. Huggins, J. S.; Benoît, H., *Polymers and neutron scattering*. Clarendon Press: Oxford, 1994.
240. Hammouda, B., SANS from homogeneous polymer mixtures: a unified overview. *Polymer Characteristics* **1993**, 87-133.
241. Bang, J.; Jain, S.; Li, Z.; Lodge, T. P.; Pedersen, J. S.; Kesselman, E.; Talmon, Y., Sphere, cylinder, and vesicle nanoaggregates in poly (styrene-b-isoprene) diblock copolymer solutions. *Macromolecules* **2006,** *39* (3), 1199-1208.
242. Pedersen, J. S., Form factors of block copolymer micelles with spherical, ellipsoidal and cylindrical cores. *Journal of applied crystallography* **2000,** *33* (3), 637-640.
243. Pedersen, J., Small-angle scattering from surfactants and block copolymer micelles. In *Soft Matter Characterization*, Springer: 2008; pp 191-233.
244. Fielding, L. A.; Lane, J. A.; Derry, M. J.; Mykhaylyk, O. O.; Armes, S. P., Thermo-responsive Diblock Copolymer Worm Gels in Non-polar Solvents. *Journal of the American Chemical Society* **2014,** *136* (15), 5790-5798.
245. Percus, J. K.; Yevick, G. J., Analysis of classical statistical mechanics by means of

collective coordinates. *Physical Review* **1958,** *110* (1), 1.
246. Hansen, J.-P.; Hayter, J. B., A rescaled MSA structure factor for dilute charged colloidal dispersions. *Molecular Physics* **1982,** *46* (3), 651-656.
247. Hayter, J. B.; Penfold, J., An analytic structure factor for macroion solutions. *Molecular Physics* **1981,** *42* (1), 109-118.

Chapter 2: The Development of Small Angle X-ray Scattering Models for Free Radical Polymerisation Chemical Reaction Kinetic Analysis: Example of Polymerisation-Induced Self-Assembly via RAFT

Chapter 2

The Development of Small Angle X-ray Scattering Models for Free Radical Polymerisation Chemical Reaction Kinetic Analysis: Example of Polymerisation-Induced Self-Assembly via RAFT

2.1 Introduction

In Chapter 1, to monitor polymerisation and polymer behaviours in-situ, various techniques have been involved.[1-26] According to these research, monomer conversion can be observed by in-situ infrared spectroscopy (IR)[1], on-line and in-situ NMR spectroscopy[2-6], in-situ Calorimetry studies[7-9], in-situ conductivity studies[10], on-line densitometry studies[11, 12], on-line viscosity studies[24], on-line DLS studies[25]. Molecular weight and its distribution can be observed by on-line mass spectroscopy (MS)[23], on-line SEC studies[26]. However, only on-line viscosity studies[24] could reveal the viscoelastic properties of the polymer. Also, not all methods can easily to determine monomer conversion.[10] For in-situ infrared spectroscopy (IR), it required the calibration to finalise the characterisation of monomer conversion.[1] Small angle x-ray scattering has also been involved to monitor polymerisation, including polymerisation-induced self-assembly (PISA) via reversible addition−fragmentation chain-transfer (RAFT) synthesis[17-22]. Nevertheless, these research have not revealed monomer conversion with the analysis of particle nucleation and particle growth. Meanwhile, SAXS models including eq 1.91 provide theoretical evident to measure number density of particles in the system. This indicates that the volume fraction of particles and further volume fractions of the compounds in the system. This also means that monomer conversion can be calculated after reaching the measurement of the volume fractions of the compounds in the system.

Herein, to measure the compounds in system in order to achieve the measurement of monomer conversion with abundant self-assembled particle properties, SAXS models for self-assembled particles are developed with mass balance to confine the volume fractions of the compounds in the system in this Chapter. After extracting the information of the volume fractions of the compound in the system, chemical kinetics of RAFT synthesis can be discussed quantitively. Further, mass transfer between the particle and medium is also available to be described quantitively.

2.2 SAXS model for analysis of PISA via RAFT synthesis

Herein, for the simplification of PISA process via RAFT synthesis, only spherical micelles are assumed for the products of self-assembled diblock copolymers. Considering previous results obtained by TEM and NMR,[27] the whole process of PISA of diblock copolymers can be subdivided at least into 5 stages (Figure 2.1). The stage 1 is associated with the preparation of a reagent mixture including solvent, macromolecular chain transfer agent (macro-CTA), composed of the stabiliser solvophilic block, and a monomer for synthesising the second solvophobic block. It is expected that all components are homogeneously distributed in the reaction vessel (Figure 2.1, Stage 1). The beginning of the second block polymerization, converting macro-CTA into an initially soluble diblock copolymer, is associated with the stage 2. Again, all reagents and the reaction products are homogeneously distributed in the reaction vessel (Figure 2.1, Stage 2). The moment

when the degree of polymerization of the second block of the copolymer reaches a critical level, corresponding to the transformation of the second block from originally soluble into an insoluble solvophobic block, is defined as the beginning of the stage 3. During this stage the synthesised diblock copolymer, becoming amphiphilic, self-assembles into spherical micelles and the system component distribution in the reaction vessel is not homogeneous anymore (Figure 2.1, Stage 3). The increase of the polymerization reaction rate at later stages of PISA, observed in the previous studies[28], has to be associated with the micelle formation resulting in a redistribution of the monomer in the reagent mixture. It is likely to expect that the monomer, more affine with the synthesised second block than with the solvent,[29] transfers into the spherical micelle core localising next to the active copolymer chain end and creating optimal reaction conditions accelerating the second block polymerization. Thus, after the copolymer self-assembly the polymerization occurs in the core of the spherical micelle and this period of the reaction is assigned to stage 4. The monomer is preferably localised in the micelle core while the solvent molecules are mostly outside of the micelles (Figure 2.1, Stage 4). When all monomer molecules in the reaction vessel are consumed, the polymerization terminates and the final stage 5 is reached (Figure 2.1, Stage 5). In brief, following the reaction order the stages could be described as the reagent mixture preparation (stage 1), the polymerization initiation (stage 2), the beginning of copolymer self-assembly (stage 3), the monomer transfer into micelle core (stage 4) and the reaction termination (stage 5). It can be expected that at a higher degree of the solvophobic block polymerization the spherical micelles transform into worm-like micelles and, subsequently, into vesicles.[30, 31] However, this study is focused on the formation of spherical micelles only. Based on the described route of the PISA process, a structural model for analysing TR SAXS data collected *in situ* during the reaction can be established.

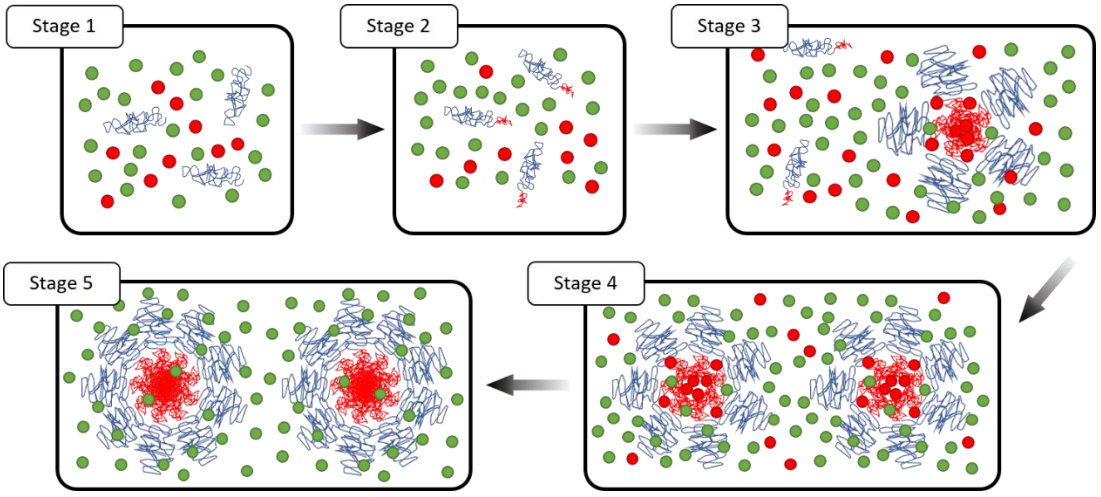

Figure 2.1**.** A schematic presentation of PISA process subdivided into five stages. The first stage (Stage 1) corresponds to the initial reagent mixture represented by a soluble macro-CTA (blue curved lines), a monomer feeding the synthesized second block (red circles) and a solvent (green circles). The second stage (Stage 2) corresponds to the initiation of polymerization occurring on the macro-CTAs and producing soluble diblock copolymers with a short second block (red curved lines attached to the blue lines).[27] The following third stage (Stage 3) is associated with diblock copolymer self-assembly into nanoparticles (spherical micelles). The micelle core may encapsulate some monomer and solvent at this stage. The fourth stage (Stage 4) is related to the monomer transferring into micelle core resulting in polymerization occurring in the hydrophobic core of the self-assembled nanoparticles. At this stage, the, solvent may be gradually excluded out of the hydrophobic core. The stage five (Stage 5) corresponds to the reaction termination when all monomer is consumed.

Based on the chemical reactions and the self-assembly process taking place during PISA *via* RAFT[27, 31, 32] (Figure 2.1) a number of assumptions can be made to simplify derivation of the structural model. First, over a course of the reaction total mass of the reagents and/or products of the reaction virtually does not change. More specifically, the masses of solvent and hydrophilic block (macro-CTA) as well as the total mass of monomer and synthesised hydrophobic block remain constant. Second, the reaction temperature and pressure are constant and density of each compound of the system does not change during PISA. Thus, volume of each compound can be calculated from its mass at any time of the reaction and the respective scattering length densities, related to the compound mass densities, can be considered as constants. This assumption also means that mass density, as well as scattering length density, of the diblock copolymers is independent of their state, that is either they are dissolved in solution or self-assembled in aggregates (spherical micelles). Third, all synthesised diblock copolymers have the same composition and the same degree of polymerization. Therefore, the monomer conversion value can be used to calculate the number of repeat units of the hydrophobic block, and the calculated number can be applied to all diblock copolymers without considering polydispersity of the molecule composition. The degree of polymerisation is used to calculate the aggregation number of the spherical micelle. Fourth, all spherical micelles formed by self-assembled diblock copolymers have the same chemical composition and, therefore, contain the same volume fraction of compounds in their core. Fifth, the system is closed and homogeneous. Thus, all elemental volumes of the system have the same composition at a given time and equally represent the whole system. This assumption also means that there are no precipitates formed as well as no gas exchange over the reaction course. These requirements are commonly achievable in a real experiment by sealing the reactor and, sometimes, by stirring the reagents[19]. Sixth, a number of diblock copolymers assembling in a micelle can vary. Thus, radius of the spherical micelles can have a disperse distribution. And the distribution is assumed as Gaussian distribution for simplification of SAXS modelling instead of the possible Lifshitz–Slyozov–Wagner (LSW) distribution[33].

In general, a scattering signal originating from the studied system at different stages of the reaction has to be composed of scattering from the solvent and monomer molecules, a homogenous polymer (macro-CTA), diblock copolymer chains (macro-CTA extended by the synthesised second block)[34], and/or diblock copolymer spherical micelles[35]. In addition, depending on the component concentration, the scattering signal should be affected by inter-component interactions in the system. Thus, a scattering equation of this system should be comprised of two sets of terms: a set associated with the shape and the internal structure of the scattering objects and a set describing their interactions between each other. The macro-CTA volume fraction in the initial reaction mixture is typically around 2% v/v, and it is likely that at the end of stage 3 the volume fraction of the synthesised diblock copolymer (and the formed micelles) is (are) at a comparatively low concentration level. Thus, interactions between the scattering objects can be neglected at the early stages of this synthesis. Thus, for the first three stages, the general equation of the total scattering intensity (differential scattering cross-section per unit sample volume) can be expressed as a combination of scattering terms from *m* kinds of individual objects:

$$I_{\text{tot}}(q) = \sum_{i=1}^{m} \phi_i I_i(q) + \left(1 - \sum_{i=1}^{m} \phi_i\right) I_{\text{bg}}$$
$$= \sum_{i=1}^{m} \phi_i \frac{\int_0^{\infty} \Psi_i(\Upsilon_i) F_i(q, \Upsilon_i) S_i(q, \Upsilon_i) d^{n_i}\Upsilon_i}{\int_0^{\infty} \Psi_i(\Upsilon_i) V_i(\Upsilon_i) d^{n_i}\Upsilon_i} + \left(1 - \sum_{i=1}^{m} \phi_i\right) I_{\text{bg}} \quad (2.1)$$

where q is the scattering vector length ($q = 4\pi\sin\theta/\lambda$, where θ is one-half of the scattering angle and λ is the radiation wavelength) (scalar form of the equation is considered); $I_i(q)$, ϕ_i and $\frac{\phi_i}{\int_0^{\infty} \Psi_i(\Upsilon_i) V_i(\Upsilon_i) d^{n_i}\Upsilon}$ is the scattering intensity, the volume fraction and the number density of the i^{th} type of the individual objects, respectively; I_{bg} is the solvent background scattering which is independent of q; $\Psi_i(\Upsilon_i)$, $F_i(q,\Upsilon_i)$ and $S_i(q, \Upsilon_i)$, are the multivariate normalised distribution function $\left(\int_0^{\infty} \Psi_i(\Upsilon_i) d^{n_i}\Upsilon_i = 1\right)$, the form factor (including volume and excess scattering length density of the components) and the structure factor of the i^{th} kind of the individual objects, respectively, and Υ_i represents n_i-tuple of structural parameters with broad dispersity describing i^{th} kind of the individual objects. At the later stages 4 and 5 (Figure 2.1), when the synthesised copolymers mainly assemble in micelles and there are virtually no free polymers in the system,[36-39] the number of types of individual objects reduces to unity ($m = 1$). In addition, since the solvophobic block degree of polymerization (DP) increases and the associated concentration of micelles growths, the inter-micelle interactions have to be counted. Thus, the scattering intensity (eq 2.1) for the last two stages can be modified as:

$$I_{\text{tot}}(q) = \phi_{\text{sm}} \frac{\int_0^{\infty} \Psi_{\text{sm}}(\Upsilon_{\text{sm}}) F_{\text{sm}}(q, \Upsilon_{\text{sm}}) S_{\text{sm}}(q, \Upsilon_{\text{sm}}) d^{n_{\text{sm}}}\Upsilon_{\text{sm}}}{\int_0^{\infty} \Psi_{\text{sm}}(\Upsilon_{\text{sm}}) V_{\text{sm}}(\Upsilon_{\text{sm}}) d^{n_{\text{sm}}}\Upsilon_{\text{sm}}} + (1 - \phi_{\text{sm}}) I_{\text{bg}} \quad (2.2)$$

where subscript "sm" denotes terms corresponding to the spherical micelle morphology, and $F_{\text{sm}}(q, \Upsilon_{\text{sm}})$ and $S_{\text{sm}}(q, \Upsilon_{\text{sm}})$ are functions describing both the form factor and the structure factor of the micelles[40]. Since only one monomer and one macro-CTA was used in the studied system, equations 2.1 and 2.2 can be rewritten for each stage as:

$$\begin{cases} I_{\text{tot}}(q) = \phi_{\text{pc}} I_{\text{pc}}(q) + (1 - \phi_{\text{pc}}) I_{\text{bg}}(q), \text{ for stage 2} & (2.3) \\ I_{\text{tot}}(q) = \phi_{\text{pc}} I_{\text{pc}}(q) + \phi_{\text{sm}} I_{\text{sm}}(q) + (1 - \phi_{\text{pc}} - \phi_{\text{sm}}) I_{\text{bg}}(q), \text{ for stage 3} & (2.4) \\ I_{\text{tot}}(q) = \phi_{\text{sm}} I_{\text{sm}}(q) + (1 - \phi_{\text{sm}}) I_{\text{bg}}(q), \text{ for stages 4 and 5} & (2.5) \end{cases}$$

where ϕ_{pc} is the soluble polymer chain volume fraction, and I_{pc} and I_{sm} are the scattering intensities of the soluble polymer chains and the spherical micelles, respectively, representing the term with integrals in equations 2.1 and 2.2.

The total scattering intensity is proportional to the component volume fractions (equations 2.1 - 2.5). In general, the total volume of the materials in the studied system composed of liquid and polymer components can be expressed as:

$$V_{\text{tot}} = V_{\text{liq}} + V_{\text{pol}}, \tag{2.6}$$

where V_{liq} and V_{pol} are the total volumes of liquid and polymer components, respectively. Making an assumption of mass conservation for PISA via RAFT, additional relationships between the volume fractions can be established. The total volume of the synthesised diblock copolymer at a particular time of the reaction can be expressed as

$$V_{\text{pol}} = V_{\text{co}} + V_{\text{br}} = conv \cdot \frac{m_{\text{ini\_mon}}}{\rho_{\text{co}}} + \frac{m_{\text{br}}}{\rho_{\text{br}}}, \tag{2.7}$$

where V_{co} is the hydrophobic block total volume which can be calculated from the monomer conversion (*conv*) the initial monomer mass ($m_{\text{ini\_mon}}$) and the hydrophobic block mass density (ρ_{co}), and V_{br} is the hydrophilic block total volume calculated from the macro-CTA (hydrophilic block) mass (m_{br}) and the hydrophilic block mass density (ρ_{br}).

Considering that only one specific monomer and a solvent or a mixture of solvents are used for the reaction, the total volume of liquids present in the system can be expressed as:

$$V_{\text{liq}} = V_{\text{mon}} + V_{\text{sol}} = V_{\text{mon}} + \sum_{j=1}^{n_{\text{sol}}} V_{\text{sol}j} = V_{\text{mon}} + \sum_{j=1}^{n_{\text{sol}}} \frac{m_{\text{sol}j}}{\rho_{\text{sol}j}}, \tag{2.8}$$

where V_{mon} is the volume of monomer remaining in the system, V_{sol} is the solvent volume composed, in general, of n_{sol} components and $V_{\text{sol}j}$ is the volume of j^{th} solvent component defined as a ratio of its mass and mass and mass density, $m_{\text{sol}j}$ and $\rho_{\text{sol}j}$, respectively. V_{mon} in eq 2.8 can be defined as

$$V_{\text{mon}} = (1 - conv) \cdot \frac{m_{\text{ini\_mon}}}{\rho_{\text{mon}}}, \tag{2.9}$$

where ρ_{mon} is mass density of the monomer.

Since the monomer relocates into the hydrophobic core of the assembled copolymer micelles during the reaction[19, 28] and the solvent (or a mixture of solvents) can partially solubilize the core[14], the liquid components have to be subdivided into two parts, one of which localised in the micelle cores and the other in the remaining system. Therefore, the total volume of solvents in the micelle cores ($V_{\text{in\_sol}}$) and outside of the cores ($V_{\text{ex\_sol}}$) can be expressed as:

$$\begin{cases} V_{\text{in\_sol}} = \sum_{j=1}^{n_{\text{sol}}} f_{\text{sol}j} V_{\text{sol}j} \\ V_{\text{ex\_sol}} = \sum_{j=1}^{n_{\text{sol}}} \left(1 - f_{\text{sol}j}\right) V_{\text{sol}j} \end{cases}, \tag{2.10}$$

where $f_{\text{sol}j}$ is the volume fraction of j^{th} solvent in the micelle cores. In analogy, the total volume of the internal and external monomer ($V_{\text{in\_mon}}$ and $V_{\text{ex\_mon}}$, respectively) can be expressed as:

$$\begin{cases} V_{\text{in\_mon}} = f_{\text{mon}} V_{\text{mon}} \\ V_{\text{ex\_mon}} = \left(1 - f_{\text{mon}}\right) V_{\text{mon}} \end{cases}, \tag{2.11}$$

where f_{mon} is the volume fraction of the monomer in the micelle cores. According to equations 2.10 and 2.11 the total volume of liquid components inside of the micelle cores can be written as:

$$V_{\text{in\_liq}} = V_{\text{in\_sol}} + V_{\text{in\_mon}} = \sum_{j=1}^{n_{\text{sol}}} f_{\text{sol}j} V_{\text{sol}j} + f_{\text{mon}} V_{\text{mon}}. \tag{2.12}$$

And the total volume of external liquid can be written as:

$$V_{\text{ex\_liq}} = V_{\text{ex\_mon}} + V_{\text{ex\_sol}}. \tag{2.13}$$

Copolymer molecules during synthesis can dissociate in the solvent and/or assemble into micelles (Figure 2.1 and Figure 2.2, equations 2.3 - 2.5). Therefore, the total amount of copolymers presents in the system, in general, should can be subdivided into two components:

$$1 = f_{\text{pc}} + f_{\text{sm}}, \tag{2.14}$$

where f_{pc} is the fraction of copolymers disassociated in the solvents and f_{sm} is the fraction of copolymers assembled in spherical micelles. Thus, the component volume fractions for the equations 2.3 - 2.5 can be expressed as:

$$\phi_{\text{pc}} = \frac{f_{\text{pc}} V_{\text{pol}}}{V_{\text{tot}}} \tag{2.15}$$

and

$$\phi_{\text{sm}} = \frac{\left(1 - f_{\text{pc}}\right) V_{\text{pol}} + V_{\text{in\_liq}}}{V_{\text{tot}}}, \tag{2.16}$$

where f_{pc} =1 for stage 3 (eq 2.3) and f_{pc} = 0 for stage 4 and 5 (eq 2.5). Accordingly, the volume fraction of external liquid responsible for the background scattering in the equations 2.3 - 2.5 can be expressed as:

$$\phi_{ex} = 1 - \phi_{pc} - \phi_{sm} = \frac{V_{ex\_liq}}{V_{tot}}. \tag{2.17}$$

In addition, the material volumes defined by equations 2.7, 2.10 and 2.11 enable volume fractions of monomer, synthesised copolymer solvophobic block and solvent localised in the micelle core to be expressed:

$$\begin{cases} xmon = \dfrac{V_{in\_mon}}{f_{sm}V_{co} + V_{in\_mon} + V_{in\_sol}} \\ xpol = \dfrac{f_{sm}V_{co}}{f_{sm}V_{co} + V_{in\_mon} + V_{in\_sol}} \\ xsol = \dfrac{V_{in\_sol}}{f_{sm}V_{co} + V_{in\_mon} + V_{in\_sol}} \end{cases}. \tag{2.18}$$

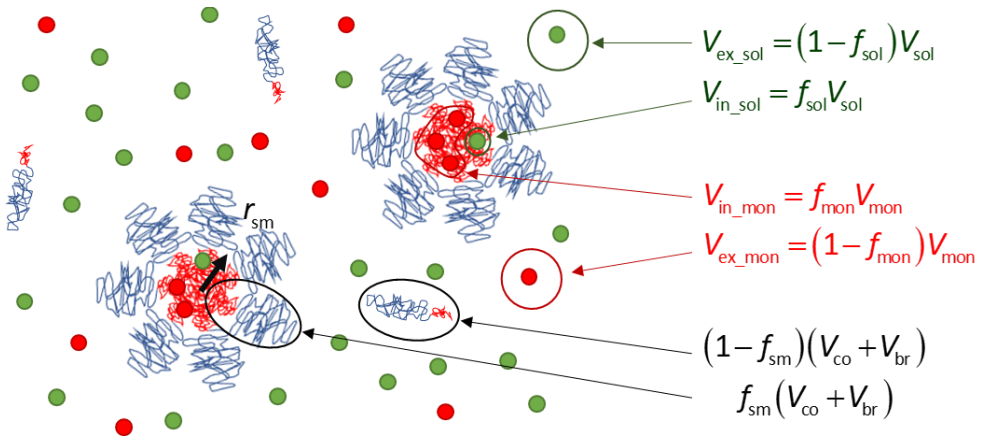

Figure 2.2. A schematic presentation of the compound situations during PISA process. The parameters f_{sol}, f_{mon} and f_{sm} are applied to separate the volume of monomer (red circles), solvents (green circles), and copolymers (red curved lines attached to the blue lines) belonged to the spherical micelle or locating in the surrounding background.

The scattering intensity block copolymers in the equations 2.1 - 2.4 can be written as:

$$I_{pc}(q) = \frac{F_{pc}(q, R_{g\_co}, R_{g\_br}) + A_{pc}^2(q, R_{g\_co}, R_{g\_br})\left[S(q, r_{mc}, r_{mc}') - 1\right]}{V_{pc}(r_{mc})}. \tag{2.19}$$

The diblock copolymer form factor in eq 2.24 is defined as:[34]

$$\begin{aligned} F_{pc}(q, R_{g\_co}, R_{g\_br}) = {} & \beta_{pc\_co}^2 F_{pc\_co}(q, R_{g\_br}) + \beta_{pc\_br}^2 F_{br}(q, R_{g\_br}) \\ & + 2\beta_{pc\_co}\beta_{pc\_br} A_{pc\_co}(q, R_{g\_br}) A_{br}(q, R_{g\_br}) \end{aligned}, \tag{2.20}$$

where the form factor amplitude of the solvophobic block is defined as $A_{\text{pc\_co}}\left(q,R_{\text{g\_co}}\right)=\frac{1-\exp\left(-q^2R_{\text{g\_co}}^2\right)}{q^2R_{\text{g\_co}}^2}$,[40] and $R_{\text{g\_co}}$ is the radius of gyration of the solvophobic block. The self-correlation term of the solvophobic block in eq 2.20 is described by the Debye function $F_{\text{pc\_co}}\left(q,R_{\text{g\_co}}\right)=\frac{2\left[\exp\left(-q^2R_{\text{g\_co}}^2\right)-1+q^2R_{\text{g\_co}}^2\right]}{q^4R_{\text{g\_co}}^4}$.[41] The form factor amplitude of the solvophilic block is defined as $A_{\text{br}}\left(q,R_{\text{g\_br}}\right)=\frac{1-\exp\left(-q^2R_{\text{g\_br}}^2\right)}{q^2R_{\text{g\_br}}^2}$,[40] and $R_{\text{g\_br}}$ is the radius of gyration of the solvophilic block. The self-correlation term of the corona block in eq 2.25 is described by the Debye function $F_{\text{br}}\left(q,R_{\text{g\_br}}\right)=\frac{2\left[\exp\left(-q^2R_{\text{g\_br}}^2\right)-1+q^2R_{\text{g\_br}}^2\right]}{q^4R_{\text{g\_br}}^4}$.[41] $\beta_{\text{pc\_co}}$ and β_{br} are excess scattering lengths of solvophobic and solvophilic blocks, respectively. The excess scattering length density of the micelle core in eq 2.25 is defined as:

$$\beta_{\text{pc\_co}}=\nu_{\text{co}}\left(\xi_{\text{co}}-\xi_{\text{bg}}\right), \tag{2.21}$$

where ξ_{co} is the scattering length densities of the solvophobic blocks. The background scattering length density in eq 2.28 is calculated as:

$$\xi_{\text{bg}}=\frac{\xi_{\text{mon}}\left(1-f_{\text{mon}}\right)V_{\text{mon}}+\sum_{j=1}^{n_{\text{sol}}}\xi_{\text{sol}j}\left(1-f_{\text{sol}j}\right)V_{\text{sol}j}+\left(1-f_{\text{sm}}\right)\left(\xi_{\text{co}}V_{\text{co}}+\xi_{\text{br}}V_{\text{br}}\right)}{\left(1-f_{\text{mon}}\right)V_{\text{mon}}+\sum_{i=1}^{n_{\text{sol}}}\left(1-f_{\text{sol}j}\right)V_{\text{sol}j}+\left(1-f_{\text{sm}}\right)\left(V_{\text{co}}+V_{\text{br}}\right)}, \tag{2.22}$$

where ξ_{mon} and $\xi_{\text{sol}j}$ are the scattering length densities of the monomer and solvents, respectively, j^{th} solvent component and solvophobic block and ξ_{br} is the solvophilic block scattering length density. The excess scattering length density of the solvophilic block in eq 2.25 is defined as:

$$\beta_{\text{br}}=\nu_{\text{br}}\left(\xi_{\text{br}}-\xi_{\text{bg}}\right), \tag{2.23}$$

where the solvophilic block volume is calculated as $\nu_{\text{br}}=\frac{M_{\text{br}}}{\rho_{\text{br}}\cdot N_{\text{A}}}$. The structure factor term in eq 2.19 was solved by the Percus-Yevick closure relation. Since the volume concertation of the scattering diblock copolymer chains was low at this stage of the synthesis, the structure factors were assumed to be unity. To connect to monomer conversion with the radius of gyration of the solvophobic block, the estimation of the radius of gyration of the solvophobic block, $R_{\text{g\_co\_est}}$, is given as $(b\cdot l_c/6)^{0.5}$ by the Gaussian chain model[42], where the contour length, l_c, is calculated as the repeat unit, DP, multiplying to the length of two carbon bonds in an all *trans* configuration, 0.255 nm, and the Kuhn length, *b*. Because the backbones and the side chains of polymers used in Chapter 3, 4, and 5 are similar to PMMA, *b* is given as 1.53 nm based on PMMA[43]. Therefore, $R_{\text{g\_co}}$ is equal to $R_{\text{g\_co\_est}}$ when using soluble diblock copolymer model.

Following a previous work on the analysis of form and structure factors for spherical micelles[40,

[44] and replacing Υ_{sm} n_{sm}-tuple with a single parameter by assuming that the micelle core radius (r_{mc}) is the only parameter with broad dispersity, the scattering intensity of spherical micelles in the equations 2.1 and 2.5 can be written as:

$$I_{sm}(q) = \frac{\int_0^{\infty} \Psi_{sm}(r_{mc}) \left(F_{sm}(q, r_{mc}) + \int_0^{\infty} \Psi_{sm}(r'_{mc}) A_{sm}(q, r_{mc}) A_{sm}(q, r'_{mc}) \left[S(q, r_{mc}, r'_{mc}) - 1 \right] dr'_{mc} \right) dr_{mc}}{\int_0^{\infty} \Psi_{sm}(r_{mc}) V_{sm}(r_{mc}) dr_{mc}} . \quad (2.24)$$

The micelle form factor in eq 2.24 is defined as:

$$\begin{aligned} F_{sm}(q, r_{mc}) = {} & n_{agg}^2 \beta_{mc}^2 A_{mc}^2(q, r_{mc}) \\ & + n_{agg}(n_{agg} - 1) \beta_{br}^2 \left[A_{br}(q, R_{g\_br}) \frac{\sin q(r_{mc} + R_{g\_br})}{q(r_{mc} + R_g)} \right]^2 \\ & + n_{agg} \beta_{br}^2 F_{br}(q, R_g) \\ & + 2 n_{agg}^2 \beta_{mc} \beta_{br} A_{mc}(q, r_{mc}) A_{br}(q, R_{g\_br}) \frac{\sin q(r_{mc} + R_{g\_br})}{q(r_{mc} + R_{g\_br})} \end{aligned} , \quad (2.25)$$

where it is assumed that no penetration of the corona chains in the micelle core occurs.[40] The micelle core scattering amplitude in eq 2.25 is expressed as:

$$A_{mc}(q, r_{mc}) = \frac{3(\sin q r_{mc} - q r_{mc} \cos q r_{mc})}{q^3 r_{mc}^3} e^{-\frac{1}{2} q^2 \sigma_t^2} , \quad (2.26)$$

where the exponent term with a width σ_t accounting for a sigmoidal interface between the two blocks at the micelle corona surface. σ_t value was fixed at 2.5 Å during fitting, which is the length of repeat unit of the corona chains. The aggregation number of copolymers in a micelle (eq 2.24) is defined as:

$$n_{agg} = xpol \cdot \frac{\frac{4}{3} \pi r_{mc}^3}{v_{co}} , \quad (2.27)$$

where v_{co} is the volume of the copolymer solvophobic block, which can be obtained from $v_{co} = \frac{M_{co}}{\rho_{co} \cdot N_A} \cdot DP$, where M_{co} is the molar mass of the solvophobic block repeat unit, N_A is the Avogadro constant and DP is the degree of polymerization of the solvophobic block calculated as $DP = \frac{m_{ini\_mon}}{M_{co}} \frac{M_{br}}{m_{br}} \cdot conv$, where M_{br} is the peak molecular weight of macro-CTA measured by NMR.

The excess scattering length density of the micelle cores in eq 2.25 is defined as:

$$\beta_{\mathrm{mc}} = \frac{v_{\mathrm{co}}}{xpol}\left(\xi_{\mathrm{mc}} - \xi_{\mathrm{bg}}\right), \tag{2.28}$$

where the scattering length density of the micelle cores is calculated as the volume average of the comprising components:

$$\xi_{\mathrm{mc}} = \frac{\xi_{\mathrm{mon}} f_{\mathrm{mon}} V_{\mathrm{mon}} + \sum_{j=1}^{n_{\mathrm{sol}}} \xi_{\mathrm{sol}j} f_{\mathrm{sol}j} V_{\mathrm{sol}j} + \xi_{\mathrm{co}} f_{\mathrm{sm}} V_{\mathrm{co}}}{f_{\mathrm{mon}} V_{\mathrm{mon}} + \sum_{j=1}^{n_{\mathrm{sol}}} f_{\mathrm{sol}j} V_{\mathrm{sol}j} + f_{\mathrm{sm}} V_{\mathrm{co}}}. \tag{2.29}$$

The scattering amplitude of spherical micelles in eq 2.25 is defined as:

$$A_{\mathrm{sm}}\left(q, r_{\mathrm{mc}}\right) = n_{\mathrm{agg}} \cdot \left[\beta_{\mathrm{mc}} A_{\mathrm{mc}}\left(q, r_{\mathrm{mc}}\right) + \beta_{\mathrm{br}} A_{\mathrm{br}}\left(q, R_{\mathrm{g\_br}}\right) \frac{\sin q\left(r_{\mathrm{mc}} + R_{\mathrm{g\_br}}\right)}{q\left(r_{\mathrm{mc}} + R_{\mathrm{g\_br}}\right)}\right]. \tag{2.30}$$

The structure factor term in eq 2.24 corresponding to the inter-micelle interactions can be described using the hardsphere structure factor solved by the Percus-Yevick closure relation (called for the sake of simplicity as hard-sphere Percus-Yevick structure factor):[44]

$$S\left(q, r_{\mathrm{mc}}, r_{\mathrm{mc}}^{'}\right) = S_{\mathrm{HS}}\left(q, R_{\mathrm{sf}}, V_{\mathrm{sf}}\right), \tag{2.31}$$

where V_{sf} is an effective volume fraction of the interacting micelles and the inter-micelle distance is defined as $2R_{\mathrm{sf}} = r_{\mathrm{mc}} + r_{\mathrm{mc}}^{'} + 2\Delta R$, where ΔR is a half of the shortest distance between core interfaces of the neighbouring micelles with their respective core radii r_{mc} and r_{mc}'.

It has been assumed in the analysis that the dispersity of the micelle core radius follows Gaussian distribution. Thus, the normalised distribution function in eq 2.24 is expressed as:

$$\Psi\left(r_{\mathrm{mc}}\right) = \frac{\exp\left[-\frac{1}{2}\left(\frac{r_{\mathrm{mc}} - R_{\mathrm{mc}}}{\sigma_{R_{\mathrm{mc}}}}\right)^2\right]}{\sqrt{2\pi}\sigma_{R_{\mathrm{mc}}}}, \tag{2.32}$$

where R_{mc} is the mean radius of the spherical micelle core and $\sigma_{R_{\mathrm{mc}}}$ is its standard deviation. And such Gaussian distribution of the radius of particles, r, is represented by $r \sim N(R, \sigma)$, where R is the mean radius of particles and σ is its standard deviation. Thus, the mean aggregation number is defined as:

$$N_{agg} = xpol \cdot \frac{V_{mc\text{-}co}}{v_{co}} = xpol \cdot \frac{\frac{4}{3}\pi R_{mc}^3}{v_{co}}, \quad (2.33)$$

where $V_{mc\text{-}co}$ is the average volume of the core of the spherical micelle.

Making an assumption that a particle of a certain size is always surrounded by particles with the same size in a studied system, a local monodisperse approximation can be used to simplify eq 2.24:[45]

$$I_{sm}(q) = \frac{\int_0^\infty \Psi_{sm}(r_{mc})\left(F_{sm}(q,r_{mc}) + A_{sm}^2(q,r_{mc})\left[S(q,r_{mc})-1\right]\right)dr_{mc}}{\int_0^\infty \Psi_{sm}(r_{mc})V_{sm}(r_{mc})dr_{mc}}, \quad (2.34)$$

where in analogy with eq 2.31 the structure factor term is expressed as $S(q,r_{mc}) = S_{HS}(q,R_{sf},V_{sf})$ and $R_{sf} = r_{mc} + \Delta R$. Fitting selected SAXS patterns recorded during PISA synthesis, using eq 2.24 and eq 2.34, has demonstrated that both approaches returned similar results. Thus, the later approach (eq 2.34), requiring a significantly shorter computer time for fitting, has been chosen for the analysis of the SAXS dataset.

According to equations 2.1 - 2.34, a set of variables necessary for describing the PISA via RAFT synthesis at different stages of the process (Figure 2.1) is different. Therefore, the fitted variables for analysing SAXS patterns associated with Stage 2 would be the following (see variables in the brackets on the right-hand side of the equation):

$$I_{tot\_Stage2}(q) = I_{tot}\begin{pmatrix} conv, \\ R_{g\_br} \end{pmatrix}. \quad (2.35)$$

The fitted variables for Stage 3 would be the following (see variables in the brackets):

$$I_{tot\_Stage3}(q) = I_{tot}\begin{pmatrix} conv, \\ R_{g\_co}, R_{g\_br}, \\ f_{sm}, R_{sm}, \sigma_{R_{sm}}, xmon, xsol, \\ V_{sf}, \Delta R_{sf} \end{pmatrix}. \quad (2.36)$$

The fitted variables for Stages 4 and 5 would be the following (see variables in the brackets):

$$I_{\text{tot\_Stage4\&5}}(q) = I_{\text{tot}}\begin{pmatrix} conv, \\ R_{\text{g\_br}}, \\ R_{\text{sm}}, \sigma_{R_{\text{sm}}}, xmon, xsol, \\ V_{\text{sf}}, \Delta R_{\text{sf}} \end{pmatrix}. \quad (2.37)$$

2.3 Relationship between SAXS Structural Model and Kinetic Equations of PISA Process via RAFT Synthesis

During the stage 4 of PISA process, the active polymer radicals are hidden in the spherical micelle cores and, therefore, the chemical reaction should be controlled by the change of compositions in the spherical micelle cores (Figure 2.3). At this stage, the mechanism of the polymerisation is similar with the interval II and Interval III of the emulsion polymerisation (Figure 1.1), and thus, the rate of polymerisation may be only determined by the monomer concentration of the spherical micelle cores. The supply of the monomer to the spherical micelle cores may be determined by the monomer mass transfer from the surrounding medium to the spherical micelle cores. This process can be named as monomer supply. Meanwhile, the solvent molecules possibly hidden in the spherical micelle cores may be expelled from the spherical micelle cores to the medium. This transportation can be named as solvent expulsion. The polymerisation, monomer supply, and solvent expulsion process can determine the composition of the spherical micelle cores. Meanwhile, because SAXS and its following modelling can measure the composition of the spherical micelle cores as *xmon*, *xsol*, and *xpol* and monomer conversion at the same time (equations 2.7, 2.9, and 2.18), the polymerisation, monomer supply, and solvent expulsion process can be possibly described by *xmon*, *xsol*, and *xpol* and monomer conversion obtained from SAXS analysis.

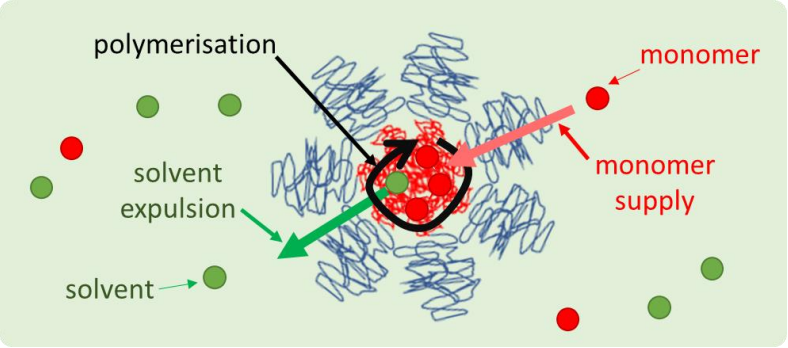

Figure 2.3**.** A schematic presentation of PISA synthesis during Stages 4 and 5 or during the final stage of emulsion polymerisation. During these stages or Interval, the polymerisation process (black annular arrow) and the rate of polymerisation depend on the monomer (red circles) concentration in the latex cores (shown as red coils representing synthesised solvophobic blocks surrounded by blue coils corresponding to stabiliser solvophilic blocks) and in the medium (green background). Therefore, the process of the transport of the monomer (red arrow) from the medium into the latex cores is named monomer supply. Meanwhile, the solvophobic latex cores are highly likely to repel the solvent molecules into the medium. This process of solvent transportation from the latex cores into the medium is named solvent expulsion (green arrow).

Because the mechanism of PISA process via RAFT synthesis at stage 4 (Figure 2.1) is similar with the mechanism of emulsion polymerisation, according to eq 1.8, the rate of polymerisation of PISA process via RAFT synthesis at stage 4 can be expressed as:

$$R_p(t) = \frac{d[conv(t)]}{dt} = k_p \cdot c_{mon}(t) \cdot c_{P\cdot}(t), \tag{2.38}$$

where k_p is the propagation rate coefficient, c_{mon} is the monomer concentration, and $c_{P\cdot}$ is the radical concentration in the system.

The solvophobic block polymerisation during PISA after the full self-assembly of diblock copolymers corresponds to a propagation process (eq 2.38), as the chemical reaction occurs in the spherical micelle core. In this case, c_{mon} is defined as the number density of the monomer in the spherical micelle core:[46]

$$c_{mon} = \frac{1}{N_A}\frac{1}{V_{mc\text{-}co}}\frac{n_{in\_mon}}{N_p}, \tag{2.39}$$

where N_P is the total number of spherical micelles defined as $N_p = \frac{n_{br}}{N_{agg}}$, where n_{br} is the number of moles of solvophilic block. Combined with the mean aggregation number definition (eq 2.33), eq 2.39 could be rewritten as:

$$c_{mon} = \frac{1}{N_A}\frac{1}{V_{mc\text{-}co}}\frac{n_{in\_mon}}{\frac{n_{br}}{xpol \cdot \frac{V_{mc\text{-}co}}{v_{co}}}} = \frac{1}{N_A}\frac{xpol}{v_{co}} \cdot \frac{n_{in\_mon}}{n_{br}}. \tag{2.40}$$

By defining $v_{co} = \frac{M_{co}}{\rho_{co} \cdot N_A} \cdot DP$ and $DP = \frac{m_{ini\_mon}}{M_{co}}\frac{M_{br}}{m_{br}} \cdot conv$, eq 2.40 could be further rewritten as:

$$\begin{aligned} c_{mon} &= \frac{1}{N_A}\frac{xpol}{\frac{M_{co}}{\rho_{co} \cdot N_A} \cdot \frac{m_{ini\_mon}}{M_{co}}\frac{M_{br}}{m_{br}} \cdot conv} \cdot \frac{n_{in\_mon}}{n_{br}} \\ &= \frac{\rho_{co}}{m_{ini\_mon}}\frac{xpol}{conv} \cdot n_{in\_mon} \end{aligned}. \tag{2.41}$$

Using the definition of *xmon* and *xpol* (eq 2.18), n_{in_mon} could be expressed as $n_{in\_mon} = \frac{\rho_{mon}}{M_{co}} \cdot V_{in\_mon} = \frac{\rho_{mon}}{M_{co}} \cdot \left(f_{sm} \cdot V_{co} \cdot \frac{xmon}{xpol} \right)$. Thus, eq 2.41 could be rewritten as:

$$\begin{aligned} c_{\text{mon}} &= \frac{\rho_{\text{co}}}{m_{\text{ini\_mon}}} \frac{xpol}{conv} \cdot \frac{\rho_{\text{mon}}}{M_{\text{co}}} \cdot \left(f_{\text{sm}} \cdot V_{\text{co}} \cdot \frac{xmon}{xpol} \right) \\ &= \frac{\rho_{\text{co}} \cdot \rho_{\text{mon}}}{m_{\text{ini\_mon}}} \frac{f_{\text{sm}} \cdot V_{\text{co}}}{M_{\text{co}} \cdot conv} \cdot xmon \end{aligned} . \tag{2.42}$$

Following the definition of V_{co} (eq 2.7), eq 2.42 can be rewritten as:

$$\begin{aligned} c_{\text{mon}} &= \frac{\rho_{\text{co}} \cdot \rho_{\text{mon}}}{m_{\text{ini\_mon}}} \frac{f_{\text{sm}} \cdot conv \cdot \frac{m_{\text{ini\_mon}}}{\rho_{\text{co}}}}{M_{\text{co}} \cdot conv} \cdot xmon \\ &= f_{\text{sm}} \cdot \frac{\rho_{\text{mon}}}{M_{\text{co}}} \cdot xmon \end{aligned} . \tag{2.43}$$

Since *xmon* is the only time-dependent variable in eq 2.43, time-dependent c_{mon} can be expressed as:

$$c_{\text{mon}}(t) = f_{\text{sm}} \cdot \frac{\rho_{\text{mon}}}{M_{\text{co}}} \cdot xmon(t) . \tag{2.44}$$

The radical concentration, $c_{\text{P}\cdot}(t)$, is defined as the spherical micelle number density multiplied by the number of radicals in the spherical micelle core:

$$c_{\text{P}\cdot}(t) = \frac{N_{\text{p}}}{V_{\text{tot}}} \cdot \frac{f_{\text{sm}} \cdot [\text{I}\cdot](t) \cdot V_{\text{tot}}}{N_{\text{p}}} = f_{\text{sm}} \cdot [\text{I}\cdot](t) . \tag{2.45}$$

$[\text{I}\cdot](t)$ is the time-dependent concentration of the radicals calculated as $\sqrt{f_{\text{i}} \cdot \frac{k_{\text{d}}}{k_{\text{t}}} \cdot \frac{n_{\text{ini}}}{V_{\text{tot}}} \cdot e^{-k_{\text{d}} \cdot t}}$, where k_{d} is the radical decomposition coefficient, k_{t} is the termination coefficient and n_{ini} is the number of moles of initiator.

Combined with 2.44 and 2.45, eq 2.38 can be rewritten as:

$$\begin{aligned} R_{\text{p}}(t) &= k_{\text{p}} \cdot \frac{\rho_{\text{mon}}}{M_{\text{co}}} \cdot {f_{\text{sm}}}^2 \cdot \sqrt{f_{\text{i}} \cdot \frac{k_{\text{d}}}{k_{\text{t}}} \cdot \frac{n_{\text{ini}}}{V_{\text{tot}}} \cdot e^{-k_{\text{d}} \cdot t}} \cdot xmon(t) \\ &= k_{\text{p}}' \cdot xmon(t) \end{aligned} , \tag{2.46}$$

where V_{tot} is defined by eq 2.6 and k_{p}' is the reduced propagation rate coefficient for the PISA synthesis. The reduced equation of polymerization rate (eq 2.45) shows that the theoretical rate of polymerisation of PISA process via RAFT synthesis is only proportional to *xmon*, and this can be detected by SAXS modelling. Also, the experimental polymerization rate could be calculated from the SAXS analysis results as:

$$R_{\mathrm{p\_exp}}\left(t_{\mathrm{frame}(h)}\right)=\frac{conv\left(t_{\mathrm{frame}(h+1)}\right)-conv\left(t_{\mathrm{frame}(h)}\right)}{t_{\mathrm{frame}(h+1)}-t_{\mathrm{frame}(h)}}, \tag{2.47}$$

where frame(h) is the h^{th} frame of time-resolved SAXS patterns corresponding to $t_{\mathrm{frame(h)}}$. Assuming that the experimental polymerization rate calculated from eq 2.47 should follow the time-dependent RAFT synthesis propagation (eq 2.46), a least square fitting was applied to minimize the difference between them, $\mathrm{MIN}\left\{\frac{1}{n_{\mathrm{frame}}-1}\sqrt{\sum_{h=1}^{n_{\mathrm{frame}}-1}\left[R_{\mathrm{p\_exp}}\left(t_{\mathrm{frame}(h)}\right)-R_{\mathrm{p}}\left(t_{\mathrm{frame}(h)}\right)\right]^2}\right\}$, where n_{frame} is the total number of recorded frames.

The rate of polymerisation during PISA process via RAFT synthesis at stage 4 (eq 2.46) indicates that the polymerisation process only depends on *xmon* which can be directly measured by SAXS modelling. This means that the chemical kinetics of the polymerisation process itself can be directly measured by SAXS technique and its following modelling. And the analysis of the polymerisation process can be performed using SAXS results directly without counting the monomer supply and the solvent expulsion. However, challenges for measuring the amounts of both the monomer supply and the solvent expulsion remains. The limitation of SAXS data providing scattering patterns averaged over a relatively large sample volume enables only averaged concentration of the liquid molecules in both the latex cores and the medium rather than their concentrations at precise locations to be obtained. Thus, the following molecule transport models are based on this limitation of SAXS experiments and SAXS modelling.

The monomer supply and the solvent expulsion processes can be described as the diffusion processes. Therefore, from Fick's diffusion equation of the liquid molecules described by eq 1.60, the fluxes of the liquid molecules, J_{lm}, are given as:

$$J_{\mathrm{lm}}=\frac{1}{A_{\mathrm{sur}}}\frac{\Delta n_{\mathrm{lm}}}{\Delta t_{\mathrm{tra}}}, \tag{2.48}$$

where A_{sur} is the boundary surface area between the medium and the reaction region, Δn_{lm} is the monomer amount transferring from the medium to the reaction region, and Δt_{tra} is average travelling time for the liquid molecules. Using eq 1.60, a time-dependent form of the Fick's diffusion equation could be rewritten as:

$$\frac{\Delta v_{\mathrm{lm}}\left(t_{\mathrm{tra}}\right)}{A_{\mathrm{sur}}\left(t_{\mathrm{tra}}\right)\cdot\Delta t_{\mathrm{tra}}}=D_{\mathrm{lm}}\frac{\Delta\phi_{\mathrm{lm}}\left(t_{\mathrm{tra}}\right)}{\Delta x_{\mathrm{lm}}\left(t_{\mathrm{tra}}\right)}, \tag{2.49}$$

where Δv_{lm} is the liquid molecule volume change in the medium during, $\Delta\phi_{\mathrm{lm}}$ is the liquid molecule volume fraction change between the medium and the reaction region, D_{lm} is diffusion coefficient of the liquid molecule, and Δx_{lm} is average travelling distance during Δt_{tra}. A_{sur} could be calculated as:

$$A_{\text{sur}} = N_{\text{p}} \cdot S_{\text{p}}, \tag{2.50}$$

where N_{p} is the number of the particles in the system and calculated as:

$$N_{\text{p}} = \frac{v_{\text{p\_co}}}{\frac{4}{3}\pi R_{\text{co}}^3}, \tag{2.51}$$

where $v_{\text{p\_co}}$ is the total volume of particle cores in the system which is equal to $V_{\text{in\_mon}}+V_{\text{in\_pol}}+V_{\text{in\_sol}}$, R_{co} is the average radius of the particle core, and S_{p} is average surface area of the particle cores defined as:

$$S_{\text{p}} = 4\pi R_{\text{co}}^2. \tag{2.52}$$

Therefore, A_{sur} defined by eq 2.49 could be expressed as:

$$A_{\text{sur}} = \frac{3v_{\text{p\_co}}}{R_{\text{co}}}. \tag{2.53}$$

The average travelling distance during Δt_{tra}, Δx_{lm}, can be described as the radius of the sphere of the surface area of A_{sur} (Figure 2.4):[47]

$$\Delta x_{\text{lm}}\left(t_{\text{tra}}\right) = \sqrt{\frac{A_{\text{sur}}\left(t_{\text{tra}}\right)}{4\pi}} = \sqrt{\frac{3}{4\pi}\frac{v_{\text{p\_co}}\left(t_{\text{tra}}\right)}{R_{\text{co}}\left(t_{\text{tra}}\right)}}. \tag{2.54}$$

For the Fick's first law counting chemical potentials for the liquid transportation from the medium to the reaction region, the liquid molecule supply could be represented as a random walk process and a process driven by a chemical potential gradient (Figure 2.5). In application to the studied system this process corresponds to the monomer supply from the medium to the reaction region, and thus, the derived model focuses solely on the monomer supply components. For the random walk process without the chemical potential, the monomer movement during Δt_{sol} can be described by eq 2.49 as:

$$\frac{\Delta v_{\text{lm}}\left(t_{\text{sol}}\right)}{A_{\text{sol}}\left(t_{\text{sol}}\right)\cdot\Delta t_{\text{sol}}} = D_{\text{ml}}\frac{\Delta\phi_{\text{lm}}\left(t_{\text{sol}}\right)}{\Delta x_{\text{sol}}\left(t_{\text{sol}}\right)}, \tag{2.55}$$

where subscripts of "sol" represent the case where movement of the monomer can be considered as a random walk. When the monomers enter the region that the chemical potentials strongly affect the movement of the monomers, the diffusion equation eq 1.64 can be rewritten as:

$$\frac{\Delta v_{\mathrm{lm}}\left(t_{\mathrm{dri}}\right)}{A_{\mathrm{dri}}\left(t_{\mathrm{dri}}\right)\cdot\Delta t_{\mathrm{dri}}}=D_{\mathrm{lm}}\cdot\frac{\Delta\mu_{\mathrm{lm}}}{k_{\mathrm{B}}\cdot N_{\mathrm{A}}\cdot T}\cdot\frac{\phi_{\mathrm{lm}}\left(t_{\mathrm{sol}}\right)}{\Delta x_{\mathrm{dri}}\left(t_{\mathrm{dri}}\right)}, \tag{2.56}$$

where k_B is Boltzmann constant, T is thermodynamic temperature with unit of K and the subscripts of "dri" are represented for the case where movement of the monomers is driven towards the reaction region by the chemical potential gradient, $\Delta\mu_{lm}$. For the random walk process, the concentration of the monomer changes from ϕ_{lm} to 0, which means that eq 2.55 can be rewritten as:

$$\frac{\Delta v_{\mathrm{lm}}\left(t_{\mathrm{sol}}\right)}{A_{\mathrm{sol}}\left(t_{\mathrm{sol}}\right)\cdot\Delta t_{\mathrm{sol}}}=D_{\mathrm{ml}}\frac{\phi_{\mathrm{lm}}\left(t_{\mathrm{sol}}\right)}{\Delta x_{\mathrm{sol}}\left(t_{\mathrm{sol}}\right)}, \tag{2.57}$$

Now, combined equations 2.56 and 2.57, the monomer supply driven by the chemical potential gradient can be expressed as:

$$\frac{\Delta v_{\mathrm{ml}}\left(t_{\mathrm{tra}}\right)}{A_{\mathrm{sur}}\left(t_{\mathrm{tra}}\right)\cdot\Delta t_{\mathrm{tra}}}= D_{\mathrm{ml}}\cdot\left(\frac{\Delta x_{\mathrm{dri}}\left(t_{\mathrm{tra}}\right)}{\Delta x_{\mathrm{dri}}\left(t_{\mathrm{tra}}\right)+\Delta x_{\mathrm{sol}}\left(t_{\mathrm{tra}}\right)}\cdot\frac{\Delta\mu_{\mathrm{ml}}}{k_{\mathrm{B}}\cdot N_{\mathrm{A}}\cdot T}\right)\cdot\frac{\phi_{\mathrm{ml}}\left(t_{\mathrm{tra}}\right)}{\Delta x_{\mathrm{dri}}\left(t_{\mathrm{tra}}\right)+\Delta x_{\mathrm{sol}}\left(t_{\mathrm{tra}}\right)}, \tag{2.58}$$

where A_{sur} and Δt_{tra} are respectively given as:

$$\begin{cases} A_{\mathrm{sur}}=4\pi\left[\Delta x_{\mathrm{dri}}\left(t\right)+\Delta x_{\mathrm{sol}}\left(t\right)\right]^2 \\ \Delta t_{\mathrm{tra}}=\Delta t_{\mathrm{dri}}+\Delta t_{\mathrm{sol}} \end{cases}. \tag{2.59}$$

This monomer supply process model may interpret the monomer transportation during PISA via RAFT synthesis, or emulsion polymerisation. In the following chapters, this diffusion model for the monomer supply will be tested using time-resolved SAXS data collected during PISA via RAFT polymerisation in nonpolar system and polar system, as well as during emulsion polymerisation.

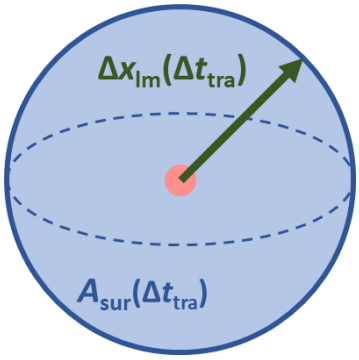

Figure 2.4. A schematic presentation of the flux of liquid molecules transporting from medium represented as the inner sphere to reaction region represented outer sphere during time period, Δt_{tra}. The sphere radius of the surface area, $A_{sur}(\Delta t_{tra})$, is $\Delta x_{lm}(\Delta t_{tra})$.

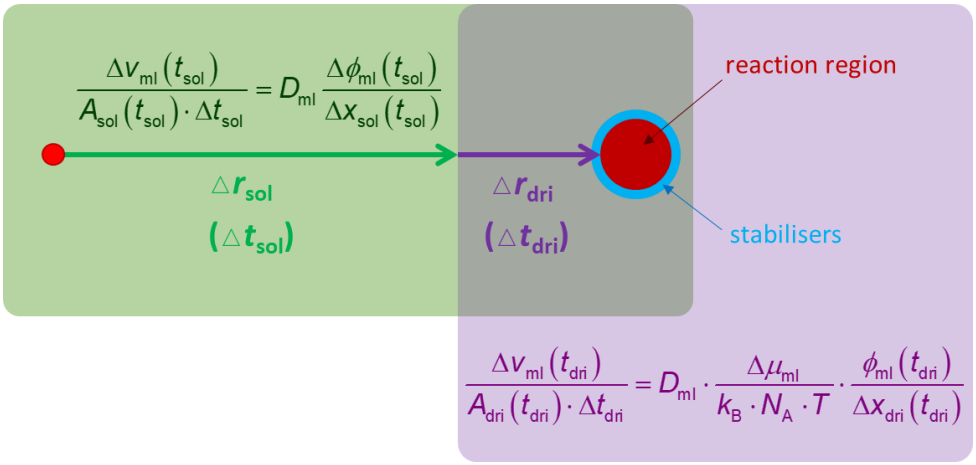

Figure 2.5. A schematic presentation of monomers as an example of liquid molecules transported from medium to reaction region (dark red) named monomer supply with the chemical potential effect which can provide an extra driving force to the monomers transported from the medium the reaction region. The monomer molecules first transported to the reaction region surrounded by stabiliser blocks (light blue) in the medium without chemical potential effects (green arrow). It can be described by the standard Fick's first law. Then, with the chemical potential effect between the reaction region and the medium, the monomers are attracted to the reaction region (purple arrow). This process can be described by the Fick's first law corrected for the chemical potential effect.

2.4 Conclusion

In this chapter, SAXS model for PISA process via RAFT synthesis is improved by mass balance. After this development, SAXS modelling can not only provide morphological information of the self-assembly nanoparticles but also monomer conversion and the compositions in the spherical micelle cores. Therefore, this development for SAXS modelling provide opportunities of more comprehensive analysis of PISA process via RAFT synthesis. It can track the compositions change and the morphological changes at the same time. Also, it provides the opportunities to measure the polymerisation and mass transfers during PISA process via RAFT synthesis at stage 4. After SAXS modelling, the reduced coefficient of the rate of polymerisation can possibly be measured independently by SAXS. For the monomer and solvent transportations between the spherical micelle cores and the medium, models based on Fick's diffusion and chemical potential effects are proposed. These diffusion models for monomer and solvent may complete the descriptions of kinetics of PISA process via RAFT synthesis at final stages of both PISA via RAFT synthesis and emulsion polymerisation.

2.5 References

1. Long, T.; Liu, H.; Schell, B.; Teegarden, D. M.; Uerz, D., Determination of solution polymerization kinetics by near-infrared spectroscopy. 1. Living anionic polymerization processes. *Macromolecules* **1993,** *26* (23), 6237-6242.

2. Keifer, P. A., NMR tools for biotechnology. *Current Opinion in Biotechnology* **1999,** *10* (1), 34-41.
3. Neudert, R.; Ströfer, E.; Bremser, W., On‐line NMR in process engineering. *Magnetic resonance in chemistry* **1986,** *24* (12), 1089-1092.
4. Woelk, K.; Bargon, J., High‐pressure NMR probes for the in situ investigation of gas/liquid reactions. *Review of scientific instruments* **1992,** *63* (6), 3307-3310.
5. Keifer, P. A., High-resolution NMR techniques for solid-phase synthesis and combinatorial chemistry. *Drug Discovery Today* **1997,** *2* (11), 468-478.
6. McDermott, R.; Trabesinger, A. H.; Muck, M.; Hahn, E. L.; Pines, A.; Clarke, J., Liquid-state NMR and scalar couplings in microtesla magnetic fields. *Science* **2002,** *295* (5563), 2247-2249.
7. Vicente, M.; BenAmor, S.; Gugliotta, L. M.; Leiza, J. R.; Asua, J. M., Control of Molecular Weight Distribution in Emulsion Polymerization Using On-Line Reaction Calorimetry. *Industrial & Engineering Chemistry Research* **2001,** *40* (1), 218-227.
8. Elizalde, O.; Azpeitia, M.; Reis, M. M.; Asua, J. M.; Leiza, J. R., Monitoring emulsion polymerization reactors: calorimetry versus Raman spectroscopy. *Industrial & engineering chemistry research* **2005,** *44* (18), 7200-7207.
9. BenAmor, S.; Colombié, D.; McKenna, T., Online reaction calorimetry. Applications to the monitoring of emulsion polymerization without samples or models of the heat-transfer coefficient. *Industrial & engineering chemistry research* **2002,** *41* (17), 4233-4241.
10. Reed, W. F.; Alb, A. M., *Monitoring Polymerization Reactions: From Fundamentals to Applications*. Wiley: Hoboken, New Jersey, 2014.
11. Canegallo, S.; Storti, G.; Morbidelli, M.; Carrà, S., Densimetry for on-line conversion monitoring in emulsion homo- and copolymerization. *Journal of Applied Polymer Science* **1993,** *47* (6), 961-979.
12. Abbey, K., Polymerization kinetics by precision densimetry. ACS Publications: 1981.
13. Levere, M. E.; Willoughby, I.; O'Donohue, S.; de Cuendias, A.; Grice, A. J.; Fidge, C.; Becer, C. R.; Haddleton, D. M., Assessment of SET-LRP in DMSO using online monitoring and Rapid GPC. *Polymer Chemistry* **2010,** *1* (7), 1086-1094.
14. Cornel, E. J.; van Meurs, S.; Smith, T.; O'Hora, P. S.; Armes, S. P., In Situ Spectroscopic Studies of Highly Transparent Nanoparticle Dispersions Enable Assessment of Trithiocarbonate Chain-End Fidelity during RAFT Dispersion Polymerization in Nonpolar Media. *Journal of the American Chemical Society* **2018,** *140* (40), 12980-12988.
15. Sandí, G.; Joachin, H.; Kizilel, R.; Seifert, S.; Carrado, K. A., In Situ SAXS Studies of the Structural Changes of Polymer Nanocomposites Used in Battery Applications. *Chemistry of Materials* **2003,** *15* (4), 838-843.
16. Doncom, K. E. B.; Pitto-Barry, A.; Willcock, H.; Lu, A.; McKenzie, B. E.; Kirby, N.; O'Reilly, R. K., Complementary light scattering and synchrotron small-angle X-ray scattering studies of the micelle-to-unimer transition of polysulfobetaines. *Soft Matter* **2015,** *11* (18), 3666-3676.
17. Derry, M. J.; Fielding, L. A.; Warren, N. J.; Mable, C. J.; Smith, A. J.; Mykhaylyk, O. O.; Armes, S. P., In situ small-angle X-ray scattering studies of sterically-stabilized diblock copolymer nanoparticles formed during polymerization-induced self-assembly in non-polar media. *Chemical Science* **2016,** *7* (8), 5078-5090.
18. Alauhdin, M.; Bennett, T. M.; He, G.; Bassett, S. P.; Portale, G.; Bras, W.; Hermida-Merino, D.; Howdle, S. M., Monitoring morphology evolution within block copolymer microparticles during dispersion polymerisation in supercritical carbon dioxide: a high pressure SAXS study. *Polymer Chemistry* **2019,** *10* (7), 860-871.
19. Brotherton, E. E.; Hatton, F. L.; Cockram, A. A.; Derry, M. J.; Czajka, A.; Cornel, E. J.; Topham, P. D.; Mykhaylyk, O. O.; Armes, S. P., In Situ Small-Angle X-ray Scattering Studies During Reversible Addition–Fragmentation Chain Transfer Aqueous Emulsion Polymerization.

Journal of the American Chemical Society **2019,** *141* (34), 13664-13675.
20. Czajka, A.; Armes, S. P., In situ SAXS studies of a prototypical RAFT aqueous dispersion polymerization formulation: monitoring the evolution in copolymer morphology during polymerization-induced self-assembly. *Chemical Science* **2020,** *11* (42), 11443-11454.
21. Takahashi, R.; Miwa, S.; Sobotta, F. H.; Lee, J. H.; Fujii, S.; Ohta, N.; Brendel, J. C.; Sakurai, K., Unraveling the kinetics of the structural development during polymerization-induced self-assembly: decoupling the polymerization and the micelle structure. *Polymer Chemistry* **2020,** *11* (8), 1514-1524.
22. Rymaruk, M. J.; O'Brien, C. T.; György, C.; Darmau, B.; Jennings, J.; Mykhaylyk, O. O.; Armes, S. P., Small-Angle X-Ray Scattering Studies of Block Copolymer Nano-Objects: Formation of Ordered Phases in Concentrated Solution During Polymerization-Induced Self-Assembly. *Angewandte Chemie International Edition* **2021,** *60* (23), 12955-12963.
23. Santos, L. S.; Metzger, J. O., On-line monitoring of Brookhart polymerization by electrospray ionization mass spectrometry. *Rapid Communications in Mass Spectrometry* **2008,** *22* (6), 898-904.
24. Florenzano, F. H.; Strelitzki, R.; Reed, W. F., Absolute, On-Line Monitoring of Molar Mass during Polymerization Reactions. *Macromolecules* **1998,** *31* (21), 7226-7238.
25. Kourti, T. Polymer latexes: production by homogeneous nucleation and methods for particle size determination. 1989.
26. Levere, M. E.; Willoughby, I.; O'Donohue, S.; Wright, P. M.; Grice, A. J.; Fidge, C.; Remzi Becer, C.; Haddleton, D. M., Cu(0) mediated polymerization in toluene using online rapid GPC monitoring. *Journal of Polymer Science Part A: Polymer Chemistry* **2011,** *49* (8), 1753-1763.
27. Warren, N. J.; Armes, S. P., Polymerization-Induced Self-Assembly of Block Copolymer Nano-objects via RAFT Aqueous Dispersion Polymerization. *Journal of the American Chemical Society* **2014,** *136* (29), 10174-10185.
28. Blanazs, A.; Madsen, J.; Battaglia, G.; Ryan, A. J.; Armes, S. P., Mechanistic insights for block copolymer morphologies: how do worms form vesicles? *Journal of the American Chemical Society* **2011,** *133* (41), 16581-16587.
29. Charleux, B.; Delaittre, G.; Rieger, J.; D'Agosto, F., Polymerization-Induced Self-Assembly: From Soluble Macromolecules to Block Copolymer Nano-Objects in One Step. *Macromolecules* **2012,** *45* (17), 6753-6765.
30. Warren, N. J.; Mykhaylyk, O. O.; Mahmood, D.; Ryan, A. J.; Armes, S. P., RAFT Aqueous Dispersion Polymerization Yields Poly(ethylene glycol)-Based Diblock Copolymer Nano-Objects with Predictable Single Phase Morphologies. *Journal of the American Chemical Society* **2014,** *136* (3), 1023-1033.
31. Derry, M. J.; Fielding, L. A.; Armes, S. P., Polymerization-induced self-assembly of block copolymer nanoparticles via RAFT non-aqueous dispersion polymerization. *Progress in Polymer Science* **2016,** *52*, 1-18.
32. Perrier, S., 50th Anniversary Perspective: RAFT Polymerization—A User Guide. *Macromolecules* **2017,** *50* (19), 7433-7447.
33. Voorhees, P. W., The theory of Ostwald ripening. *Journal of Statistical Physics* **1985,** *38* (1), 231-252.
34. Hammouda, B., SANS from homogeneous polymer mixtures: a unified overview. In *Polymer Characteristics*, Springer: 1993; pp 87-133.
35. Pedersen, J. S.; Gerstenberg, M. C., Scattering form factor of block copolymer micelles. *Macromolecules* **1996,** *29* (4), 1363-1365.
36. Lund, R.; Willner, L.; Richter, D.; Dormidontova, E. E., Equilibrium chain exchange kinetics of diblock copolymer micelles: Tuning and logarithmic relaxation. *Macromolecules* **2006,** *39* (13), 4566-4575.
37. Lund, R.; Willner, L.; Stellbrink, J.; Lindner, P.; Richter, D., Logarithmic chain-exchange kinetics of diblock copolymer micelles. *Physical review letters* **2006,** *96* (6), 068302.

38. Lund, R.; Willner, L.; Monkenbusch, M.; Panine, P.; Narayanan, T.; Colmenero, J.; Richter, D., Structural Observation and Kinetic Pathway in the Formation of Polymeric Micelles. *Physical Review Letters* **2009,** *102* (18), 188301.
39. Lund, R.; Willner, L.; Lindner, P.; Richter, D., Structural Properties of Weakly Segregated PS− PB Block Copolymer Micelles in n-Alkanes: Solvent Entropy Effects. *Macromolecules* **2009,** *42* (7), 2686-2695.
40. Pedersen, J. S., Structure factors effects in small-angle scattering from block copolymer micelles and star polymers. *The Journal of Chemical Physics* **2001,** *114* (6), 2839-2846.
41. Pedersen, J. S.; Svaneborg, C.; Almdal, K.; Hamley, I. W.; Young, R. N., A Small-Angle Neutron and X-ray Contrast Variation Scattering Study of the Structure of Block Copolymer Micelles: Corona Shape and Excluded Volume Interactions. *Macromolecules* **2003,** *36* (2), 416-433.
42. Flory, P. J., *Principles of Polymer Chemistry*. Cornell University Press: ITHACA, New York, 1953.
43. Fetters, L.; Lohse, D.; Colby, R., Chain dimensions and entanglement spacings. In *Physical properties of polymers handbook*, Springer: 2007; pp 447-454.
44. Kinning, D. J.; Thomas, E. L., Hard-sphere interactions between spherical domains in diblock copolymers. *Macromolecules* **1984,** *17* (9), 1712-1718.
45. Pedersen, J. S., Analysis of small-angle scattering data from colloids and polymer solutions: modeling and least-squares fitting. *Advances in Colloid and Interface Science* **1997,** *70*, 171-210.
46. Lovell, P. A.; El-Aasser, M. S., *Emulsion Polymerization and Emulsion Polymers*. Wiley: 1997.
47. Houston, P. L., *Chemical Kinetics and Reaction Dynamics*. Dover Publications: 2012.

Chapter 3: *In Situ* Small-angle X-ray Scattering Studies of Kinetics of Polymerization-induced Self-assembly of Block Copolymers in Nonpolar Media

Chapter 3

In Situ Small-angle X-ray Scattering Studies of Kinetics of Polymerization-induced Self-assembly of Block Copolymers in Nonpolar Media

3.1 Introduction

Well-studied block copolymer self-assembly provides opportunities for potential applications in biology[1, 2], templating[3-5], sensors[6-8] and other technologies[9-12]. Its wide prospects encourage further research on block copolymer synthesis including one of the most convenient and versatile reversible addition–fragmentation chain transfer (RAFT) polymerization.[13] RAFT as the living radical polymerization is capable to provide a good control of the molecular weight distribution for functional block copolymers and, as a result, helps to achieve intentional and well-defined self-assembled morphologies.[14, 15] To overcome the low concentration limit (< 1.0% w/w) of the self-assembled nanoparticles in block-copolymer dispersions obtained by using post-polymerization routes, polymerization-induced self-assembly (PISA) via RAFT was developed to reach a relatively high solid content level (25 – 50% w/w) of block copolymers in the dispersions.[16] Moreover, the later method is suitable for a wide range of solvents, including polar solvents, nonpolar solvents and ionic liquids.[17-19] PISA via RAFT dispersion polymerization is realised by a chain-extension of a solvophilic block (brush chain), a soluble homopolymer, using a miscible monomer added to the precursor solution polymerised into a solvophobic block (core chain) during reaction up to a critical degree of polymerization when the produced diblock copolymers self-assemble into conventional particle morphologies such as spherical micelles, worm-like micelles, jellyfish-like objects, vesicles, multi-lamellar vesicles and lamellar-like structures relying on the block-copolymer chemical composition, molecular weight and concentration.[17, 18]

The PISA products synthesised by RAFT have been well-investigated in the past by numerous techniques, including electron microscopy, dynamic light scattering (DLS), nuclear magnetic resonance (NMR) and gel permeation chromatography (GPC). However, most of these techniques could provide only partial information about the reaction product composition and the structure of the formed nano-objects. While commonly used scanning electron microscopy (SEM) and transmission electron microscopy (TEM) could provide structural information about the synthesised products, these techniques require *ex situ* sample preparation before imaging.[17, 18] In addition, the preparation could change the morphologies of the nano-objects as the process includes reduction of the copolymer concentration in solutions and sample drying.[17, 18, 20] To overcome this problem, a liquid cell TEM has been recently proposed for studying PISA process *in situ*.[21] However, the measurements could be performed only at special conditions [polymerisation is initiated by the electron beam generating radicals, and a low-flux electron beam and high concentration of macromolecular chain transfer agent (macro-CTA) have to be used] and there was a lack of resolution for accurate measurements of the self-assembled nano-objects. A relatively simple experimental setup would be required for monitoring the formation of copolymer nano-objects during PISA by DLS. However, this scattering technique has limited capabilities for measuring particle size and shape[22] and can effectively be used only for measuring diameter of spherical particles[17, 18]. Moreover, standard DLS is not suitable for highly concentrated particle dispersions,[23] in particular, for the PISA via RAFT synthesis. Neither of the discussed techniques could assess

the reaction product composition. In this respect, NMR is routinely used to detect the chemical composition, especially the monomer conversion for the PISA via RAFT synthesis.[17, 18] This technique has also successfully been exploited to monitor RAFT polymerization (and the monomer conversion) *in situ*.[15, 24-26] GPC provides valuable information about molecular weight of synthesised polymers which can be linked to their chemical composition.[17, 18] However, this technique is not designed for in situ measurements and commonly used for characterisation of final reaction products.

Consequently, these mainly post-synthesis characterising methods provide very useful but limited information about kinetics of both the block copolymer synthesis and the formation of self-assembled morphologies without deep quantitative analysis of the processes taking place during the reaction. This disadvantage, in some respect, could be overcame by *in situ* time-resolved small angle X-ray scattering (TR SAXS) measurements, which can effectively be used to determine not only geometrical parameters of the self-assembled morphologies but also their compositions and distribution in the sample. A few recent reports have demonstrated the power of SAXS analysis for a characterisation of block copolymer self-assembly during PISA process,[27-33] but the full potential of this technique is yet to be revealed. An attempt has been made[27] to study kinetics of PISA of poly(stearyl methacrylate)–poly(benzyl methacrylate) (PSMA–PBzMA) diblock copolymer by applying *in situ* TR SAXS.

The research of PSMA–PBzMA diblock copolymer is related to the environmental-friendly background. As the global energy consumption growth, friction effect significantly contributes to CO_2 emission from industry, public, and personal activities.[34-37] Lubrication is one of the methods used to reduce the friction effect. In particular, boundary lubrication, mixed lubrication, elastohydrodynamic lubrication and hydrodynamic lubrication play critical role in reducing the friction effect.[38] Boundary lubrication can possibly prevent or reduce friction and wear effects between the two surfaces by introducing extra materials to separate these two surfaces or reduce the roughness between these two surfaces.[39] Without the lubrication, the collisions between two surfaces may produce fractures and deformations of the materials, and the friction effect, producing heat, can increase the energy consumption at the same time. Applications of boundary lubrication are not limited only to machines but are also common in medicine for articular joints.[40] Therefore, the research in boundary lubrication area can provide valuable information for its various applications.

Liquid lubricants are normally applied in boundary lubrication. These materials are absorbed by the surfaces via physical or chemical reactions, and they form a boundary film. The mechanism and the theories of boundary lubrication are still not clear, and the research of boundary lubrication heavily depends on the experimental results.[41] To improve the liquid lubricant performance, according to usage purposes, the additives of the liquid lubricants can be classified as oily, tackifier, extreme pressure, and anti-wear.[41] And it can be classified as organomolybdenum compounds and organic friction modifiers.[38] For organic friction modifiers, polymers are introduced, which included the self-assembled block copolymers (micelles) to enhance performance of boundary lubrication.[42] The following research of block copolymers in boundary lubrication[27, 43] and friction reduction[44, 45] areas also indicated the wide application prospects. Therefore, it requires deeper investigations of the formations of diblock copolymers in liquid lubricants.

Even though *in situ* SAXS studies of poly(stearyl methacrylate)-poly(benzyl methacrylate) (PSMA–PBzMA) have been presented before[27], this SAXS analysis required an additional quantitative information about both the monomer conversion and the solvent content in the spherical micelle core obtained by ^{1}H NMR measurements performed offline independently of the synchrotron SAXS experiments. It has been found that the reaction rate during SAXS

measurements was significantly faster than for the NMR measurements because of a possible reaction acceleration by X-ray radiation and, as a result, undesirable corrections for the observed systematic errors had to be incorporated in the analysis which was not ideal for the study of a complex process such as PISA. The SAXS analysis used in this study required additional information from other techniques which was indirectly incorporated in the SAXS models. However, this approach demonstrated a lack of consistency between rate of polymerisation performed using standard laboratory conditions and a reactor cell at synchrotron performed [27]. Herein, PISA process via RAFT synthesis of $PSMA_{31}$–$PBzMA_{2000}$ in mineral oil with *in situ* SAXS studies[27] will be reviewed and SAXS modelling with mass balance, described in Chapter 2, eq 2.1, will be applied. The SAXS modelling and the following results will be presented in detail. Also, these SAXS modelling results and analysis will be compared with the results reported previously[27] in order to validate the developed SAXS model with mass balance, eq 2.1.

3.2 Poly(stearyl methacrylate)-poly(benzyl methacrylate) Block Copolymer ($PSMA_{31}$–$PBzMA_{2000}$) Synthesis in Mineral Oil

The benzyl methacrylate (BzMA) monomers were purchased from Sigma-Aldrich (UK) and passed through a basic alumina column prior to use to remove inhibitor. Tert-butyl peroxy-2-ethylhexanoate (T21s) initiator was purchased from AkzoNobel (The Netherlands). Industrial-grade mineral oil was provided by Lubrizol Corporation Ltd.

A previously studied PISA synthesis of poly(stearyl methacrylate)-poly(benzyl methacrylate) block copolymer ($PSMA_{31}$–$PBzMA_{2000}$) in mineral oil (Scheme 3.1)[27] has been chosen to test the proposed SAXS model. PSMA macro-CTA was synthesized by RAFT solution polymerisation of stearyl methacrylate (SMA) in toluene at 70 °C using cumyl dithiobenzoate (CDB), characterised using ^{1}H NMR spectroscopy and the mean degree of polymerization (DP) was calculated to be 31.[27] PISA synthesis of $PSMA_{31}$-$PBzMA_{2000}$ diblock copolymer in mineral oil at 90 °C as well as the experimental setup for a simultaneous SAXS data collection have been described elsewhere.[27] In brief, the benzyl methacrylate (BzMA) monomer (0.217 g; 1.23 mmol), tert-butyl peroxy-2-ethylhexanoate (T21s) initiator (0.274 mg; 0.127 µmol; dissolved at 10.0 % v/v in mineral oil) and $PSMA_{31}$ macromolecular chain transfer agent (macro-CTA) (6.63 mg; 0.633 µmol; macro-CTA/initiator molar ratio equals 5.0; target degree of PBzMA polymerization equals 2000) were dissolved in mineral oil (2.02 g). Herein, BzMA were purchased from Sigma-Aldrich (UK) and passed through a basic alumina column prior to use to remove inhibitor. Tert-butyl peroxy-2-ethylhexanoate (T21s) initiator was purchased from AkzoNobel (The Netherlands). Industrial-grade mineral oil was provided by Lubrizol Corporation Ltd. The reaction mixture was sealed in a 10 mL round-bottomed flask and purged with nitrogen gas for 30 min before a portion of the deoxygenated solution was transferred into a 2 mm diameter glass capillary for X-ray measurements (WJM-Glas, Berlin, Germany). The reaction was initiated by connecting the brass stage, via a pneumatic switch, to a water circulator pre-heated to 90 °C. After completing the SAXS measurements the sample was taken for further offline characterisations: the final BzMA conversion was measured by ^{1}H NMR to be 98 %, and the number average molecular weight (M_n) was determined by gel permeation chromatography (GPC) to be 140,200 g·mol^{-1} with dispersity index (DI = M_w/M_n) 1.91.[27] Although dispersity index was relatively high, no significant negative effect occurs, because

this dispersity index only affect the calculation of the spherical micelle aggregation number.

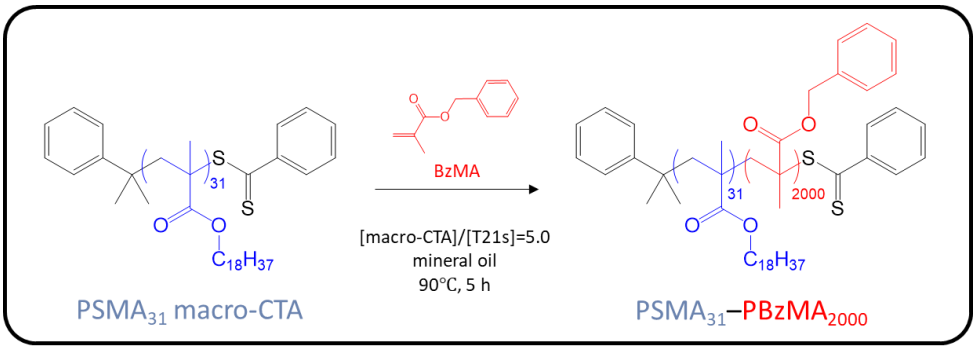

Scheme 3.1 Synthesis of poly(stearyl methacrylate)-poly(benzyl methacrylate) block copolymer ($PSMA_{31}$–$PBzMA_{2000}$) via extension of $PSMA_{31}$ macromolecular chain transfer agent by RAFT dispersion polymerization of BzMA in mineral oil at 90 °C.

3.3 The Characterisation of $PSMA_{31}$–$PBzMA_{2000}$ Synthesis in Mineral Oil

Density measurement

The densities of BzMA monomer, mineral oil and $PSMA_{31}$ in mineral oil at the reaction temperature, 90 °C, were determined by oscillating U-tube method[46] using DMA 5000 M density meter (Anton Paar, Graz, Austria). 3 measurement results were averaged per sample. Although the density repeatability is 0.000001 g/cm³, densities are presented in three significant digits for further use, which indicates that no uncertainties are given.

Small-Angle X-ray Scattering (SAXS)

SAXS patterns were recorded at 90 °C on a synchrotron X-ray beamline (station I22, Diamond Light Source, Didcot, UK)[47] from initiation of the chemical reaction every 2 minutes for 194 min (97 frames in total) using monochromatic X-ray radiation (λ = 1.24 Å, q-range from 0.0015 to 0.13 $Å^{-1}$) and a Pilatus 2M two-dimensional (2D) pixel detector (Dectris, Switzerland). 2D SAXS patterns were reduced [integrated, normalized by the sample transmission coefficient and calibrated to absolute intensity, I_{exp} (Figure 3.2), using SAXS patterns of deionized water measured at 21 °C and then adjusted the intensity to 90 °C assuming that the differential scattering cross-section of water at 21 °C is 0.0162 cm^{-1}] to 1D SAXS profiles using Dawn software supplied by Diamond Light Source[48].

Hansen solubility parameter measurements

In order to measure Flory-Huggins parameters by Hansen solubility parameters[49-52], 5 mL of selected solvents, including acetone, acetonitrile, BzMA, chloroform, diethyl ether, dimethyl sulfoxide (DMSO), 1,4-Dioxane, ethanol, ethyl acetate, hexane, ethyl methacrylate, N,N-dimethyl formamide (DMF), 2-Propanol, styrene, tetrahydrofuran (THF), and toluene were respectively mixed with 0.5 mL of mineral oil in 10 mL vials at 25 °C, and the solubility of the mineral oil were determined after 24 h since the solvents mixed. Immiscible pairs were visually observed. For scores of the Solubility, good solvents are indicated with a "1", and poor solvents are indicated with a "0". The Hansen solubility parameters (HSP) were calculated determined by HSPiP software [51, 52].

3.4 SAXS Modelling and Assumptions for $PSMA_{31}$–$PBzMA_{2000}$ Synthesis in Mineral Oil

Before fitting the SAXS model described by eq 2.1, the experimental 1D SAXS profiles were further corrected by subtracting a pre-recorded background scattering of the empty glass capillary heated to 90 °C. Since the solvent composition changes during the PISA synthesis because of the monomer consumption during polymerization of the PBzMA block and an exchange of the solvent molecules (including BzMA monomer) between the self-assembled objects formed by the reaction products and the surrounding solvent (Figure 2.1), the solvent background scattering term, I_{bg}, is included in the SAXS model (eq 2.1). In order to count I_{exp_bg} changes over the reaction time, SAXS patterns of the mineral oil with different mass concentration of BzMA monomer (w_{mon}) from 2 w/w% to 10 w/w% (including initial monomer concentration of 8 w/w% used for the studied reaction) heated to 90 °C have been recorded. I_{exp_bg} of the solvents, independent of q, has been obtained from the reduced and empty capillary scattering subtracted SAXS patterns (Figure 3.1). Since the BzMA monomer concentration was relatively low and the exposure time during SAXS data collection was short (1s per sample), no extra reaction due to thermal initiation was considered here. As it would be expected for a system of mixed molecules, I_{exp_bg} increases upon increase of the BzMA monomer content. The observed dependence can be interpolated by a cubic polynomial:

$$I_{bg} = I_{bg}\left(w_{mon}\right) = A_1 + A_2 \cdot w_{mon} + A_3 \cdot w_{mon}^2 + A_4 \cdot w_{mon}^3 , \qquad (3.1)$$

where A_1, A_2, A_3 and A_4 are the fitting parameters. w_{mon}, a variable related to the studied PISA system, is expressed as

$$w_{mon} = \frac{\left(1 - f_{mon}\right) m_{mon}}{\left(1 - f_{mon}\right) m_{mon} + \sum_{j=1}^{n_{sol}} \left(1 - f_{sol\,j}\right) m_{sol\,j}} . \qquad (3.2)$$

The empirical equation (eq 3.2) chosen to describe the solvent background scattering (I_{exp_bg}) produced a good match to the experimental data with the coefficient of determination, R^2, equal to 0.993 (Figure 3.1), and thus it has been used in the model for SAXS analysis (eq 2.1).

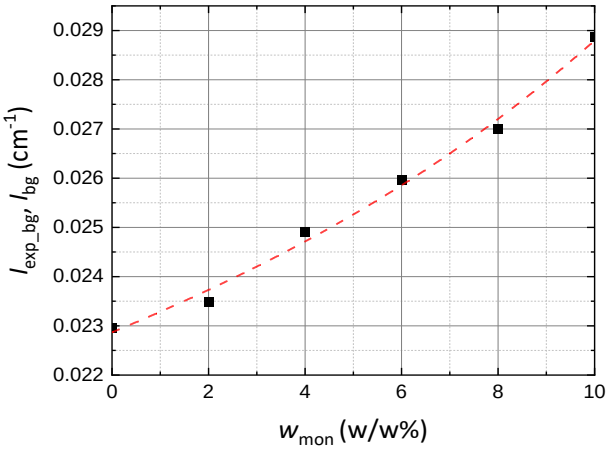

Figure 3.1. I_{exp_bg} vs. w_{mon} (black squares) and fitted by a cubic polynomial equation (eq 3.1) (red dashed line) with the fitting result as I_{bg}= 0.0229 + 4.09×10^{-4} · w_{mon} + 9.40×10^{-6} · w_{mon}^2 + 8.95×10^{-7} · w_{mon}^3.

The densities of BzMA and mineral oil at the reaction temperature, 90 °C, were 0.975 g·cm^{-3} and 0.785 g·cm^{-3}, respectively. The density of $PSMA_{31}$ in mineral oil, measured at 90 °C by the same method using a set of solutions with different $PSMA_{31}$ concentration, was determined to be 0.890 g·cm^{-3}. The density of PBzMA at 90 °C was estimated to be 1.14 g·cm^{-3} using a helium pycnometer measurement on a dry powder at room temperature and assuming that the PBzMA has the same thermal expansion coefficient as poly(methyl methacrylate)[53].[54] Scattering length densities of BzMA, $PSMA_{31}$, PBzMA and mineral oil at 90 °C used for SAXS analysis are 8.82×10^{10} cm^{-2}, 9.17×10^{10} cm^{-2}, 1.03×10^{11} cm^{-2} and 7.63×10^{10} cm^{-2}, respectively.[27] These values have been calculated using molecular composition and mass density of the components.

Calculations and fitting of the SAXS data were performed using *Irena*[55], a macro package for small angle scattering (SAS) data analysis within the commercial *Igor Pro* application (Figure 3.2). The SAXS models (eq 2.1) were programmed using a user function option in the *Irena* SAS macros. In order to preserve connections between different relationships and scattering object populations, some of the SAXS model parameters (such as ϕ_{sm}, *conv*, *xmon* and *xsol*) were set as global variables.

3.5 Results and Discussion

Considering the NMR results indicating that virtually all BzMA monomer has been converted into PBzMA during PISA process via RAFT synthesis and that the final reaction product is spherical micelles formed by self-assembled PSMA-PBzMA copolymers (Figure 2.1, Stage 5), it

could be assumed that the final frame of the time-resolved SAXS data (frame 97 recorded at 194 min of the synthesis) corresponds to spherical micelles only. This assumption enabled the developed SAXS models to be verified first on the known (final) product and then effectively applied frame-by-frame backwards from the final product to the beginning of the reaction. Therefore, no uncertainties for fitted variables will be given under this frame-by-frame backwards SAXS modelling methods. Following eq 2.2, also combined with equations 2.31 and 3.1, the total scattering intensity for the final frame, as well as frames associated with stage 4 of the synthesis (Figure 2.1), can be expressed as:

$$I_{\mathrm{tot}}(q)=\phi_{\mathrm{sm}}\frac{\int_0^{\infty}\Psi_{\mathrm{sm}}(r_{\mathrm{mc}})\left(F_{\mathrm{sm}}(q,r_{\mathrm{mc}})+A_{\mathrm{sm}}^2(q,r_{\mathrm{mc}})\left[S(q,r_{\mathrm{mc}})-1\right]\right)dr_{\mathrm{mc}}}{\int_0^{\infty}\Psi_{\mathrm{sm}}(r_{\mathrm{mc}})V_{\mathrm{sm}}(r_{\mathrm{mc}})dr_{\mathrm{mc}}}+(1-\phi_{\mathrm{sm}})I_{\mathrm{bg}}(w_{\mathrm{mon}}) \qquad (3.3)$$

Indeed, eq 3.3 produced a good fit to SAXS pattern of the final product (Figure 3.2, top pattern) revealing the spherical micelle core radius of R_{sm} = 61.2 nm and $\sigma_{R_{\mathrm{mc}}}$ = 5.4 nm. Defined the polydispersity index (PDI) as the coefficient of variance, $\sigma_{R_{\mathrm{sm}}}/R_{\mathrm{sm}}$, the PDI of the final product is 0.088 indicating a relatively low dispersity of the particle size (Figure 3.3). The SAXS data fitting has also shown that the final spherical micelle core is only slightly solubilised by the solvent (*xsol* = 0.07) (Figure 3.3) in agreement with the previous SAXS results confirmed by NMR[27]. The $R_{\mathrm{g\_br}}$ is around 1.6 nm. The validation of the $R_{\mathrm{g\_br}}$ is estimated by the Gaussian chain model as $(b\cdot l_c/6)^{0.5}$ [56], where the contour length of such $PSMA_{31}$, l_c, is calculated as the repeat unit, 31, multiplying to the length of two carbon bonds in an all *trans* configuration, 0.255 nm, and the Kuhn length, *b*, is given as 1.53 nm based on PMMA[57]. This theoretical calculation gives 1.33 nm, which is consistent with measured by SAXS and the following SAXS modelling. Subsequently, the fitting results of the last SAXS data frame have been used as initial parameters for fitting SAXS pattern of the penultimate frame and the complete SAXS data analysis was performed in the same fashion backward from frame *m* to its previous frame (*m* – 1) during SAXS collection time, *t*, corresponding to the frame number as *t*/2.

The derived intensity equation (eq 3.3) produced reasonably good fits to most of the SAXS patterns collected during the time-resolved experiment starting from the last frame (frame 97, 194 min) down to frame 7 inclusive (Figure 3.2). Since eq 3.3 describes only scattering from products corresponding to stages 4 or 5 of the synthesis, this indicates that from about 14 minutes of synthesis there were no soluble diblock copolymers in the system, or their amount was negligibly small to be detectable by SAXS measurements. However, the scattering equation based on a traditional spherical micelle model (eq 2.31) for assembled block copolymers could not provide satisfactory fitting results for the first 6 frames even if considering that a population of free copolymer molecules, associated with stage 3 of the synthesis (Figure 2.1), is present (eq 2.2).

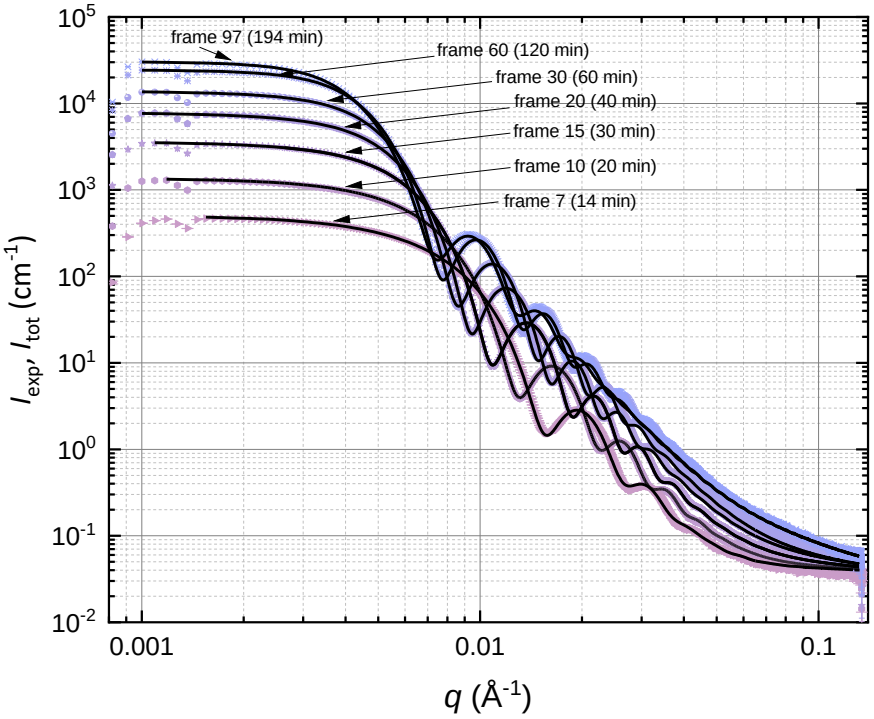

Figure 3.2**.** Selected experimental SAXS patterns, I_{exp}, (red symbols) with respective fitting curves, I_{tot}, (blue lines) recorded *in situ* during PISA process via RAFT synthesis of $PSMA_{31}$–$PBzMA_{2000}$ diblock copolymer at 90 °C in mineral oil at 10% w/w solids.

SAXS results have shown that the spherical micelle core radius was continuously increasing after the copolymer micelle formation for the entire period of SAXS data collection (Figure 3.3). This expected observation matches the previous findings.[27] However, The PDI of R_{mc} rapidly decreased to a valley, and then after 45 min, it constantly rose till the end of the SAXS data collection (Figure 3.3). To satisfy the reason of the tendency of R_{mc} and its PDI, monomer conversion (Figure 3.4), which is straight accessorized with DP, might be one of the critical factors to determine to the size self-assembled diblock copolymer nanoparticle by scaling relation.

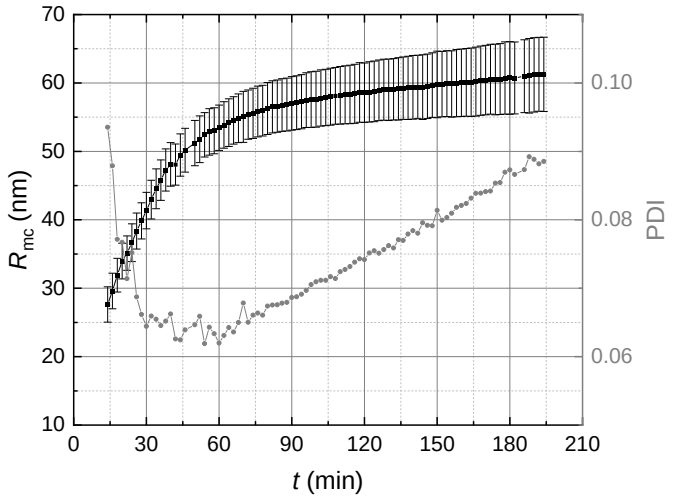

Figure 3.3. R_{mc} (black squares) and its PDI (gray circles) vs. time curve with standard deviation of PISA process via RAFT synthesis of $PSMA_{31}$–$PBzMA_{2000}$ diblock copolymer at 90 °C in mineral oil at 10% w/w solids.

Another important characteristic of the synthesis which could obtained directly from the performed SAXS analysis is the monomer conversion with time (Figure 3.4). The results show that nearly all BzMA monomer is converted into the PBzMA block within 120 mins of the reaction. This is about 3 times faster than the time required for the complete monomer conversion measured by NMR during a standard laboratory synthesis (Figure 3.4). This apparent inconsistency between two independent experiments (at a synchrotron and in a laboratory, respectively) is likely to be related to an acceleration of the reaction by high-flux X-ray synchrotron radiation.[58] Unlike in the previous report, where a single logistic function was used to model NMR data for the monomer conversion,[27, 59] a double logistic function was employed in this study:

$$f(x,B,p,k_1,k_2,x_{c_1},x_{c_2}) = B\left[1-\frac{p}{1+e^{-k_1(x-x_{c_1})}}-\frac{1-p}{1+e^{-k_2(x-x_{c_2})}}\right], \qquad (3.4)$$

where B, k_1, k_2, x_{c1}, x_{c2}, and p are the function parameters. Compared with the single logistic function in the previous research, the double logistic function produced a better fitting to the monomer conversion values obtained from both NMR and SAXS measurements (Figure 3.4). This result indicates that after the diblock copolymer self-assembly the monomer conversion could be controlled by at least two processes with different timescales. The obvious one is the monomer polymerization inside of the copolymer micelles working as individual reactors and the other one could be the transportation of BzMA monomer from the surrounding medium to the micelle core where the reaction takes place (Figure 2.1, stage 4). The obtained results have revealed a strong acceleration of one of the processes during SAXS data collection ($k_{2\_SAXS}/k_{2\_NMR} > k_{1\_SAXS}/k_{1\_NMR}$, see Figure 3.4 and eq 3.4) possibly caused by intense synchrotron radiation. However, in order to perform a further analysis a detailed theoretical model considering interactions between components in the system and diffusion of the components through the interfaces created by the copolymer self-assembly would be required which is beyond the scope of this study.

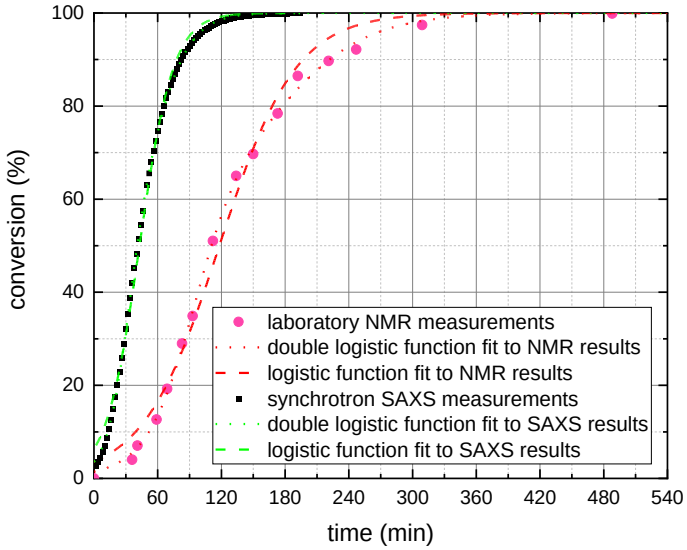

Figure 3.4. BzMA monomer conversion calculated from both synchrotron SAXS data (squares) and laboratory NMR results (circles) collected during PISA via RAFT synthesis of $PSMA_{31}$–$PBzMA_{2000}$ diblock copolymer at 90 °C in mineral oil at 10% w/w solids. under double logistic function fit (pink dashes). Data fitting by a single logistic function (dashed curves) and a double logistic function (dotted curves) of both the NMR results (red curves) and the SAXS results (green curves) returned the following respective sets of parameters expressed in terms of eq 3.4: $conversion_{NMR} = f(t, 100, 0, 0.0001, 0, 118, 0)$ (R^2=0.990) (red dashed curve eq 3.4), $conversion_{NMR} = f(t, 100, 0.618, 0.00078, 0.00038, 92, 176)$ (R^2=0.999) (red dotted curve eq 3.4), $conversion_{SAXS} = f(t, 100, 0, 0.00063, 0, 43, 0)$ (R^2=0.997) (green dashed curve eq 3.4) and $conversion_{SAXS} = f(t, 100, 0, 0.550, 0.0017, 0.00097, 32, 60)$ (R^2=0.999) (green dotted curve eq 3.4).

According to monomer conversion (Figure 3.4), the polymerisation was close to the end at 150 min. However, R_{co} was still increasing after 150 min, which might be led by Ostwald ripening[31, 60-68]. Ostwald ripening theories indicated that the spherical micelle radius change should follow,[69]

$$\frac{dR_{mc}^3}{dt} = Const.. \quad (3.5)$$

The *Const.* in eq 3.5 interfacial energy of spherical micelle, the diffusion coefficient of diblock copolymers, and the bulk solubility of the block copolymers.[69] Therefore, dR_{mc}^3/dt should be time-independent when Ostwald ripening played the critical roles of spherical micelle radius change. Therefore, after 100 min of the polymerisation (*conv* > 95%), the spherical micelle core increase might depend on Ostwald ripening process (Figure 3.5). Also, the PDI increase might result from the Ostwald ripening process. However, the Ostwald ripening could not predict the possible maximum spherical micelle core radius.

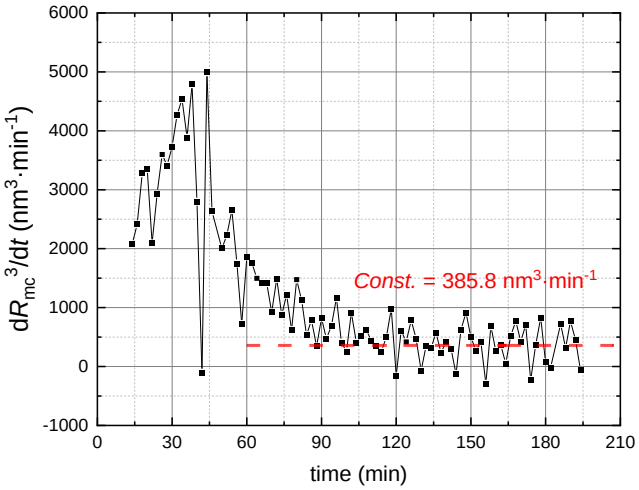

Figure 3.5. dR_{mc}^3/dt vs. time curve (black squares) of PISA process via RAFT synthesis of $PSMA_{31}$–$PBzMA_{2000}$ diblock copolymer at 90 °C in mineral oil at 10% w/w solids. Data fitting (red dash line) by a constant function (*Const.* = 385.8 $nm^3 \cdot min^{-1}$) (eq 3.5) from 150 min to 194 min provided a reference for the identification of the possible Ostwald ripening process after the end of polymerisation.

The scale relation studies of self-assembled particle core size (diameter) vs. DP of solvophobic block have been applied to $PSMA_{31}$-PBzMA spherical micelles, and this research revealed that the diameter of $PSMA_{31}$-PBzMA spherical micelle core, D_{sm} is proportional to $DP^{0.5}$.[27] Herein, even though the change of R_{mc} along DP was struggled in the chemical kinetic process, scaling relation, $R_{mc} = k_{R\text{-}DP} \cdot DP^{\omega}$, where $k_{R\text{-}DP}$ and ω are constants, might be able to interpret the relationship of R_{sm} and DP, and this relationship can be divided into 3 sections for the stage 4 and stage 5 (Figure 3.6). The 1st section, $\omega_1 = 0.36$ (R^2=0.997), was from around DP = 200 (frame 7, 14 min) to DP = 880 (frame 20, 40 min). PDI steadily reduced to a plateau around 0.065. Within 2nd section from around DP = 880 (frame 20, 40 min) to DP = 1780 (frame 43, 86 min), $\omega_2 = 0.26$ (R^2=0.995) . At this section, PDI remained nearly the same. The 3rd section which did not follow any scaling relationship was from around DP = 1780 (frame 43, 86 min) to the end of the SAXS data collection. R_{mc} and PDI continuously increased even though monomer conversion reached 99% at frame 66 (132 min).

Because the empirical monomer conversion (eq 3.4) suggested the liquid transports between medium and the spherical micelle cores, the spherical micelle size might also correlate to the tendencies of volume fractions in the spherical micelle (Figure 3.7). *xsol* gradually dropped from 0.17 down to a plateau around 0.07 at the first 30 min, and then almost remained on the same level till the end of the SAXS data collection. *xmon* constantly increase within the 40 min, and then gradually decreased to 0. This SAXS modelling results of *xmon* was different from the experimental measurements and estimations of *xmon* in previous research[27]. As the discussions in the renormalization of the kinetics of this PISA process via RAFT synthesis by NMR, the discussion of the SAXS modelling and the following analysis with mass balance might be required to be consistent within itself rather than more comparisons with the previous SAXS modelling and the following analysis[27]. *xpol* slightly decreased from 0.6 to a valley of 0.5 at around 30 min, and finally steadily increased. Also referring to the three sections by scaling relations of R_{sm} and DP (Figure 3.6), in the 1st section, *xsol* almost only slightly continuously decreased. This tendency might be more obvious presented in Figure

3.7. Also, during the 1st section, *xmon* generally increased. This retention of monomer in the spherical micelle cores also slightly reduced the *xpol*. Although PBzMA was still the dominant composition in the spherical micelle cores, at the *xpol* valley, *xpol* was already above 0.5, and with large *xmon*, PBzMA might be relatively soluble in the spherical micelle cores. If considering that DP was still the main factor to control the spherical micelle cores,[27, 70-72] ω_1 was close to 1/3, which means that the behaviour of the spherical micelle core might be similar to a droplet. And because in the 1st section, the increase of the spherical micelle cores depended on the potential monomer supply, and the deformable spherical micelle cores, the size of the spherical micelle might be more flexible to be uniform, which reduced PDI. In the 2nd section, the *xmon* decline might indicate that the monomer in the medium cannot remain vigorous supply to the spherical micelle core, and thus, ω_2 became smaller because of the volume stretch by the reduced polymer density from the monomer density. And the monomer supply might still stabilise the PDI in this 2nd section. In the 3rd section, *xmon* was above *xsol*, which might devote no critical effect to the change of the spherical micelle cores. And because in the 2nd section, both the size and the increase of size measured scaling relations were controlled by the chemical kinetics and mass transports, which was not followed the scaling relation of $2R_{mc} \sim DP^{0.5}$ determined by the final products of $PSMA_{31}$-PBzMA nanoparticle *via* RAFT [27]. After the absence of the monomer in the spherical micelle cores, the stretched spherical micelle cores might require other mechanisms, the spherical micelle fusion and chain exchange mechanism [60-67], for the size ascent, which was also the reason why scaling relation failed at the end of stage 4 and in stage 5. Also, PDI increased from the relatively low level by monomer contribution to higher stage possibly because of the polydispersity index of the diblock copolymers.

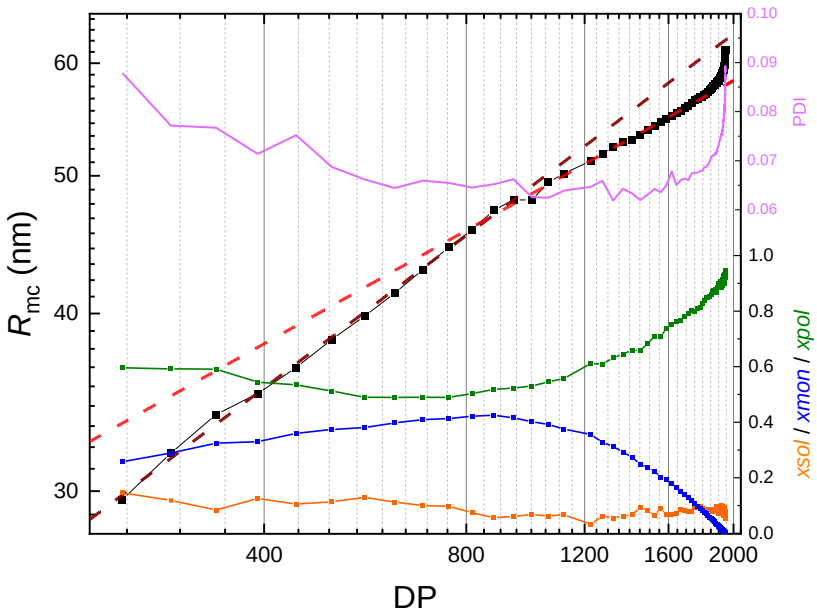

Figure 3.6. R_{mc} of PISA process via RAFT synthesis of $PSMA_{31}$–$PBzMA_{2000}$ diblock copolymer at 90 °C in mineral oil at 10% w/w solids vs. DP (black squares) curve (left) in log-log plot. PDI of R_{mc} vs. DP (pink line) curve (top left) in semi-log plot. *xmon* (blue squares), *xsol* (orange squares), and *xpol* (blue squares) vs. DP curves in semi-log plot (bottom right). Scaling relations of R_{mc} and DP (dash lines of the brown for the 1st section and the red for the 2nd section, respectively) separated the reaction in three sections.

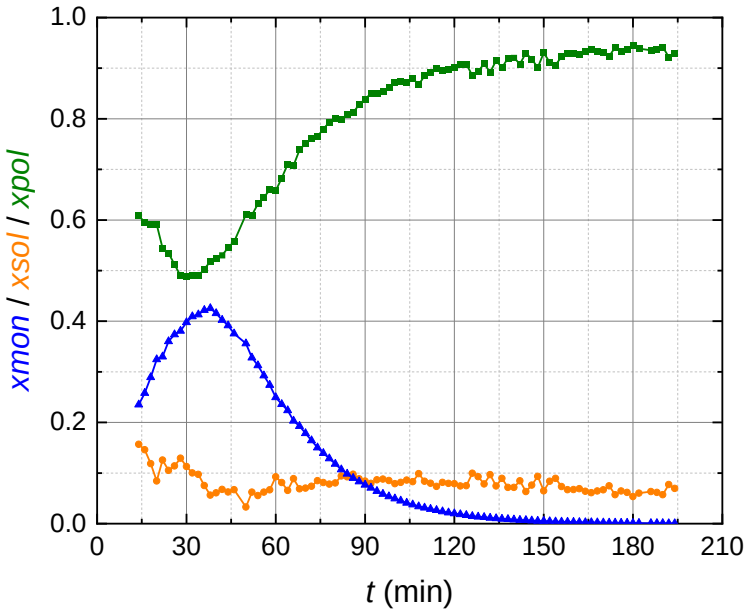

Figure 3.7. *xmon* (blue triangles), *xsol* (orange circles), and *xpol* (green squares) vs. time curves of PISA process via RAFT synthesis of $PSMA_{31}$–$PBzMA_{2000}$ diblock copolymer at 90 °C in mineral oil at 10% w/w solids vs.

For the chemical reaction, it is important to determine factors which affects the rate of polymerisation for deeper understanding of the synthesis. Also, in this PISA process via RAFT synthesis, the reaction region is in the spherical micelle cores. This synthesis condition is similar to the condition of Interval III of emulsion polymerisation. Therefore, the equation of Interval III of emulsion polymerisation (eq 2.43) could be invited here for the analysis of the rate of polymerisation of PISA process via RAFT synthesis of $PSMA_{31}$–$PBzMA_{2000}$ diblock copolymer. Because this SAXS and the following SAXS modelling have given the monomer conversion and *xmon*, the rate of polymerisation by eq 2.43 can be rewritten as:

$$R_{p\_BzMA}(t) = k_{p\_BzMA} \cdot \frac{\rho_{BzMA}}{M_{PBzMA}} \cdot f_{sm}{}^{2} \cdot \sqrt{\frac{k_d}{k_t} \frac{n_{T21s}}{V_{tot}} e^{-k_d \cdot t}} \cdot xmon(t) \quad , \qquad (3.6)$$

$$= k_{p\_BzMA}{}' \cdot xmon(t)$$

where n_{T21s} is the number of moles of initiator, T21s, and k_{p_BzMA}' is the reduced propagation rate coefficient for the PISA process via RAFT synthesis. According to the polymerization rate given by the SAXS modelling results, $R_{p\_exp\_BzMA}$, given by eq 2.44 as,

$$R_{p\_exp\_BzMA}\left(t_{frame(h)}\right)=\frac{conv\left(t_{frame(h+1)}\right)-conv\left(t_{frame(h)}\right)}{t_{frame(h+1)}-t_{frame(h)}}, \quad (3.7)$$

by $MIN\left\{\frac{1}{n_{frame}-6}\sqrt{\sum_{h=6}^{n_{frame}-6}\left[R_{p\_exp\_BzMA}\left(t_{frame(h)}\right)-R_{p\_BzMA}\left(t_{frame(h)}\right)\right]^2}\right\}$, this method gave a fitting result of k_{p_BzMA}'= 3.94 x 10^{-2} min^{-1} = 2.37 h^{-1} (R^2=0.998), (Figure 3.8). This result suggests that the monomer concentration in the copolymer micelles (*xmon*) is highly likely to be the dominant factor for this PISA synthesis predicted by the basic RAFT mechanism. This analysis also demonstrates that time-resolved SAXS could be a powerful method for *in situ* characterisation of PISA via RAFT synthesis as it provides direct measurements of the reaction kinetics. In addition, the established linear relationship could be used to simplify SAXS analysis of products produced by other PISA systems.

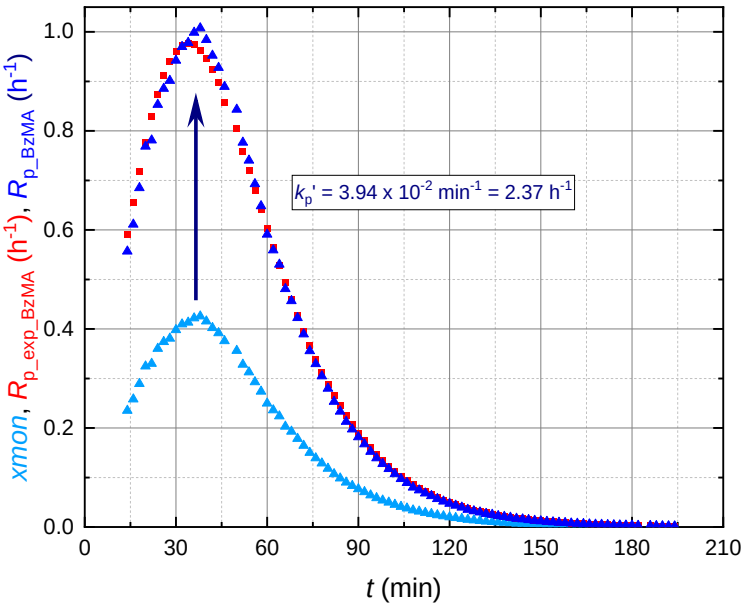

Figure 3.8**.** Time-dependence of *xmon* and $R_{p\_exp\_BzMA}$ obtained from SAXS modelling results (light blue triangles and red squares, respectively). The *xmon* curve matches the $R_{p\_exp\_BzMA}$ curve if multiplied by k_{p_BzMA}' calculated using Euclidean distance method for $R_{p\_exp\_BzMA}$ (eq 3.7) and R_{p_BzMA} (eq 3.6) (dark blue triangles). For the sake of clarity, h^{-1} unit was used for $R_{p\_exp\_BzMA}$ and R_{p_BzMA}.

The analysis of the rate of polymerisation indicated that *xmon* was the critical parameter for the chemical kinetics of PISA process via RAFT synthesis of $PSMA_{31}$–$PBzMA_{2000}$. While BzMA monomer was consumed in the PBzMA spherical micelle core, the volume fraction of BzMA

monomer in the spherical micelle core was increased during the period of the reaction from 14 to 194 min. Therefore, while BzMA was consumed, it required sources to supply BzMA monomers from the medium into the spherical micelle cores. Because the BzMA monomers were dissolved in the mineral oil, the transportation of BzMA monomer from the medium into the spherical micelle cores might be considered as the diffusion process. And such transportation of BzMA monomer could be named as monomer supply. Also, *xmon* was over 0.2 which was even higher the initial monomer volume fraction. Therefore, extra driving forces might be required to interpret such monomer supply. One of the possible reasons could be the chemical potential difference of BzMA monomer between the medium and the PBzMA spherical micelle cores. Therefore, to describe the monomer supply during this PISA process via RAFT synthesis, eq 2.57 with chemical potential effect can be used. The diffusion coefficient of BzMA at reaction temperature of 90 °C is $D_{\text{BzMA\_90°C}}$. This estimation of this diffusion coefficient, $D_{\text{BzMA\_90°C\_est}}$, could be made using the following Stoke-Einstein equation[73], as:

$$D_{\text{BzMA\_90°C\_est}} = \frac{k_{\text{B}} \cdot T_{\text{BzMA\_90°C}}}{6\pi \cdot \eta_{\text{oil}} \cdot R_{\text{BzMA}}}, \tag{3.8}$$

where $T_{\text{BzMA\_90°C}}$ is the reaction temperature, 90 °C, η_{oil} is the viscosity of mineral oil and R_{BzMA} is the hydrodynamic radius of the BzMA molecule. Taking η_{oil} as the viscosity of dodecane[27] at 90 °C, 6.02×10^{-4} Pa·s [74], and calculating R_{BzMA} from $[(3N_{\text{A}}\cdot \text{M}_{\text{BzMA}})/(4\pi\cdot\rho_{\text{BzMA}})]^{1/3}$ to be 4.17×10^{-10} m, $D_{\text{BzMA\_90°C\_est}}$ could be estimated to be about 1.06×10^{-9} $\text{m}^2\cdot\text{s}^{-1}$. The total average travelling distance at time t as the sum of average travelling distance without chemical potential effect, $\Delta x_{\text{sol}}(t)$, and average travelling distance with chemical potential effect, $\Delta x_{\text{dri}}(t)$, $\Delta x_{\text{sol}}(t) + \Delta x_{\text{dri}}(t)$, is given as $\sqrt{\frac{3v_{\text{PBzMA}}(t)}{4\pi R_{\text{mc}}(t)}}$ (see eq 2.53), where $v_{\text{PBzMA}}(t)$ is the time-dependent total volume of PBzMA and $R_{\text{mc}}(t)$ is the time-dependent mean radius of the spherical micelle cores. The BzMA chemical potential difference between medium and spherical micelle cores, $\Delta\mu_{\text{BzMA}}$, can be described as: [75]

$$\begin{aligned}\Delta\mu_{\text{BzMA}} = {} & k_{\text{B}}T_{\text{BzMA\_90°C}}\left(\ln c_{\text{ex\_mon}} + \chi_{\text{ms}}\cdot c_{\text{ex\_mon}}\cdot c_{\text{ex\_sol}}\right) \\ & -k_{\text{B}}T_{\text{BzMA\_90°C}}\begin{bmatrix} \ln(xmon)+\left(1-\frac{1}{DP}\right)\cdot xpol \\ +\chi_{\text{pm}}\cdot xpol\cdot(1-xmon) \\ +\chi_{\text{ms}}\cdot xsol\cdot(1-xmon) \\ -\chi_{\text{sp}}\cdot xsol\cdot xpol \end{bmatrix},\end{aligned} \tag{3.9}$$

where χ_{ms}, χ_{sp}, and χ_{pm} are Flory-Huggins parameters of monomer-solvent, solvent-polymer, and polymer-monomer, respectively. The Flory-Huggins parameters can be set as a row vector $\chi(\chi_{\text{ms}}, \chi_{\text{sp}}, \chi_{\text{pm}})$. Thus, the generalized eq 2.57 derived for the SAXS modelling (Chapter 2), relating total volume change of BzMA monomer (Δv_{BzMA}), the boundary surface area between the medium and the PBzMA spherical micelle cores ($A_{\text{sur\_p\_PBzMA}}$), $\Delta\mu_{\text{BzMA}}$, $D_{\text{BzMA\_90°C}}$, Δx_{sol}, and Δx_{dri} at time $t_{\text{frame}(h)}$ can be rewritten for the particular PISA process taking place during PBzMA polymerisation as:

$$\frac{\Delta v_{\mathrm{BzMA}}\left(t_{\mathrm{frame}(h)}\right)}{A_{\mathrm{sur\_p\_PBzMA}}\left(t_{\mathrm{frame}(h)}\right)\cdot\Delta t_{\mathrm{frame}(h)}} = D_{\mathrm{BzMA\_90^{\circ}C\_est}}\cdot\left(\frac{\Delta x_{\mathrm{dri}}\left(t_{\mathrm{frame}(h)}\right)}{\Delta x_{\mathrm{dri}}\left(t_{\mathrm{frame}(h)}\right)+\Delta x_{\mathrm{sol}}\left(t_{\mathrm{frame}(h)}\right)}\cdot\frac{\Delta\mu_{\mathrm{BzMA}}\left(t_{\mathrm{frame}(h)}\right)}{k_{\mathrm{B}}\cdot N_{\mathrm{A}}\cdot T_{\mathrm{BzMA\_90^{\circ}C}}}\right)\cdot\frac{\phi_{\mathrm{BzMA}}\left(t_{\mathrm{frame}(h)}\right)}{\Delta x_{\mathrm{dri}}\left(t_{\mathrm{frame}(h)}\right)+\Delta x_{\mathrm{sol}}\left(t_{\mathrm{frame}(h)}\right)}. \quad (3.10)$$

And $A_{\mathrm{sur\_p\_PBzMA}}$ is given by eq 2.52 as:

$$A_{\mathrm{sur\_p\_PBzMA}} = \frac{3\left(V_{\mathrm{co}}+V_{\mathrm{in\_mon}}+V_{\mathrm{in\_sol}}\right)}{R_{\mathrm{mc}}}, \quad (3.11)$$

where V_{co} is the hydrophobic block total volume (eq 2.7), $V_{\mathrm{in\_sol}}$ is the total volume of solvents in the micelle cores (eq 2.10), $V_{\mathrm{in\_mon}}$ is the total volume of the internal monomer (eq 2.11). And Δx_{sol} is given by eq 2.58 as:

$$\Delta x_{\mathrm{sol}} = \sqrt{\frac{A_{\mathrm{sur\_p\_PBzMA}}}{4\pi}} - \Delta x_{\mathrm{dri}}. \quad (2.12)$$

Therefore, the remained parameters in eq 3.10 are $\Delta x_{\mathrm{dri}}(t)$, χ_{ms}, χ_{sp}, and χ_{pm}, and these 4 parameters were set as the fitted variables determined by least square fitting of $\mathrm{MIN}\left\{\frac{1}{n_{\mathrm{frame}}-6}\sqrt{\sum_{h=6}^{n_{\mathrm{frame}}-6}\left[\frac{\Delta v_{\mathrm{BzMA}}\left(t_{\mathrm{frame}(h)}\right)}{A_{\mathrm{sur\_p\_PBzMA}}\left(t_{\mathrm{frame}(h)}\right)\cdot\Delta t_{\mathrm{frame}(h)}} - D_{\mathrm{BzMA\_90^{\circ}C\_est}}\cdot\left(\frac{\Delta x_{\mathrm{dri}}\left(t_{\mathrm{frame}(h)}\right)}{\Delta x_{\mathrm{dri}}\left(t_{\mathrm{frame}(h)}\right)+\Delta x_{\mathrm{sol}}\left(t_{\mathrm{frame}(h)}\right)}\cdot\frac{\Delta\mu_{\mathrm{BzMA}}\left(t_{\mathrm{frame}(h)}\right)}{k_{\mathrm{B}}\cdot N_{\mathrm{A}}\cdot T_{\mathrm{BzMA\_90^{\circ}C}}}\right)\cdot\frac{\phi_{\mathrm{BzMA}}\left(t_{\mathrm{frame}(h)}\right)}{\Delta x_{\mathrm{dri}}\left(t_{\mathrm{frame}(h)}\right)+\Delta x_{\mathrm{sol}}\left(t_{\mathrm{frame}(h)}\right)}\right]^2}\right\}$. This gives least square fitting results from SAXS modelling as $\chi_{\mathrm{SAXS}}(\chi_{\mathrm{ms\_SAXS}}, \chi_{\mathrm{sp\_SAXS}}, \chi_{\mathrm{pm\_SAXS}})$ = (0.21, 0.35, -4.69) and $\Delta x_{\mathrm{dri}}(t) = 2.26 \times 10^{-3}$ m (R^2=0.994), (Figure 3.9). And $\Delta x_{\mathrm{dri}}(t)$ is a constant during the reaction, which indicated that the chemical potential effect occurred when BzMA monomers were close to the spherical micelle cores. This linear relationship between $\frac{\Delta v_{\mathrm{BzMA}}\left(t_{\mathrm{frame}(h)}\right)}{A_{\mathrm{sur\_p\_PBzMA}}\left(t_{\mathrm{frame}(h)}\right)\cdot\Delta t_{\mathrm{frame}(h)}}$ and $D_{\mathrm{BzMA\_90^{\circ}C\_est}}\cdot\left(\frac{\Delta x_{\mathrm{dri}}\left(t_{\mathrm{frame}(h)}\right)}{\Delta x_{\mathrm{dri}}\left(t_{\mathrm{frame}(h)}\right)+\Delta x_{\mathrm{sol}}\left(t_{\mathrm{frame}(h)}\right)}\cdot\frac{\Delta\mu_{\mathrm{BzMA}}\left(t_{\mathrm{frame}(h)}\right)}{k_{\mathrm{B}}\cdot N_{\mathrm{A}}\cdot T_{\mathrm{BzMA\_90^{\circ}C}}}\right)\cdot\frac{\phi_{\mathrm{BzMA}}\left(t_{\mathrm{frame}(h)}\right)}{\Delta x_{\mathrm{dri}}\left(t_{\mathrm{frame}(h)}\right)+\Delta x_{\mathrm{sol}}\left(t_{\mathrm{frame}(h)}\right)}$ indicated that the proposal diffusion model with chemical potential (eq 3.10) could reasonably interpret the monomer supply process. However, it would be interesting to compare the Flory-Huggins parameters obtained from SAXS analysis to Flory-Huggins parameters corresponding to the studied pairs of chemical substances. This least fitting results indicated that Flory-Huggins parameter of PBzMA-BzMA given by SAXS modelling and the least square fitting, $\chi_{\mathrm{pm\_SAXS}}$, was negative. The negative Flory-Huggins parameter might indicate relatively strong attraction between two compounds.[76-78] However, the interaction between PBzMA and BzMA might not considered as a strong attraction, and the possible interactions between PBzMA and BzMA could be represented by Hansen solubility parameters relating to dispersion force, dipolar intermolecular force, and hydrogen bond interaction. In addition, such negative Flory-Huggins parameter may indicate that the chemical potential, described by Flory-Huggins mean-field theory, which is a thermodynamic theory, may not be suitable for monomer supply. Perhaps,

more factors and more complex monomer supply kinetic model constructure are required.

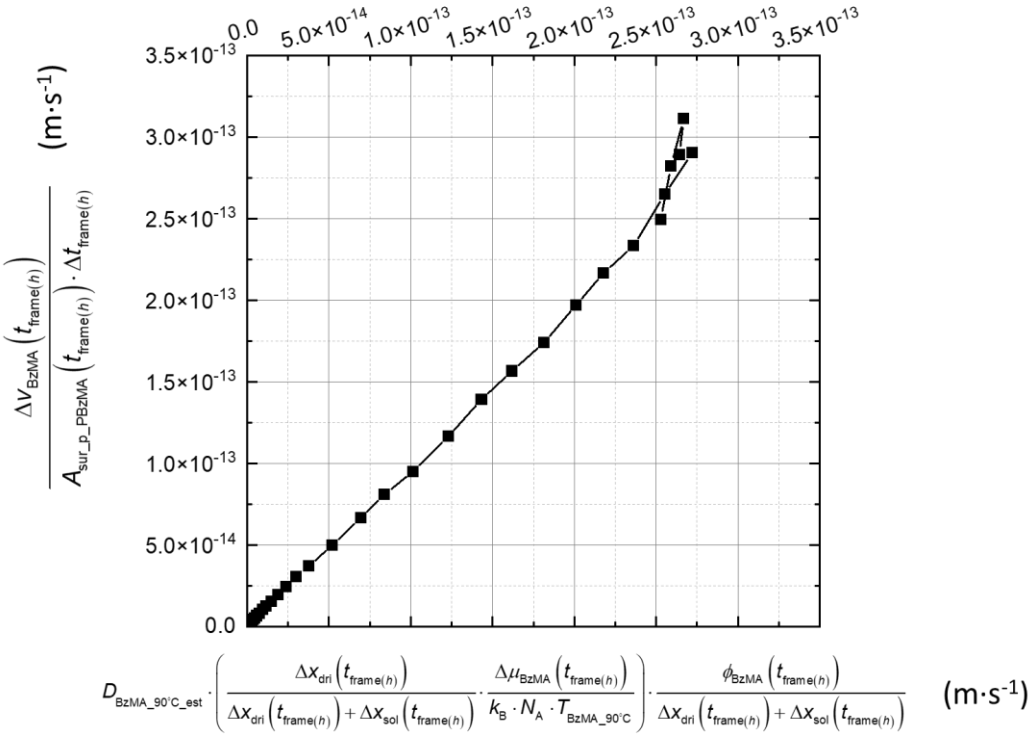

Figure 3.9**.** The diffusion model with chemical potential effect of PISA process via RAFT synthesis of $PSMA_{31}$–$PBzMA_{2000}$ diblock copolymer at 90 °C in mineral oil at 10% w/w solids (eq 3.10) after fitting.

Flory-Huggins parameters are not always available from literature but sometimes it is possible to calculate them from Hansen solubility parameters [51, 52] (eq 1.49), which are often available or could be measured [42, 43]. Hansen solubility parameters of the mineral oil were determined using commonly available solvents (Table 6.1). Using the obtained solubility scores, it was calculated that HSP of the mineral oil is [16.3, 0, 0]. The mineral oil HSP is very similar to HSP of dodecane available from literature - [16.0, 0, 0] [52]. The obtained result is consistent with the fact that main component of the studied mineral oil is dodecane.[27] It can be found from literature that HSP of PBzMA and BzMA are [17.8, 6.88, 7.64] and [16.8, 4.10, 4.10], respectively.[51, 52] Thus, using eq 1.49, Flory-Huggins parameters of BzMA-mineral oil, mineral oil-PBzMA, and PBzMA-BzMA pairs could be calculated as $\chi_{ms\_H\_Han} = 0.52$, $\chi_{sp\_H\_Han} = 0.31$, and $\chi_{pm\_H\_Han} = 0.18$. Or the set of Flory-Huggins parameter row of the studied system can be represented as $\chi_{H\_Han} = (0.52, 0.31, 0.18)$. It has to be noted that the Flory-Huggins parameters calculated from HSP show deviations from the Flory-Huggins parameters obtained from SAXS measurements. While $\chi_{sp\_H\_Han}$ is reasonably close to χ_{sp_SAXS}, $\chi_{ms\_H\_Han}$ and $\chi_{pm\_H\_Han}$ are significantly different from the Flory-Huggins parameters of BzMA-mineral oil and BzMA-PBzMA pairs determined by SAXS modelling using mass transfer model. During the PISA process, *xsol* was relatively constant, which might provide relatively similar results of Flory-Huggins parameter of mineral oil-PBzMA between SAXS modelling and HSP. The reason of the difference of Flory-Huggins parameter of BzMA-mineral oil between SAXS modelling and HSP might be that the concentration of monomer in the medium was relatively low and *xsol* was

low during the polymerisation. Therefore, the monomer supply model interpreted by eq 3.10 might not be sensitive of the interaction between BzMA and mineral oil. Thus, Flory-Huggins parameter of BzMA-mineral oil provided by SAXS modelling and mass transfer model did not match Flory-Huggins parameter of BzMA-mineral oil given by HSP. For Flory-Huggins parameter of PBzMA-BzMA, HSP could not indicate a negative result, and thus, Flory-Huggins parameter of PBzMA-BzMA given by HSP was certainly different from Flory-Huggins parameter of PBzMA-BzMA provided by SAXS modelling and mass transfer model. The Flory-Huggins parameter of PBzMA-BzMA given by HSP is relatively reasonable, because BzMA is the repeat unit of PBzMA. This means that the potential strong attraction was hardly found between BzMA and PBzMA. However, *xmon* was higher than the BzMA monomer concentration in the medium. This indicated that BzMA was attracted by the spherical micelle core. Therefore, the phenomenon of BzMA attraction from the mineral oil transported into the spherical micelle cores was reflected in Flory-Huggins parameter of PBzMA-BzMA provided by SAXS modelling and mass transfer model. This might force Flory-Huggins parameter of PBzMA-BzMA provided by SAXS modelling and mass transfer model to be negative.

Table 3.1 Solubility of mineral oil in commonly used solvents. Good solvents are marked by "1" and poor solvents are marked by "0". The obtained results were used to calculate Hansen solubility parameters according to HSPiP software [51, 52].

SOLVENTS	SOLUBILITY
Acetone	1
Acetonitrile	0
BzMA	1
Chloroform	0
Diethyl Ether	0
Dimethyl Sulfoxide (DMSO)	0
1,4-Dioxane	1
Ethanol	0
Ethyl Acetate	1
Hexane	0
Methyl Methacrylate	1
N,N-Dimethyl Formamide (DMF)	1
2-Propanol	0
Styrene	1
Tetrahydrofuran (THF)	1
Toluene	1

Regarding to the R_{mc} and volume fractions of each compound (*xmon*, *xsol*, and *xpol*), the generalised parameters, average aggregation number of the spherical micelle (N_{agg}), the average number of copolymer chains per unit surface area (S_{agg}), and the average core–shell interface (d_{int}), can be used for the further insight of properties of the spherical micelle (Figure 3.10). During the 1st section with $R_{mc} \sim DP^{0.36}$, N_{agg} is nearly proportional to *xpol*, and with the decrease of *xpol*, N_{agg} also decreased. This decrease of N_{agg} indicated the increase of the number of spherical micelles. Therefore, with a large amount of monomer transporting into the spherical micelle cores during the 1st section, it might release diblock copolymers within the spherical micelle cores, and these diblock copolymers fast formed spherical micelles

because SAXS modelling cannot detect any soluble diblock copolymers. After the 2nd section, N_{agg} continuously increased, and in the section, *xpol* ~ $DP^{1.21}$. This indicated that N_{agg} is nearly proportional to DP. This meant that during the 2nd section, the change of N_{agg} depended on the rate of polymerisation. N_{agg} continuously increased after the 2nd section and even increased obviously after the completion of the polymerisation. This possible spherical micelle fusion and chain exchange mechanism discussed above has also been revealed by N_{agg}. S_{agg} and d_{int} provided the packing density of the solvophilic $PSMA_{31}$ chains on the spherical micelle surfaces. During the 2nd section, fast drop of S_{agg} and fast increase of d_{int} indicated that when a large amount of monomer transported into the spherical micelle cores, the number of the solvophilic $PSMA_{31}$ chains requested to stabilise the spherical micelle cores might be reduced. After the 2nd section, PBzMA was gradually dominant the spherical micelle cores, which might require relatively dense packing density of $PSMA_{31}$ chains, which the decrease of d_{int} was observed.

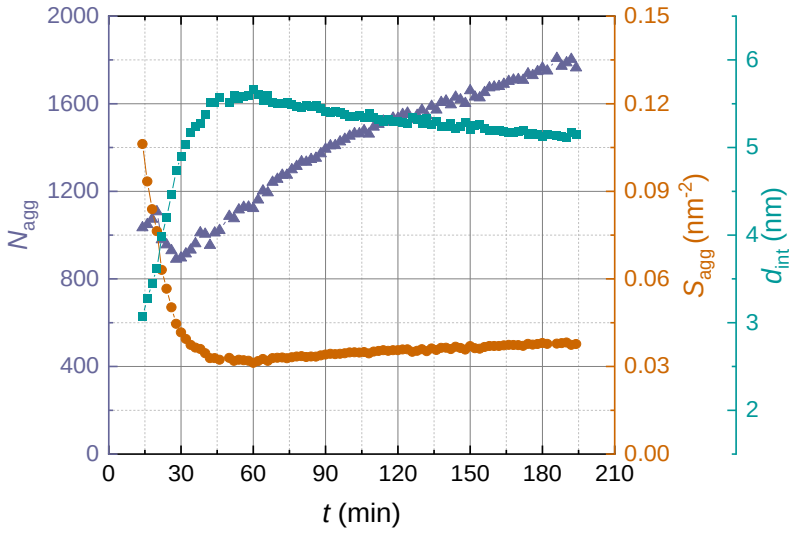

Figure 3.10. N_{agg} (triangles), S_{agg} (circles), and d_{int} (squares) vs. *t* curves, respectively, reveal the circumstances of the spherical micelle cores of PISA process via RAFT synthesis of $PSMA_{31}$–$PBzMA_{2000}$ diblock copolymer at 90 °C in mineral oil at 10% w/w solids.

3.6 Conclusion

The SAXS model counting mass balance of components in a developing system has been successfully applied for analysing chemical reaction kinetics during the PISA process via RAFT synthesis of $PSMA_{31}$–$PBzMA_{2000}$ diblock copolymer at 90 °C in mineral oil at 10% w/w solids. It was found that the model fit well to time-resolved scattering patterns recorded during the PISA process after a point when all copolymer molecules assemble into particles. The SAXS analysis using structural spherical micelle model incorporating the reaction component mass

balance approach has shown that the first 14 minutes of the SAXS measurements, corresponding to the beginning of the reaction, could not be satisfactorily described by the developed model. This finding together with the fact that no SAXS patterns corresponding to a pure stage of molecularly dissolved copolymers (stage 2) during the PISA via RAFT synthesis were observed suggests that other processes, uncounted by the SAXS model, take place in the system. The SAXS modelling provided an opportunity to measure modelling variables, including BzMA monomer conversion, the radius and its polydispersity of spherical micelle core, the radius of gyration of PSMA solvophilic block, the volume fractions of BzMA monomer, mineral oil, and PBzMA in the spherical micelle core. With mass balance modification of the SAXS model, BzMA monomer conversion and the volume fractions of the compounds in the spherical micelle core now are available. And the volume fractions of the compounds in the spherical micelle core might be only measured *in situ* by SAXS for the first time. According to these measured modelling variables, spherical micelle core was increasing during the polymerisation. After polymerisation, the spherical micelle core still increased via Ostwald ripening process. With scaling relation analysis between spherical micelle core and DP, the spherical micelle core growth could be divided into three sections. The volume fraction of mineral oil in the spherical micelle core slightly reduced and remained in a low level from 14 min of the synthesis. The volume fraction of BzMA monomer, *xmon*, in the spherical micelle core increased until 40 min of the reaction and then reduced. Also, with the fitted variable *xmon*, the tendency of the spherical micelle core growth could be related to the change of *xmon*. With x-ray acceleration effect, the monomer conversion rate measured by SAXS was relatively faster than the monomer conversion rate of laboratory scale synthesis measured by NMR. To estimate more accurate, double logistic function was invited, which also indicated at least two processes controlling the PISA process via RAFT synthesis. And with BzMA monomer conversion and *xmon*, these two processes might include polymerisation and transportation of BzMA monomer from the medium to the spherical micelle core. Thus, to measure the chemical kinetics of such polymerisation by SAXS, the equation of the rate of polymerisation for RAFT synthesis presented with the factor of *xmon*. The BzMA monomer conversion with *xmon* revealed that the rate of polymerisation of such PISA process via RAFT synthesis followed classical chemical kinetic equation. And it is first time to confirm such theoretical chemical kinetics during PISA process via RAFT synthesis. Further, SAXS analysis with mass balance now is available to monitor the kinetics of polymerisation. In turn, the known chemical kinetics might be applied to SAXS modelling to reduce the fitted parameters and the difficulty of fitting. The other potential process indicated by double logistic function was monomer supply from medium to spherical micelle core. The mass transfer model in Chapter 2 was introduced to tackle such process and relatively successfully describe the monomer supply process. However, such monomer supply process described be the mass transfer model in Chapter 2 provided a row vector Flory-Huggins parameters as $\chi_{SAXS}(\chi_{ms\_SAXS}, \chi_{sp\_SAXS}, \chi_{pm\_SAXS})$ = (0.21, 0.35, -4.69). Compared with row vector Flory-Huggins parameters given by Hansen solubility parameter as $\chi_{H\_Han}(\chi_{ms\_Han}, \chi_{sp\_Han}, \chi_{pm\_Han})$ = (0.52, 0.31, 0.18), χ_{sp_SAXS} and χ_{sp_Han} were relatively mateched, but χ_{ms} and χ_{pm} given by SAXS and HSP were not closed. And the negative χ_{pm_SAXS} indicated a strong attraction of the monomer transportation from medium in spherical micelle core. By SAXS analysis of N_{agg}, S_{agg}, and d_{int}, these three parameters confirmed that the size of spherical micelle core depended on DP and the radius of gyration of PSMA. Therefore, this SAXS modelling and analysis with mass balance was available to interpret the PISA process via RAFT in non-polar system. However, a numerous of experimental parameters were required the measurements of scattering backgrounds of different monomer concentrations in medium, the densities of compounds at reaction temperature. Also, the number of the fitted parameters were not relatively large, and therefore, it required relatively long computing time for the fitting process via Igor Pro. Therefore, with confirmed well-known chemical kinetics, SAXS model might be further improved for deeper analysis.

3.7 References

1. Blanazs, A.; Armes, S. P.; Ryan, A. J., Self-Assembled Block Copolymer Aggregates: From Micelles to Vesicles and their Biological Applications. *Macromolecular Rapid Communications* **2009,** *30* (4‐5), 267-277.
2. Tanner, P.; Baumann, P.; Enea, R.; Onaca, O.; Palivan, C.; Meier, W., Polymeric Vesicles: From Drug Carriers to Nanoreactors and Artificial Organelles. *Accounts of Chemical Research* **2011,** *44* (10), 1039-1049.
3. Albert, J. N. L.; Epps, T. H., Self-assembly of block copolymer thin films. *Materials Today* **2010,** *13* (6), 24-33.
4. Fasolka, M. J.; Mayes, A. M., Block Copolymer Thin Films: Physics and Applications. *Annual Review of Materials Research* **2001,** *31* (1), 323-355.
5. Darling, S. B., Directing the self-assembly of block copolymers. *Progress in Polymer Science* **2007,** *32* (10), 1152-1204.
6. Alexandridis, P., Amphiphilic copolymers and their applications. *Current Opinion in Colloid & Interface Science* **1996,** *1* (4), 490-501.
7. Smith, A. E.; Xu, X.; McCormick, C. L., Stimuli-responsive amphiphilic (co)polymers via RAFT polymerization. *Progress in Polymer Science* **2010,** *35* (1), 45-93.
8. Dai, S.; Ravi, P.; Tam, K. C., pH-Responsive polymers: synthesis, properties and applications. *Soft Matter* **2008,** *4* (3), 435-449.
9. Schacher, F. H.; Rupar, P. A.; Manners, I., Functional Block Copolymers: Nanostructured Materials with Emerging Applications. *Angewandte Chemie International Edition* **2012,** *51* (32), 7898-7921.
10. Black, C. T.; Ruiz, R.; Breyta, G.; Cheng, J. Y.; Colburn, M. E.; Guarini, K. W.; Kim, H.; Zhang, Y., Polymer self assembly in semiconductor microelectronics. *IBM Journal of Research and Development* **2007,** *51* (5), 605-633.
11. Kim, J. K.; Yang, S. Y.; Lee, Y.; Kim, Y., Functional nanomaterials based on block copolymer self-assembly. *Progress in Polymer Science* **2010,** *35* (11), 1325-1349.
12. Motornov, M.; Roiter, Y.; Tokarev, I.; Minko, S., Stimuli-responsive nanoparticles, nanogels and capsules for integrated multifunctional intelligent systems. *Progress in Polymer Science* **2010,** *35* (1), 174-211.
13. Braunecker, W. A.; Matyjaszewski, K., Controlled/living radical polymerization: Features, developments, and perspectives. *Progress in Polymer Science* **2007,** *32* (1), 93-146.
14. Chiefari, J.; Chong, Y. K.; Ercole, F.; Krstina, J.; Jeffery, J.; Le, T. P. T.; Mayadunne, R. T. A.; Meijs, G. F.; Moad, C. L.; Moad, G.; Rizzardo, E.; Thang, S. H., Living Free-Radical Polymerization by Reversible Addition−Fragmentation Chain Transfer: The RAFT Process. *Macromolecules* **1998,** *31* (16), 5559-5562.
15. Moad, G.; Rizzardo, E.; Thang, S. H., Living radical polymerization by the RAFT process–a third update. *Australian Journal of Chemistry* **2012,** *65* (8), 985-1076.
16. Canning, S. L.; Smith, G. N.; Armes, S. P., A Critical Appraisal of RAFT-Mediated Polymerization-Induced Self-Assembly. *Macromolecules* **2016,** *49* (6), 1985-2001.
17. Warren, N. J.; Armes, S. P., Polymerization-Induced Self-Assembly of Block Copolymer Nano-objects via RAFT Aqueous Dispersion Polymerization. *Journal of the American Chemical Society* **2014,** *136* (29), 10174-10185.
18. Derry, M. J.; Fielding, L. A.; Armes, S. P., Polymerization-induced self-assembly of block copolymer nanoparticles via RAFT non-aqueous dispersion polymerization. *Progress in*

Polymer Science **2016,** *52*, 1-18.
19. Zhang, Q.; Zhu, S., Ionic Liquids: Versatile Media for Preparation of Vesicles from Polymerization-Induced Self-Assembly. *ACS Macro Letters* **2015,** *4* (7), 755-758.
20. Mai, Y.; Eisenberg, A., Self-assembly of block copolymers. *Chemical Society Reviews* **2012,** *41* (18), 5969-5985.
21. Touve, M. A.; Figg, C. A.; Wright, D. B.; Park, C.; Cantlon, J.; Sumerlin, B. S.; Gianneschi, N. C., Polymerization-induced self-assembly of micelles observed by liquid cell transmission electron microscopy. *ACS central science* **2018,** *4* (5), 543-547.
22. Baalousha, M.; Stolpe, B.; Lead, J. R., Flow field-flow fractionation for the analysis and characterization of natural colloids and manufactured nanoparticles in environmental systems: A critical review. *Journal of Chromatography A* **2011,** *1218* (27), 4078-4103.
23. Schmitz, K. S., CHAPTER 1 - Introduction. In *Introduction to Dynamic Light Scattering by Macromolecules*, Schmitz, K. S., Ed. Academic Press: Oxford, 1990; pp 1-10.
24. Pound, G.; McLeary, J. B.; McKenzie, J. M.; Lange, R. F.; Klumperman, B., In-situ NMR spectroscopy for probing the efficiency of RAFT/MADIX agents. *Macromolecules* **2006,** *39* (23), 7796-7797.
25. Perrier, S.; Haddleton, D. M., In Situ NMR Monitoring of Living Radical Polymerization. In *In Situ Spectroscopy of Monomer and Polymer Synthesis*, Puskas, J. E.; Long, T. E.; Storey, R. F.; Shaikh, S.; Simmons, C. L., Eds. Springer US: Boston, MA, 2003; pp 125-146.
26. McLeary, J.; Calitz, F.; McKenzie, J.; Tonge, M.; Sanderson, R.; Klumperman, B., A 1H NMR investigation of reversible addition− fragmentation chain transfer polymerization kinetics and mechanisms. Initialization with different initiating and leaving groups. *Macromolecules* **2005,** *38* (8), 3151-3161.
27. Derry, M. J.; Fielding, L. A.; Warren, N. J.; Mable, C. J.; Smith, A. J.; Mykhaylyk, O. O.; Armes, S. P., In situ small-angle X-ray scattering studies of sterically-stabilized diblock copolymer nanoparticles formed during polymerization-induced self-assembly in non-polar media. *Chemical Science* **2016,** *7* (8), 5078-5090.
28. Jones, E.; Mykhaylyk, O.; Semsarilar, M.; Boerakker, M.; Wyman, P.; Armes, S., How do spherical diblock copolymer nanoparticles grow during RAFT alcoholic dispersion polymerization? *Macromolecules* **2015,** *49* (1), 172-181.
29. Gonzato, C.; Semsarilar, M.; Jones, E. R.; Li, F.; Krooshof, G. J. P.; Wyman, P.; Mykhaylyk, O. O.; Tuinier, R.; Armes, S. P., Rational Synthesis of Low-Polydispersity Block Copolymer Vesicles in Concentrated Solution via Polymerization-Induced Self-Assembly. *Journal of the American Chemical Society* **2014,** *136* (31), 11100-11106.
30. Warren, N. J.; Mykhaylyk, O. O.; Ryan, A. J.; Williams, M.; Doussineau, T.; Dugourd, P.; Antoine, R.; Portale, G.; Armes, S. P., Testing the Vesicular Morphology to Destruction: Birth and Death of Diblock Copolymer Vesicles Prepared via Polymerization-Induced Self-Assembly. *Journal of the American Chemical Society* **2015,** *137* (5), 1929-1937.
31. Cornel, E. J.; van Meurs, S.; Smith, T.; O'Hora, P. S.; Armes, S. P., In Situ Spectroscopic Studies of Highly Transparent Nanoparticle Dispersions Enable Assessment of Trithiocarbonate Chain-End Fidelity during RAFT Dispersion Polymerization in Nonpolar Media. *Journal of the American Chemical Society* **2018,** *140* (40), 12980-12988.
32. Warren, N. J.; Mykhaylyk, O. O.; Mahmood, D.; Ryan, A. J.; Armes, S. P., RAFT Aqueous Dispersion Polymerization Yields Poly(ethylene glycol)-Based Diblock Copolymer Nano-Objects with Predictable Single Phase Morphologies. *Journal of the American Chemical Society* **2014,** *136* (3), 1023-1033.
33. Lopez-Oliva, A. P.; Warren, N. J.; Rajkumar, A.; Mykhaylyk, O. O.; Derry, M. J.; Doncom, K. E. B.; Rymaruk, M. J.; Armes, S. P., Polydimethylsiloxane-Based Diblock Copolymer Nano-objects Prepared in Nonpolar Media via RAFT-Mediated Polymerization-Induced Self-Assembly. *Macromolecules* **2015,** *48* (11), 3547-3555.
34. Holmberg, K.; Kivikytö-Reponen, P.; Härkisaari, P.; Valtonen, K.; Erdemir, A., Global

energy consumption due to friction and wear in the mining industry. *Tribology International* **2017,** *115*, 116-139.
35. Holmberg, K.; Andersson, P.; Erdemir, A., Global energy consumption due to friction in passenger cars. *Tribology International* **2012,** *47*, 221-234.
36. Holmberg, K.; Andersson, P.; Nylund, N.-O.; Mäkelä, K.; Erdemir, A., Global energy consumption due to friction in trucks and buses. *Tribology International* **2014,** *78*, 94-114.
37. Holmberg, K.; Erdemir, A., Global impact of friction on energy consumption, economy and environment. *Fme Trans* **2015,** *43* (3), 181-5.
38. Tang, Z.; Li, S., A review of recent developments of friction modifiers for liquid lubricants (2007–present). *Current Opinion in Solid State and Materials Science* **2014,** *18* (3), 119-139.
39. Ludema, K. C.; Ajayi, L., *Friction, Wear, Lubrication: A Textbook in Tribology, Second Edition*. CRC Press: 2018.
40. Crockett, R., Boundary lubrication in natural articular joints. *Tribology Letters* **2009,** *35* (2), 77-84.
41. Wen, S.; Huang, P., *Principles of Tribology*. Wiley: 2017.
42. Wei, H.; Zhuo, R.-X.; Zhang, X.-Z., Design and development of polymeric micelles with cleavable links for intracellular drug delivery. *Progress in Polymer Science* **2013,** *38* (3), 503-535.
43. Derry, M. J.; Smith, T.; O'Hora, P. S.; Armes, S. P., Block Copolymer Nanoparticles Prepared via Polymerization-Induced Self-Assembly Provide Excellent Boundary Lubrication Performance for Next-Generation Ultralow-Viscosity Automotive Engine Oils. *ACS Applied Materials & Interfaces* **2019,** *11* (36), 33364-33369.
44. Growney, D. J.; Mykhaylyk, O. O.; Armes, S. P., Micellization and Adsorption Behavior of a Near-Monodisperse Polystyrene-Based Diblock Copolymer in Nonpolar Media. *Langmuir* **2014,** *30* (21), 6047-6056.
45. Growney, D. J.; Mykhaylyk, O. O.; Middlemiss, L.; Fielding, L. A.; Derry, M. J.; Aragrag, N.; Lamb, G. D.; Armes, S. P., Is Carbon Black a Suitable Model Colloidal Substrate for Diesel Soot? *Langmuir* **2015,** *31* (38), 10358-10369.
46. Fitzgerald, D., Technical Assessment of the Anton Paar DMA5000 density meter. *H&D Fitzgerald Ltd* **2000**.
47. Smith, A.; Alcock, S.; Davidson, L.; Emmins, J.; Hiller Bardsley, J.; Holloway, P.; Malfois, M.; Marshall, A.; Pizzey, C.; Rogers, S., I22: SAXS/WAXS beamline at Diamond Light Source–an overview of 10 years operation. *Journal of synchrotron radiation* **2021,** *28* (3).
48. Basham, M.; Filik, J.; Wharmby, M. T.; Chang, P. C.; El Kassaby, B.; Gerring, M.; Aishima, J.; Levik, K.; Pulford, B. C.; Sikharulidze, I., Data analysis workbench (DAWN). *Journal of synchrotron radiation* **2015,** *22* (3), 853-858.
49. Lindvig, T.; Michelsen, M. L.; Kontogeorgis, G. M., A Flory–Huggins model based on the Hansen solubility parameters. *Fluid Phase Equilibria* **2002,** *203* (1-2), 247-260.
50. Bongiardina, N. J.; Sinha, J.; Bowman, C. N., Flory–Huggins Parameters for Thiol-ene Networks Using Hansen Solubility Parameters. *Macromolecules* **2021,** *54* (24), 11439-11448.
51. Abbott, S.; Hansen, C. M., *Hansen solubility parameters in practice*. Hansen-Solubility: 2008.
52. Hansen, C. M., *Hansen solubility parameters: a user's handbook*. CRC press: 2007.
53. Mark, J. E., *Physical Properties of Polymers Handbook*. Springer New York: 2007.
54. Fielding, L. A.; Lane, J. A.; Derry, M. J.; Mykhaylyk, O. O.; Armes, S. P., Thermo-responsive Diblock Copolymer Worm Gels in Non-polar Solvents. *Journal of the American Chemical Society* **2014,** *136* (15), 5790-5798.
55. Ilavsky, J.; Jemian, P. R., Irena: tool suite for modeling and analysis of small-angle scattering. *Journal of Applied Crystallography* **2009,** *42* (2), 347-353.
56. Flory, P. J., *Principles of Polymer Chemistry*. Cornell University Press: ITHACA, New York,

1953.
57. Fetters, L.; Lohse, D.; Colby, R., Chain dimensions and entanglement spacings. In *Physical properties of polymers handbook*, Springer: 2007; pp 447-454.
58. Brotherton, E. E.; Hatton, F. L.; Cockram, A. A.; Derry, M. J.; Czajka, A.; Cornel, E. J.; Topham, P. D.; Mykhaylyk, O. O.; Armes, S. P., In Situ Small-Angle X-ray Scattering Studies During Reversible Addition–Fragmentation Chain Transfer Aqueous Emulsion Polymerization. *Journal of the American Chemical Society* **2019,** *141* (34), 13664-13675.
59. Winnik, M.; Lukas, R.; Chen, W.; Furlong, P. In *Studies of the dispersion polymerisation of methyl methacrylate in nonaqueous media*, Makromolekulare Chemie. Macromolecular Symposia, Wiley Online Library: 1987; pp 483-501.
60. Doi, M.; Edwards, S. F., *The theory of polymer dynamics*. oxford university press: 1988; Vol. 73.
61. Choi, S.-H.; Bates, F. S.; Lodge, T. P., Molecular Exchange in Ordered Diblock Copolymer Micelles. *Macromolecules* **2011,** *44* (9), 3594-3604.
62. Choi, S.-H.; Lodge, T. P.; Bates, F. S., Mechanism of molecular exchange in diblock copolymer micelles: hypersensitivity to core chain length. *Physical review letters* **2010,** *104* (4), 047802.
63. Lund, R.; Willner, L.; Monkenbusch, M.; Panine, P.; Narayanan, T.; Colmenero, J.; Richter, D., Structural Observation and Kinetic Pathway in the Formation of Polymeric Micelles. *Physical Review Letters* **2009,** *102* (18), 188301.
64. Halperin, A.; Alexander, S., Polymeric micelles: their relaxation kinetics. *Macromolecules* **1989,** *22* (5), 2403-2412.
65. Lund, R.; Willner, L.; Richter, D.; Dormidontova, E. E., Equilibrium chain exchange kinetics of diblock copolymer micelles: Tuning and logarithmic relaxation. *Macromolecules* **2006,** *39* (13), 4566-4575.
66. Lund, R.; Willner, L.; Stellbrink, J.; Lindner, P.; Richter, D., Logarithmic chain-exchange kinetics of diblock copolymer micelles. *Physical review letters* **2006,** *96* (6), 068302.
67. Nicolai, T.; Colombani, O.; Chassenieux, C., Dynamic polymeric micelles versus frozen nanoparticles formed by block copolymers. *Soft Matter* **2010,** *6* (14), 3111-3118.
68. Lebouille, J. G. J. L.; Vleugels, L. F. W.; Dias, A. A.; Leermakers, F. A. M.; Cohen Stuart, M. A.; Tuinier, R., Controlled block copolymer micelle formation for encapsulation of hydrophobic ingredients. *The European Physical Journal E* **2013,** *36* (9), 107.
69. Baldan, A., Review Progress in Ostwald ripening theories and their applications to nickel-base superalloys Part I: Ostwald ripening theories. *Journal of Materials Science* **2002,** *37* (11), 2171-2202.
70. Jones, E. R.; Semsarilar, M.; Wyman, P.; Boerakker, M.; Armes, S. P., Addition of water to an alcoholic RAFT PISA formulation leads to faster kinetics but limits the evolution of copolymer morphology. *Polymer Chemistry* **2016,** *7* (4), 851-859.
71. Förster, S.; Zisenis, M.; Wenz, E.; Antonietti, M., Micellization of strongly segregated block copolymers. *The Journal of Chemical Physics* **1996,** *104* (24), 9956-9970.
72. Bates, F. S.; Fredrickson, G. H., Block Copolymer Thermodynamics: Theory and Experiment. *Annual Review of Physical Chemistry* **1990,** *41* (1), 525-557.
73. Crank, J., *The mathematics of diffusion*. Oxford university press: Oxford, 1979.
74. Feng, S.; Liu, Z.; Bi, Q.; Pan, H., Viscosity Measurements of n-Dodecane at Temperatures between 303 K and 693 K and Pressures up to 10 MPa. *Journal of Chemical & Engineering Data* **2018,** *63* (3), 671-678.
75. Favre, E.; Nguyen, Q. T.; Clement, R.; Neel, J., Application of Flory-Huggins theory to ternary polymer-solvents equilibria: A case study. *European Polymer Journal* **1996,** *32* (3), 303-309.
76. Zhao, Y.; Inbar, P.; Chokshi, H. P.; Malick, A. W.; Choi, D. S., Prediction of the Thermal Phase Diagram of Amorphous Solid Dispersions by Flory–Huggins Theory. *Journal of*

Pharmaceutical Sciences **2011,** *100* (8), 3196-3207.
77. Thakral, S.; Thakral, N. K., Prediction of Drug–Polymer Miscibility through the use of Solubility Parameter based Flory–Huggins Interaction Parameter and the Experimental Validation: PEG as Model Polymer. *Journal of Pharmaceutical Sciences* **2013,** *102* (7), 2254-2263.
78. McMaster, L. P., Aspects of Polymer-Polymer Thermodynamics. *Macromolecules* **1973,** *6* (5), 760-773.

Chapter 4: *In Situ* Small-angle X-ray Scattering Studies of Early Stages of Polymerization-induced Self-assembly of Block Copolymers in Nonpolar Media

Chapter 4

In Situ Small-angle X-ray Scattering Studies of Early Stages of Polymerization-induced Self-assembly of Block Copolymers in Nonpolar Media

4.1 Introduction

In Chapter 3, SAXS models, counting mass balance of chemical reaction components, described in Chapter 2 have been applied to PISA via RAFT synthesis of poly(stearyl methacrylate)-poly(benzyl methacrylate) ($PSMA_{31}$-$PBzMA_{2000}$) diblock copolymer at 90 °C in mineral oil at 10% w/w solids. It has been found that the SAXS modelling, based preferably on spherical copolymer micelle structure, were not successful for describing scattering patterns of initial stages of synthesis/experiment corresponding to the first 12 minutes. According to scenario of traditional PISA process via RAFT synthesis described in Chapter 2 (Figure 2.1), soluble diblock copolymer chains should be present in the system before the synthesized diblock copolymer chains increasing in length formed spherical micelles. However, no satisfactory fits to the initial scattering patterns corresponding to the first 12 minutes of the experiment were obtained using a SAXS model for soluble diblock copolymer chains (eq 2.19) with or without a population of spherical micelles (eq 2.24). Consequently, extra SAXS analysis and modelling would be required for this initial period of PISA process. Herein, starting from pair-distance distribution function (PDDF) analysis of the SAXS patterns corresponding to the initial products of PISA via RAFT synthesis of $PSMA_{31}$-$PBzMA_{2000}$, SAXS models will be proposed for analysing structural morphologies of the products formed during first few minutes of the synthesis. Eventually, the SAXS modelling results obtained for the initial stage of chemical reaction will be combined with the SAXS results obtained in Chapter 3 for the remaining period of the PISA via RAFT synthesis of $PSMA_{31}$–$PBzMA_{2000}$ diblock copolymers mainly corresponding to the self-assembled copolymer micelle growth.

4.2 PDDF Analysis of SAXS Patterns of PISA via RAFT Synthesis of $PSMA_{31}$–$PBzMA_{2000}$ Block Copolymer Diblock Copolymer

According to the SAXS analysis of PISA via RAFT synthesis of $PSMA_{31}$-$PBzMA_{2000}$, SAXS model based on the traditional PISA process cannot satisfactory describe SAXS patterns of this PISA process within the first 14 min (Figures 3.2) in Chapter 3. Therefore, extra SAXS modelling and analysis are required for the first six frames of this PISA process (Figure 4.1). Close inspection of the SAXS data reveals that the first recorded SAXS pattern contains the first minimum of the particle form factor function, which is located at a slightly lower q value than that for the second pattern (0.020 $Å^{-1}$ *versus* 0.023 $Å^{-1}$, respectively) (Figure 4.1). This suggests that the initial nascent particles formed within the first 2 min are actually larger than those observed at a later stage. In addition, the scattering intensity for the second and third patterns has a non-zero gradient in the Guinier region (0.0035 $Å^{-1} < q < 0.015$ $Å^{-1}$)

(Figure 4.1). In principle of only considering monodisperse spherical particle as the main population in the system, this suggests the formation of weakly anisotropic nascent particles. This hypothesis is supported by analysis using a PDDF, indicating the possible presence of particle dimers (Figure 4.2, pattern corresponding to frame 2 in Figure 4.1). It is conceivable that the initial micelles might immediately become elongated (or undergo fission to form two smaller micelles)[1] before regaining their sphericity at a later stage (Figure 4.2, pattern corresponding to frame 7 in Figure 4.1). However, micelle fusion cannot be ignorable, but here, there was no clear evidence for possible fission or fusion[1] during the early stage of PISA via RAFT synthesis of $PSMA_{31}$-$PBzMA_{2000}$. At 2 min of the reaction, the formations of $PSMA_{31}$-$PBzMA_{2000}$ were highly in spherical shapes. Surprisingly, at 4 min of the reaction, the formations are more complicated. The peak maximum of the PDDF (Figure 4.2) was at 200 Å and a pronounced shoulder of this PDDF was at around 400 Å with the PDDF closed to be 0 at around 800 Å. Also, this PDDF indicated that the particles at 4 min should not be considered as simply core-shell structure[2]. And these three sequential numbers possibly indicated that the formations might be included spherical micelle dimers[3]. After 4 min, the shoulders of PDDF gradually disappeared, and at 14 min, the formation of $PSMA_{31}$-$PBzMA_{2000}$ was detected as spherical micelle only. Thus, these PDDF within 14 min of PISA process via RAFT synthesis of $PSMA_{31}$-$PBzMA_{2000}$ indicated an extra morphological transition from some undefined particles to spherical micelles. Therefore, this morphological transition is required extra SAXS analysis and SAXS modelling to clarify the observed particle morphology transformations.

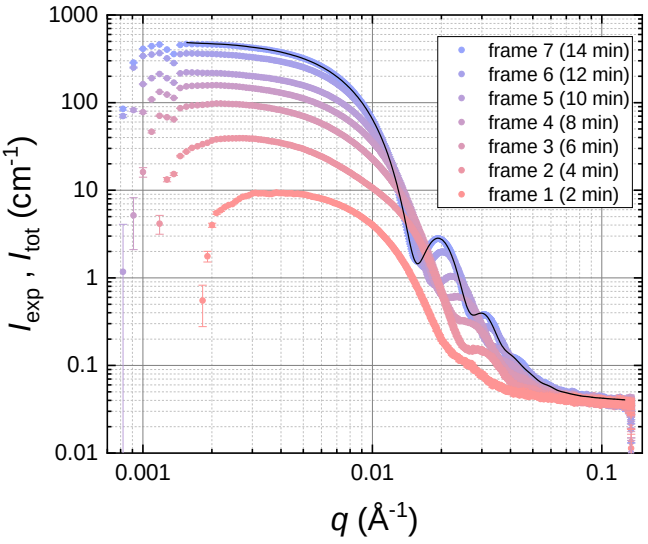

Figure 4.1**.** Experimental SAXS patterns (circles), recorded every 2 min from frame 1 (2 min) to frame 7 (14 min) during PISA process via RAFT synthesis of $PSMA_{31}$–$PBzMA_{2000}$ diblock copolymer spheres at 90 °C in mineral oil, with respective fitting curves (solid lines) produced by SAXS model according to the transitional PISA process described in Chapter 2.

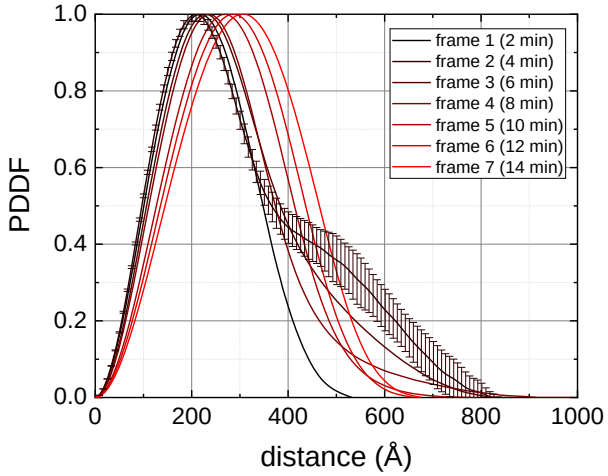

Figure 4.2**.** Normalized pair-distance distribution functions (PDDFs) obtained from experimental SAXS patterns with representative error bars are shown for PDDFs associated with frame 2.

4.3 Possible Morphologies and Morphological Transitions of Particles at the Initial stage of PISA Process via RAFT Synthesis of $PSMA_{31}$–$PBzMA_{2000}$ Copolymer in Mineral Oil

Based on PDDF analysis of PISA process via RAFT synthesis of $PSMA_{31}$-PBzMA, the early stage of this PISA process can be deliberately separated by the relatively unique formation at 2 min and the morphological transition during 4 – 14 min. However, this separation does not indicate the utter independence of the formations between 2 min and the time region of 4 – 14 min but reveals an opportunity to construct the morphological transition models based on the formations at 2 min. Also, the analysis of the early stage of PISA process via RAFT synthesis of $PSMA_{31}$-$PBzMA_{2000}$ should be performed forward from the first frame at 2 min rather than backward from the 7th frame as it has been done for the rest of the particle synthesis based on a unimodal population of spherical micelles (Chapter 3, eq 2.24). Thus, the first frame of SAXS patterns is used to construct the initial particle morphology.

According to PDDF of the first frame, the morphology formed by $PSMA_{31}$-PBzMA was likely to be of a spherical shape, and therefore, a spherical particle (or micelle) should be one of the options considered for the initial particle formation. Also, at stages 1 and 2 (Figure 2.1), instead of observing soluble $PSMA_{31}$ chains in traditional PISA process, BzMA monomers with solvent molecules might form emulsions in the medium required $PSMA_{31}$ chains to stabilise the BzMA suspensions, which could be observed as the spherical particles in the medium. Thus, at least two structural options for the particles formed at the initial stage could be considered. For the spherical micelle morphology, a SAXS model has already been developed (Chapter 2, equations 2.1 – 2.37). For the suspension particles stabilized by $PSMA_{31}$ chains, at least two possible SAXS models could be proposed. For the first model, the synthesised PBzMA block can be described as independent Gaussian chains within the cores of suspension particles stabilised by PSMA block on such particle core surfaces which are full of BzMA monomers and

solvent molecules. For the second model, such suspension particles stabilised by PSMA block on such particle core surfaces can be described by core-shell model with the core formed by BzMA monomer and solvent molecules and the shell formed by a mixture of PBzMA blocks, BzMA monomer and solvent molecules (Figure 4.3).

After the formation of spherical particles during first 2 min of the chemical reaction, a particle morphological transition might take place between 4 min and 14 min. Since this morphological transition was now only observed by SAXS, it might require further microscopy studies, for instance, cryogenic transmission electron microscopy (cryo-TEM)[4, 5]. Even though PDDF analysis suggests the possible dimer structure in the medium, there are no direct structural methods which could determine the particle morphology during this period. Therefore, a number of structural models for the particle morphologies formed at the initial stage of the studied synthesis, including the dimer structure suggested by PDDF analysis (Figure 4.2), should be examined. PDDF should not be considered as the best robust method to determine the particle morphologies if the system is highly polydisperse and/or contain a few populations of different particles. Thus, the dimer formation should be assumed only as one of the opinions to describe this morphological transition. Another option (or other options) could be a system composed of a few populations of particles. Consequently, two-population systems of spherical shape particles were analysed.

It has to be noted that the formation of initial particles at 2 min of the reaction and then the morphological transition during the period of 4 – 14 min could require a number of combinations of the possibilities of different particle formations with different morphological transitions. In order to simplify the task, SAXS modelling and analysis of the early stage of PISA process via RAFT synthesis of $PSMA_{31}$-$PBzMA_{2000}$ was performed using structural models developed for the first SAXS frame corresponding to 2 min of the $PSMA_{31}$-PBzMA synthesis.

4.4 Structural Models for SAXS Analysis of Particle Morphologies Formed at the Initial Stage of PISA Process via RAFT Synthesis of $PSMA_{31}$–$PBzMA_{2000}$ in Mineral Oil

According to the proposed descriptions of the particles formed during the initial stage of PISA process via RAFT synthesis of $PSMA_{31}$-$PBzMA_{2000}$ (the first 2 min of reaction), three SAXS models should be considered. In particular, a spherical micelle model (eq 2.24), a suspension particle with Gaussian PBzMA block chain model and a suspension particle with core-shell structure model (Figure 4.3). For the latter two proposed models, BzMA monomer and solvent molecules are assumed to be mixed together.

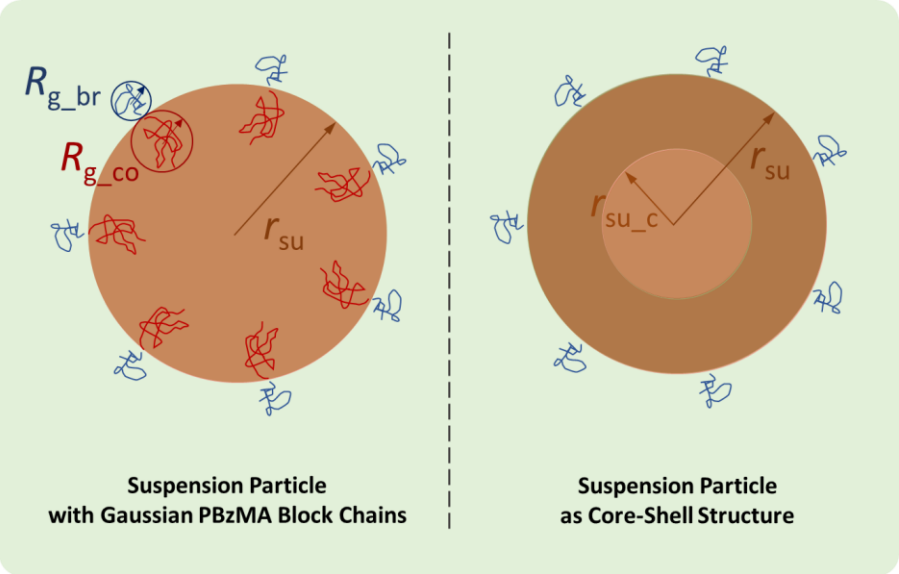

Figure 4.3. Schematic Presentation of two possible suspension particle morphologies. The suspension particle with Gaussian block chains (left) is described as a spherical particle of the r_{su} radius with the radii of gyration of the PBzMA block, R_{g_co}, and the radii of gyration of the brush (stabiliser) PSMA block, R_{g_br}. The suspension particle as core-shell structure (right) is described as a spherical particle of core radius of the suspension particle as r_{su_c} and the radius of the suspension particle as r_{su} with the radii of gyration of the PSMA, R_{g_br}.

Suspension Particle with Gaussian PBzMA Block Chain Model

Based on the description of the suspension particle with Gaussian PBzMA block chains (Figure 4.3, left), the scattering intensity can be given as:

$$I_{su\_GC}(q) = \phi_{su\_GC} \frac{\int_0^\infty \Psi_{su}(r_{su}) \left(F_{su\_GC}(q, r_{su}) + \int_0^\infty \Psi_{su}(r_{su}') A_{su\_GC}(q, r_{su}) A_{su\_GC}(q, r_{su}') \left[S(q, r_{su}, r_{su}') - 1 \right] dr_{su}' \right) dr_{su}}{\int_0^\infty \Psi_{su}(r_{su}) V_{su}(r_{su}) dr_{su}}, \quad (4.1)$$

where ϕ_{su_GC} is the volume fraction of suspension particle with Gaussian PBzMA block chains, r_{su} is the suspension particle core radius. It is assumed for the analysis that the distribution function of the particle radius, Ψ_{su}, follows the Gaussian distribution:

$$\Psi(r_{su}) = \frac{\exp\left[-\frac{1}{2} \left(\frac{r_{su} - R_{su}}{\sigma_{R_{su}}} \right)^2 \right]}{\sqrt{2\pi}\sigma_{R_{su}}}, \quad (4.2)$$

And the Gaussian distribution can be represented as:

$$r \sim N(R, \sigma). \quad (4.3)$$

where R is the mean radius of particles and σ is its standard deviation. Therefore, such

Gaussian distribution Ψ_{su}, can be written as $r_{su} \sim N\left(R_{su}, \sigma_{R_{su}}\right)$. $S\left(q, r_{su}, r_{su}^{'}\right)$ is the hard sphere structure factor solved by the Percus-Yevick closure relation.[6] Since the volume concertation of the scattering objects was low at this stage of the synthesis, the structure factors were assumed to be unity. The form factor of the suspension particle with Gaussian PBzMA block chains in eq 4.1 is defined as:

$$
\begin{aligned}
F_{su\_GC}\left(q, r_{su}\right) = {} & \beta_{su}^2 A_{su\_c\_GC}^2\left(q, r_{su}\right) V_s^2\left(r_{su}\right) \\
& + n_{agg\_su\_GC}\beta_{br}^2 F_{br}\left(q, R_{g\_br}\right) + n_{agg\_su\_GC}\left(n_{agg\_su\_GC}-1\right)\beta_{br}^2\left[A_{br}\left(q, R_{g\_br}\right)\frac{\sin q\left(r_{su}+R_{g\_br}\right)}{q\left(r_{su}+R_{g\_br}\right)}\right]^2 \\
& + n_{agg\_su\_GC}\beta_{co}^2 F_{co}\left(q, R_{g\_co}\right) + n_{agg\_su\_GC}\left(n_{agg\_su\_GC}-1\right)\beta_{co}^2\left[A_{co}\left(q, R_{g\_co}\right)\frac{\sin q\left(r_{su}-R_{g\_co}\right)}{q\left(r_{su}-R_{g\_co}\right)}\right]^2, \\
& + 2n_{agg\_su\_GC}\beta_{su}\beta_{br}A_{su\_c\_GC}\left(q, r_{su}\right)A_{br}\left(q, R_{g\_br}\right)\frac{\sin q\left(r_{su}+R_{g\_br}\right)}{q\left(r_{su}+R_{g\_br}\right)} \\
& + 2n_{agg\_su\_GC}\beta_{su}\beta_{co}A_{su\_c\_GC}\left(q, r_{su}\right)A_{co}\left(q, R_{g\_co}\right)\frac{\sin q\left(r_{su}-R_{g\_co}\right)}{q\left(r_{su}-R_{g\_co}\right)} \\
& + 2n_{agg\_su\_GC}^2\beta_{br}\beta_{co}A_{br}\left(q, R_{g\_br}\right)A_{co}\left(q, R_{g\_co}\right)\frac{\sin q\left(r_{su}+R_{g\_br}\right)}{q\left(r_{su}+R_{g\_br}\right)}\frac{\sin q\left(r_{su}-R_{g\_co}\right)}{q\left(r_{su}-R_{g\_co}\right)}
\end{aligned}
\tag{4.4}
$$

where the form factor amplitude of the core block is defined as $A_{co}\left(q, R_{g\_co}\right) = \frac{1-\exp\left(-q^2R_{g\_co}^2\right)}{q^2R_{g\_co}^2}$, and R_{g_co} is the radius of gyration of the core block. The self-correlation term of the core block in eq 4.4 is described by the Debye function $F_{co}\left(q, R_{g\_co}\right) = \frac{2\left[\exp\left(-q^2R_{g\_co}^2\right)-1+q^2R_{g\_co}^2\right]}{q^4R_{g\_co}^4}$. The excess scattering length density of the liquid core is $\beta_{su} = \left(\xi_{su}-\xi_{bg}\right)$, where the scattering length density of the suspension is calculated as the volume average of the comprising components as $\xi_{su} = \frac{\xi_{mon}f_{mon}V_{mon} + \sum_{j=1}^{n_{sol}}\xi_{solj}f_{solj}V_{solj}}{f_{mon}V_{mon} + \sum_{j=1}^{n_{sol}}f_{solj}V_{solj}}$. The excess scattering length density of the solvophobic block copolymer is $\beta_{co} = v_{co}\left(\xi_{co}-\xi_{su}\right)$. The form factor amplitude of the suspension particle in eq 4.4 is taken as $A_{su\_GC}\left(q, r_{su}\right) = \beta_{su}A_{su\_c\_GC}\left(q, r_{su}\right) + n_{agg\_su\_GC}\cdot\left[\beta_{br}A_{br}\left(q, R_{g\_br}\right)\frac{\sin q\left(r_{su}+R_{g\_br}\right)}{q\left(r_{su}+R_{g\_br}\right)} + \beta_{co}A_{co}\left(q, R_{g\_co}\right)\frac{\sin q\left(r_{su}-R_{g\_co}\right)}{q\left(r_{su}-R_{g\_co}\right)}\right]$, where $A_{su\_c\_GC}$ is the suspension particle core scattering amplitude defined as

$A_{su\_c\_GC}\left(q, r_{su}\right) = A_s\left(q, r_{su}\right)\cdot e^{-\frac{1}{2}q^2\sigma_t^2}$, where the exponent term with a width σ_t accounting for a sigmoidal interface between solvophilic block and suspension core at surface. σ_t value was fixed at 2.5 Å during fitting. The aggregation number is defined as $n_{agg\_su\_GC} = xpol\cdot\frac{\frac{4}{3}\pi r_{su}^3}{v_{co}}$. The mean aggregation number is defined as $N_{agg\_su\_GC} = xpol\cdot\frac{\frac{4}{3}\pi R_{su}^3}{v_{co}}$. The variables used to fit the

suspension particle with Gaussian PBzMA block chain model to experimental SAXS pattern could be listed as the following (see brackets on the right-hand side of the equation):

$$I_{\mathrm{su\_GC}}(q) = I_{\mathrm{su\_GC}}\begin{pmatrix} conv, \\ R_{\mathrm{su}}, \sigma_{R_{\mathrm{su}}}, R_{\mathrm{g\_co}} \\ xmon, xsol \end{pmatrix}, \tag{4.5}$$

where *xmon* and *xsol* are volume fractions of monomer and solvent in the suspension particle cores, respectively.

Suspension Particle as Core-Shell Structure Model

Based on the description of the suspension particle as core-shell structure (Figure 4.3, right), the scattering intensity of the suspension particle as core-shell structure contribution can be expressed as:

$$I_{\mathrm{su\_cs}}(q) = \phi_{\mathrm{su\_cs}} \frac{\int_0^\infty \Psi_{\mathrm{su}}(r_{\mathrm{su}})\Psi_{\mathrm{su\_c}}(r_{\mathrm{su\_c}}) \begin{pmatrix} F_{\mathrm{su\_cs}}(q, r_{\mathrm{su}}, r_{\mathrm{su\_c}}) \\ +\int_0^\infty \Psi_{\mathrm{su}}(r'_{\mathrm{su}})\Psi_{\mathrm{su\_c}}(r'_{\mathrm{su\_c}}) A_{\mathrm{su\_cs}}(q, r_{\mathrm{su}}, r_{\mathrm{su\_c}}) A_{\mathrm{su\_cs}}(q, r'_{\mathrm{su}}, r'_{\mathrm{su\_c}}) \left[S(q, r_{\mathrm{su}}, r'_{\mathrm{su}}, r_{\mathrm{su\_c}}, r'_{\mathrm{su\_c}}) - 1 \right] dr'_{\mathrm{su}} \end{pmatrix} dr_{\mathrm{su\_c}} dr_{\mathrm{su}}}{\int_0^\infty \Psi_{\mathrm{su}}(r_{\mathrm{su}}) V_{\mathrm{su}}(r_{\mathrm{su}}) dr_{\mathrm{su}}}, \tag{4.6}$$

where $\phi_{\mathrm{su\_cs}}$ is the volume fraction of the suspension particle as core-shell structure. Ψ_{su} follows the Gaussian distribution as $r_{\mathrm{su}} \sim N(R_{\mathrm{su}}, \sigma_{R_{\mathrm{su}}})$, and $\Psi_{\mathrm{su\_c}}$ follows the Gaussian distribution as $r_{\mathrm{su\_c}} \sim N(R_{\mathrm{su\_c}}, \sigma_{R_{\mathrm{su\_c}}})$. $S\left(q, r_{\mathrm{su}}, r'_{\mathrm{su}}, r_{\mathrm{su\_c}}, r'_{\mathrm{su\_c}}\right)$ is the hard sphere structure factor solved by the Percus-Yevick closure relation.[6] The form factor of the suspension particle with Gaussian core block chains in eq 4.6 is defined as:

$$\begin{aligned} F_{\mathrm{su\_cs}}(q, r_{\mathrm{su}}, r_{\mathrm{su\_c}}) = {} & \beta_{\mathrm{su}}^2 A_{\mathrm{s}}^2(q, r_{\mathrm{su\_c}}) V_{\mathrm{s}}^2(r_{\mathrm{su\_c}}) + \beta_{\mathrm{su\_s}}^2 A_{\mathrm{su\_s\_cs}}^2(q, r_{\mathrm{su}}, r_{\mathrm{su\_c}}) \\ & + n_{\mathrm{agg\_su\_cs}} \beta_{\mathrm{br}}^2 F_{\mathrm{br}}(q, R_{\mathrm{g\_br}}) + n_{\mathrm{agg\_su\_cs}}(n_{\mathrm{agg\_su\_cs}} - 1)\beta_{\mathrm{br}}^2 \left[A_{\mathrm{br}}(q, R_{\mathrm{g\_br}}) \frac{\sin q(r_{\mathrm{su}} + R_{\mathrm{g\_br}})}{q(r_{\mathrm{su}} + R_{\mathrm{g\_br}})} \right]^2, \\ & + 2 n_{\mathrm{agg\_su\_cs}} \beta_{\mathrm{su}} \beta_{\mathrm{br}} A_{\mathrm{s}}^2(q, r_{\mathrm{su\_c}}) V_{\mathrm{s}}(r_{\mathrm{su\_c}}) A_{\mathrm{br}}(q, R_{\mathrm{g\_br}}) \frac{\sin q(r_{\mathrm{su}} + R_{\mathrm{g\_br}})}{q(r_{\mathrm{su}} + R_{\mathrm{g\_br}})} \\ & + 2 n_{\mathrm{agg\_su\_cs}} \beta_{\mathrm{su\_s}} \beta_{\mathrm{br}} A_{\mathrm{su\_h\_cs}}(q, r_{\mathrm{su}}) A_{\mathrm{br}}(q, R_{\mathrm{g\_br}}) \frac{\sin q(r_{\mathrm{su}} + R_{\mathrm{g\_br}})}{q(r_{\mathrm{su}} + R_{\mathrm{g\_br}})} \end{aligned} \tag{4.7}$$

where the form factor amplitude of the shell of the suspension particle as core-shell structure is defined as $A_{\mathrm{su\_s\_cs}}(q, r_{\mathrm{su}}, r_{\mathrm{su\_c}}) = \left\{ V_{\mathrm{s}}(r_{\mathrm{su}}) A_{\mathrm{s}}(q, r_{\mathrm{su}}) - V_{\mathrm{s}}(r_{\mathrm{su\_c}}) A_{\mathrm{s}}\left[q, (r_{\mathrm{su}} - r_{\mathrm{su\_c}}) \right] \right\} e^{-\frac{1}{2} q^2 \sigma_{\mathrm{t}}^2}$, where the exponent term with a width σ_{t} accounting for a sigmoidal interface between the core and the shell. σ_{t} value was fixed at 2.5 Å during fitting. The excess scattering length density of the shell of the suspension particle as core-shell structure is $\beta_{\mathrm{su\_s}} = (\xi_{\mathrm{su\_s}} - \xi_{\mathrm{su}})$, where the scattering length density of the shell of the suspension particle as core-shell structure is calculated as the

volume average of the comprising components as $\xi_{\mathrm{su\_s}} = \frac{\xi_{\mathrm{pol}} V_{\mathrm{pol}} + \xi_{\mathrm{mon}} f_{\mathrm{mon}} V_{\mathrm{mon}} + \sum_{j=1}^{n_{\mathrm{sol}}} \xi_{\mathrm{sol}j} f_{\mathrm{sol}j} V_{\mathrm{sol}j}}{V_{\mathrm{pol}} + f_{\mathrm{mon}} V_{\mathrm{mon}} + \sum_{j=1}^{n_{\mathrm{sol}}} f_{\mathrm{sol}j} V_{\mathrm{sol}j}}$. The form factor amplitude of the suspension particle as core-shell structure in eq 4.7 is taken as $A_{\mathrm{su\_GC}}(q, r_{\mathrm{su}}) = \beta_{\mathrm{su}} A_{\mathrm{s}}(q, r_{\mathrm{su\_c}}) V_{\mathrm{s}}(r_{\mathrm{su\_c}}) + \beta_{\mathrm{su\_s}} A_{\mathrm{su\_s\_cs}}(q, r_{\mathrm{su}}, r_{\mathrm{su\_c}}) + n_{\mathrm{agg\_su\_cs}} \beta_{\mathrm{br}} A_{\mathrm{br}}(q, R_{\mathrm{g\_br}}) \frac{\sin q(r_{\mathrm{su}} + R_{\mathrm{g\_br}})}{q(r_{\mathrm{su}} + R_{\mathrm{g\_br}})}$, where the aggregation number is defined as $n_{\mathrm{agg\_su\_ch}} = xpol \cdot \frac{\frac{4}{3}\pi r_{\mathrm{su}}^3}{v_{\mathrm{co}}}$. The mean aggregation number is defined as $N_{\mathrm{agg\_su\_ch}} = xpol \cdot \frac{\frac{4}{3}\pi R_{\mathrm{su}}^3}{v_{\mathrm{co}}}$. The variables used to fit the suspension particle as core-shell structure model could be listed as the following (see brackets on the right-hand side of the equation):

$$I_{\mathrm{su\_cs}}(q) = I_{\mathrm{su\_cs}}\begin{pmatrix} conv, \\ R_{\mathrm{su}}, \sigma_{R_{\mathrm{su}}}, R_{\mathrm{su\_c}}, \sigma_{R_{\mathrm{su\_c}}}, \\ xmon, xsol \end{pmatrix}. \quad (4.8)$$

4.5 SAXS Analysis of the Initial Stage of PISA Process via RAFT Synthesis of PSMA$_{31}$–PBzMA$_{2000}$ Synthesis in Mineral Oil at 2 Min

For the insight of the core structure of the spherical particles formed at the initial stage, the proposed three SAXS models are applied to the SAXS pattern collected after the first 2 minutes of RAFT synthesis of PSMA$_{31}$-PBzMA$_{2000}$. It is anticipated that the SAXS modelling results can be used as a guidance for detecting structure of initial particle morphology. The spherical micelle model (eq 2.24) can provide a relatively good SAXS fitting results with χ^2 produced by Igor Pro least square fitting algorithm as 2095 (Figure 4.4 (a)) and suggests that the radius of the spherical micelle was 17.0 ± 2.4 nm with *xmon* = 0.06, *xsol* = 0.81, and *xpol* = 0.13. The monomer conversion, *conv*, was determined as 0.026. Meanwhile, the suspension particle models were also given the same monomer conversion with relatively good fittings of χ^2 = 1766 and χ^2 = 1656 [Figure 4.4 (b) and (c)], respectively. The radius of suspension particle with Gaussian PBzMA block chain model was 16.3 ± 2.8 nm and the volume fractions of the components were *xmon* = 0.13, *xsol* = 0.75, and *xpol* = 0.12. $R_{\mathrm{g\_co}}$ was 4.3 nm, which was considered to be large when the monomer conversion was only 0.026, and the DP reaching 50. For the suspension particle as core-shell structure model, the core radius of the suspension particle as core-shell structure was 1.98 ± 0.63 nm, and the total radius of the suspension particle as core-shell structure was 14.4 ± 4.18 nm. And the volume fractions of the compounds of the suspension particle as core-shell structure were *xmon* = 0.06, *xsol* = 0.81, and *xpol* = 0.13. This tiny core radius of the suspension particle might indicate the suspension particle was similar to spherical micelle.

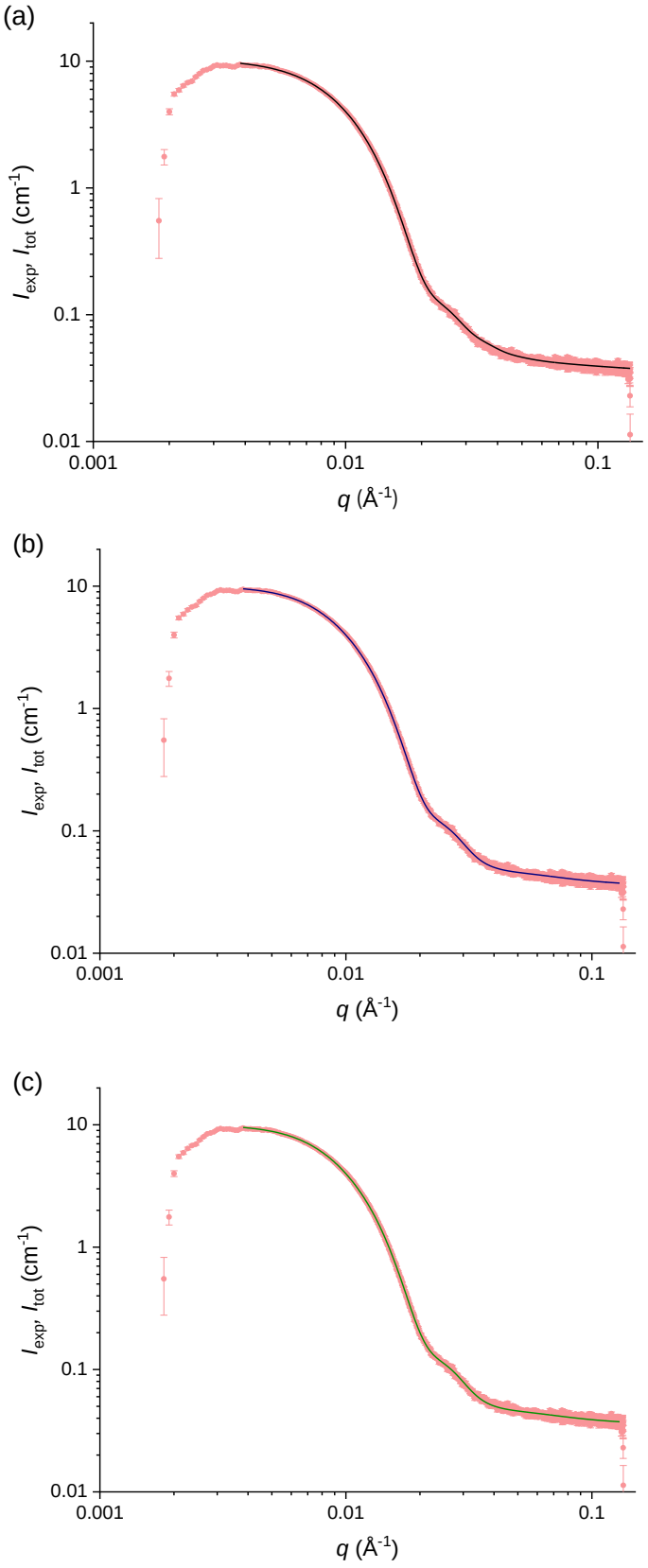

Figure 4.4**.** SAXS model fitting (solid curve), I_{tot}, to the experimental SAXS pattern (symbols), I_{exp}, recorded during the first 2 minutes of RAFT synthesis of $PSMA_{31}$-$PBzMA_{2000}$ diblock copolymer at 90 °C in mineral oil: spherical micelle model (a), suspension particle with Gaussian PBzMA block chain model (b), and suspension particle as core-

shell structure model (c).

The spherical particle radii given by the spherical micelle model and the suspension particle with Gaussian PBzMA block chain model were very close, and the radius provided by the suspension particle as core-shell structure was relatively close to the radii obtained by using the other proposed models. For the volume fractions of the components given by the proposed SAXS models, the spherical micelle model and the suspension particle as core-shell structure both suggested the same results, while the suspension particle with Gaussian PBzMA block chain model produced a slightly higher *xmon* and a slightly lower *xsol*. Therefore, according to the radii and the volume fractions of the components obtained by SAXS modelling, the considered three SAXS models provided a similar both particle size of the spherical particles and composition of the spherical particle cores. These SAXS models mainly distinguish from each other by the way the core structure is described. According to the fact that the suspension particle as core-shell structure model returned the lowest χ^2, this model might be the most appropriate for the describing the spherical particles formed at the initial stage of reaction during the first 2 minutes. Thus, the initial spherical particles formed during RAFT synthesis of $PSMA_{31}$-$PBzMA_{2000}$ could be considered as particles with liquid cores composed of BzMA monomer and solvent molecules stabilized by the $PSMA_{31}$-PBzMA diblock copolymers. According to the SAXS modelling results, DP of PBzMA after the first 2 minutes of synthesis is around 50. The validation of the $R_{g\_co\_est}$ is estimated by the Gaussian chain model as $(b \cdot l_c/6)^{0.5}$ [7], where the contour length of such $PBzMA_{50}$, l_c, is calculated as the repeat unit, 50, multiplying to the length of two carbon bonds in an all *trans* configuration, 0.255 nm, and the Kuhn length, b, is given as 1.53 nm based on PMMA[8]. Thus, it could be estimated that radius of gyration of the $PBzMA_{50}$ Gaussian coil, $R_{g\_co\_est}$, is 3.58 nm. The the contour length of such $PBzMA_{50}$, l_c, is 12.8 nm, and the radius of gyration of rod with length as l_c, is given as $l_c/2\sqrt{3}$ [9], 3.68 nm. The suspension particle with Gaussian PBzMA block chain model returned R_{g_co} value of 4.3 nm which is close but slightly higher than the value estimated from the BzMA monomer conversion. Meanwhile, the shell thickness returned by the suspension particle as core-shell structure model is 12.4 ± 3.55 nm, which is close to the $PBzMA_{50}$ contour length. Thus, this result combined together with the conversion value suggests that the PBzMA block in the initially formed suspension particles is stretched. This is likely to be due to a good compatibility of the PBzMA block with the solvent and BzMA monomer at low DP. Thus, both suspension particle models could be considered as reasonable models to describe the structural morphology of initial spherical particles. However, these two proposed suspension particle models produced slightly different sizes and the volume fractions of the components, and, thus, some uncertainty about the particle structure remains unresolved. Moreover, the spherical micelle could also be considered as a good approximation for the initial spherical particle morphology because the PBzMA block volume fraction of the spherical micelle core was small which means that the spherical micelle model with PBzMA core block averagely mixed with BzMA monomer and solvent molecules could be valid for the spherical particles formed after 2 minutes of the PBzMA block synthesis. This is also supported by a relatively small χ^2 and a good fitting produced by the spherical micelle model to the SAXS pattern collected at 2 min.

4.6 SAXS Models for Possible Morphological Transition during Initial Stages of PISA via RAFT Synthesis of $PSMA_{31}$–$PBzMA_{2000}$ in Mineral Oil

SAXS fitting results have shown that all three SAXS models can be used as potential candidates for describing the structural morphology of initial particles formed PISA of $PSMA_{31}$-$PBzMA_{2000}$. Thus, all these morphologies should be considered for analyzing further stes of the sysnthesis taking place during 4 – 14 minutes. According to PDDF analysis of the second frame at 4 min (Figure 4.2), the particle morphology could correspond to dimers formed by spherical particles. However, without any confident evident of morphological transition of particles observed, four scenarios of morphology transition are proposed herein. In particular, the first scenario includes dimers constructed by spherical micelles and spherical micelles (MT-I_ds-s, Figure 4.5). The second scenario includes relatively large spherical micelles, relatively small spherical micelles and the dimers constructed by spherical micelles a morphology transition (MT-II_ls-ds-ss, Figure 4.6). The third scenario includes relatively large suspension particle as core-shell structure and relatively small suspension particles as core-shell structure (MT-III_cs, Figure 4.7). Finally, the fourth scenario includes suspension particles with Gaussian PBzMA block chains and spherical micelles (MT-IV_GC-s, Figure 4.8). However, considering the difficulties of SAXS modelling during the proposed morphology transition, each volume fraction of the components (*xmon*, *xsol*, and *xpol*) are assumed to be the same for all populations of particles at a particular time frame.

4.6.1 SAXS Model for MT-I_ds-s Particle Morphology Transition

Scattering intensity of a system corresponding to the MT-I_ds-s morphology transition (Figure 4.5), including the dimers constructed by spherical micelles and the spherical micelles, can be given as:

$$I_{\mathrm{tot}}(q)=\phi_{\mathrm{ds}}I_{\mathrm{ds}}(q)+\phi_{\mathrm{sm}}I_{\mathrm{sm}}(q)+\left(1-\phi_{\mathrm{ds}}-\phi_{\mathrm{sm}}\right)I_{\mathrm{bg}}(q), \tag{4.9}$$

where ϕ_{ds} is the volume fraction of dimers, and I_{ds} is the scattering intensity of spherical particle dimers:

$$I_{\mathrm{ds}}(q)=\frac{\int_0^{\infty}\Psi_{\mathrm{ds}}(r_{\mathrm{ds}})\left[F_{\mathrm{sm}}(q,r_{\mathrm{ds}})\cdot S_{\mathrm{d}}(q,r_{\mathrm{ds}},2R_{\mathrm{g\_br}})\right]dr_{\mathrm{ds}}}{\int_0^{\infty}\Psi_{\mathrm{ds}}(r_{\mathrm{mc}})\left[2\cdot V_{\mathrm{sm}}(r_{\mathrm{ds}})\right]dr_{\mathrm{ds}}}, \tag{4.10}$$

where $S_{\mathrm{d}}(q, r_{\mathrm{ds}}, 2R_{\mathrm{g\_br}})$ is the structure factor for dimer structure by spherical particles. $S_{\mathrm{d}}(q, r_{\mathrm{ds}}, 2R_{\mathrm{g\_br}})$ is a special case of the structure factor for pearl necklace chains[10] given as:

$$S_{\mathrm{pearl}}(q,N_{\mathrm{pearl}},r_{\mathrm{ds}},d_{\mathrm{d}})=N_{\mathrm{pearl}}+2\cdot\sum_{i_{\mathrm{pearl}}=1}^{N_{\mathrm{pearl}}}\left(N_{\mathrm{pearl}}-i_{\mathrm{pearl}}\right)\frac{\sin\left[q\cdot i_{\mathrm{pearl}}\cdot\left(2r_{\mathrm{ds}}+d_{\mathrm{d}}\right)\right]}{q\cdot i_{\mathrm{pearl}}\cdot\left(2r_{\mathrm{ds}}+d_{\mathrm{d}}\right)}, \tag{4.11}$$

where N_{pearl} is the number of the particles of the chains, d_d is the closed distance between the particles of the chains. The dimer structure factor is obtained when $N_{pearl} = 2$ and $d_d = 2R_{g\_br}$:

$$S_d\left(q, r_{ds}, 2R_{g\_br}\right) = S_{pearl}\left(q, 2, r_{ds}, 2R_{g\_br}\right) = 2\left\{1 + \frac{\sin\left[q \cdot \left(2r_{ds} + 2R_{g\_br}\right)\right]}{q \cdot \left(2r_{ds} + 2R_{g\_br}\right)}\right\}. \quad (4.12)$$

The variables used to fit the morphology transition (MT-I_ds-s) including the dimers constructed by spherical micelles and the spherical micelles could be listed as the following (see the bracket on the right-hand side of the equation):

$$I_{tot}(q) = I_{tot}\begin{pmatrix} conv, \phi_{sm}, \\ R_{ds}, \sigma_{R_{ds}}, R_{mc}, \sigma_{R_{mc}}, \\ xmon, xsol \end{pmatrix}. \quad (4.13)$$

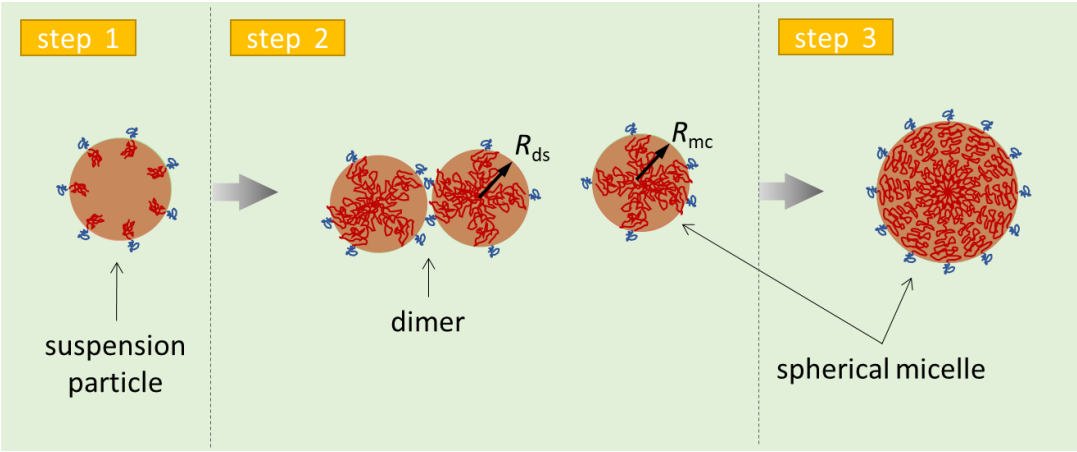

Figure 4.5. Schematic presentation of the proposed morphology transition (MT-I_ds-s) including the dimers constructed by spherical micelles and the spherical micelles. The mean radius of the spherical micelles and spherical micelles constructing the dimers are R_{mc} and R_{ds}, respectively.

4.6.2 SAXS Model for MT-II_ls-ds-ss Particle Morphology Transition

Scattering intensity of a system corresponding to the MT-II_ls-ds-ss morphology transition (Figure 4.6) including large spherical micelles, dimers constructed by spherical micelles and small spherical micelles can be given as:

$$\begin{aligned} I_{tot}(q) = {} & \phi_{lsm} I_{lsm}\left(q, r_{lmc}\right) + \phi_{ds} I_{ds}\left(q, r_{ds}\right) + \phi_{ssm} I_{ssm}\left(q, r_{smc}\right) \\ & + \left(1 - \phi_{lsm} - \phi_{ds} - \phi_{ssm}\right) I_{bg}(q) \end{aligned}, \quad (4.14)$$

where ϕ_{lsm} is the volume fraction of relatively large spherical particles with radius of r_{lsm}, ϕ_{ds} is the volume fraction of dimer formed by spherical particles with radius of r_{ds}, and ϕ_{ssm} is the

volume fraction of relatively small spherical particles with radius of r_{ssm}. $I_{lsm}(q, r_{lmc})$ is the scattering intensity of the relatively large spherical particles with core radius of r_{lmc}, $I_{ds}(q, r_{ds})$ is the scattering intensity of the dimers formed by spherical particles with core radius of r_{ds}, and $I_{ssm}(q, r_{smc})$ is the scattering intensity of the relatively small spherical particles with core radius of r_{smc}. It is assumed that polydispersity of the particle radii corresponding to different populations follow Gaussian distribution as $r_{lmc} \sim N(R_{lmc}, \sigma_{R_{lmc}})$, $r_{ds} \sim N(R_{ds}, \sigma_{R_{ds}})$, and $r_{smc} \sim N(R_{smc}, \sigma_{R_{smc}})$, respectively. The variables used to fit the MT-II_ls-ds-ss morphology transition including relatively large spherical micelles, the dimers constructed by spherical micelles and the relatively small spherical micelles could be listed as the following (see the brackets on the right-hand side of the equation):

$$I_{tot}(q) = I_{tot}\begin{pmatrix} conv, \phi_{lsm}, \phi_{ssm}, \\ R_{lmc}, \sigma_{R_{lmc}}, R_{ds}, \sigma_{R_{ds}}, R_{smc}, \sigma_{R_{smc}}, \\ xmon, xsol \end{pmatrix}. \quad (4.15)$$

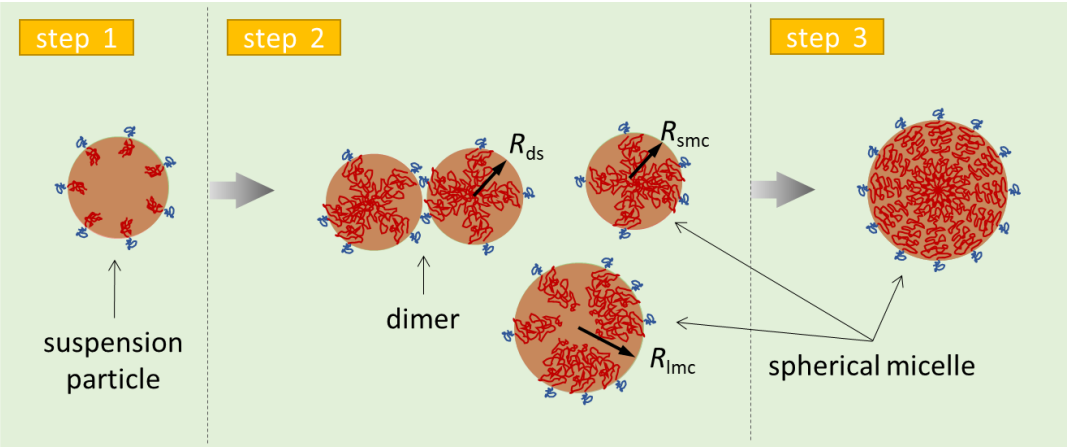

Figure 4.6. Schematic presentation of the proposed morphology transition (MT-II_ls-ds-ss) including relatively large spherical micelles, the dimers constructed by spherical micelles and relatively small spherical micelles. The mean radius of the relatively large and relatively spherical micelles, spherical micelles constructing the dimers are R_{lmc}, R_{smc}, and R_{ds}, respectively.

4.6.3 SAXS Model for MT-III_cs Particle Morphology Transition

Scattering intensity of a system corresponding to the MT-III_cs morphology transition (Figure 4.7) including large suspension particles as core-shell structure and small suspension particles as core-shell structure can be given as:

$$\begin{aligned} I_{tot}(q) = {} & \phi_{lsu\_cs} I_{lsu\_cs}(q, r_{lsu}, r_{lsu\_c}) + \phi_{ssu\_cs} I_{ssu\_cs}(q, r_{ssu}, r_{ssu\_c}) \\ & + (1 - \phi_{lsu\_cs} - \phi_{ssu\_cs}) I_{bg}(q) \end{aligned}, \quad (4.16)$$

where ϕ_{lsu_cs} is the volume fraction of relatively large suspension particles as core-shell

structure, ϕ_{ssu_cs} is the volume fraction of relatively small suspension particles as core-shell structure, and ϕ_{sm} is the volume fraction of spherical micelles. $I_{lsu\_cs}(q, r_{lsu}, r_{lsu\_c})$ is the scattering intensity of the relatively large suspension particles as core-shell structure with the total radius of r_{lsu} and the core radius of r_{lsu_c}. $I_{ssu\_cs}(q, r_{ssu}, r_{ssu\_c})$ is the scattering intensity of the relatively small suspension particles as core-shell structure with the total radius of r_{ssu} and the core radius of r_{ssu_c}. Because the shells of the suspension particles are considered to be formed by PBzMA blocks together with BzMA monomer and solvent molecules, the shell thickness and its polydispersity is considered to be the same for the relatively large suspension particles and the relatively small suspension particles, which means $r_{lsu} - r_{lsu\_c} = r_{ssu} - r_{ssu\_c}$. If the core radius of the suspension particle as core-shell structure was equal or close to 0, the suspension particle as core-shell structure was considered to be degenerated as the spherical micelle. IT was assumed in the model that the polydispersity of the particle radii follow Gaussian distribution as $r_{lsu} \sim N(R_{lsu}, \sigma_{R_{lsm}})$, $r_{lsu\_c} \sim N(R_{lsu\_c}, \sigma_{R_{lsm\_c}})$, $r_{ssu} \sim N(R_{ssu}, \sigma_{R_{ssu}})$, and $r_{ssu\_c} \sim N(R_{ssu\_c}, \sigma_{R_{ssu\_c}})$, respectively. The variables used to fit the MT-III_cs morphology transition including the relatively large suspension particles as core-shell structure and the relatively small suspension particles as core-shell structure could be listed as the following (see the brackets on the right-hand side of the equation):

$$I_{tot}(q) = I_{tot}\begin{pmatrix} conv, \phi_{lsu\_cs}, \\ R_{lsu}, \sigma_{R_{lsm}}, R_{lsu\_c}, \sigma_{R_{lsm\_c}}, R_{ssu}, \sigma_{R_{ssm}}, R_{ssu\_c}, \sigma_{R_{ssm\_c}}, \\ xmon, xsol \end{pmatrix}. \quad (4.17)$$

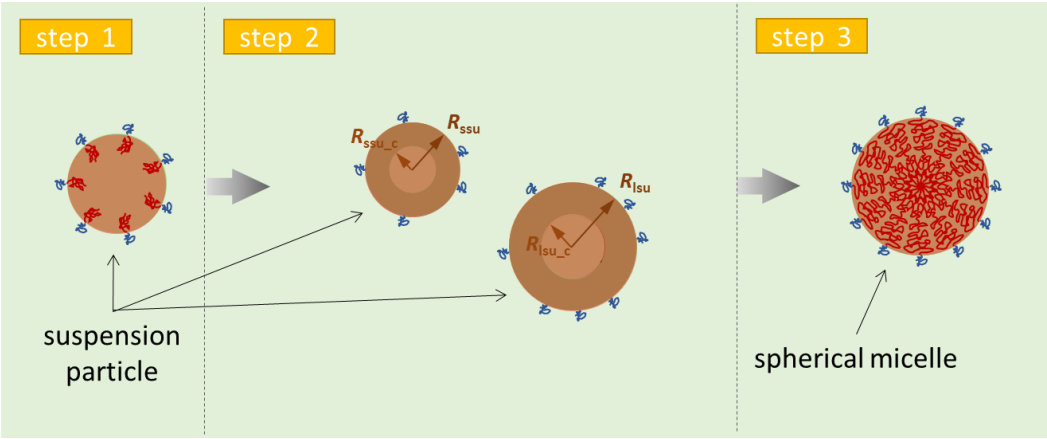

Figure 4.7. Schematic presentation of the proposed morphology transition (MT-III_cs) including the relatively large suspension particles as core-shell structure and the relatively small suspension particles as core-shell structure. The mean radius of the relatively large and relatively small suspension particles as core-shell structure are R_{lsu} and R_{ssu}, respectively, and the mean core radius of the relatively large and relatively small suspension particles as core-shell structure are R_{lsu_c} and R_{ssu_c}, respectively.

4.6.4 SAXS Model for MT-IV_GC-s Particle Morphology Transition

Scattering intensity of a system corresponding to the MT-IV_GC-s morphology transition

(Figure 4.8) including the suspension particles with Gaussian PBzMA block chains and spherical micelles can be given as:

$$I_{tot}(q) = \phi_{su\_GC} I_{su\_GC}(q, r_{su}, R_{g\_co}) + \phi_{sm} I_{sm}(q, r_{mc}) + (1 - \phi_{su\_GC} - \phi_{sm}) I_{bg}(q) \quad (4.18)$$

where ϕ_{su_GC} is the volume fraction of suspension particles as Gaussian PBzMA block chains, $I_{su\_GC}(q, r_{su}, R_{g\_co})$ is the scattering intensity of the suspension particles as Gaussian PBzMA block chains with the total radius of r_{su} and radius of gyration of the core block of R_{g_co}. The variables used to fit the MT-IV_GC-s morphology transition including the suspension particles with Gaussian PBzMA block chains and spherical micelles could be listed as the following (see the brackets on the right-hand side of the equation):

$$I_{tot}(q) = I_{tot}\left(q, \begin{matrix} conv, \phi_{sm}, \\ R_{su}, \sigma_{R_{su}}, R_{g\_co}, R_{mc}, \sigma_{R_{mc}}, \\ xmon, xsol \end{matrix}\right). \quad (4.19)$$

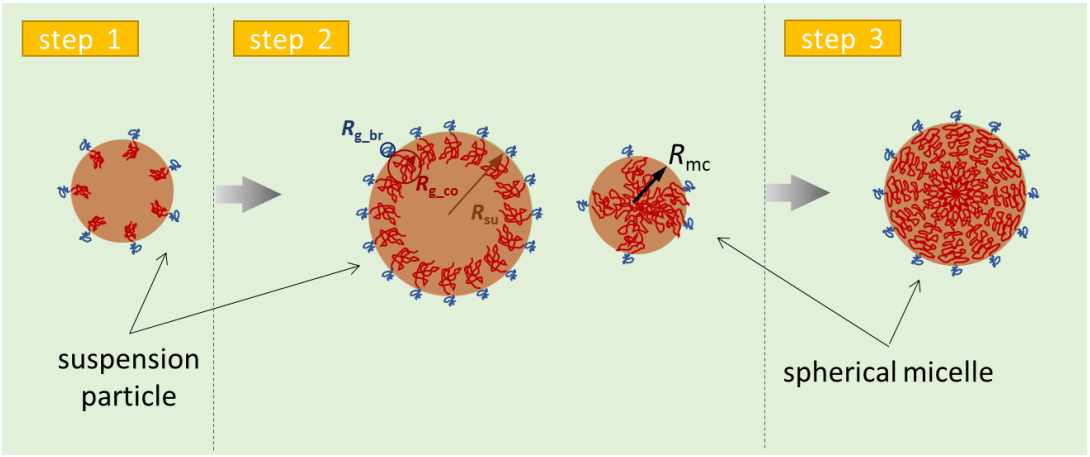

Figure 4.8. Schematic presentation of the proposed morphology transition (MT-IV_GC-s) including the suspension particles with Gaussian core block chains and spherical micelles. The mean radius of the suspension particle with Gaussian core block chains is R_{su}, the radius of gyration of the core block R_{g_co}, and the radius of gyration of the solvophilic block R_{g_br}.

4.7 SAXS Analysis of Morphological Transition at the Initial Stage of PISA of $PSMA_{31}$–$PBzMA_{2000}$ during RAFT Synthesis in Mineral Oil

4.7.1 MT-I_ds-s Particle Morphology Transition Model

According to the PDDF analysis of the SAXS pattern at 4 min (Figure 4.2), the dimer structure was an obvious particle morphology to be considered for the transitions. Therefore, MT-I_ds-

s including dimer structures as one of the populations in the system was firstly examined for the SAXS analysis (Figure 4.9). The MT-I_ds-s model (eq 4.9) produced a relatively good fitting to the SAXS pattern corresponding to 4 min, and therefore, MT-I_ds-s model was applied to the SAXS patterns collected during 4 – 14 min of PISA via RAFT synthesis of $PSMA_{31}$–$PBzMA_{2000}$ diblock copolymer spheres in mineral oil at 90 °C (Figure 4.10). This indicated that during 4 – 12 min, the particle morphology could be interpreted as a mixture of dimers of spherical micelles and single spherical micelles. At 12 min of the PISA process, a single population described by the spherical micelle model produced an acceptable fit. Considering that the only species in the studied system after 2 minutes of synthesis were spherical micelles, the population of dimers of spherical micelles observed at 4 min together with the population of single spherical micelle (Figure 4.11) could be considered as a product of a possible fusion of spherical micelles or a fission of large spherical micelles. The possible fusion and fission of the spherical micelles could be used as a ratio between two populations to detect whether the MT-I_ds-s model is suitable to describe the initial stage of the studied PISA process. A validation of the proposed model could be based on the radii of spherical micelles comprising the dimers and the other spherical micelles (Figure 4.12), mean aggregation number of copolymers (Figure 4.13) which were determined by BzMA monomer conversion (Figure 4.14) and the volume fractions of the components in the particle cores (Figure 4.15). After 4 minutes of the synthesis, the radius of spherical micelles composing the dimers was significantly larger than the radius of the single spherical micelles, and the aggregation number of the dimer spherical micelles was twice as the aggregation number of spherical micelles, which meant the aggregation number of dimers were four times as the aggregation number of spherical micelles. This detected aggregation number ratio between the dimers and the single spherical micelles cannot be acceptable for the possible fusion or fission of the spherical micelles, because ideally for the fusion case, the single spherical micelles should have the same structural characteristics as the dimer spherical micelles, and for the fission case, the aggregation number of the single spherical micelles should be twice as the dimer spherical micelles. Thus, structural parameters produced by the proposed MT-I_ds-s model did not support the conditions required for the possible fusion or fission of spherical micelles. After 6 min of the synthesis, the mean radii of the single spherical micelles were always larger than the mean radii of the dimer spherical micelles. This may suggest a morphological transition of relatively small spherical micelles to relatively large spherical micelles via the fusion of spherical micelles. However, the aggregation number of the dimer spherical micelles remained nearly constant during 6 – 10 min, while the aggregation number of the single spherical micelles was gradually increasing. Moreover, the aggregation number of the single spherical micelles was around 1.5 times larger than the aggregation number of the dimer spherical micelles. Considering the aggregation number results produced by the MT-I_ds-s model, it could be suggested that during 4 – 14 minutes the spherical micelles merge into larger spherical micelles via fusion (Figure 4.13). This SAXS analysis also provided information about the BzMA monomer conversion (Figure 4.14). The particle core components have shown the following: *xsol* rapidly dropped from 0.8 to 0.15, which indicated the solvent molecules were expelled from the particle core; *xpol* increased from 0.15 to 0.60, and BzMA monomer gradually increased from 0.05 to 0.25, which might be interpreted by a preferable diffusion of the monomer from the surrounding media to the formed particles discussed in Chapter 2 (Figure 2.1). Even though the proposed MT-I_ds-s model could be used to describe the morphological transition of the particles during 4 - 14 min of the synthesis, the contradictions of SAXS modelling results obtained for the SAXS pattern recorded after 2 minutes of the synthesis does not support this model. Thus, the MT-I_ds-s model was modified by introducing an additional population of spherical micelles with different mean radius (MT-II_ls-ds-ss model, Figure 4.5).

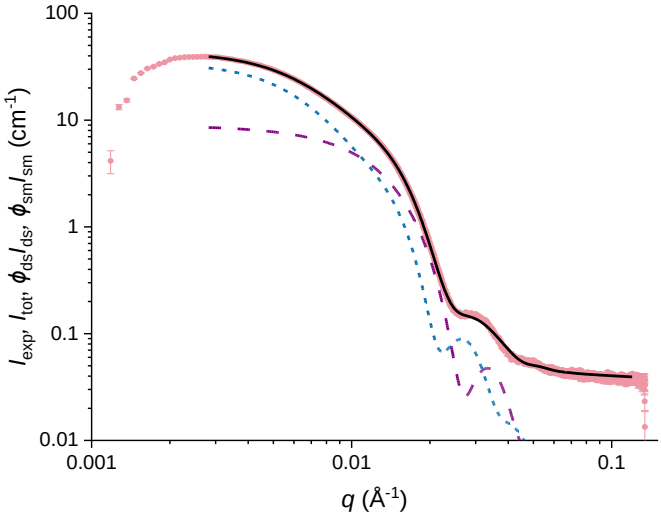

Figure 4.9**.** SAXS pattern collected during PISA via RAFT synthesis of $PSMA_{31}$–$PBzMA_{2000}$ diblock in mineral oil at 90 °C (frame 2, 4 min), I_{exp}, (symbols) fitted by the MT-I_ds-s morphology transition model including dimers of spherical micelles and single spherical micelles, I_{tot}, (solid curve). Scattering intensity of separate populations are shown by blue dots (dimers of spherical micelles, $\phi_{ds}I_{ds}$) and purple dashes (spherical micelles, $\phi_{sm}I_{sm}$).

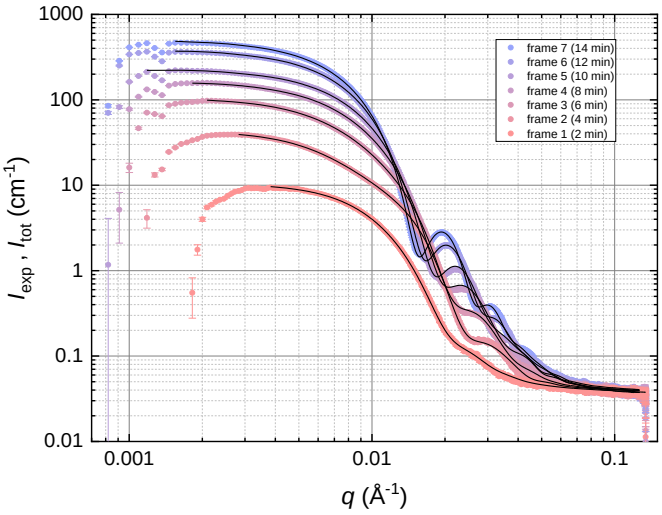

Figure 4.10**.** Experimental SAXS patterns (circles), recorded every 2 min from 2 min (frame 1) to 14 min (frame 7) during PISA via RAFT synthesis of $PSMA_{31}$–$PBzMA_{2000}$ diblock copolymers in mineral oil at 90 °C with respective fitting curves (solid lines) produced by the MT-I_ds-s morphology transition model including dimers of spherical micelles and spherical micelles (eq 4.9).

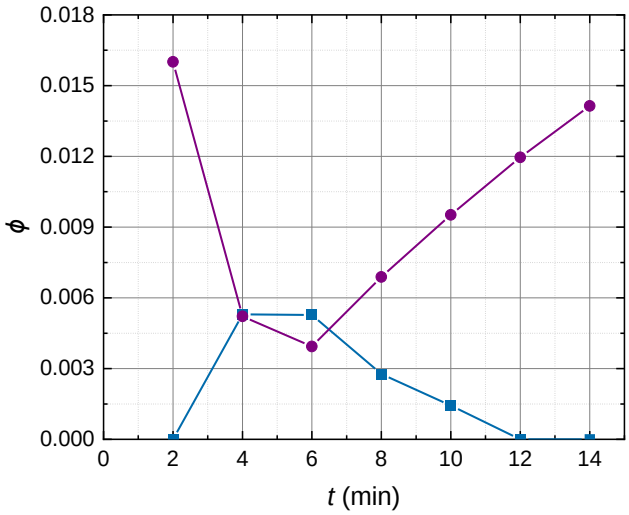

Figure 4.11**.** Time-dependence of the volume fraction of spherical micelle dimers, ϕ_{ds}, (blue squares) and the volume fraction of single spherical micelles, ϕ_{sm}, (purple circles) at the initial stage of $PSMA_{31}$–$PBzMA_{2000}$ diblock copolymer synthesis in mineral oil at 90 °C (during 2-14 minutes of the synthesis) obtained by SAXS analysis using MT-I_ds-s morphology transition model (eq 4.9). The measured points are connected by lines for a guidance only.

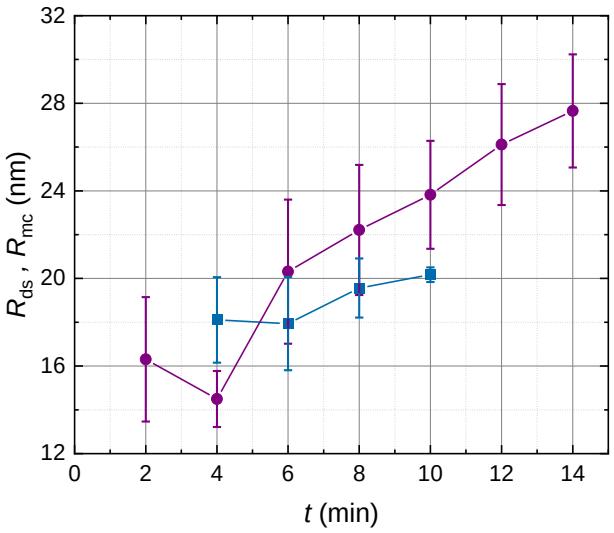

Figure 4.12**.** Time-dependence of the mean core radius of the dimer spherical micelles, R_{ds}, (blue squares) and the mean core radius of the single spherical micelles, R_{mc}, (purple circles) at the initial stage of $PSMA_{31}$–$PBzMA_{2000}$ diblock copolymer synthesis in mineral oil at 90 °C (during 2 - 14 minutes of the synthesis) obtained by SAXS analysis using MT-I_ds-s morphology transition model (eq 4.9). The measured points are connected by lines for a guidance only. The bars show respective standard deviations of the measured radii.

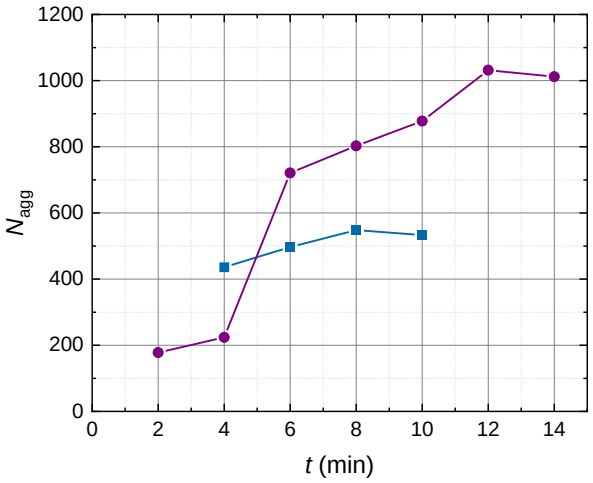

Figure 4.13**.** Time-dependence of the mean copolymer aggregation number, N_{agg}, of the dimer spherical micelles, N_{agg_ds}, (blue squares) and the single spherical micelles, N_{agg_sm}, (purple circles) at the initial stage of $PSMA_{31}$–$PBzMA_{2000}$ diblock copolymer synthesis in mineral oil at 90 °C (during 2 - 14 minutes of the synthesis) calculated from results obtained by SAXS analysis using MT-I_ds-s morphology transition model (eq 4.9). The measured points are connected by lines for a guidance only.

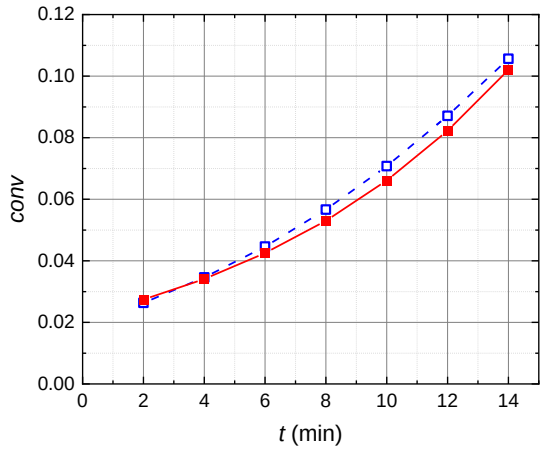

Figure 4.14**.** Time-dependence of BzMA conversion, *conv*, at the initial stage of $PSMA_{31}$–$PBzMA_{2000}$ diblock copolymer synthesis in mineral oil at 90 °C (during 2 - 14 minutes of the synthesis) obtained by SAXS analysis using MT-I_ds-s morphology transition model (eq 4.9) (red squares) and MT-IV_GC-s morphology transition model (eq 4.18) (blue hollow squares). The measured points are connected by lines for a guidance only.

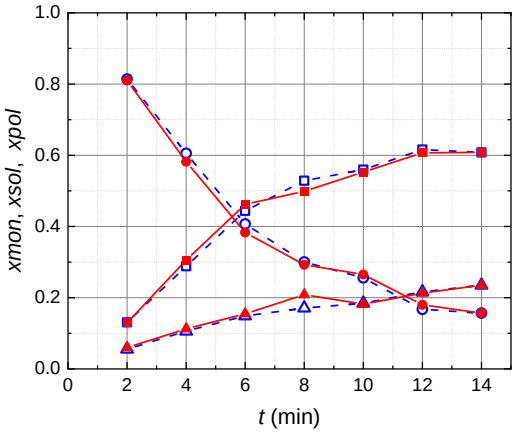

Figure 4.15**.** Time-dependence of *xmon* (triangles), *xsol* (circles), and *xpol* (squares) at the initial stage of $PSMA_{31}$–$PBzMA_{2000}$ diblock copolymer synthesis in mineral oil at 90 °C (during 2 - 14 minutes of the synthesis) obtained by SAXS analysis using MT-I_ds-s morphology transition model (eq 4.9) (red symbols) and MT-IV_GC-s morphology transition model (eq 4.18) (open blue symbols). The measured points are connected by lines for a guidance only.

4.7.2 MT-II_ls-ds-ss Particle Morphology Transition Model

A modification of the MT-I_ds-s morphology transition model by introducing an extra (third) population of particles represented by large spherical micelles provided a better fit to the experimental SAXS pattern corresponding to 4 minutes of synthesis (Figure 4.16) than the original MT-I_ds-s model (Figure 4.5) (χ^2 = 1999.9 versus χ^2 =5144.9, respectively). Thus, the MT-II_ls-ds-ss model was applied to the set of SAXS patterns corresponding to the initial stage of the $PSMA_{31}$–$PBzMA_{2000}$ diblock copolymer synthesis (4 – 14 min of the synthesis) (Figure 4.17). The SAXS analysis using the MT-II_ls-ds-ss model has shown that the large spherical micelles could form and exist in the system only for the first 8 min of synthesis (Figure 4.18). This suggests that at this point the MT-II_ls-ds-ss model with the additional third population degenerates into the MT-I_ds-s model. Therefore, the SAXS modelling results for the period of 8 – 14 min of the synthesis could be adopted from the analysis using the MT-I_ds-s model (Figures 4.14 - 4.16). The measured volume fraction of the large spherical micelles was relatively small in a comparison with the dominating small spherical micelles. The volume fraction of the spherical micelles forming dimers was nearly half of the volume fraction of the small spherical micelles. There is a relatively smooth transition between the results obtained for both the dimers and the spherical micelles using the MT-II_ls-ds-ss model (for the period of 2-6 minutes) and the MT-I_ds-s model (for the period of 8-14 minutes). The MT-II_ls-ds-ss model has shown that the mean radius of the small spherical micelles gradually increased from 16.5 to 20.1 nm, and the radius of the dimer spherical micelles increased from 13.0 to 16.1 nm (corresponding to 2 and 6 minutes of synthesis, respectively). This result may suggest that relatively smaller spherical micelles forming the dimers may merge into the small spherical micelles. Moreover, the aggregation number of the small spherical micelles at 2 min of synthesis is nearly the same as the aggregation number of the spherical micelles forming dimers at 4 min, and consequently the aggregation number of the small spherical micelles at 4 min is nearly twice as the aggregation number of the spherical micelles forming dimers at 4 min suggesting that small spherical micelles after their formation at 2 min possibly collide into dimers which is followed by a further fusion of the dimer spherical micelles. This relationship

between aggregation numbers of the dimer spherical micelles and the small spherical micelles observed at the first few minutes of the synthesis holds at the later stage (Figure 4.16). Thus, the obtained result indicates that the size of small spherical micelles grew by the collisions and fusions of the small spherical micelles formed at the previous stage. However, the large spherical micelles after the formation reduce their radius from 31.7 to 27.1 nm, which does not show an obvious connection with the dimer and spherical micelle radius behavior. Also, both the radii of large spherical micelle and small spherical micelle were closed to the radius of the spherical micelles constructed dimers. This cannot interpret the further aggregation number change without detecting dimer structure by the fusion or split mechanism for spherical miclelles[11]. These two inexplicable SAXS modelling results indicates that the morphological transition described by the MT-II_ls-ds-ss model may not be valid and other particle morphologies rather than dimer structures should be considered. Thus, particle morphology transitions excluding dimer structures, MT-III_cs-s and MT-IV_GC-s models, were considered for the SAXS analysis.

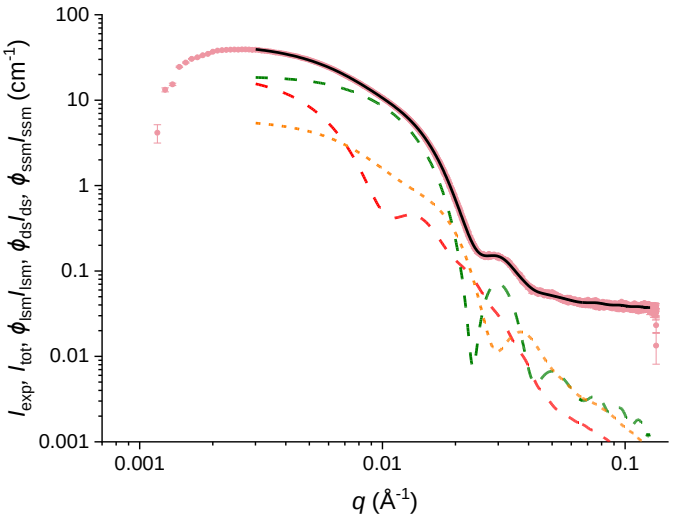

Figure 4.16**.** SAXS pattern collected during PISA via RAFT synthesis of $PSMA_{31}$–$PBzMA_{2000}$ diblock in mineral oil at 90 °C (frame 2, 4 min), I_{exp}, (symbols) fitted by the MT-II_ls-ds-ss morphology transition model including large spherical micelles, dimers of spherical micelles and small spherical micelles, I_{tot}, (solid curve). Scattering intensity of separate populations are shown by red dashes (large spherical micelle, $\phi_{lsm}I_{lsm}$), orange dots (dimers of spherical micelles, $\phi_{ds}I_{ds}$) and green dashes (small spherical micelles, $\phi_{ssm}I_{ssm}$).

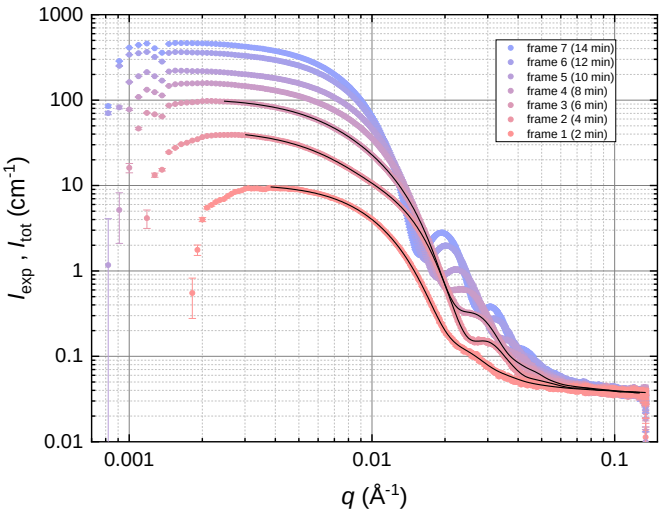

Figure 4.17**.** Experimental SAXS patterns (circles), recorded every 2 min from 2 min (frame 1) to 14 min (frame 7) during PISA process via RAFT synthesis of $PSMA_{31}$–$PBzMA_{2000}$ diblock copolymers in mineral oil at 90 °C with respective fitting curves (solid lines) produced by the MT-II_ls-ds-ss morphology transition model including large spherical micelles, dimers of spherical micelles and small spherical micelles (eq 4.14).

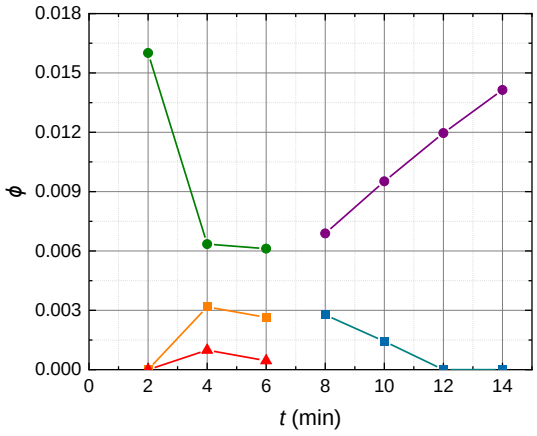

Figure 4.18**.** Time-dependence of the volume fraction of large spherical micelle, ϕ_{lmc}, (red triangles), the volume fraction of spherical micelle dimers, ϕ_{ds}, (orange triangles) and the volume fraction of small spherical micelles, ϕ_{smc}, (green circles) at the initial stage of $PSMA_{31}$–$PBzMA_{2000}$ diblock copolymer synthesis in mineral oil at 90 °C (during 2-6 minutes of the synthesis) obtained by SAXS analysis using MT-II_ls-ds-ss morphology transition model (eq 4.14). Time-dependence of the volume fractions of spherical micelle dimers, ϕ_{ds}, and the volume fraction of small spherical micelles, ϕ_{smc}, during 8-14 minutes of the synthesis are presented by results obtained from SAXS analysis using MT-I_ds-s model (Figure 4.7) (blue squares and purple circles, respectively). The measured points are connected by lines for a guidance only.

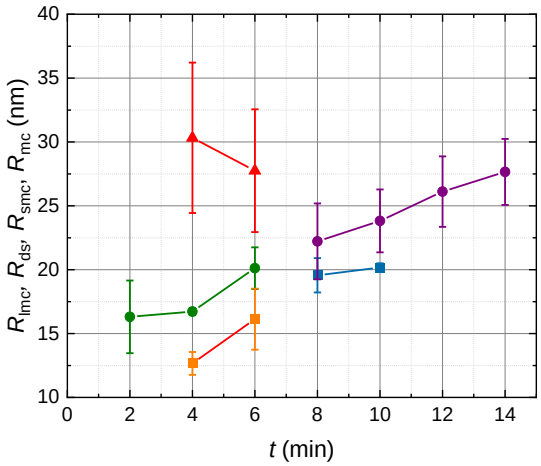

Figure 4.19**.** Time-dependence of the mean core radius of the large spherical micelles, R_{lmc}, (red triangles), the mean core radius of the dimer spherical micelles, R_{ds}, (orange squares) and the mean core radius of small spherical micelles, R_{smc}, (green circles) at the initial stage of $PSMA_{31}$–$PBzMA_{2000}$ diblock copolymer synthesis in mineral oil at 90 °C (during 2-6 minutes of the synthesis) obtained by SAXS analysis using the MT-II_ls-ds-ss morphology transition model (eq 4.14). Time-dependence of the mean core radius of the dimer spherical micelles, R_{ds}, and the mean core radius of small spherical micelles, R_{smc}, during 8-14 minutes of the synthesis are presented by results obtained from SAXS analysis using MT-I_ds-s model (Figure 4.8) (blue squares and purple circles, respectively). The measured points are connected by lines for a guidance only. The bars show respective standard deviations of the measured radii.

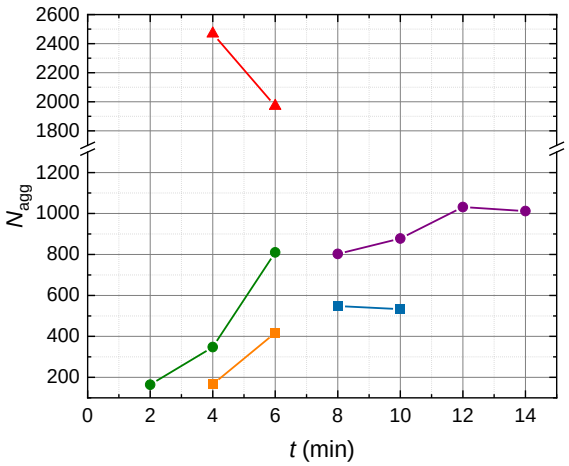

Figure 4.20**.** Time-dependence of the mean copolymer aggregation number, N_{agg}, of the large spherical micelles, N_{agg_lmc}, (red triangles), the dimer spherical micelles, N_{agg_ds}, (orange squares) and the small spherical micelles, N_{agg_smc}, (green circles) at the initial stage of $PSMA_{31}$–$PBzMA_{2000}$ diblock copolymer synthesis in mineral oil at 90 °C (during 2-6 minutes of the synthesis) calculated from results obtained by SAXS analysis using MT-II_ls-ds-ss morphology transition model (eq 4.14). Time-dependence of the mean copolymer aggregation number, N_{agg}, of the dimer spherical micelles, N_{agg_ds}, and the small spherical micelles, N_{agg_smc}, during 8-14 minutes of the synthesis are presented by results obtained from SAXS analysis using MT-I_ds-s model (Figure 4.9) (blue squares and purple circles, respectively).

4.7.3 MT-III_cs Particle Morphology Transition Model

Following the result that the suspension particle as core-shell structure model produced the best fit to the experimental SAXS pattern collected after 2 minutes of $PSMA_{31}$-$PBzMA_{2000}$ synthesis [Figure 4.4 (c)], this particle morphology could be selected as the starting point for analyzing time-resolved SAXS patterns corresponding to the initial stage of the synthesis (2-14 minutes of the synthesis). However, this particle model on its own would fail to fit SAXS patterns collected during 4-14 minutes of the synthesis. It has to be noted that particle morphology transition models incorporating particle dimers (MT-I_ds-s and MT-II_ls-ds-ss models), suggested by the PDDF analysis (Figure 4.2), produced results contradicting to physical principles of the particle system development. Assuming that a single population of core-shell suspension particles is formed at the beginning of the synthesis (after 2 minutes), the obtained PDDFs, especially the pair-distance distribution function corresponding to 4 minutes of the synthesis (Figure 4.2), could be interpreted as a product of at least two populations of spherical particles. Thus, a particle morphology transition model incorporating large and small suspension particles with core-shell structural morphology was tested for fitting SAXS patterns collected during 2-14 minutes of $PSMA_{31}$-$PBzMA_{2000}$ synthesis. This model (MT-III_cs) produced a good fit to the SAXS patterns corresponding to 4 min (Figure 4.21) and 6 min (Figure 4.18). However, the model was not successful to produce a reasonable fit to the patterns collected at a later stage (Figure 4.18). The SAXS analysis of the reaction products at 4 min indicated that the volume fractions of the large suspension particles and the small suspension particles were 0.0016 and 0.0089, respectively. The core radii of the large suspension particles and the small suspension particles were 14.9 ± 7.5 and 0.7 ± 0.18nm, and the total particle radii were 29.2 ± 8.0 and 15.0 ± 1.7 nm, respectively. The SAXS analysis of the products at 6 min of the synthesis has shown that the volume fractions of the large suspension particles and the small suspension particles were 0.0018 and 0.0075, respectively. The core radii of the large suspension particles and the small suspension particles were 20.1 ± 0.1 and 0.63 ± 0.16 nm, and the total particle radii were 36.5 ± 2.1 and 17.0 ± 1.7 nm, respectively. Thus, the MT-III_cs model suggests that particle radius for both populations of the suspension particles increase during the first 2 – 6 min of the synthesis. Also, the core radius measured for the small suspension particles was less than 5 % of the total particle radius, which could indicate that such small suspension particles with a core-shell structure should be considered as spherical micelles rather than core-shell suspension particles. Meanwhile, the copolymer aggregation number of the small suspension particles estimated from the SAXS fitting results increased from 130 at 2 min to 235 at 4 min, and then to 397 at 6 min. Simultaneously, the copolymer aggregation number of the large suspension particles increased from 2013 at 4 min to 3930 at 6 min. Thus, comparing to the SAXS analysis results obtained from MT-I_ds-s and MT-II_ls-ds-ss models (Figures 4.9 and 4.16), there is no obvious relationship between the aggregation numbers produced by the MT-III_cs model for both suspension particle populations. Nevertheless, the obtained results may indicate that the large suspension particles release diblock copolymer chains or small diblock copolymer particles to form spherical micelles. The failure of the proposed MT-III_cs model to fit SAXS patterns after 8 minutes of synthesis may be related to the confinement that $r_{lsu} - r_{lsu\_c} = r_{ssu} - r_{ssu\_c}$ (eq 4.16), and, as a result, the spherical micelle morphology formed at the later stage may not follow the assumption. A possible solution for resolving this problem, while keeping the number of fitted structural parameters to a minimum, is to replace the two populations of particles with a core-shell morphology used for the MT-III_cs model by an alternative set of particle populations comprised of suspension particles with Gaussian PBzMA block chains and spherical micelles

(Figure 4.7 and eq 4.18). Also, the core radius the small suspension particles as 0.63 ± 0.16 nm were too small to form the proper suspension particle, and therefore, the small suspension particles should be considered as spherical micelles, instead. Thus, this MT-III_cs particle morphology transition model should not be considered as a reasonable transition assumption.

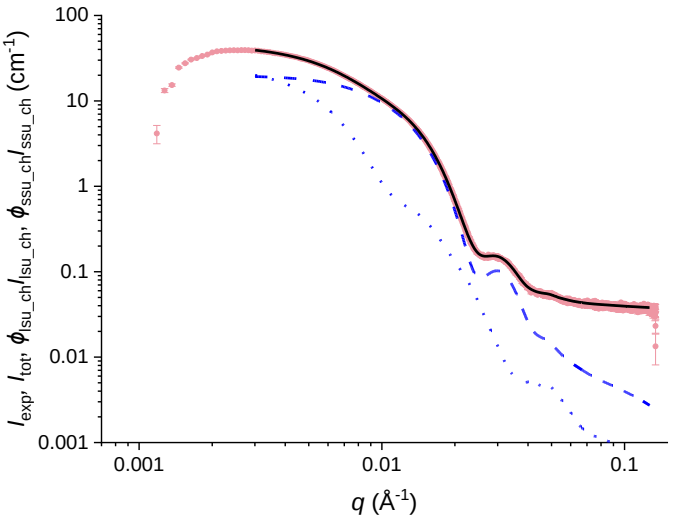

Figure 4.21. SAXS pattern collected during PISA via RAFT synthesis of $PSMA_{31}$–$PBzMA_{2000}$ diblock in mineral oil at 90 °C (frame 2, 4 min), I_{exp}, (symbols) fitted by the MT-III_cs morphology transition model including large suspension particle as core-shell structure and small suspension particle as core-shell structure, I_{tot}, (solid curve). Scattering intensity of separate populations are shown by blue dashes (large suspension particles as core-shell structure, $\phi_{lsu\_ch}I_{lsu\_ch}$) and blue dots (small suspension particles as core-shell structure, $\phi_{ssu\_ch}I_{ssu\_ch}$).

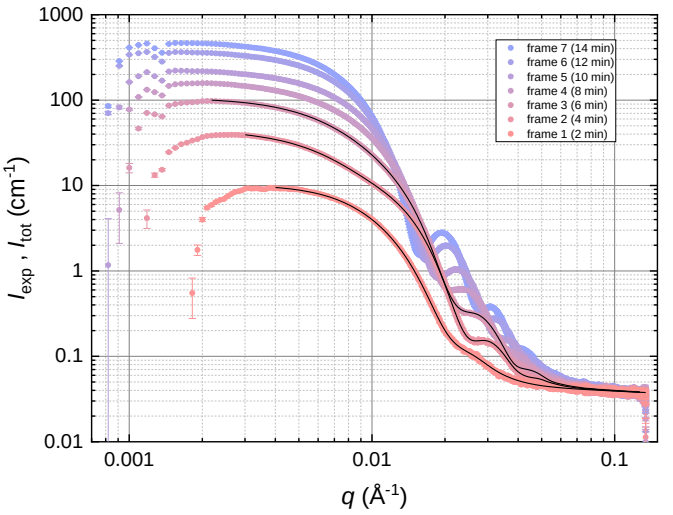

Figure 4.22. Experimental SAXS patterns (circles), recorded every 2 min from 2 min (frame 1) to 14 min (frame 7) during PISA via RAFT synthesis of $PSMA_{31}$–$PBzMA_{2000}$ diblock copolymers in mineral oil at 90 °C with respective fitting curves (solid lines) produced by MT-III_cs morphology transition model including large suspension particle

as core-shell structure and small suspension particle as core-shell structure (eq 4.16).

4.7.4 MT-IV_GC-s Particle Morphology Transition Model

To avoid physical restrictions imposed by the equality of shell thickness of the large and small core-shell suspension particles an alternative model (MT-IV_GC-s) has been considered for analyzing SAXS patterns collected at the initial stage of the $PSMA_{31}$-$PBzMA_{2000}$ synthesis. The MT-IV_GC-s model is based on a principle of two (large and small) particle populations similar to the MT-III_cs model but using a different approach for the particle morphology description. In particular, the two populations of particles in this model are represented by the suspension particles with Gaussian PBzMA block chains (Figure 4.3, left) and spherical diblock copolymer micelles (Figure 4.8) (eq 4.18). In analogy to the MT-III_cs model the alternative MT-IV_GC-s model produced a good fit to the SAXS pattern recorded after 4 minutes of the synthesis (compare Figure 4.17 and Figure 4.23). Thus, the proposed MT-IV_GC-s model was fitted to the other SAXS patterns corresponding to 6-14 minutes of the synthesis. It was found that the model could produce reasonably good fits to all of the analyzed SAXS patterns (Figure 4.24). PDDFs of these SAXS fittings (Figure 4.25) presented similar patterns as the PDDF results of original SAXS patterns (Figure 4.2). The analysis revealed that the spherical micelle population had appeared after 4 minutes of the synthesis, and it had been the dominating particle population after its appearance (Figure 4.26). The mean radius of the suspension particles with Gaussian PBzMA block chains increases from about 16 nm at 2minutes to about 28 nm at 4 minutes and remains at this level until this population of particles disappears at 12 minutes of the synthesis (Figure 4.26). The mean core radius of the spherical micelles gradually grows after their appearance at 4 minutes. The copolymer aggregation number of the suspension particles with Gaussian PBzMA block chains increases during the first 2-8 minutes of the synthesis, when the particle size increases, and then the aggregation number reduces to around 1200 (Figure 4.28). The aggregation number of the spherical micelles continuously increase to 1200 during the analyzed period simultaneously with the micelle size growth. It has to be noted that the MT-IV_GC-s model fitted to the SAXS patterns produced values of the monomer conversion and the volume fractions of the components in the particle cores very similar to the MT-I_ds-s model results (Figures 4.10 and 4.11, respectively). A combined analysis of the particle radii (Figure 4.22) and the population volume fractions (Figure 4.21) suggests that the overwhelming majority of the suspension particles changes into the spherical micelles at the initial stage between 2 to 4 minutes of the sysnthesis. Possibly, with the increasing volume fraction of the PBzMA block in the particles causing fast expelling of the solvent turns the suspension particles into spherical micelles. Meanwhile, the radius of gyration of the Gaussian core block chains of the suspension particles were compared with the estimations (Figure 4.27). The estimations of R_{g_co} at 2 min was given when PBzMA core block chains were fully extended as $l_c/2\sqrt{3}$, 3.68 nm, and the estimations during 4 - 14 min were assumed that the conformations of the PBzMA core block chains were Gaussian chains. Compared with estimations of R_{g_co}, the SAXS modelling results of R_{g_co}, which were all assumed as Guassian chains and modelled by Debye function (equations 2.20 and 2.24), during 4 – 14 min indicated that the PBzMA core block chains could be described as Gaussian chains. Thus, the results obtained by using the MT-IV_GC-s model show no significant contradictions in a comparison with the other three (MT-I_ds-s, MT-II_ls-ds-ss, and MT-III_cs) models. Despite of the contradictions the three unsuccessful morphological transition models as well as the MT-IV_GC-s model pointed out that the large suspension particles after their

formation transform to spherical micelles at the later stage of the synthesis (Figure 4.30). In this PISA process, the PSMA-PBzMA diblock copolymers firstly form suspension particles (step 1 in Figure 4.30), and then these suspension particles transform into spherical micelles by releasing diblock copolymer chains and/or relatively small particles, and/or a possible fission of the large suspension particles into dimers (step 2 in Figure 4.30). And eventually, only spherical micelles are present in the system at the later synthesis stage (step 3 in Figure 4.30). Unfortunately, the process of the transformations from the large suspension particles to the spherical micelles were not fully clarified by the performed SAXS analysis. Therefore, it cannot connivingly determine the morphologies only by PDDF analysis, though the PDDFs of these SAXS fittings were similar with PDDFs of original SAXS patterns.

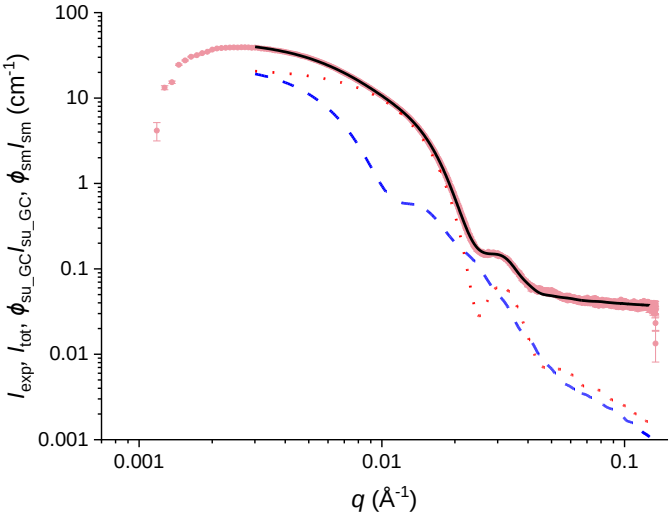

Figure 4.23**.** SAXS pattern collected during PISA via RAFT synthesis of $PSMA_{31}$–$PBzMA_{2000}$ diblock in mineral oil at 90 °C (frame 2, 4 min), I_{exp}, (symbols) fitted by the MT-IV_GC-s morphology transition model including suspension particles with Gaussian PBzMA block chains and spherical micelles, I_{tot}, (solid curve). Scattering intensity of separate populations are shown by blue dots (the suspension particles with Gaussian PBzMA block chains, $\phi_{su\_GC}I_{su\_GC}$) and red dashes (the spherical micelles, $\phi_{sm}I_{sm}$).

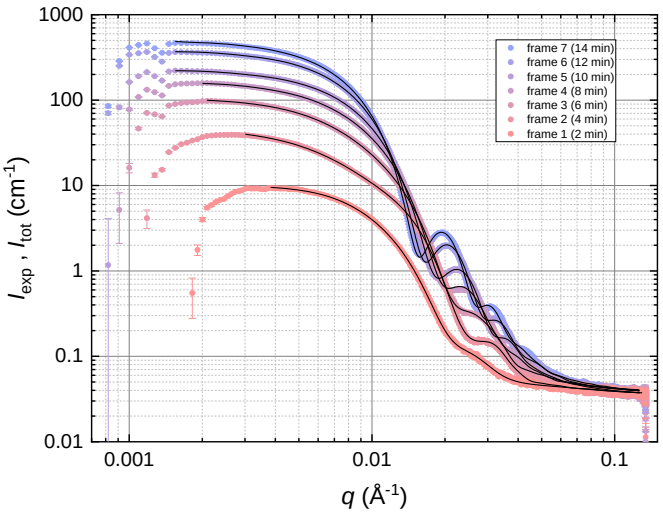

Figure 4.24**.** Experimental SAXS patterns (circles), recorded every 2 min from 2 min (frame 1) to 14 min (frame 7) during PISA via RAFT synthesis of $PSMA_{31}$–$PBzMA_{2000}$ diblock copolymers in mineral oil at 90 °C with respective fitting curves (solid lines) produced by the MT-IV_GC-s morphology transition model including suspension particles with Gaussian PBzMA block chains and spherical micelles (eq 4.18).

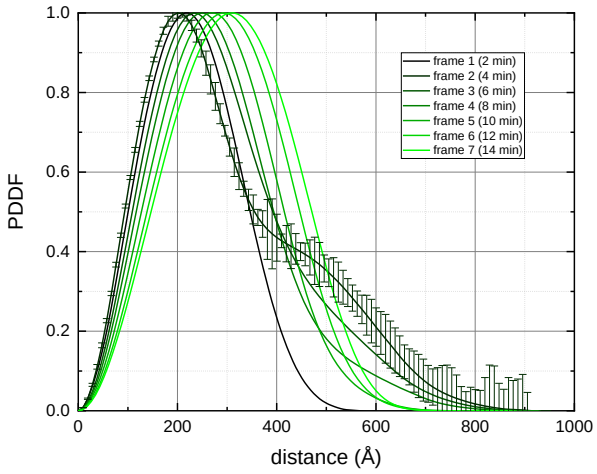

Figure 4.25**.** Normalized pair-distance distribution functions (PDDFs) obtained from model fitting curves of eq SAXS patterns with representative error bars are shown for PDDFs associated with frame 2.

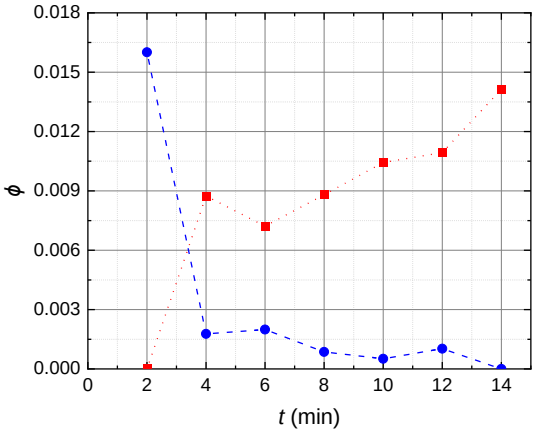

Figure 4.26**.** Time-dependence of the volume fraction of suspension particles with Gaussian PBzMA block chains, ϕ_{su_GC}, (blue circles) and the volume fraction of spherical micelles, ϕ_{sm}, (red squares) at the initial stage of $PSMA_{31}$–$PBzMA_{2000}$ diblock copolymer synthesis in mineral oil at 90 °C (during 2-14 minutes of the synthesis) obtained by SAXS analysis using the MT-IV_GC-s morphology transition model (eq 4.18). The measured points are connected by dash and dot lines for a guidance only.

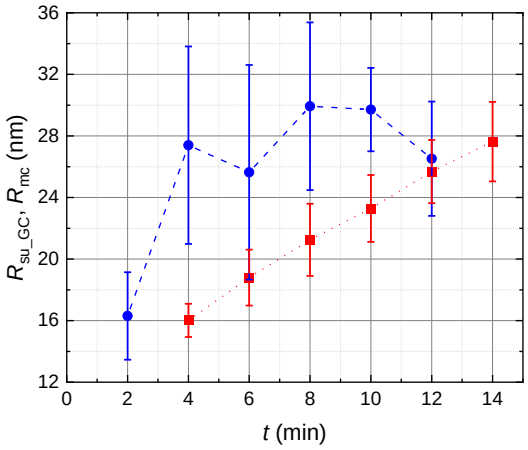

Figure 4.27**.** Time-dependence of the mean radius of the suspension particles with Gaussian PBzMA block chains, R_{su_GC}, (blue circles) and the mean radius of the spherical micelle cores, R_{mc}, (red squares) at the initial stage of $PSMA_{31}$–$PBzMA_{2000}$ diblock copolymer synthesis in mineral oil at 90 °C (during 2-14 minutes of the synthesis) obtained by SAXS analysis using the MT-IV_GC-s morphology transition model (eq 4.18). The measured points are connected by dash and dot lines for a guidance only. The bars show respective standard deviations of the measured radii.

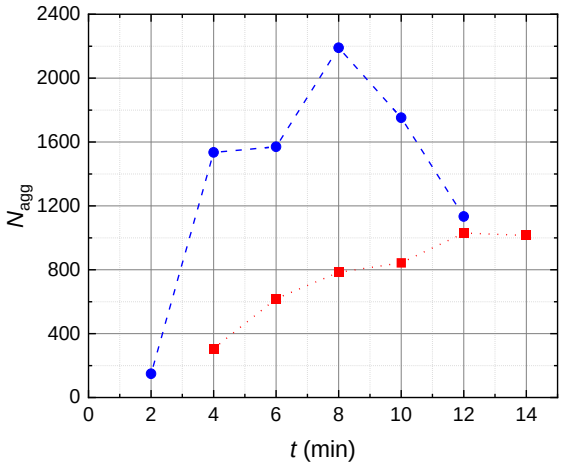

Figure 4.28**.** Time-dependence of the mean copolymer aggregation number, N_{agg}, of the suspension particles with Gaussian PBzMA block chains, $N_{agg\_su\_GC}$, (blue circles) and the spherical micelles, N_{agg_sm}, (red squares) at the initial stage of $PSMA_{31}$–$PBzMA_{2000}$ diblock copolymer synthesis in mineral oil at 90 °C (during 2-14 minutes of the synthesis) calculated from results obtained by SAXS analysis using the MT-IV_GC-s morphology transition model (eq 4.18). The measured points are connected by dash and dot lines for a guidance only.

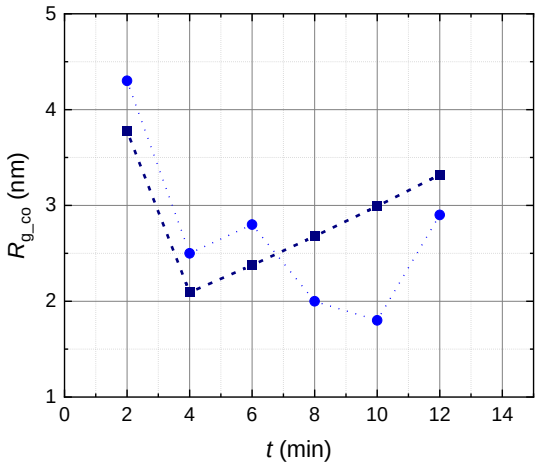

Figure 4.29. Time-dependence of the radius of gyration, R_{g_co}, of the suspension particle Gaussian PBzMA block chains at the initial stage of $PSMA_{31}$–$PBzMA_{2000}$ diblock copolymer synthesis in mineral oil at 90 °C (during 2-12 minutes of the synthesis) obtained by SAXS analysis using the MT-IV_GC-s morphology transition model (eq 4.18) (blue circles) and the estimated from values measured for the BzMA monomer conversion (dark blue squares). The data points are connected by dashed and dotted lines for a guidance only.

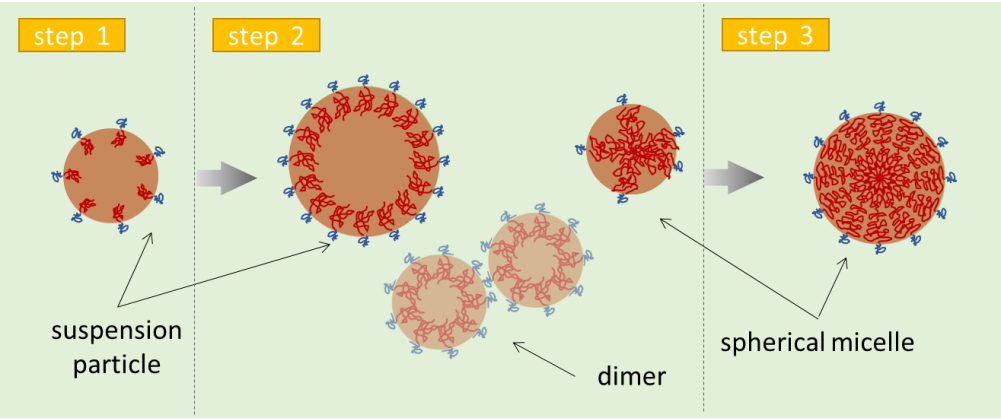

Figure 4.30. A scenario for the particle morphology transition at the initial stage of PISA during RAFT synthesis of $PSMA_{31}$–$PBzMA_{2000}$ diblock copolymers at 90 °C in mineral oil. At the initial step (corresponding to 2 min of synthesis, frame 1 of the SAXS pattern) spherical suspension particles stabilized by short PSMA-PBzMA diblock copolymer chains are formed (step 1). At the next step (corresponding to 4-12 min of synthesis, frames 2-6 of the SAXS data) the suspension particles transformed to spherical micelles where a mixture of the suspension particles, the spherical micelles and potential transient products such as particle dimers could be expected (step 2). At the final step (corresponding to 14 min of synthesis onwards, frame 7 to the last frame of the SAXS data) only spherical copolymer micelles are present (step 3).

The results obtained for the initial stages of $PSMA_{31}$–$PBzMA_{2000}$ diblock copolymer synthesis by fitting the MT-IV_GC-s model to the time-resolved SAXS patterns corresponding to 2-14 minutes of the synthesis could be combined with the SAXS modelling results obtained for later stages of the PISA via RAFT synthesis of $PSMA_{31}$–$PBzMA_{2000}$ diblock copolymers (see Chapter 3). Thus, previously measured R_{mc} of the spherical micelles with its PDI values and volume fractions of the components in the spherical micelle core, the chemical kinetic parameters, and the monomer diffusion parameters can be extended with the results obtained for the initial 4-14 minutes of the synthesis (Figure 4.31, 4.27, and 4.28). The $R_{mc} = k_{R\text{-}DP} \cdot DP^{\omega}$ scaling relation used previously for the micelle core radius (Figure 3.5), could be successfully applied to R_{mc} measured for 4-14 minutes of the synthesis. It was found that the scaling exponent ω = 0.48 (R^2 = 0.992). This parameter is close to 0.5 indicating a weak segregation between the $PSMA_{31}$ block and the PBzMA micelle core block[12]. For the chemical kinetics, a comparison of the rate of polymerisation calculated by eq 3.5, R_{p_BzMA}, and the experimental rate of the monomer conversion during 2 – 14 min, $R_{p\_exp\_BzMA}$, calculated from SAXS results using eq 3.6 has shown that the reduced coefficient $k_{p\_BzMA}' = 3.94 \times 10^{-2}$ min^{-1} = 2.37 h^{-1} obtained from SAXS analysis of later stages of the synthesis, when only the spherical micelles exist (see Chapter 3 and results associated with eq 3.6), could be applied to the initial period of synthesis when no spherical micelles are formed. However, it should be noted that some deviations between $R_{p\_exp\_BzMA}$ and R_{p_BzMA} were observed for the very first (2 - 4) minutes of the synthesis. It was found that parameters describing the monomer transportation from the medium to the copolymer micelle cores such as the diffusion coefficient, $D_{BzMA\_90°C\_est} = 1.06 \times 10^{-9}$ m^2·s^{-1}, Flory-Higgins parameters, $\chi_{SAXS}(\chi_{ms\_SAXS}, \chi_{sp\_SAXS}, \chi_{pm\_SAXS})$ = (0.21, 0.35, -4.69) and traveling distance, $\Delta x_{dri}(t) = 2.26 \times 10^{-3}$ m, determined for the later stages of PISA via RAFT synthesis of $PSMA_{31}$–$PBzMA_{2000}$ diblock copolymers (see eq 3.8 and Figure 3.7), were suitable for describing the monomer diffusion during the initial stages (2 - 14 minutes) of the synthesis when the spherical copolymer micelles just formed (Figure 4.28). Thus, the chemical reaction kinetics and the monomer supply process set at the very beginning of the copolymer micelle formation and hold through the whole course of the reaction.

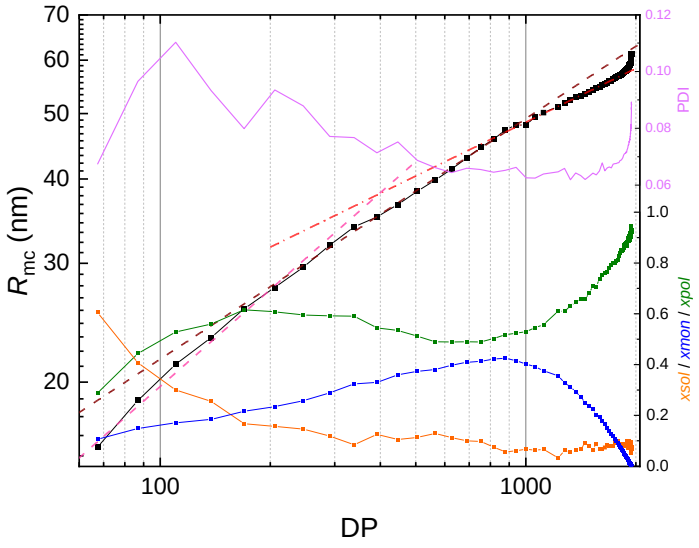

Figure 4.31. Double logarithmic plot of R_{mc} versus DP (black squares), semi-logarithmic plot of PDI of R_{mc} versus DP (pink line), and semi-logarithmic plots of *xmon* (blue triangles), *xsol* (orange circles), and *xpol* (green squares) versus DP obtained from analysis of SAXS data corresponding to later stages (16-194 minutes) of PISA via RAFT synthesis of $PSMA_{31}$–$PBzMA_{2000}$ diblock copolymers at 90 °C in mineral oil (Figure 3.5) extended with analogous results obtained for the initial stage of the synthesis using the MT-IV_GC-s model based on suspension particles with Gaussian PBzMA block chains and spherical micelles. An extra scaling relationship between R_{mc} and DP for the period of 2-14 minutes of synthesis is shown by the purple dash line.

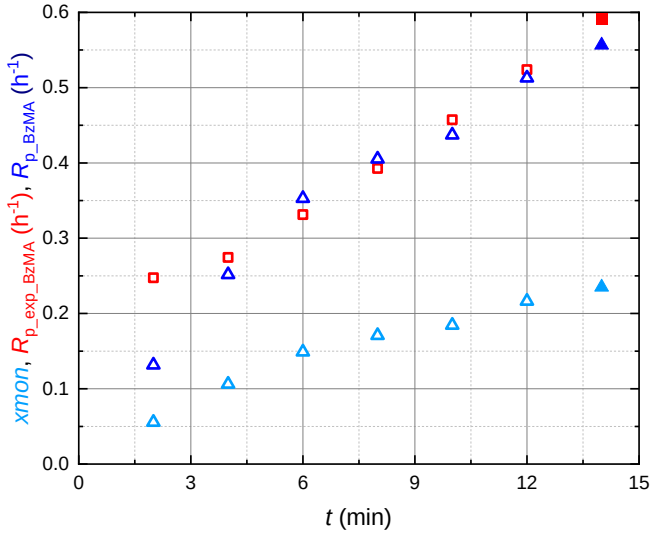

Figure 4.32. Consistent with Figure 3.6, time-dependence of *xmon*, R_{p_BzMA} (calculated using eq 3.5 with the reduced coefficient k_{p_BzMA}'= 3.94 x 10^{-2} min^{-1} = 2.37 h^{-1}) and $R_{p\_exp\_BzMA}$ (calculated using eq 3.6) obtained for the initial stages (2-14 minutes) of PISA via RAFT synthesis of $PSMA_{31}$–$PBzMA_{2000}$ diblock copolymers at 90 °C in mineral oil using the MT-IV_GC-s model based on suspension particles with Gaussian PBzMA block chains and spherical micelles (light blue hollow triangles, dark hollow blue triangles, and red hollow squares, respectively). Pay attention that $R_{p\_exp\_BzMA}$ and R_{p_BzMA} are plotted using h^{-1} units.

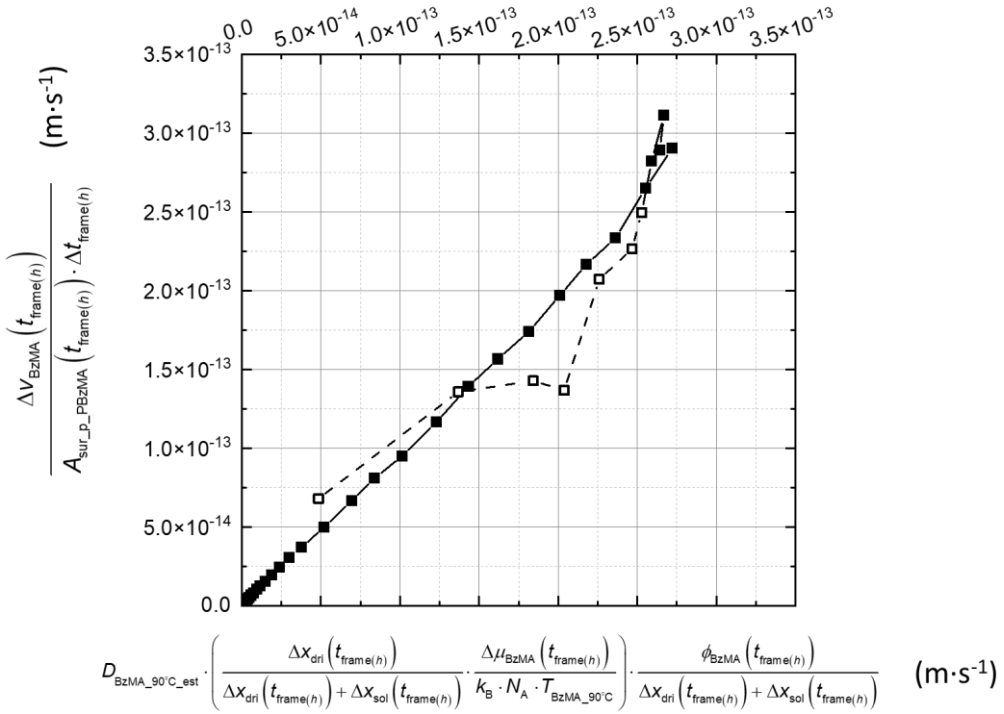

Figure 4.33. Combined with Figure 3.7 presenting the diffusion model with chemical potential effect of PISA process via RAFT synthesis of $PSMA_{31}$–$PBzMA_{2000}$ diblock copolymer at 90 °C in mineral oil at 10% w/w solids (eq 3.8) with $D_{BzMA\_90°C\_est}$ as 1.06×10^{-9} $m^2 \cdot s^{-1}$, χ_{SAXS}(χ_{ms_SAXS}, χ_{sp_SAXS}, χ_{pm_SAXS}) = (0.21, 0.35, -4.69), and $\Delta x_{dri}(t)$ = 2.26×10^{-3} m during 2 – 14 min (black hollow squares) in Chapter 3, , extra total volume change of BzMA monomer (Δv_{BzMA}), the boundary surface area between the medium and the PBzMA spherical micelle cores ($A_{sur\_p\_PBzMA}$), BzMA chemical potential difference between medium and spherical micelle cores ($\Delta\mu_{BzMA}$) now were given by the updated SAXS modelling results by equations 4.6 and 4.18 and then provided $\frac{\Delta v_{BzMA}\left(t_{frame(h)}\right)}{A_{sur\_p\_PBzMA}\left(t_{frame(h)}\right)\cdot\Delta t_{frame(h)}}$ and $D_{BzMA\_90°C\_est}\cdot\left(\frac{\Delta x_{dri}\left(t_{frame(h)}\right)}{\Delta x_{dri}\left(t_{frame(h)}\right)+\Delta x_{sol}\left(t_{frame(h)}\right)}\cdot\frac{\Delta\mu_{BzMA}\left(t_{frame(h)}\right)}{k_B\cdot N_A\cdot T_{BzMA\_90°C}}\right)\cdot\frac{\phi_{BzMA}\left(t_{frame(h)}\right)}{\Delta x_{dri}\left(t_{frame(h)}\right)+\Delta x_{sol}\left(t_{frame(h)}\right)}$ in eq 3.9 (hollow squares). And these squares relatively followed the diffusion model with chemical potential effect described in Chapter 3.

4.8 Conclusion

Experimental SAXS results shows that at the initial stage of RAFT synthesis of $PSMA_{31}$–$PBzMA_{2000}$ diblock copolymers the reaction components and products form a few populations of particles which transform into a single population of copolymer spherical micelles at the

later stage of the synthesis. SAXS model analysis suggested that the first products assembled during the studied reaction correspond to a suspension of spherical particles formed by short copolymer chains locating in the particle shell and a mixture of solvent (mineral oil) and BzMA monomer in the particle core. Pair distance distribution function analysis of the time-resolved SAXS patterns collected during the first 14 minutes of the $PSMA_{31}$–$PBzMA_{2000}$ diblock copolymer synthesis indicated that the copolymer molecules could self-assemble into particles forming dimers. However, the results of SAXS analysis based on structural models, incorporating the dimers of particles including copolymers, did not support the PDDF analysis outcome. A strong inconsistency of the copolymer aggregation numbers, and the particle radii were observed between the populations of particles which could form the dimers and the particles comprising the dimers. Four scattering models have been developed to describe morphological transitions of particles formed at the initial stage of the $PSMA_{31}$–$PBzMA_{2000}$ diblock copolymer synthesis. Each model is composed of a few populations of spherical particles: dimers composed of spherical micelles and single spherical micelles (MT-I_ds-s model); large spherical micelles, dimers composed of spherical micelles and small spherical micelles (MT-II_ls-ds-ss model); large and small suspension particles with core-shell structure (MT-III_cs model); suspension particles with Gaussian PBzMA block chains and spherical micelles (MT-IV_GC-s model). Model fittings to the time-resolved SAXS patterns corresponding to the initial stage of the synthesis have shown that the MT-IV_GC-s model produced the most satisfactory fits and, moreover, physically meaningful structural parameters including the particle radii evolution, the volume fractions of particle populations, the copolymer aggregation numbers. Thus, at the initial stage of the synthesis some reaction components and products can assemble into two populations of particles: a population of spherical particles formed by short PSMA-PBzMA copolymer chains locating in the particle shell and a mixture of solvent (mineral oil) and BzMA monomer in the particle core and a population of spherical PSMA-PBzMA diblock copolymer micelles. The performed SAXS analysis leads to a conclusion that the morphological transition pathway of particles assembled at the initial stage of the $PSMA_{31}$–$PBzMA_{2000}$ diblock copolymer synthesis is composed of three steps: the PSMA-PBzMA diblock copolymers firstly form suspension particles (step 1) and then these suspension particles transform into spherical micelles by releasing diblock copolymer chains and/or relatively small particles, and/or a possible fission of the large suspension particles into dimers (step 2) followed by a single population of spherical micelles present in the system until completion of the synthesis (step 3). Analysis of structural parameters, obtained by fitting the MT-IV_GC-s model to SAXS patterns corresponding to the initial stage of the $PSMA_{31}$–$PBzMA_{2000}$ diblock copolymer synthesis, revealed that the chemical reaction kinetics and the monomer supply process to the reaction point controlled by the monomer diffusion from the medium to the copolymer micelle cores set at the very beginning of the copolymer micelle formation and hold through the whole course of the reaction.

4.9 References

1. Landazuri, G.; Fernandez, V. V. A.; Soltero, J. F. A.; Rharbi, Y., Length of the Core Forming Block Effect on Fusion and Fission Dynamics at Equilibrium in PEO–PPO–PEO Triblock Copolymer Micelles in the Spherical Regime. *Macromolecules* **2021,** *54* (5), 2494-2505.
2. Mykhaylyk, O. O.; Ryan, A. J.; Tzokova, N.; Williams, N., The application of distance distribution functions to structural analysis of core–shell particles. *Journal of Applied Crystallography* **2007,** *40* (s1), s506-s511.

3. Glatter, O.; Kratky, O.; Kratky, H. C., *Small Angle X-ray Scattering*. Academic Press: London, 1982.
4. Danino, D., Cryo-TEM of soft molecular assemblies. *Current opinion in colloid & interface science* **2012,** *17* (6), 316-329.
5. Kuntsche, J.; Horst, J. C.; Bunjes, H., Cryogenic transmission electron microscopy (cryo-TEM) for studying the morphology of colloidal drug delivery systems. *International journal of pharmaceutics* **2011,** *417* (1-2), 120-137.
6. Kinning, D. J.; Thomas, E. L., Hard-sphere interactions between spherical domains in diblock copolymers. *Macromolecules* **1984,** *17* (9), 1712-1718.
7. Flory, P. J., *Principles of Polymer Chemistry*. Cornell University Press: ITHACA, New York, 1953.
8. Fetters, L.; Lohse, D.; Colby, R., Chain dimensions and entanglement spacings. In *Physical properties of polymers handbook*, Springer: 2007; pp 447-454.
9. Zemb, T.; Lindner, P., *Neutrons, X-rays and Light: Scattering Methods Applied to Soft Condensed Matter*. Elsevier: North Holland, 2002.
10. Schweins, R.; Huber, K., Particle scattering factor of pearl necklace chains. *Macromolecular Symposia* **2004,** *211* (1), 25-42.
11. Jones, E. R.; Semsarilar, M.; Wyman, P.; Boerakker, M.; Armes, S. P., Addition of water to an alcoholic RAFT PISA formulation leads to faster kinetics but limits the evolution of copolymer morphology. *Polymer Chemistry* **2016,** *7* (4), 851-859.
12. Matsen, M. W.; Bates, F. S., Unifying weak-and strong-segregation block copolymer theories. *Macromolecules* **1996,** *29* (4), 1091-1098.

Chapter 5: *In Situ* Small-angle X-ray Scattering Studies of Kinetics of Polymerization-induced Self-assembly of Block Copolymers in Polar Media

Chapter 5

In Situ Small-angle X-ray Scattering Studies of Kinetics of Polymerization-induced Self-assembly of Block Copolymers in Polar Media

5.1. Introduction

Because of the wide applications of near-monodisperse polymer nanoparticles[1-4], the synthesis of such polymer nanoparticles has to face various synthesis conditions. In previous Chapters, the PISA synthesis *via* RAFT in mineral oil, or nonpolar system, has been studied by SAXS modelling with mass balance and following chemical kinetics and mass transfer model analysis. This Chapter focuses on PISA via RAFT synthesis of diblock copolymers in a polar medium system. Recent studies of RAFT synthesis of diblock copolymers designed for PISA in alcoholic medium have shown that the copolymers could self-assemble in spherical micelles, worm-like micelles, and vesicles.[5-8]

One of the disadvantages of the RAFT synthesis in alcohol was that the rates of polymerisation were relatively low. For example, RAFT synthesis of benzyl methacrylate (BzMA) block in ethanol using poly(2-(dimethylamino)ethyl methacrylate) (PDMA) as macro-CTA took 12 h – 24 h to reach 99 % BzMA monomer conversion.[9, 10] These findings encouraged further developments of approaches for PISA via RAFT synthesis of copolymers in polar media. One of the approaches was to modify the solvent composition in reaction mixtures. In particular, it was found that a substitution of ethanol by ethanol/water mixture significantly increased rate of polymerization of BzMA monomer during RAFT synthesis of PBzMA-poly(methacrylic acid-*co*-poly(ethylene oxide) monomethyl ether methacrylate) (P(MAA–PEOMA)) diblock copolymers[11] as well as an increase of the rate of polymerisation during homopolymerisation of styrene with PNVP stabilisers[12-14]. These studies indicated that after the nucleation, the polymerisation occurred in the monomer-swollen micelles, which increased the rate of polymerisation. Because water is a poor solvent for styrene and BzMA, the increase of the rate of polymerisation by using an ethanol/water mixture in those studies should be effective for the BzMA block synthesis as the water-based solvent would facilitate self-assembly of copolymers composed of the PBzMA block creating particles acting as nanoreactors accelerating the synthesis. In this respect, a further study on BzMA polymerization during RAFT synthesis of PDMA-PBzMA diblock copolymer was undertaken,[15] which confirmed the increase of the rate of polymerisation of BzMA. However, it could be expected that the morphologies of PDMA-PBzMA self-assembled nanoparticles could change with different water content.

SAXS has been successfully used in the past to obtain detailed information about particle morphologies formed during PISA synthesis of PDMA-PBzMA in ethanol.[10] Herein, SAXS models descried in Chapter 2 are applied for analyzing PISA synthesis of $PDMA_{43}$-$PBzMA_{200}$ in ethanol/water 80/20 mixture. An approach of reaction component mass balance used in

SAXS models developed in Chapter 2 revealed its power in Chapter 3 producing valuable information about particle morphology transitions and reaction kinetics during PISA via RAFT synthesis in nonpolar media. Thus, in this Chapter SAXS modelling will be attempted again for analyzing the particle morphology transition and the reaction kinetics during PISA via RAFT synthesis of diblock copolymer in polar media, in particular, $PDMA_{43}$-$PBzMA_{200}$ copolymer in ethanol/water 80/20 mixture.

5.2. Synthesis of PDMA–PBzMA synthesis in Ethanol/Water 80/20 w/w Mixture

All reagents were purchased from Sigma-Aldrich (UK). RAFT synthesis of $PDMA_{43}$-$PBzMA_{200}$ diblock copolymer in ethanol/water 80/20 w/w mixture at 70 °C as well as the experimental setup for a simultaneous SAXS data collection have been described before.[15] BzMA (0.75 g), $PDMA_{43}$ macro-CTA (0.14 g) and AIBN (1.90 mg, 0.011 mmol) were dissolved in ethanol (5.6 g) and water (1.0 g) as a co-solvent. The reaction mixture sealed in a 10 mL round-bottomed flask and purged with nitrogen gas for 20 min to prevent exposure to oxygen was transferred into a 2 mm diameter glass capillary for X-ray measurements (WJM-Glas, Berlin, Germany) for further SAXS measurement. The reaction was initiated by connecting the brass stage, via a pneumatic switch, to a water circulator pre-heated to 70 °C. The final monomer conversion of the products was determined by ^{1}H NMR analysis in $CDCl_3$ by comparing the integrated PBzMA signal at 4.9 ppm to the integrated signals of the two methylene vinyl groups of BzMA monomer at 5.2 and 5.4 ppm. The final BzMA conversion was measured by ^{1}H NMR to be 99 %, and the number average molecular weight (M_n) was determined by gel permeation chromatography (GPC) to be 31,600 g·mol^{-1} with dispersity index (DI = M_w/M_n) 1.15.[15]

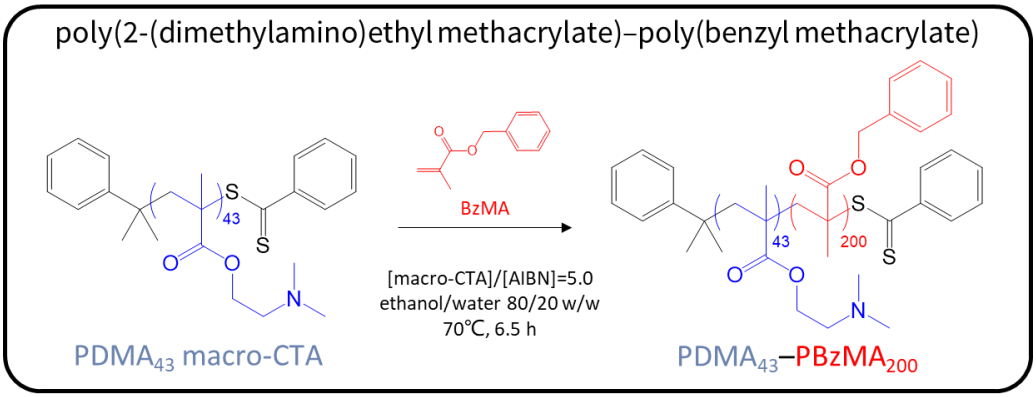

Scheme 3.1 Synthesis of poly(2-(dimethylamino)ethyl methacrylate)–poly(benzyl methacrylate) block copolymer ($PDMA_{43}$–$PBzMA_{200}$) via extension of $PDMA_{43}$ macromolecular chain transfer agent by RAFT of BzMA in ethanol/water 80/20 w/w at 70 °C.

5.3. The Characterisation of PDMA–PBzMA Synthesis in Ethanol/Water 80/20 w/w Mixture

Small-Angle X-ray Scattering (SAXS)

Time-resolved SAXS patterns of PDMA-PBzMA synthesis products were recorded every 64 seconds for 6.5 h at a synchrotron source (European Synchrotron Radiation Facility, ESRF, station ID02, Grenoble, France) by Elizabeth Jones using monochromatic X-ray radiation (λ = 0.995 Å, q range from 0.0003 to 0.25 $Å^{-1}$) and a Rayonix MX-170HS CCD detector. A glass capillary (2 mm diameter) was used as a sample holder. Before the start of SAXS data collection, the reaction was initiated by connecting the holding heating brass stage, via a pneumatic switch, to a water circulator pre-heated to 70 °C. The SAXS pattern of ethanol/water 80/20 background was measured in the glass capillary for 1 s at 70 °C. 2D SAXS patterns were reduced (integrated, normalized by the sample transmission coefficient and calibrated to absolute intensity, I_{exp}, using SAXS patterns of deionized water assuming that the differential scattering cross-section of water at 21 °C is 0.0162 cm^{-1}) to 1D SAXS profiles using SAXSutilities software supplied by ESRF.[16] Calculations and fitting of the SAXS data were performed using *Irena*[17], a macro package for small angle scattering (SAS) data analysis within the commercial *Igor Pro* application. All SAXS models were programmed using a user function option in the *Irena* SAS macros. Confinement relationships between the parameters describing different populations of scattering objects in the studied system, some of the SAXS model parameters were set as global variables.

Density measurement

The densities of liquid compounds at the reaction temperature, 70 °C, were determined by oscillating U-tube method[18] using DMA5000 density meter (Anton Paar, Graz, Austria). To avoid bubble presented during the measurements, the liquid samples were pre-heated to 70 °C. Liquid compounds were kept at 70 °C for further measurements. 3 measurement results were averaged per sample. Although the density repeatability is 0.000001 g/cm^3, densities are presented in three significant digits for further use, which indicates that no uncertainties are given.

Transmission Electron Microscopy (TEM)

Copper/palladium TEM grids (Agar Scientific, UK) were coated in-house to yield a thin film of

amorphous carbon, which were then plasma glow-discharged for 30 s for generating a hydrophilic surface. The synthesised product, diluted by ethanol/water 80/20 w/w mixtures to 0.20% w/w, was placed onto the glow-discharged grids and then the excess solution was blotted by a filter paper. The sample loaded on the grid was stained using a uranyl formate solution (0.75% w/v, 10 µL) at 20 °C, the excess of staining solution was removed after 20 s of its application. The grid was dried by a vacuum hose at the final stage of the sample preparation. TEM images were collected on a Phillips CM100 instrument at 100 kV, the instrument was equipped with a Gatan 1 k CCD camera.

^{1}H NMR Spectroscopy

^{1}H NMR spectra were recorded in C_2D_5OD at 25 °C using a 400 MHz Bruker Avance-400 spectrometer (64 scans averaged per spectrum).

5.4. SAXS Modelling and Assumptions for PDMA–PBzMA synthesis in Ethanol/Water 80/20 w/w Mixture

According to PISA process via RAFT synthesis of diblock copolymers, described in Chapter 2 (Figure 2.3) and the previous research[15], $PDMA_{43}$–$PBzMA_{200}$ copolymers synthesised in 80/20 w/w ethanol/water mixture form spherical micelles from initially soluble molecules. This means that the total scattering intensity of this system can be described by equations 2.3 - 2.5 (see Chapter 2).

The mass densities of BzMA, $PDMA_{43}$, ethanol and water at 70 °C are 0.98 g·cm^{-3}, 1.14 g·cm^{-3} [19], 0.73 g·cm^{-3}, and 0.97 g·cm^{-3} . Thus, the scattering length densities of BzMA, $PDMA_{43}$, ethanol and water at 70 °C can be calculated as 8.91×10^{10} cm^{-2}, 1.00×10^{11} cm^{-2}, 6.96×10^{10} cm^{-2} and 9.16×10^{10} cm^{-2}, respectively. Calculations and fitting of the SAXS data were performed using *Irena*[17], a macro package for small angle scattering (SAS) data analysis within the commercial *Igor Pro* application. The SAXS models were programmed using a user function option in the *Irena* SAS macros. In order to express relationships between time-dependent parameters corresponding to different populations, some of the SAXS model parameters (such as ϕ_{sdp}, ϕ_{sm}, *conv*, *xmon*, *xsol,* R_{g_br}, and f_{sm}) were set as Global Variables in Igor Pro. In order to count the background scattering intensity of the reagent solution, I_{bg}, SAXS measurements of ethanol/water 80/20 mixture was performed. It was found that I_{bg} was about 0.0416 cm^{-1}.

For this PISA synthesis of PDMA–PBzMA copolymer in ethanol/water 80/20 w/w mixture, the solvent was a combination of ethanol and water molecules. Since the solvent contains two compounds, it may be expected that a redistribution of the compounds could take place

between the solvent trapped in the self-assembled micelles and in the surrounding media. Thus, the solvent compositions in the spherical micelle cores would need to be counted in the SAXS modelling. However, this extra fitting parameter, in addition to the others, would increase uncertainties of the SAXS fitting results complicating the analysis. Thus, in order to stabilise the fitting procedure, it was assumed that the ethanol and water content in the spherical micelle cores is the same as their content in the surrounding medium. This assumption further in the text is called as Assumption 1.

5.5. Results and Discussion

TEM results have suggested that the final product of the $PDMA_{43}$–$PBzMA_{200}$ PISA synthesis in 80/20 w/w ethanol/water mixture was spherical micelles (Figure 5.1). The ^{1}H NMR measurements have confirmed that the monomer conversion, after the synthesis completion, is over 99%. Thus, the synthesised PDMA-PBzMA copolymers self-assemble into spherical micelles (Figure 2.1, stage 5) and, therefore, it can be assumed that the final frame of the time-resolved SAXS data (frame 366 recorded at 6.5 h of the synthesis) corresponds to spherical micelles only (Figure 5.2). Indeed, eq 2.2 produced a good fit to the SAXS pattern of the final product (Figure 5.2, top pattern). The SAXS analysis revealed that the spherical micelle core radius R_{mc} = 20.3 nm and its standard deviation $\sigma_{R_{mc}}$ = 2.0 nm and suggesting low PDI of the spherical micelles in the final product. These results are in a good agreement with TEM (Figure 5.2). R_{g_br} in the final product, measured by SAXS, is around 1.9 nm. This value is in a good agreement with a theoretical R_{g_br} value of 1.67 nm estimated by the Gaussian chain model $[(b \cdot l_c/6)^{0.5}]$ [20], where the contour length of corona block ($PDMA_{43}$), l_c, is calculated as the number of repeat units, 43, multiplied by the length of two carbon bonds in an all *trans* configuration, 0.255 nm, and the Kuhn length, b, taken as 1.53 nm (based on data available for PMMA[21]). The SAXS data analysis shows that the spherical micelle model fitting produced results which correlate well with the other techniques.

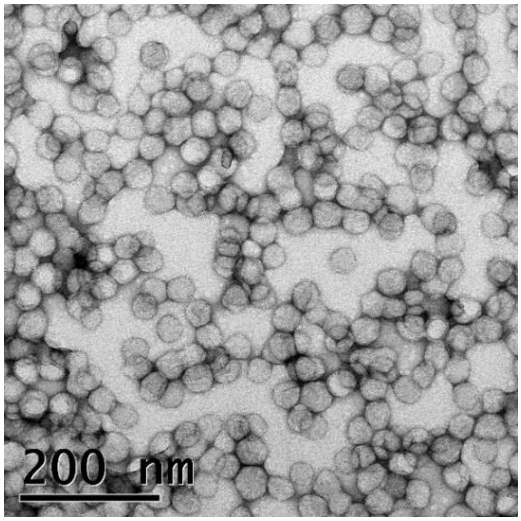

Figure 5.1 TEM image of the final product of PISA process via RAFT synthesis of $PDMA_{43}$–$PBzMA_{200}$ diblock copolymer at 70 °C in 80/20 w/w ethanol/water mixture at 10% w/w solids for 6.5h. The spherical micelle diameter is around 40 nm.

The first frame of time-resolved SAXS patterns collected during the RAFT synthesis of $PDMA_{43}$–$PBzMA_{200}$ diblock copolymers suggests that there are large scattering objects, indicated by the pronounced upturn of scattering intensity at low q, and a relatively small objects, indicated by a shape of the scattering pattern from q = 0.01 $Å^{-1}$ to q = 0.1 $Å^{-1}$ which could be assigned to their Guinier region. This observation is in a good agreement with an expected composition of the initial reagent mixture comprising of large BzMA monomer emulsion droplets and small coils of dissolved $PDMA_{43}$ macro-CTA molecules. Thus, it can be suggested that the first frame of the time-resolved SAXS patterns could correspond to the stage 2 of the PISA process via RAFT synthesis of copolymers (Figure 2.1). Indeed, equations describing scattering intensity of Gaussian polymer chains associated with the stage 2 (eq 2.3) produced a reasonably good fits to the first frame of SAXS data (Figure 5.3). This analysis revealed that the radius of gyration of the dissolved $PDMA_{43}$ polymer chain, R_{g_br}, is around 1.9 nm, which was consistent with the R_{g_br} value measured for the final product. The SAXS model fitting also indicated that the BzMA monomer conversion was around 1.4%. Such a small value is an expected result for the first stage of this synthesis. The fact that the first frame and the last frame of the time-resolved SAXS patterns could be fitted using scattering equations based on a Gaussian polymer coil and spherical micelles of diblock copolymers, respectively, suggests that the entire set of the time-resolved SAXS patterns could be modelled by a combination of these two scattering equations (equations 2.4 and 2.5) which describes stages 3 and 4 (Figure 2.1).

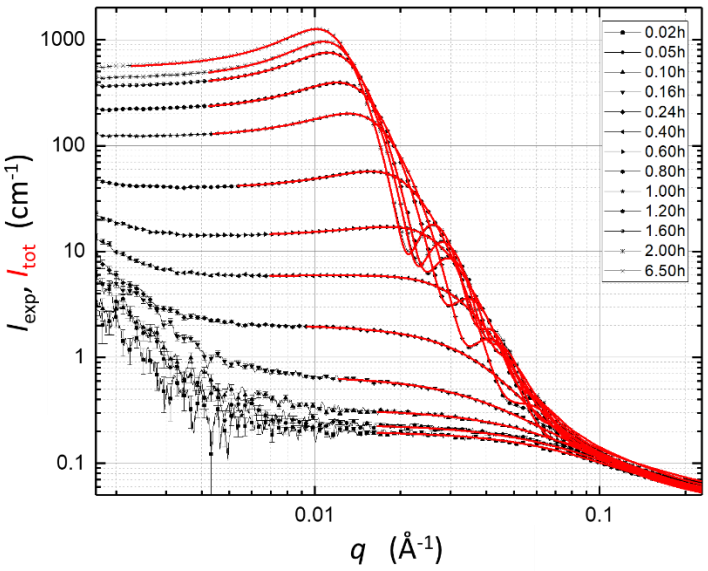

Figure 5.2 Selected experimental time-resolved SAXS patterns, I_{exp}, (black symbols) recorded during PISA process via RAFT synthesis of $PDMA_{43}$–$PBzMA_{200}$ diblock copolymers at 70 °C in 80/20 w/w ethanol/water mixture at 10% w/w solids recorded for 6.5 h. The solid red lines are respective SAXS model fittings.

Scattering equations corresponding to stages 3 and 4 of the PISA process during RAFT synthesis produced fitting curves matching well to time-resolved SAXS patterns recorded for the $PDMA_{43}$–$PBzMA_{200}$ diblock copolymer synthesis (Figure 5.2). It is expected that upon a DP increase, PBzMA blocks become solvophobic resulting at some point of the synthesis in self-assembly of the PDMA-PBzMA copolymers into nanoparticles. It The performed SAXS analysis has shown that copolymer spherical micelles appear at around 0.1 h (frame 6) when the SAXS fitting model indicated that the volume fraction of this population, f_{sm}, in the reaction mixture was about 0.01 (Figure 5.3). This nucleation point of micelles corresponds to the BzMA monomer conversion of 7.9% and the PBzMA DP of 15 (Figure 5.4). There is a dramatic increase of the micelle volume fraction at DP = 22. This increase could be caused by an acceleration of the micelle nucleation process and/or change of the reaction conditions due to a localisation of the BzMA monomer around reaction points inside of the self-assembled copolymer micelles. Details with aggregation number, N_{agg}, and nucleation number, N_{nuc}, of the spherical micelle might produce more information about this process in the following text. A transition from stage 3 to stage 4, the point when all copolymers present in the system self-assemble into particles (f_{sm} = 1) took place at around 0.52 h (Figure 5.3). At the end of the particle formation coinciding with the beginning of the stage 4, the BzMA monomer conversion was around 17.3%, and the corresponding PBzMA DP was around 33 (Figure 5.4).

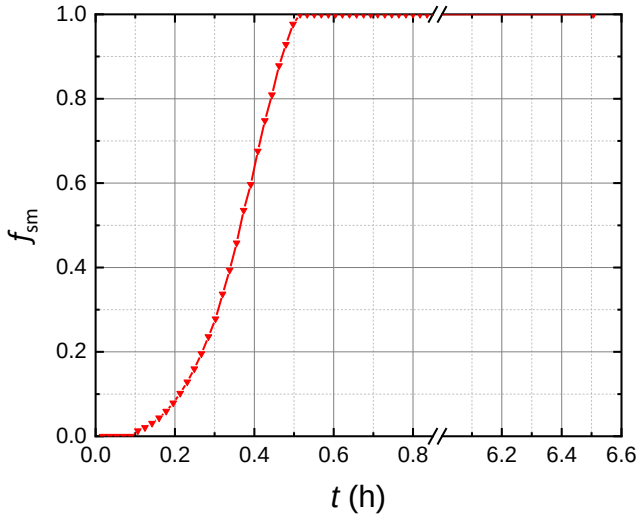

Figure 5.3 Time-dependence of volume fraction of copolymer spherical micelles, f_{sm}, for PISA process via RAFT synthesis of $PDMA_{43}$–$PBzMA_{200}$ diblock copolymers at 70 °C in 80/20 w/w ethanol/water mixture measured from time-resolved SAXS patterns recorded during the synthesis.

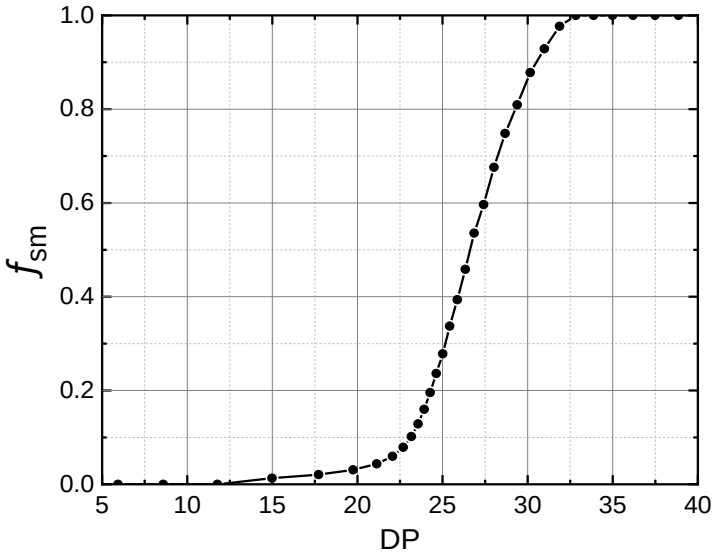

Figure 5.4 Volume fraction of spherical micelles, f_{sm}, vs. PBzMA DP measured by SAXS for the PISA process via RAFT synthesis of $PDMA_{43}$–$PBzMA_{200}$ diblock copolymers (at 70 °C in 80/20 w/w ethanol/water mixture).

The radius of the spherical micelle cores steadily grows after the copolymer particle nucleation (Figure 5.5). However, the PDI of the spherical micelle core radius demonstrates some

fluctuations which are more pronounced during stage 3. It has to be noted that the PDI remains virtually constant at around 0.1 after the synthesis completion at around 2.5 h. However, the PDI before 0.5 h of the reaction was not certainly reliable, because the scattering length intensities of the spherical micelles before 0.5 h was relatively low, and therefore, the scattering intensities of solvent background and soluble polymeric PDMA chains both covered the minimum of spherical micelles. For this reason, the polydispersity of the spherical micelle could not be measured accurately.

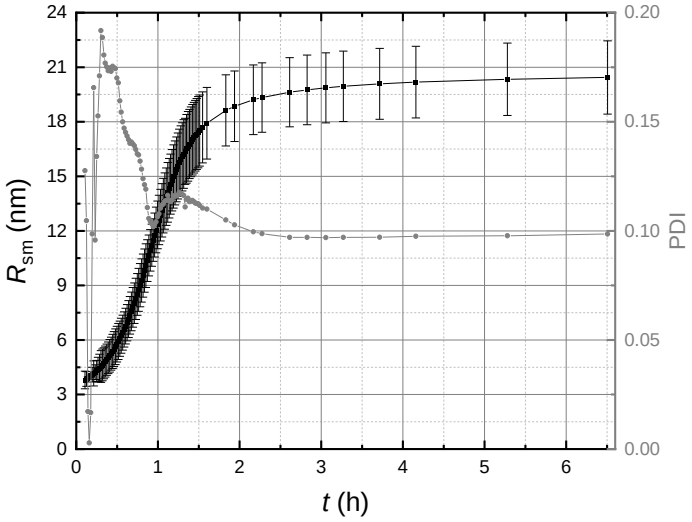

Figure 5.5 Time-dependence of the spherical micelle core mean radius, R_{mc}, (black squares), its standard deviation (shown as error bars) and PDI (grey circles) for the PISA process via RAFT synthesis of $PDMA_{43}$–$PBzMA_{200}$ diblock copolymers at 70 °C in 80/20 w/w ethanol/water mixture measured from time-resolved SAXS patterns recorded during the synthesis.

The BzMA monomer conversion measured by SAXS revealed some acceleration of the BzMA polymerisation (Figure 5.6). For the *in situ* SAXS experiment, the monomer conversion was more than 99% at around 1.9 h. Whereas for the laboratory $PDMA_{43}$–$PBzMA_{200}$ PISA synthesis, the 99% of monomer was converted only after 5 h [15]. Such an acceleration of the synthesis during SAXS measurements is likely to be caused by high-flux X-ray synchrotron radiation.[22] However, the reaction acceleration observed for this RAFT synthesis performed in ionic medium is moderate, mainly at a later stage of the synthesis, in a comparison with the RAFT synthesis in non-ionic medium (PISA process via RAFT synthesis of $PSMA_{31}$–$PBzMA_{2000}$ diblock copolymer at 90 °C in mineral oil at 10% w/w solids, see Chapter 3, Scheme 3.1).

In analogy with the RAFT synthesis in non-ionic medium, BzMA rate of polymerisation can be calculated from SAXS results using the following equation (eq 2.38):

$$R_p(t) = \frac{d[conv(t)]}{dt}. \quad (5.1)$$

It was found that R_p increases until 0.10 h of the synthesis, which corresponds to the nucleation point of PDMA–PBzMA spherical micelles. The R_p value drops suddenly to 0.30 h^{-1} after 0.25 h of the synthesis and then increases once again to the top value of 3.1 h^{-1} at 1.03 h which is followed by a steady decrease to 0 h^{-1} at around 3 h corresponding to 100% BzMA monomer conversion. It has to be noted that the R_p behaviour is in an anti-correlation with PDI of the spherical micelle core radius. The R_p increase before 0.10 h coincides with a relatively low PDI value followed by the R_p decrease between 0.10 h and 0.25 h coinciding with a rapid increase of PDI. The R_p increase between 0.25 h and 1.03 h correlates with a PDI decrease, and then the R_p decrease between 1.03 h and 1.50 h correlates with a slight increase of PDI.

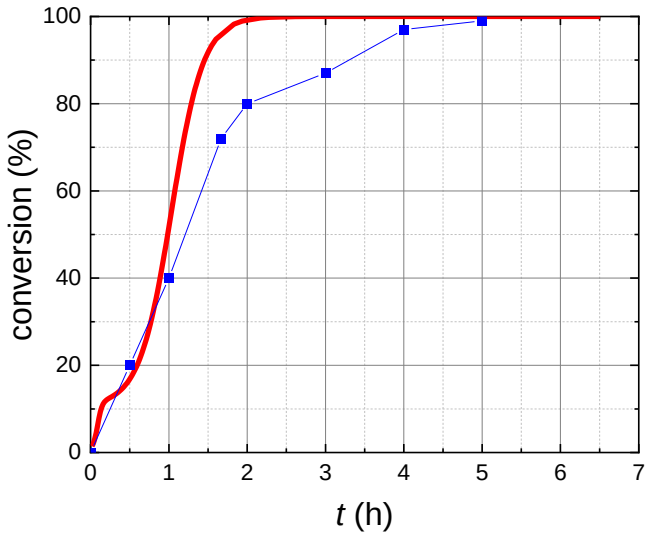

Figure 5.6 Conversion of BzMA monomer during RAFT synthesis of $PDMA_{43}$–$PBzMA_{200}$ diblock copolymers at 70 °C in 80/20 w/w ethanol/water mixture measured by ^{1}H NMR method [15] (blue squares) and by SAXS analysis (red line).

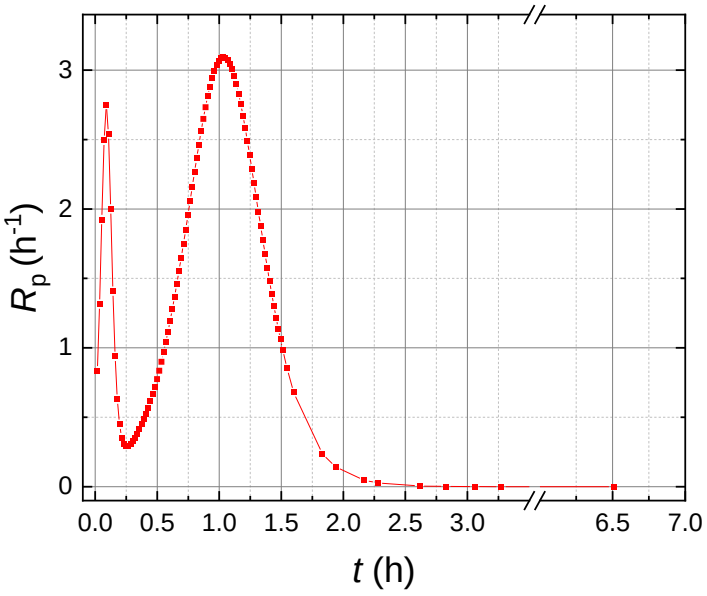

Figure 5.7 Time-dependence of the BzMA polymerisation rate, R_p, measured by SAXS for the PISA process via RAFT synthesis of $PDMA_{43}$–$PBzMA_{200}$ diblock copolymers at 70 °C in 80/20 w/w ethanol/water mixture.

It can be demonstrated that the spherical micelle size increases with the BzMA monomer conversion (Figure 5.8). The R_{mc} increase rapidly at the monomer conversion of about 11% 13%, and the following rate of the R_{mc} increase reduced. This suggests that the increase of volume fraction at PBzMA DP = 22 (Figure 5.4) is preferably related to the micelle growth. After the monomer conversion value reaches 99%, the size of the spherical micelles core mean radius still grows from 19.6 nm to 20.4 nm. This behaviour is very similar to the PISA process via RAFT synthesis of $PSMA_{31}$–$PBzMA_{2000}$ diblock copolymer spheres at 90 °C in mineral oil discussed in Chapter 3 (Figures 3.3). Possibly, in analogy with the PISA in non-ionic medium, the slow particle size increase after the synthesis completion is related to an equilibration process of the spherical micelle self-assembly.

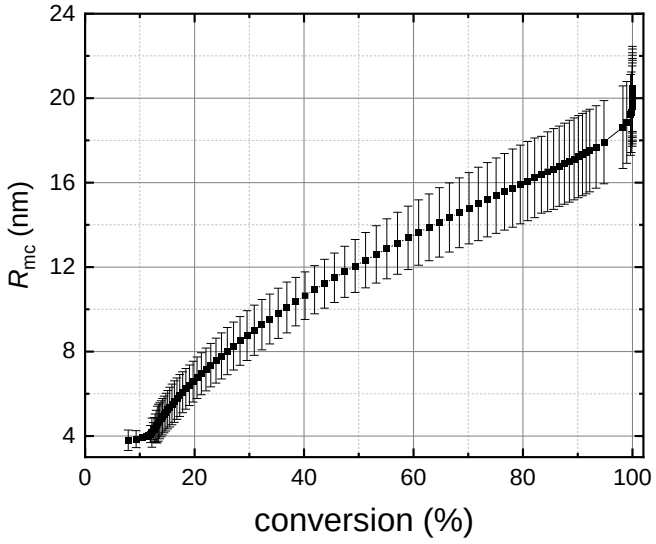

Figure 5.8 Dependence of R_{mc} on the BzMA monomer conversion measured by SAXS during PISA process via RAFT synthesis of $PDMA_{43}$–$PBzMA_{200}$ diblock copolymers at 70 °C in 80/20 w/w ethanol/water mixture. Standard deviations of R_{mc} are shown by the error bars.

The volume fractions of the compounds in the spherical micelle cores could be detected by the SAXS modelling from stage 3 starting at around 0.10 h (Figure 5.9). After the micelle formation, the monomer volume fraction value, *xmon*, after a couple of oscillations, reduces virtually to zero at the final stage of the synthesis (t > 1.5 h) as expected. It has to be noted that the oscillations of *xmon* could be related to the morphological transformations in the system. In particular, the second oscillation of *xmon* starting at 0.5 h coincides with the beginning of stage 4 when no population of free (non-assembled) copolymers is detected. However, the observed oscillations could also be an artefact caused by imperfection of the SAXS model simplifying the studied PISA process. After The volume fraction of the solvent in the micelle cores, *xsol*, rapidly increases after the micelle formation and reaches the top value of 0.35 at 0.5 h. This changes of *xmon* and *xsol* detected by SAXS during stage 3 indicated that the PDMA-PBzMA copolymers might encapsulate a significant amount of BzMA monomer possibly detached from the BzMA emulsion droplets at the very beginning of the initial spherical micelle formation, and then, when more PDMA-PBzMA were captured by the existing spherical micelles, the captured PDMA-PBzMA might drag some solvent molecules into the spherical micelle cores, which resulted in the increase of *xsol*. The rapid *xmon* drop was related to the increase of *xsol*. However, the R_p did not correlate well with the changes of *xmon* and *xsol* observed during stage 3 (Figure 5.7). The drop of *xmon* between 0.10 h and 0.16 h might correspond to the drop of R_p between 0.10 h to 0.16 h, but later the R_p value continued to drop while the *xmon* value remained high between 0.16 h and 0.25 h, even though the f_{sm} value continued increasing. Within 0.16 h and 0.25 h, *xmon* remained around 0.67, which was higher than the volume fraction of the initial BzMA monomer in the whole system (8.1% v/v). Since the *xmon* value stays high during this period, R_p should be increasing, but in fact, R_p reduced from 0.63 h^{-1} to 0.25 h^{-1} (Figure 5.7). At a later stage, 0.25 h < t < 0.50 h, the *xmon* value reduced from 0.83 to 0.40, while R_p increased from

0.31 h^{-1} to 0.83 h^{-1}. This counter-intuitive behaviour observed for *xmon* and R_p may suggest that the SAXS model used for scattering data analysis requires a further improvement. However, the increase of R_p observed during the 0.25-0.5 h period could be a result of the f_{sm} increase.

After the PISA process turned to stage 4 at t = 0.5 h, *xmon* slightly increased from 0.40 to 0.42 at t = 0.65 h, while *xsol* gradually decreased (Figure 5.9). On the contrary, R_p still increased (Figure 5.7). *xmon* continuously decreased between t = 0.65 h and 1.03 h, and *xsol* also gradually decreased. And at t = 1.03 h, *xmon* becomes smaller than *xsol*. Meanwhile, R_p continuously increased between t = 0.65 h and 1.03 h, and R_p reached the top value of 3.09 h^{-1} at 1.03 h. After 1.03 h, *xmon* and R_p were continuously reducing while *xsol* was nearly at a plateau. At t = 1.50 h, while *xmon* reached nearly 0, indicating a full consumption of the monomer available in the system, *xsol* began to decrease again. Meanwhile, the R_p decrease slowed down. This later observation might indicate that the copolymer synthesis from t = 1.50 h to 2.00 h depends on the diffusion of the BzMA monomer, still remaining in the medium, to the spherical micelle cores. The described, rather complex, behaviour of the reaction components shows that in contrast to the synthesis in non-polar media no linear relationship is observed between *xmon* and R_p during PISA via RAFT synthesis of $PDMA_{43}$–$PBzMA_{200}$ at 70 °C in 80/20 w/w ethanol/water mixture.

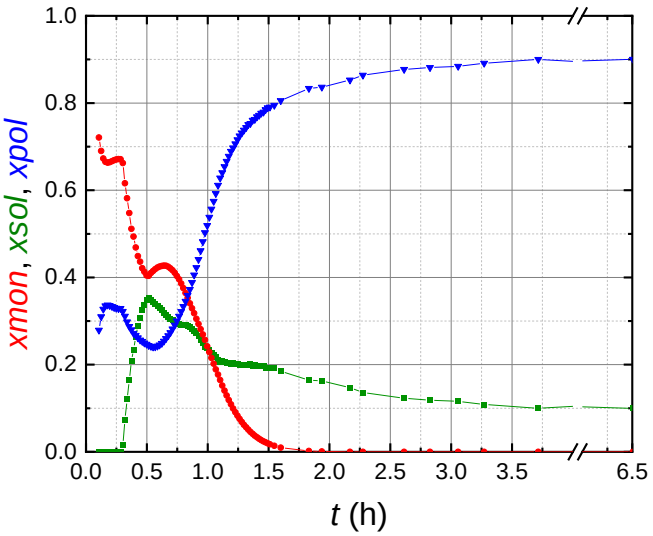

Figure 5.9 Time-dependence of the volume fractions of the compounds in the spherical micelle cores (*xmon*, red circles; *xsol*, green squares; and *xpol*, blue triangles) measured by SAXS during PISA process via RAFT synthesis of $PDMA_{43}$–$PBzMA_{200}$ diblock copolymers at 70 °C in 80/20 w/w ethanol/water mixture.

For a further discussion of the $PDMA_{43}$–$PBzMA_{200}$ diblock copolymer spherical micelle formation during PISA, a few more indicative structural parameters were considered: N_{agg} (Figure 5.10), normalised amount of spherical micelles in the system (N_{nuc}) (Figure 5.11), S_{agg}

(Figure 5.12), and d_{int} (Figure 5.13). Here, N_{nuc} is given as N_p/N_A, with eq 2.51. N_{agg} slightly increased during a period of time from 0.10 h to 0.50 h, corresponding to stage 3. At a later stage, during period of t = 0.50 h to 1.50 h, N_{agg} rapidly increased to 400 h. After completion of the polymerisation reaction at t = 2.50 h, N_{agg} was increasing further. This behaviour, similar to the PISA process in non-polar media (Figure 3.3), is dictated by the fact that R_{mc} of the spherical particles continue to increase and *xsol* decreases after the reaction completion. The relative amount of spherical particles increases drastically up to 0.88 mmol at the beginning of the synthesis during stage 3 (0.10 h < t < 0.50 h) (Figure 5.11). After reaching the peak value during the micelle nucleation process, N_{nuc} rapidly decreases to 0.13 mmol at 1.03 h. This observation is consistent with the polymerisation rate development as at this time point R_p. reaches its maximum (Figure 5.7). The N_{nuc} decrease may indicate that a spherical micelle fusion takes place during stage 4 and stage 5. At a later stage N_{nuc} decreases further to a plateau value of 0.04 mmol (Figure 5.11). The density of copolymer packing on the micelle surface, S_{agg}, after the micelle nucleation reduces from 0.09 nm^{-2} to 0.06 nm^{-2} at the end of stage 3. S_{agg} rapidly increases to 0.10 at around 1.25 h after which S_{agg} gradually increases to 0.13 nm^{-2} at 3.25 h and remains at this value for the rest of SAXS measurements. Another characteristic parameter of the copolymer surface packing is the average distance between adjacent chains in the micelle interface, d_{int}, which can be compared with R_{g_br} of $PDMA_{43}$ (measured by SAXS as 1.9 nm). Since R_{g_br} is radius of gyration of $PDMA_{43}$, it could be suggested that d_{int} between the $PDMA_{43}$ chains freely packed on the micelle surface chould be twice as R_{g_br}. This means that when d_{int} is smaller than 3.8 nm, $PDMA_{43}$ could be entangled with other $PDMA_{43}$ chains or compressed by neighbouring molecules. SAXS results have shown that d_{int} certainly increases during stage 3 from 3.3 nm to 4.2 nm and then it decreases to 3.2 nm at t = 1.25 h. After 1.25 h, d_{int} gradually decreases to 2.8 nm at t = 3.25 h and remains at this value virtually unchanged until the end of SAXS measurements. Thus, at a later stage of the PISA process d_{int} is less than $2R_{g\_br}$. This observation suggests that the $PDMA_{43}$ blocks in the final spherical micelles are compressed by the neighbouring molecules and extended along the micelle radius. It was reported previously that $PDMA_{43}$–$PBzMA_{200}$ copolymers during PISA process in either alcohol or alcohol/water 80/20 medium could assemble into either vesicles or spherical micelles.[15]

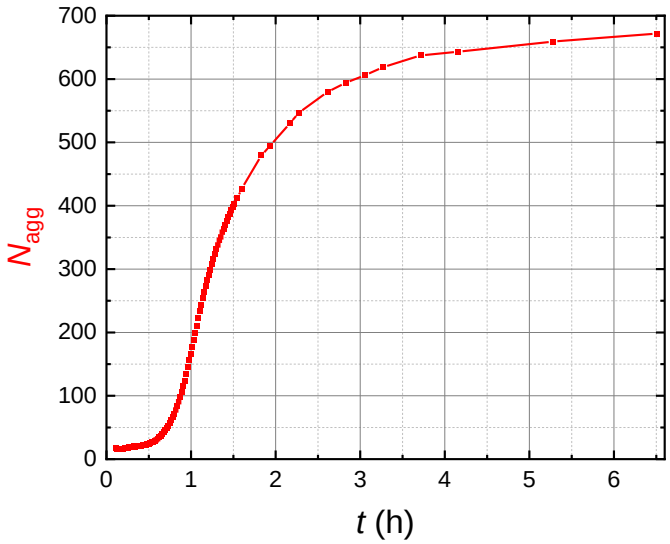

Figure 5.10 Time-dependence of copolymer aggregation number in the spherical micelle, N_{agg}, measured by SAXS for the PISA process via RAFT synthesis of $PDMA_{43}$–$PBzMA_{200}$ diblock copolymers at 70 °C in 80/20 w/w ethanol/water mixture.

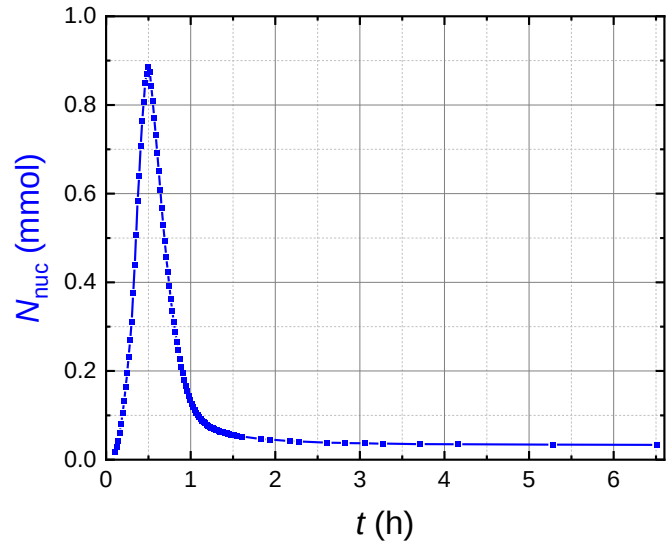

Figure 5.11 Time-dependence of the normalised number of spherical micelles in the system, N_{nuc}, measured by SAXS for the PISA process via RAFT synthesis of $PDMA_{43}$–$PBzMA_{200}$ diblock copolymers at 70 °C in 80/20 w/w ethanol/water mixture.

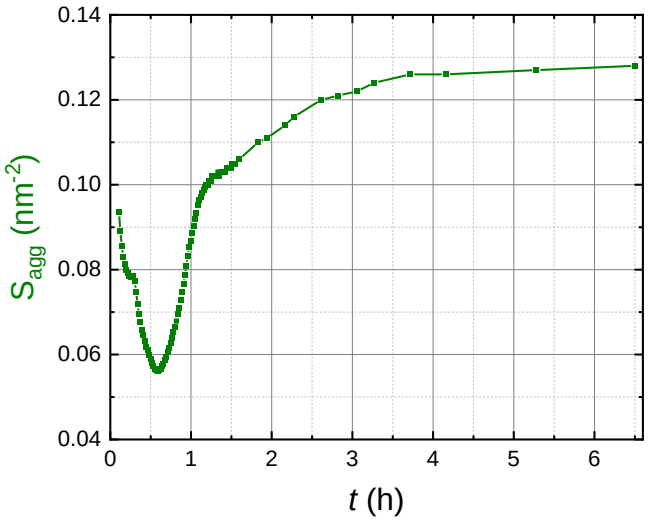

Figure 5.12 Time-dependence of the copolymer packing density on the micelle surface, S_{agg}, measured by SAXS for the PISA process via RAFT synthesis of $PDMA_{43}$–$PBzMA_{200}$ diblock copolymers at 70 °C in 80/20 w/w ethanol/water mixture.

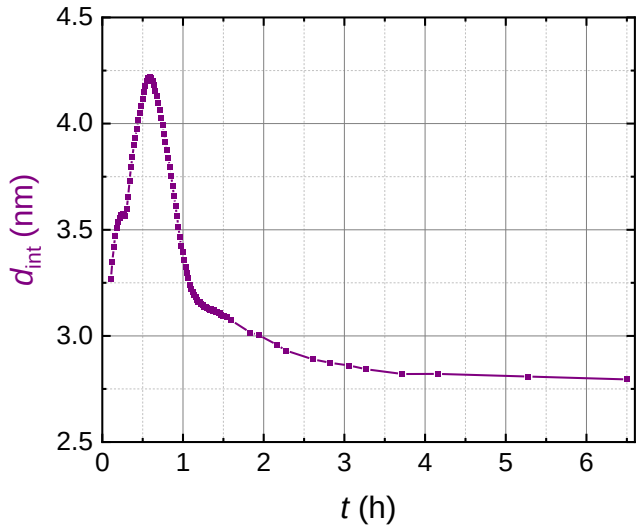

Figure 5.13 Time-dependence of the average distance between adjacent chains in the micelle interface, d_{int}, measured by SAXS for the PISA process via RAFT synthesis of $PDMA_{43}$–$PBzMA_{200}$ diblock copolymers at 70 °C in 80/20 w/w ethanol/water mixture.

The discussion of results produced by SAXS analysis where it was assumed that the solvent

composition in the spherical micelle cores is the same as in the surrounding media (Assumption 1) has demonstrated some contradiction between the measured structural parameters. This indicates that the structural model based on the Assumption 1 may not be realistic and a redistribution of the solvent components (ethanol and water) between the micelle particles and the medium may take place. Since an addition of water into a reagent mixture dominated by alcohol can promote the rate of polymerisation and change the morphological transition of the self-assembled nanoparticles,[15] the composition of the solvent in the spherical micelle cores can be assigned to ethanol only (Assumption 2). However, fitting of the experimental SAXS patterns using a model based on the Assumption 2 was not as successful as the fitting based on the assumption that the solvent, located in the micelle cores, is composed of the 80/20 w/w ethanol/water mixture. The Assumption 2 model produced good fits to the experimental time-resolved SAXS patterns corresponding to the period of synthesis when the studied system is dominated by spherical micelles (after 0.82 h). However, no satisfactory fitting parameters were obtained for the initial period corresponding to the micelle nucleation (stage 3). In particular, large fluctuations of the BzMA conversion were obtained for this initial period. Therefore, only SAXS analysis results corresponding to $t > 0.82$ h are considered in the further discussion (Figure 5.14).

Since only solvent composition of the micelle cores differentiates models based on Assumption 1 and Assumption 2, the mean micelle core radius and its standard deviation obtained by both models are the same. In contrast to the model based on Assumption 1, the Assumption 2 model demonstrated that no BzMA monomer was in the spherical micelle cores. Thus, according to this result *xmon* could be close to 0 during the PISA process (Figure 5.14). The volume fraction of the solvent, *xsol*, (or to be more specific, the volume fraction of the ethanol) gradually reduces from $t = 0.82$ h to 1.25 h and then slightly changes at a later stage. Trends observed for *xsol* values obtained by SAXS analysis using Assumption 1 and Assumption 2 are similar after 0.82 h. The *xsol* value of the final product measured using Assumption 2 (0.16) is slightly higher than the result produced by Assumption 1. Both results indicate that the spherical micelle cores were swollen by the solvent molecules in the final product. In analogy to the copolymer system synthesised in non-polar medium (Chapter 3), a scaling power law relation was applied to establish a relationship between the diblock copolymer micelle core mean radius and PBzMA DP. It was found that $R_{mc} \sim DP^{0.667}$ ($R^2 = 0.999$) (Figure 5.15). This exponent of 0.667 indicates a strong segregation[23] between PDMA and PBzMA in 80/20 w/w ethanol/water mixture. According to this exponent of 0.667, given $v = 0.50$ by eq 1.48, also indicates that PBzMA blocks in spherical micelle cores could be considered as ideal chains with around 20 percentages volume fraction of solvent presented in the spherical micelle cores. In addition, the SAXS modelling using Assumption 2 cannot reach nucleation process (Figure 2.1, stage 3) but the SAXS modelling using Assumption 1 detailly provides nucleation process. This indicated that the solvent compositions during spherical micelle nucleation process should be the mixture of ethanol and water.

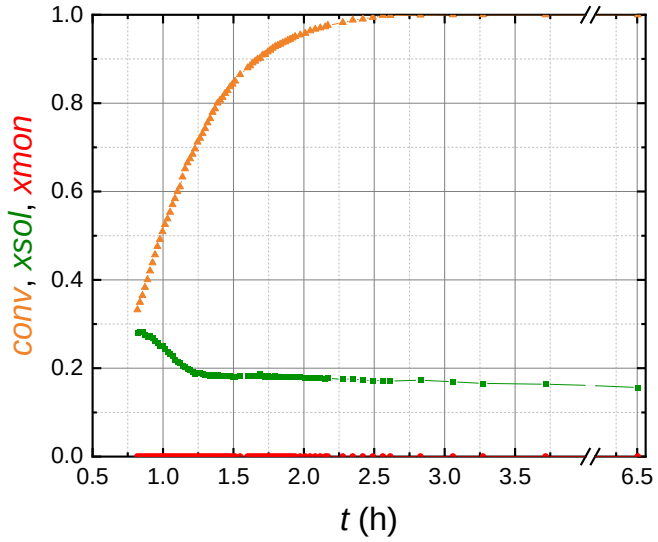

Figure 5.14 Time-dependence of the BzMA monomer conversion, *conv* (orange triangles), the monomer volume fraction in the micelle cores, *xmon* (red squares) and the ethanol volume fraction in the micelle cores, *xsol* (green triangles) measured by SAXS for the PISA via RAFT synthesis of $PDMA_{43}$–$PBzMA_{200}$ diblock copolymers at 70 °C in 80/20 w/w ethanol/water mixture with Assumption 2.

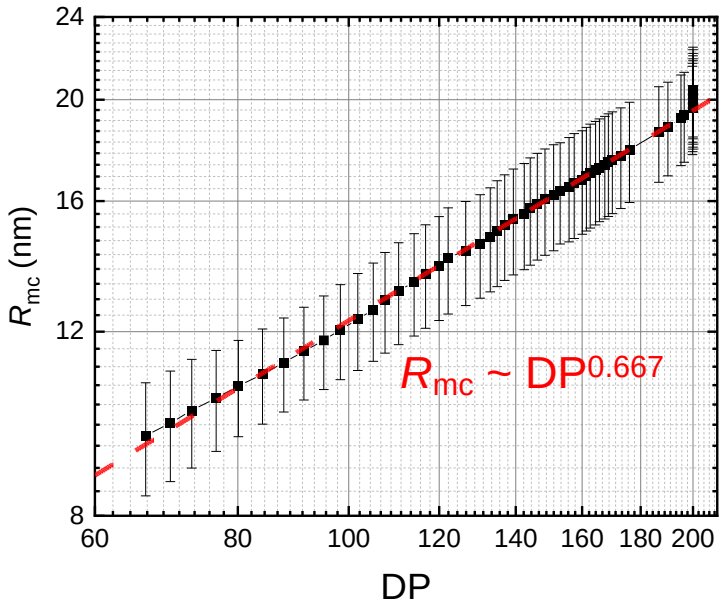

Figure 5.15 A double logarithmic plot of relationship between R_{mc} of diblock copolymer micelles formed during $PDMA_{43}$–$PBzMA_{200}$ synthesis at 70 °C in 80/20 w/w ethanol/water mixture and PBzMA DP (squares). The error bars show standard deviation of R_{mc} curve in log-log plot. The red dashed line shows a scaling power law relation between R_{mc} and DP with the exponent of 0.667 with Assumption 2.

The spherical micelle growth after the end of polymerisation might also be led by Ostwald ripening, and therefore, following eq 3.5 and the constant functioned fitted from 5.5 h to 6.5 h (Figure 5.16), the increase of the spherical micelle core radius resulted from Ostwald ripening after 5.0 h. Compared with *conv* and *xsol* (Figure 5.16), though BzMA monomer conversion reached 100 % at 3 h, the expelling of ethanol solvent molecules from the spherical micelle cores mainly controlled the spherical micelle core increase until 5.0 h of the SAXS data collection. In addition, the PDI of the spherical micelle core radius turned to increase after the spherical micelle core growth relied on Ostwald ripening, which has been observed in Chapter 3.

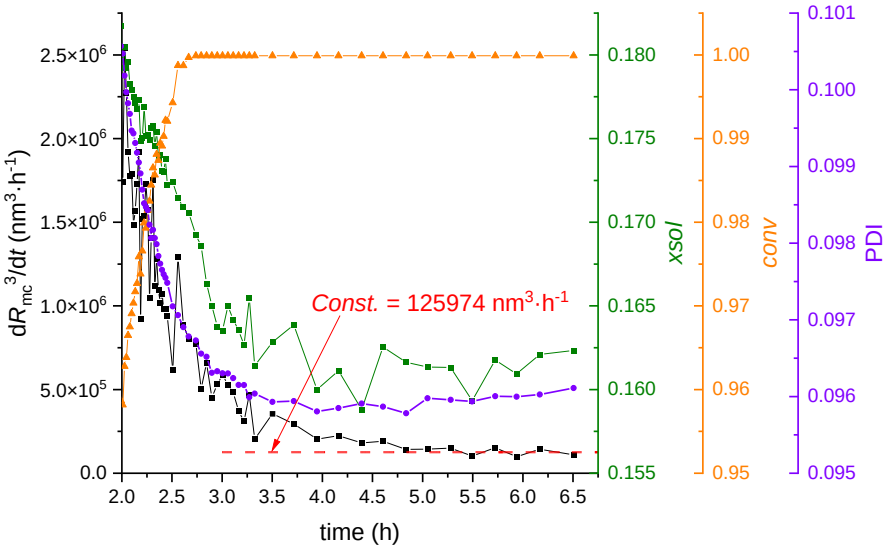

Figure 5.16 dR_{mc}^3/dt (black squares), *xsol* (green squares), *conv* (orange triangles), and the PDI of spherical micelle core (purple circles) vs. time curve of PISA process via RAFT synthesis of $PDMA_{43}$–$PBzMA_{200}$ synthesis at 70 °C in 80/20 w/w ethanol/water mixture with Assumption 2. Data fitting (red dash line) by a constant function (eq 3.5) from 5.5 h to 6.5 h provided a reference for the possible Ostwald ripening process after the end of polymerisation.

The absence of the monomer in the spherical micelle cores, determined by SAXS analysis using Assumption 2, indicated that the rate of polymerisation of the $PDMA_{43}$–$PBzMA_{200}$ PISA synthesis might be controlled by the BzMA monomer diffusion only. When the BzMA monomer diffused in the spherical micelle cores, the polymerisation in the spherical micelle core was too fast to allow the BzMA monomer to be detected by the SAXS analysis. This situation was different from the $PSMA_{31}$-$PBzMA_{2000}$ PISA synthesis. Thus, the Fick's first law, without considering the chemical potentials for the $PDMA_{43}$–$PBzMA_{200}$ PISA synthesis, can be given as:

$$J_{\mathrm{BzMA}}(t) = D_{\mathrm{BzMA}} \frac{\Delta\phi_{\mathrm{BzMA}}(t)}{\Delta x_{\mathrm{BzMA}}(t)}, \tag{5.2}$$

where D_{BzMA} is the diffusion coefficient for BzMA at reaction temperature, 70 °C, $\Delta\phi_{\mathrm{BzMA}}(t)$ is a change of ϕ_{BzMA} during time period from t+Δt to t, and $\Delta x_{\mathrm{BzMA}}(t)$ is given as $\sqrt{\frac{3v_{\mathrm{BzMA}}(t)}{4\pi R_{\mathrm{sm}}(t)}}$ at t according to eq 2.54. $J_{\mathrm{BzMA}}(t)$ is the diffusion flux of the BzMA at t, which could be calculated from experimental SAXS results as

$$J_{\mathrm{BzMA}}(t) = \frac{\Delta v_{\mathrm{BzMA}}(t)}{A_{\mathrm{mc}}(t) \cdot \Delta t}, \tag{5.3}$$

where Δv_{BzMA} is the BzMA volume change during the period of time from t+Δt to t, defined as $v_{\mathrm{BzMA}}(t+\Delta t)$-$v_{\mathrm{BzMA}}(t)$, and $A_{\mathrm{mc}}(t)$ is the total surface area of the spherical micelle cores at time t, defined as $\frac{3v_{\mathrm{BzMA}}(t)}{R_{\mathrm{sm}}(t)}$. Thus, equations 5.2 and 5.3 enable D_{BzMA} to be measured using a least square fitting minimizing the difference between $J_{\mathrm{BzMA}}(t)$ and $\Delta\phi_{\mathrm{BzMA}}(t)/\Delta x_{\mathrm{BzMA}}(t)$, $\mathrm{MIN}\left\{\frac{1}{n_{\mathrm{frame}}-1}\sqrt{\sum_{h=1}^{n_{\mathrm{frame}}}\left[J_{\mathrm{BzMA}}\left(t_{\mathrm{frame}(h)}\right)-D_{\mathrm{BzMA}}\frac{\Delta\phi_{\mathrm{BzMA}}\left(t_{\mathrm{frame}(h)}\right)}{\Delta x_{\mathrm{BzMA}}\left(t_{\mathrm{frame}(h)}\right)}\right]^2}\right\}$, where n_{frame} is the total number of recorded frames. A linear regression between $J_{\mathrm{BzMA}}(t)$ and $\Delta\phi_{\mathrm{BzMA}}(t)/\Delta x_{\mathrm{BzMA}}(t)$ produced D_{BzMA} = 1.17 × 10^{-10} $m^2 \cdot s^{-1}$ (Figure 5.16). The diffusion coefficient, $D_{\mathrm{BzMA\_est}}$, could be expressed as $(k_B T_{\mathrm{BzMA}})/(6\pi \cdot \eta_{\mathrm{ethonal}} \cdot R_{\mathrm{BzMA}})$, where T_{BzMA} is the reaction temperature, 70 °C, η_{ethonal} is the viscosity of ethanol and R_{BzMA} is the hydrodynamic radius of the BzMA molecule. The reason why the viscosity of the solvent was taken to equal to the ethanol viscosity is because water is not a dominant component of the solvent and BzMA molecules might prefer to stay close to ethanol. R_{BzMA}, estimated by $[(3M_{\mathrm{BzMA}})/(4\pi \cdot \rho_{\mathrm{BzMA}})]^{1/3}$, is 6.32 × 10^{-10} m. Therefore, $D_{\mathrm{BzMA\_est}}$ is given as 1.21 × 10^{-9} $m^2 \cdot s^{-1}$, which is 10 times larger than D_{BzMA} obtained from SAXS results using the linear regression between $J_{\mathrm{TFEMA}}(t)$ and $\Delta\phi_{\mathrm{TFEMA}}(t)/\Delta x_{\mathrm{TFEMA}}(t)$. One of reasons for such inconsistency could be the fact that chemical potentials where not counted in eq 5.2.

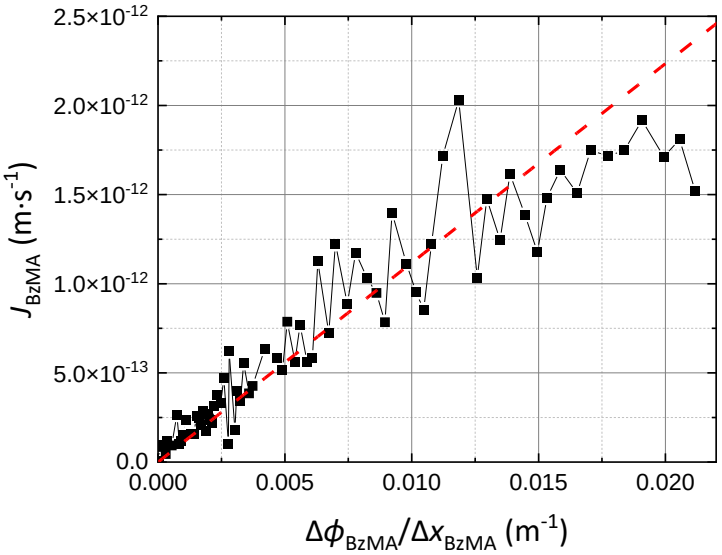

Figure 5.17 The fitted linear relationships (red dashed line) between the diffusion flux of the BzMA at t and the $\Delta\phi_{BzMA}(t)/\Delta x_{BzMA}(t)$ of the SAXS modelling results (black squares) by eq 5.2 gave the diffusion coefficient of BzMA in ethanol/water 80/20 w/w mixture at 70 °C as 1.17 × 10^{-10} $m^2 \cdot s^{-1}$, which was significantly smaller than estimated diffusion coefficient of BzMA by Stokes-Einstein equation.

Therefore, the simplified approach used for the BzMA diffusion should be revisited using eq 2.55:

$$\frac{\Delta v_{BzMA}\left(t_{frame(h)}\right)}{A_{mc}\left(t_{frame(h)}\right)\cdot\Delta t_{frame(h)}} = D_{BzMA\_70^{\circ}C\_est}\cdot\left(\frac{\Delta x_{dri}\left(t_{frame(h)}\right)}{\Delta x_{dri}\left(t_{frame(h)}\right)+\Delta x_{sol}\left(t_{frame(h)}\right)}\cdot\frac{\Delta\mu_{BzMA}\left(t_{frame(h)}\right)}{k_B\cdot N_A\cdot T}\right)\cdot\frac{\phi_{BzMA}\left(t_{frame(h)}\right)}{\Delta x_{dri}\left(t_{frame(h)}\right)+\Delta x_{sol}\left(t_{frame(h)}\right)} \quad (5.4)$$

The BzMA chemical potential difference, $\Delta\mu_{BzMA}$, in eq 5.4 could be considered as chemical potential difference of BzMA molecules between in ethanol/water 80/20 w/w mixture and in pure BzMA liquid. Thus, $\Delta\mu_{BzMA}$ can be expressed as:

$$\Delta\mu_{BzMA} = k_B T_{BzMA\_70^{\circ}C}\begin{pmatrix}\ln c_{ex\_mon}\\ +\chi_{mE}\cdot c_{ex\_mon}\cdot c_{ex\_EtOH}\\ +\chi_{mw}\cdot c_{ex\_mon}\cdot c_{ex\_water}\\ -\chi_{wE}\cdot c_{ex\_water}\cdot c_{ex\_EtOH}\end{pmatrix}, \quad (5.5)$$

where χ_{mE}, χ_{mw}, and χ_{wE} are Flory-Higgins parameters of monomer-ethanol, monomer-water, and water-ethanol pairs, respectively, and c_{ex_mon}, c_{ex_EtOH}, and c_{ex_water} are volume fractions of BzMA monomer, ethanol and water outside of the spherical micelle cores, respectively. Using eq 1.52 and known Hansen solubility parameters of ethanol and water as [15.8, 8.8, 19.4]

and [15.5, 16, 42.8],[24, 25] respetviely, χ_{mE}, χ_{mw}, and χ_{wE} can be calculated as 1.53, 2.93, and 1.05, respectively. Therefore, the only parameter of eq 5.4 remaining undefined is Δx_{dri}. In analogy to the PISA in non-polar medium (Chapter 3), this parameter is considered to be constant and does not change over the reaction course. This parameter can be calculated from SAXS results using least square fitting of

$$\mathrm{MIN}\left\{\frac{1}{n_{frame}-51}\sqrt{\sum_{h=51}^{n_{frame}-51}\left[\frac{\Delta v_{BzMA}\left(t_{frame(h)}\right)}{A_{sur\_p\_PBzMA}\left(t_{frame(h)}\right)\cdot\Delta t_{frame(h)}} - D_{BzMA\_70^{\circ}C\_est}\cdot\left(\frac{\Delta x_{dri}\left(t_{frame(h)}\right)}{\Delta x_{dri}\left(t_{frame(h)}\right)+\Delta x_{sol}\left(t_{frame(h)}\right)}\cdot\frac{\Delta\mu_{BzMA}\left(t_{frame(h)}\right)}{k_B\cdot N_A\cdot T_{BzMA\_70^{\circ}C}}\right)\cdot\frac{\phi_{BzMA}\left(t_{frame(h)}\right)}{\Delta x_{dri}\left(t_{frame(h)}\right)+\Delta x_{sol}\left(t_{frame(h)}\right)}\right]^2}\right\}$$

. It was found that $\Delta x_{dri}(t) = 8.09 \times 10^{-2}$ m (R^2=0.970) (Figure 5.18). The linear relationship between $\frac{\Delta v_{BzMA}\left(t_{frame(h)}\right)}{A_{mc}\left(t_{frame(h)}\right)\cdot\Delta t_{frame(h)}}$ and $D_{BzMA\_70^{\circ}C\_est}\cdot\left(\frac{\Delta x_{dri}\left(t_{frame(h)}\right)}{\Delta x_{dri}\left(t_{frame(h)}\right)+\Delta x_{sol}\left(t_{frame(h)}\right)}\cdot\frac{\Delta\mu_{BzMA}\left(t_{frame(h)}\right)}{k_B\cdot N_A\cdot T_{BzMA\_70^{\circ}C}}\right)\cdot\frac{\phi_{BzMA}\left(t_{frame(h)}\right)}{\Delta x_{dri}\left(t_{frame(h)}\right)+\Delta x_{sol}\left(t_{frame(h)}\right)}$ indicated that the proposed diffusion model with chemical potentials (eq 5.4) could reasonably well describe the monomer supply process. Compared with clear dispersion polymerisation in Chapter 3, the travelling distance with chemical potential effect, Δx_{dri}, of PDMA-PBzMA in ethanol/water mixture was significant longer than PSMA-PBzMA in mineral oil. This indicated the repulsion of BzMA monomer from water molecules. Therefore, this polymerisation might be not clearly classified as dispersion polymerisation. And possibly, BzMA emulsions might exit during the polymerisation (observed by SAXS in Figure 5.2), though such PISA synthesis of $PDMA_{43}$–$PBzMA_{200}$ diblock copolymers at 70 °C in ethanol/water 80/20 w/w mixture at 70 °C was commented as dispersion polymerisation previously[9, 15]. These research[9, 15] also observed kinetically trapped spherical micelles of PDMA-PBzMA synthesis in ethanol/water 82.5/17.5 w/w and 80/20 w/w mixture. The explanation given in these research[9, 15] was that the cationic PDMA blocks avoided the fusion of the spherical micelles with low Zeta potential on the particle surfaces when water was added in the system. However, such kinetically trapped spherical micelles[26-32] were highly likely to be observed in PISA synthesis by emulsion polymerisation. Also, with SAXS modelling with mass balance, no detectable monomer was in the spherical micelle cores using Assumption 2. This finding was also against the comment[15] that the addition of water could increase the local monomer concentration (or monomer concentration in the spherical micelle cores). And because there was no detectable monomer in the spherical micelle cores, this polymerisation was diffusion-controlled reaction. For these reasons, this polymerisation could be classified as emulsion polymerisation rather than dispersion polymerisation against previous research[9, 15].

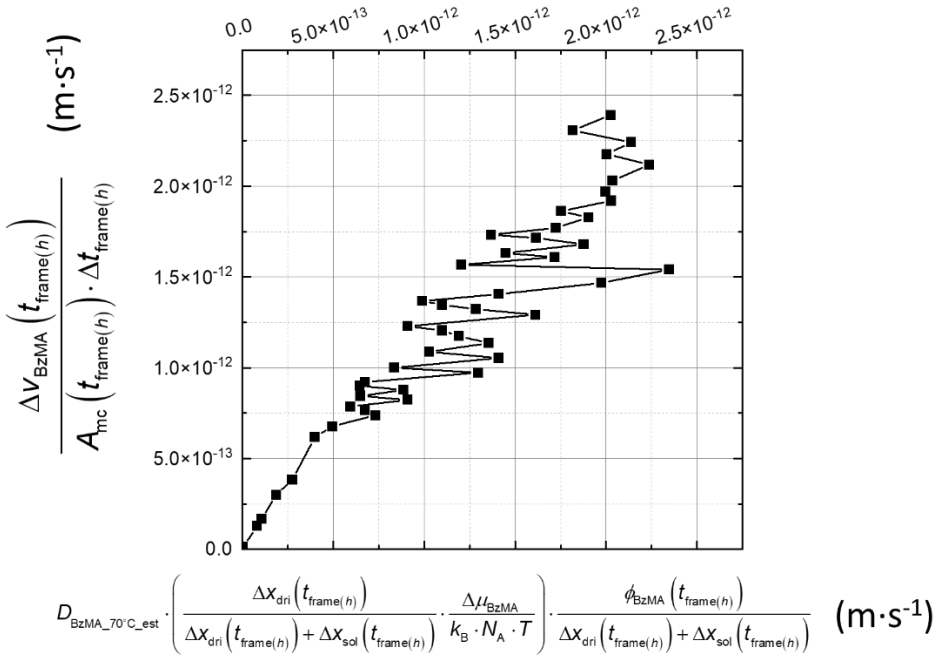

Figure 5.18**.** A diffusion model of eq 5.4 incorporating chemical potential effect for PISA process via RAFT synthesis of $PDMA_{43}$–$PBzMA_{200}$ diblock copolymers at 70 °C in ethanol/water 80/20 w/w mixture at 70 °C (eq 5.4) after least square fitting of the traveling distance with the chemical potential effect $\Delta x_{dri}(t) = 8.09 \times 10^{-2}$ m (R^2=0.970).

5.6. Conclusion

It is shown that time-resolved SAXS measurements could be successfully used to monitor products of PISA process during RAFT synthesis of copolymers from possible emulsions in polar solutions. The data provide information about evolution of initially dissolved stabiliser blocks into copolymers forming spherical micelles at a later stage of the synthesis. It is demonstrated that developed SAXS model, based on a mass balance of synthesised products and reagents used for the polymerisation, can be employed to measure transfer of the reaction components in the system. During the reaction course the copolymers self-assemble into micelles acting as small independent reactors. The fact that structural parameters of the micelles, including their composition, could be measured by fitting scattering equations of micelle model to experimental SAXS patterns provides a unique opportunity to detect the amount of reaction components in the micelles. A mixture of ethanol and water, used in the studied system as a solvent, complicated the SAXS analysis. It could be expected that the composition of the solvent penetrated in the micelle core might be different from the solvent composition in the surrounding media. However, fitting experimental SAXS patterns using scattering equations incorporating parameters describing solvent composition in both the micelle cores and the surrounding medium has not

produced stable results. In order to stabilise the model fitting, two assumptions have been considered for the SAXS analysis: the solvent composition in the spherical micelle core is the same as the composition in the medium (ethanol/water ratio is 80/20 w/w, respectively) (Assumption 1) or only ethanol penetrates into the micelle cores (Assumption 2). The SAXS analysis based on Assumption 1 identified all four stages of PISA process (stages 2-5) during RAFT synthesis of $PDMA_{43}$–$PBzMA_{200}$ diblock copolymer in polar medium: the polymerization initiation when the system was composed of $PDMA_{43}$ molecules, monomer and solvent (stage 2); the beginning of copolymer self-assembly when the system was composed of two populations of scattering objects such as dissolved copolymers and spherical copolymer micelles (stage 3), completion of the copolymer self-assembly when only population of spherical micelles was detected in the system (stage 4) and the reaction termination (stage 5). The analysis revealed that the nucleation process begun at PBzMA DP of 15 and finished at PBzMA DP of 33. The SAXS results based on Assumption 1 has shown that the monomer concentration in the PDMA-PBzMA micelle cores (*xmon*) measured for the stage 4 was not linearly proportional to the rate of polymerisation as it was observed for the RAFT synthesis in a non-polar medium. This result may indicate that the assumption of a similar solvent composition in both the medium and in the spherical micelle cores may not be fully valid and causes some inconsistency between the obtained and the expected results. It was found that aggregation number of copolymers (N_{agg}) after the micelle nucleation increases over the reaction course. Moreover, N_{agg} increases after the synthesis completion which is likely to be related to Ostwald ripening. This behaviour is similar to the N_{agg} increase during the PISA process in non-polar media (Figure 3.9). Normalised amount of spherical micelles in the system calculated from SAXS results (N_{nuc}) has demonstrated dynamics of the copolymer micelle nucleation. N_{nuc} increases drastically at the beginning of the synthesis during stage 3 and after reaching a peak value rapidly decreases to a plateau value. The later results could indicate that a spherical micelle fusion takes place during stages 4 and 5. S_{agg} and d_{int} might explain the reason why the morphology of this $PDMA_{43}$–PBzMA synthesis was spherical micelle, which depended on R_g of solvophilic block $PDMA_{43}$. However, the non-linear relationship of *xmon* and the rate of polymerisation in stage 4 might indicate water might always stay outside of the spherical micelle cores. This encouraged Assumption 2 of only ethanol hidden in the spherical micelle cores. A satisfactory fitting curves to the time-resolved experimental SAXS patterns corresponding to stages 4 and 5 was obtained during SAXS analysis based on Assumption 2. However, this analysis produced unsatisfactory results for the stage 3. It was found, making Assumption 2, that concentration of BzMA monomer in the micelle cores was close to zero. This suggested that the rate of polymerisation of the PBzMA block might be controlled only by the BzMA monomer diffusion from the possible small BzMA emulsion particles through the solvent medium to the spherical micelles. In this case BzMA concentration in the solvent medium is very low and supply of the monomer is constrained by its solubility in the ethanol/water mixture used for the synthesis. This circumstance makes the PDMA-PBzMA RAFT polymerisation in polar medium significantly different from the PSMA-PBzMA RAFT polymerisation in non-polar medium, both studied in this work. In the case of this polymerisation, supply of the BzMA monomer, abundant in the medium, to the reaction point (inside of the micelles) is virtually unrestricted and as a result a high concentration of the monomer in the micelles is reached during this synthesis. The

increase of spherical micelle core after the polymerisation was highly likely also controlled by Ostwald ripening, which was also observed in Chapter 3. Supply of the BzMA monomer to the reaction point is hindered by the monomer transfer through the medium and as a result the monomer concentration in the micelles is low and as soon as a monomer molecule reach a micelle it will be consumed by the reaction. This conclusion makes Assumption 2 as a more likely scenario for the micelle core formation. However, a further improvement of the SAXS model based on this assumption would be required in order to obtain satisfactory results for the initial stages (stages 2 and 3) of the RAFT polymerisation. Fick's first law was exploited to measure parameters describing the BzMA monomer transfer from medium to spherical micelle cores. The diffusion coefficient measured from SAXS results based on Assumption 2 was significantly (about ten times) smaller than the diffusion coefficient estimated by Stokes-Einstein equation without considering chemical potential effect. However, an incorporation of the chemical potential difference of BzMA in medium and in spherical micelle cores in the mass transfer equation enabled the BzMA monomer transfer from ethanol/water mixture to spherical micelle cores to be described satisfactory. After gathering the evident from SAXS patterns and SAXS modelling, this PISA synthesis of $PDMA_{43}$–$PBzMA_{200}$ in ethanol/water 80/20 w/w mixture should be classified as emulsion polymerisation.

5.7. References

1. Arshady, R., Microspheres for biomedical applications: preparation of reactive and labelled microspheres. *Biomaterials* **1993,** *14* (1), 5-15.
2. Margel, S., Affinity separation with polyaldehyde microsphere beads. *Journal of Chromatography A* **1989,** *462*, 177-189.
3. Rembaum, A.; Yen, S. P. S.; Cheong, E.; Wallace, S.; Molday, R. S.; Gordon, I. L.; Dreyer, W. J., Functional Polymeric Microspheres Based on 2-Hydroxyethyl Methacrylate for Immunochemical Studies. *Macromolecules* **1976,** *9* (2), 328-336.
4. Skjeltorp, A. T., One- and Two-Dimensional Crystallization of Magnetic Holes. *Physical Review Letters* **1983,** *51* (25), 2306-2309.
5. Semsarilar, M.; Jones, E. R.; Blanazs, A.; Armes, S. P., Efficient Synthesis of Sterically-Stabilized Nano-Objects via RAFT Dispersion Polymerization of Benzyl Methacrylate in Alcoholic Media. *Advanced Materials* **2012,** *24* (25), 3378-3382.
6. Gonzato, C.; Semsarilar, M.; Jones, E. R.; Li, F.; Krooshof, G. J. P.; Wyman, P.; Mykhaylyk, O. O.; Tuinier, R.; Armes, S. P., Rational Synthesis of Low-Polydispersity Block Copolymer Vesicles in Concentrated Solution via Polymerization-Induced Self-Assembly. *Journal of the American Chemical Society* **2014,** *136* (31), 11100-11106.
7. Semsarilar, M.; Ladmiral, V.; Blanazs, A.; Armes, S. P., Poly(methacrylic acid)-based AB and ABC block copolymer nano-objects prepared via RAFT alcoholic dispersion polymerization. *Polymer Chemistry* **2014,** *5* (10), 3466-3475.
8. Semsarilar, M.; Penfold, N. J. W.; Jones, E. R.; Armes, S. P., Semi-crystalline diblock

copolymer nano-objects prepared via RAFT alcoholic dispersion polymerization of stearyl methacrylate. *Polymer Chemistry* **2015,** *6* (10), 1751-1757.

9. Jones, E. R.; Semsarilar, M.; Blanazs, A.; Armes, S. P., Efficient Synthesis of Amine-Functional Diblock Copolymer Nanoparticles via RAFT Dispersion Polymerization of Benzyl Methacrylate in Alcoholic Media. *Macromolecules* **2012,** *45* (12), 5091-5098.

10. Jones, E.; Mykhaylyk, O.; Semsarilar, M.; Boerakker, M.; Wyman, P.; Armes, S., How do spherical diblock copolymer nanoparticles grow during RAFT alcoholic dispersion polymerization? *Macromolecules* **2015,** *49* (1), 172-181.

11. Zhang, X.; Rieger, J.; Charleux, B., Effect of the solvent composition on the morphology of nano-objects synthesized via RAFT polymerization of benzyl methacrylate in dispersed systems. *Polymer Chemistry* **2012,** *3* (6), 1502-1509.

12. Xiao, X.; He, S.; Dan, M.; Su, Y.; Huo, F.; Zhang, W., Brush macro-RAFT agent mediated dispersion polymerization of styrene in the alcohol/water mixture. *Journal of Polymer Science Part A: Polymer Chemistry* **2013,** *51* (15), 3177-3190.

13. Wang, X.; Xu, J.; Zhang, Y.; Zhang, W., Polymerization of styrene in alcohol/water mediated by a macro-RAFT agent of poly(N-isopropylacrylamide) trithiocarbonate: From homogeneous to heterogeneous RAFT polymerization. *Journal of Polymer Science Part A: Polymer Chemistry* **2012,** *50* (12), 2452-2462.

14. Huo, F.; Wang, X.; Zhang, Y.; Zhang, X.; Xu, J.; Zhang, W., RAFT Dispersion Polymerization of Styrene in Water/Alcohol: The Solvent Effect on Polymer Particle Growth during Polymer Chain Propagation. *Macromolecular Chemistry and Physics* **2013,** *214* (8), 902-911.

15. Jones, E. R.; Semsarilar, M.; Wyman, P.; Boerakker, M.; Armes, S. P., Addition of water to an alcoholic RAFT PISA formulation leads to faster kinetics but limits the evolution of copolymer morphology. *Polymer Chemistry* **2016,** *7* (4), 851-859.

16. Sztucki, M. SAXSutilities2: a Graphical User Interface For Processing and Analysis of Small-Angle X-ray Scattering Data 2021.

17. Ilavsky, J.; Jemian, P. R., Irena: tool suite for modeling and analysis of small-angle scattering. *Journal of Applied Crystallography* **2009,** *42* (2), 347-353.

18. Fitzgerald, D., Technical Assessment of the Anton Paar DMA5000 density meter. *H&D Fitzgerald Ltd* **2000**.

19. Cornel, E. J.; van Meurs, S.; Smith, T.; O'Hora, P. S.; Armes, S. P., In Situ Spectroscopic Studies of Highly Transparent Nanoparticle Dispersions Enable Assessment of Trithiocarbonate Chain-End Fidelity during RAFT Dispersion Polymerization in Nonpolar Media. *Journal of the American Chemical Society* **2018,** *140* (40), 12980-12988.

20. Flory, P. J., *Principles of Polymer Chemistry*. Cornell University Press: ITHACA, New York, 1953.

21. Fetters, L.; Lohse, D.; Colby, R., Chain dimensions and entanglement spacings. In *Physical properties of polymers handbook*, Springer: 2007; pp 447-454.

22. Brotherton, E. E.; Hatton, F. L.; Cockram, A. A.; Derry, M. J.; Czajka, A.; Cornel, E. J.; Topham, P. D.; Mykhaylyk, O. O.; Armes, S. P., In Situ Small-Angle X-ray Scattering Studies During Reversible Addition–Fragmentation Chain Transfer Aqueous Emulsion Polymerization. *Journal of the American Chemical Society* **2019,** *141* (34), 13664-13675.

23. Förster, S.; Zisenis, M.; Wenz, E.; Antonietti, M., Micellization of strongly segregated

block copolymers. *The Journal of Chemical Physics* **1996,** *104* (24), 9956-9970.

24. Abbott, S.; Hansen, C. M., *Hansen solubility parameters in practice*. Hansen-Solubility: 2008.

25. Hansen, C. M., *Hansen solubility parameters: a user's handbook*. CRC press: New York, 2007.

26. Cunningham, V. J.; Alswieleh, A. M.; Thompson, K. L.; Williams, M.; Leggett, G. J.; Armes, S. P.; Musa, O. M., Poly(glycerol monomethacrylate)–Poly(benzyl methacrylate) Diblock Copolymer Nanoparticles via RAFT Emulsion Polymerization: Synthesis, Characterization, and Interfacial Activity. *Macromolecules* **2014,** *47* (16), 5613-5623.

27. Rieger, J.; Zhang, W.; Stoffelbach, F.; Charleux, B., Surfactant-free RAFT emulsion polymerization using poly (N, N-dimethylacrylamide) trithiocarbonate macromolecular chain transfer agents. *Macromolecules* **2010,** *43* (15), 6302-6310.

28. Truong, N. P.; Dussert, M. V.; Whittaker, M. R.; Quinn, J. F.; Davis, T. P., Rapid synthesis of ultrahigh molecular weight and low polydispersity polystyrene diblock copolymers by RAFT-mediated emulsion polymerization. *Polymer Chemistry* **2015,** *6* (20), 3865-3874.

29. Rieger, J.; Stoffelbach, F.; Bui, C.; Alaimo, D.; Jérôme, C.; Charleux, B., Amphiphilic poly (ethylene oxide) macromolecular RAFT agent as a stabilizer and control agent in ab initio batch emulsion polymerization. *Macromolecules* **2008,** *41* (12), 4065-4068.

30. Zhang, W.; D'Agosto, F.; Boyron, O.; Rieger, J.; Charleux, B., One-pot synthesis of poly (methacrylic acid-co-poly (ethylene oxide) methyl ether methacrylate)-b-polystyrene amphiphilic block copolymers and their self-assemblies in water via RAFT-mediated radical emulsion polymerization. A kinetic study. *Macromolecules* **2011,** *44* (19), 7584-7593.

31. Chaduc, I.; Zhang, W.; Rieger, J.; Lansalot, M.; d'Agosto, F.; Charleux, B., Amphiphilic Block Copolymers from a Direct and One‐pot RAFT Synthesis in Water. *Macromolecular rapid communications* **2011,** *32* (16), 1270-1276.

32. Chaduc, I.; Girod, M.; Antoine, R.; Charleux, B.; D'Agosto, F.; Lansalot, M., Batch emulsion polymerization mediated by poly (methacrylic acid) macroRAFT agents: One-pot synthesis of self-stabilized particles. *Macromolecules* **2012,** *45* (15), 5881-5893.

Chapter 6: *In Situ* Small-Angle X-Ray Scattering Studies of the Formation of Polymer/silica Nanocomposite Particles in Aqueous Solution

Reproduced from [A. Czajka, G. Liao, O. O. Mykhaylyk and S. P. Armes, *Chem. Sci.*, 2021, 12, 14288]

Chapter 6

In Situ Small-Angle X-Ray Scattering Studies of the Formation of Polymer/silica nanocomposite particles in Aqueous Solution

6.1 Introduction

After the SAXS modelling and following SAXS analysis of PISA process via RAFT synthesis, including the synthesis $PSMA_{31}$-$PBzMA_{2000}$ diblock copolymer in mineral oil and the synthesis of PDMA–PBzMA in ethanol/water 80/20 w/w mixture, SAXS model with mass balance is relatively successful to fit these in-situ SAXS patterns. Further, the following SAXS modelling results also are relatively reasonable to interpret PISA process, including particle growth, monomer conversion and rate of polymerisation, and mass transfer of monomer. However, RAFT synthesis or other control/living polymerisation methods are just part of free radical polymerisation, and conventional free radical polymerisation is widely applied to industrial products[1-3] . Therefore, SAXS model with mass balance ought to be applied to investigation of conventional free-radical polymerisation. A typical example could be polymer/silica nanocomposite particles.

Polymer/silica nanocomposite particles have various potential applications, such as durable transparent coatings, synthetic mimics, and Pickering emulsifiers.[4] The history of preparation of such polymer/silica nanocomposite particles could be tracked back to 1974[4] with the synthesis of copolymer of urea with formaldehyde stabilised by silica particles. Then more polymer/silica nanocomposite particles have been developed via oxidative polymerization for the applications of the immunodiagnostic assays and synthetic mimics.[5, 6] The potentials of the polymer/silica nanocomposite particles continuously extended when vinyl monomers were exploited for pH-responsive Pickering emulsifiers, architecture coatings, and laser toners.[7-9] To further expand the applications of the polymer/silica nanocomposite particles, by overcoming the relatively low aggregation efficiency, a glycerol-functionalised ultrafine anionic silica sol combined with a cationic azo initiator was introduced to enhance the silica nanoparticles absorption on the polymer core surface.[10]

To investigate the polymer/silica nanocomposite particles and the mechanism of the aggregation process, particle growth process, and the silica nanoparticles packing structure, different characteristic techniques, such as transmission electron microscopy (TEM), dynamic light scattering (DLS) and disk centrifuge photosedimentometry (DCP), have been actively applied to characterise various properties of the nanocomposite particles.[11-13] However, these post-mortem techniques may not fully reveal the formation mechanism of the polymer/silica nanocomposite particles. Small angle x-ray scattering (SAXS) technique could not only measure intermediate products of the targeted polymer/silica nanocomposite particles providing comprehensive information about their structural morphology but also track the synthesis process in-situ. In the past two SAXS models were proposed to describe the monolayer silica nanoparticle packing on a spherical polymer core.[14, 15] However, there is

no comparison between these two models temporarily.

2,2,2-trifluoroethyl methacrylate (TFEMA), as a common fluorine-containing monomer, and the targeted poly(2,2,2-trifluoroethyl methacrylate) (PTFEMA) demonstrate outstanding resistance to oxygen permeability and water repellent capacity.[16, 17] Also, TFEMA with relatively low refractive index can be potentially manufactured as optical materials.[13, 18, 19] Herein, PTFEMA/silica nanocomposite particles were prepared in water by emulsion polymerisation monitored in-situ by time-resolved SAXS for analysing the nanocomposite particle formation. In addition, such polymerisation with TFEMA in water could be well-measured by SAXS, because the scattering length densities of TFEMA and PTFEMA are both far away from the medium, water.[20] Similar with the previous chapters of reversible addition−fragmentation chain-transfer (RAFT) polymerisation, the analysis of this free-radical emulsion polymerisation still involve structural characterisation of the particle morphology and the chemical reaction kinetics. Thus, in order to perform SAXS analysis, details of particle structural models including the geometrical confinements and their validations are presented before the discussions of PTFEMA/silica nanocomposite particles synthesis.

6.2 PTFEMA/silica Nanocomposite Particle Synthesis in Water

The chemicals were used without further purification unless stated. 2,2,2- Trifluoroethyl methacrylate (TFEMA; Aldrich, 99%) was passed through a MEHQ (monomethyl ether hydroquinone) inhibitor removal column prior to use to remove inhibitors. The Bindzil CC401 glycerol-modified aqueous silica sol (19 nm diameter; 40% w/w) was supplied by Nouryon (Bohus, Sweden). 2,2'-Azobis(2-isobutyramidine) dihydrochloride (AIBA; 97%), $MgSO_4$ (98%) and $CDCl_3$ (99.8%) were from Sigma-Aldrich (UK). Deionized water was provided from an Elga DV25 water purifier.

Laboratory-scale synthesis of PTFEMA/silica nanocomposite particles

AIBA initiator (74.8 mg; 1.0 mol % based on TFEMA), Bindzil CC401 silica sol (4.71 g of a 40% w/w dispersion, or 1.89 g dry silica) and deionized water (55.3 mL) were weighed into a 100 mL round-bottom flask containing a magnetic stirrer bar. The reaction mixture was adjusted to pH 8.9 by addition of 200 µL of a 0.1 M NaOH solution and then degassed with N_2 gas for approximately 30 min. After removing its MEHQ inhibitor, cold TFEMA was degassed separately using N_2 gas for 30 min with the aid of an ice bath. Degassed TFEMA (4.53 g) was then added to the reaction mixture. The reaction solution was degassed for a further 5 min prior to immersion in a 60 ^oC oil bath and stirred magnetically at 800 rpm. The 'zero time' (t = 0 min) for this polymerization was arbitrarily taken to be the point when the degassed reaction solution was first immersed in the oil bath, rather than the time at which the reaction solution

had reached this temperature. Aliquots were subsequently removed under N_2 via syringe at various time intervals for DLS and TEM analysis. Each 1.0 mL aliquot was quenched by cooling using an ice bath with concomitant exposure to air. For both TEM and DLS analysis, each aliquot was diluted fifty-fold using deionized water at 20 ^oC to produce 0.20% w/w dispersions.

In situ SAXS studies of nanocomposite particle formation using the stirrable reaction cell

The compounds of the mixture of AIBA initiator (3.0 mg), Bindzil CC401 silica sol (0.187 g of a 40% w/w dispersion) and deionized water (2.21 mL) were weighed respectively and adjusted to pH 8.9 by addition of 10 µL of a 0.1 M NaOH solution and then degassed with N_2 gas for approximately 30 min. TFEMA was degassed separately using N_2 gas for 30 min within an ice bath after removing its MEHQ inhibitor. Degassed TFEMA (0.18 g) was added to the reaction mixture. The prepared reaction mixture was transferred via degassed syringe to the stirrable reaction cell[21] (Figure 6.1) which had also been degassed using N_2 gas for 20 min. TFEMA polymerisation was initiated by a water-circulating jacket to raise the temperature to 60 ^oC. The polymerisation was monitored until no obvious further evolution in the 1D SAXS pattern was observed, at which point it was assumed that the reaction was complete.

6.3 The Characterisation of the Polymer/silica Nanocomposite Particles

Small-Angle X-ray Scattering

Time-resolved SAXS patterns of the PTFEMA/silica nanocomposite particle formation during the PTFEMA synthesis after the initiation by raising the temperature to 60 ^oC in a stirrable reaction cell (Figure 6.1) were recorded every 10 seconds for 10 min, then every 30 seconds for the next 30 min followed by every 60 seconds until no further change in the SAXS patterns observed. The measurements were performed at I22 station of the Diamond Light Synchrotron (Didcot, The United Kingdom) using monochromatic X-ray radiation (λ = 1.24 Å, q-range from 0.0015 to 0.13 $Å^{-1}$) and a 2D Pilatus 2M two-dimensional (2D) pixel detector (Dectris, Switzerland). 2D SAXS patterns were reduced (integrated, normalized by the sample transmission coefficient and calibrated to absolute intensity using SAXS patterns of deionized water assuming that the differential scattering cross-section of water at 21 °C is 0.0162 cm^{-1}) to 1D SAXS profiles using Dawn software supplied by Diamond Light Source[22]. Calculations and fitting of the SAXS data were performed using *Irena*[23], a macro package for small angle scattering (SAS) data analysis within the commercial *Igor Pro* application. All SAXS models were programmed using a user function option in the *Irena* SAS macro. In order to preserve connections between different relationships and scattering object populations, some of the SAXS model parameters were set as global variables.

Density measurement

The densities of water and TFEMA at the reaction temperature, 60 °C, were determined by oscillating U-tube method[24] using DMA5000 density meter (Anton Paar, Graz, Austria). 3 measurement results were averaged per sample. Although the density repeatability is 0.000001 g/cm³, densities are presented in three significant digits for further use, which indicates that no uncertainties are given.

Dynamic Light Scattering

DLS studies were conducted on 0.20% w/w aqueous dispersions at 25 °C in disposable plastic cuvettes using a Malvern Zetasizer NanoZS instrument detecting the back-scattered light at an angle of 173°. A non-negative least squares (NNLS) algorithm[25] was applied to calculate intensity-average hydrodynamic diameter of the synthesised particles. The Stokes−Einstein equation was used to calculate the particle diameter. Volume-average hydrodynamic diameters were converted from the intensity-average hydrodynamic diameters using the Malvern Zetasizer Software (Version 7.01).

Transmission Electron Microscopy

Copper/palladium TEM grids (Agar Scientific, UK) were coated in-house to yield a thin film of amorphous carbon, which were then plasma glow-discharged for 30 s for generating a hydrophilic surface. Samples of PTFEMA/silica nanocomposite particles prepared in water (0.20% w/w, 5 µL) were placed onto the glow-discharged grids and then excess solution was removed after 1 min by a filter paper. This was followed by application of uranyl formate solution (0.75% w/v, 5 µL) for staining the PTFEMA/silica nanocomposite particles on the sample-loaded grid, the staining solution excess was removed after 20 s. Finally, the grids were dried by a vacuum hose. Imaging was collected on a Technai T12 Spirit instrument at 120 kV equipped with a Gatan 1 k CCD camera.

Optical Microscopy

Aliquots of PTFEMA/silica nanocomposite particle solution were extracted from the reaction mixture at 60 °C and the TFEMA polymerization was quenched by cooling to 20 °C with concomitant exposure to air. Optical microscopy images were recorded immediately at 20 °C using a Motic DMBA300 digital biological microscope equipped with a built-in camera and Motic Images Plus 2.0 ML software.

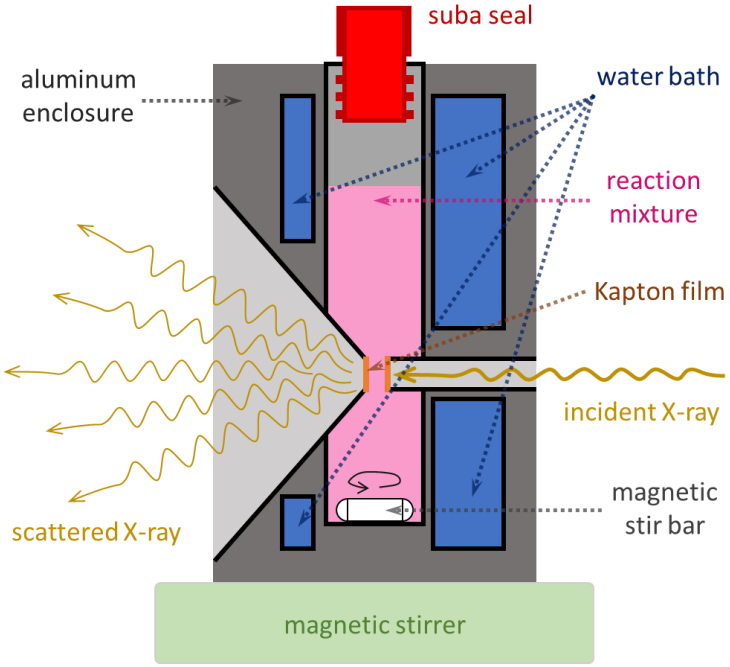

Figure 6.1 Schematic representation of a cross-section of the stirrable reaction cell used for various types of polymerisations.[21] The reaction mixture in the aluminium enclosure can be efficiently heated or cooled by water bath. By extra magnetics stirrer, the magnetics stir bar can efficiently force the reaction mixture uniform distributed in the reaction cell. With suba seal, atmosphere in the reaction cell can be well-controlled during polymerisation. X-ray scattered by reaction mixture through Kapton film windows of 75 µm thickness is collected for in-situ SAXS studies. The SAXS path length is approximately 1.0 mm. The reaction solution volume is approximately 2.0 mL.

6.4 SAXS models For Structural Characterisation of Polymer/Silica Nanocomposite Particles

As TEM results suggest for the final product of the PTFEMA/silica nanocomposite particles synthesis in water (Figure 6.2), the silica nanoparticles are absorbed on the surface of the polymer cores. Thus, this structural morphology was replicated in the developed SAXS models. It was assumed that the polymer/silica nanoparticle had a core-particulate shell structure[14] with the polymer forming the core and the silica nanoparticles forming the particulate shell. The other proposal publicised as the raspberry model[15] described the polymer/silica nanocomposite particles as the modified spherical micelle SAXS model. In such modified spherical micelle SAXS model, the solvophilic brushes were replaced by the silica instead. Also, TEM suggested that some silica nanoparticles remain in medium phase, and thus, an extra population of the non-absorbed silica nanoparticles is required to be counted in the SAXS modelling. Meanwhile, such PTFEMA/silica nanocomposite particles

were observed by DLS and TEM (Figure 6.3) before 20 min of the polymerisation. At 5 min, there was no obvious polymer/silica nanoparticle observed by DLS and TEM, and only silica with the diameter of 21 nm could be observed. At 10 min, extra larger size particles formed according to DLS and TEM. At 15 min, an extra peek represented larger size particles obviously appeared, and TEM results indicated that the potential polymer/silica nanoparticles might form in the system. At 20 min, with the diameter of the particles of 90 nm from DLS results and relatively clear core-shell structure of the particles from TEM results, PTFEMA/silica nanocomposite particles were highly likely to be the dominate species in the system. This indicated that this *in-situ* SAXS studies and following SAXS modelling only focused on the patterns with analysis after 20 min of the reaction with relatively certain PTFEMA/silica nanocomposite particles in the system.

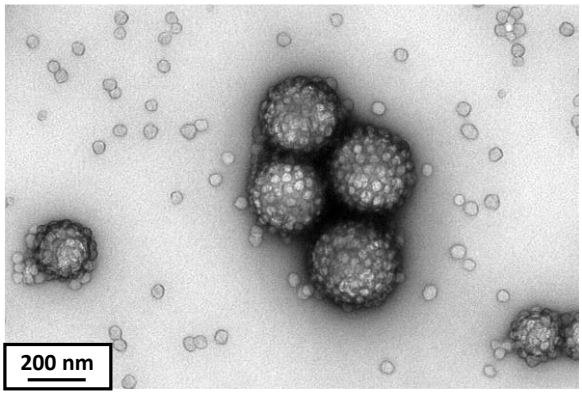

Figure 6.2 TEM images recorded for PTFEMA/silica nanocomposite particles prepared by aqueous emulsion polymerisation of TFEMA in the presence of glycerol-functionalized silica nanoparticles using a cationic azo (AIBA) initiator at 60 °C in the stirrable reaction cell used for the in situ SAXS experiments.

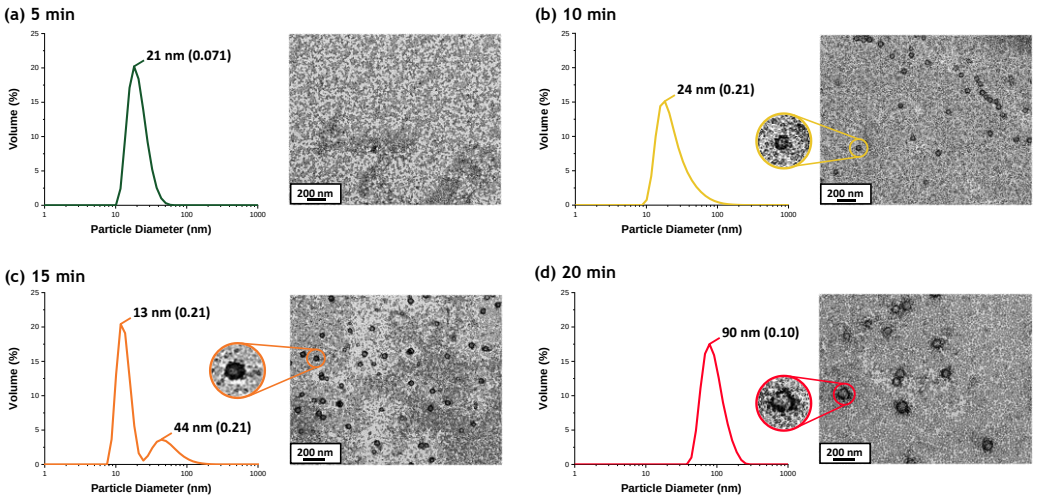

Figure 6.3 Volume-average size distributions of synthesised particles with their polydispersities determined by

DLS after 5 (a), 10 (b), 15 (c), and 20 (d) min of the surfactant-free polymerisation of TFEMA in the presence of the glycerol-functionalized silica nanoparticles using a cationic azo initiator at 60 °C. Corresponding TEM images of the reaction products are shown at the right side of the DLS graphs.

6.4.1 Core-particulate Shell with Non-absorbed Silica (c-ps&silica) Model with Mass Balance

The total scattering intensity of the polymer/silica nanocomposite particles could be described as the scattering intensity of the polymer/silica (core-particulate shell) structure, $I_{c\text{-}ps}(q)$, the self-correlation scattering intensity of the absorbed silica nanoparticles within the particle shell, $I_{silica\_c\text{-}ps}(q)$, the scattering intensity of the non-absorbed silica nanoparticles in medium phase, $I_{silica\_med}(q)$, and the scattering intensity of the background medium, I_{bg}. Therefore, the scattering intensity of the polymer/silica nanocomposite particles, $I_{c\text{-}ps\text{-}silica}(q)$, is given as the sum of $I_{c\text{-}ps}(q)$ and $I_{silica\_c\text{-}ps}(q)$ (Figure 6.4). And SAXS model of the studied particles, named as c-ps&silica model, is given as,

$$I_{c-ps\&silica}(q) = I_{c\text{-}ps}(q) + I_{silica\_c\text{-}ps}(q) + I_{silica\_med}(q) + I_{bg}, \tag{6.1}$$

The intensity of the polymer/silica core-particulate shell structure is given as,

$$I_{c\text{-}ps}(q) = \phi_{c\text{-}ps} \cdot \int_0^\infty \int_0^\infty F_{c\text{-}ps}(q) \cdot \Psi(r_{c\_c\text{-}ps}) \cdot \Psi(t_{ps\_c\text{-}ps}) \mathrm{d}r_{c\_c\text{-}ps} \mathrm{d}t_{ps\_c\text{-}ps}, \tag{6.2}$$

where $\phi_{c\text{-}ps}$ is the volume fraction of the cores-particulate shell population, and $F_{c\text{-}ps}(q)$ is the form factor of the core-particulate shell, which is written as,

$$F_{c\text{-}ps}(q) = \left[\begin{array}{l} (\xi_{c\_c\text{-}ps} - \xi_{sp\_c\text{-}ps}) \cdot A_s(q, r_{c\_c\text{-}ps}) \cdot V_s(r_{c\_c\text{-}ps}) \\ + (\xi_{ps\_c\text{-}ps} - \xi_{med}) \cdot A_s(q, r_{c\_c\text{-}ps} + t_{ps\_c\text{-}ps}) \cdot V_s(r_{c\_c\text{-}ps} + t_{ps\_c\text{-}ps}) \end{array} \right]^2, \tag{6.3}$$

where $\xi_{c\_c\text{-}ps}$, $\xi_{ps\_c\text{-}ps}$ and ξ_{med} are the scattering length densities of the polymer core, particulate shell, and the medium, $r_{c\_c\text{-}ps}$ is the radius of the polymer core, and $t_{ps\_c\text{-}ps}$ is the thickness of the particulate shell. $\Psi(r_{c\_c\text{-}ps})$ and $\Psi(t_{ps\_c\text{-}ps})$ are the polydispersity distributions of the radius of the polymer cores and the thickness of the particulate shells, respectively. Therefore, $\Psi(r_{c\_c\text{-}ps})$ is given as $r_{c\_c\text{-}ps} \sim N(R_{c\_c\text{-}ps}, \sigma_{c\_c\text{-}ps})$, and $\Psi(t_{ps\_c\text{-}ps})$ is given as $t_{ps\_c\text{-}ps} \sim N(T_{ps\_c\text{-}ps}, \sigma_{ps\_c\text{-}ps})$. $A_s(q,r)$ is the amplitude of sphere particle of the radius as r for scattering model in eq 1.93, and $V_s(r)$ is the volume of the sphere particle of the radius as r in eq 1.93.

The self-correlation intensity of the absorbed silica nanoparticles within the particulate shell (eq 6.1) is given as,

$$I_{\text{silica\_c-ps}}(q) = \phi_{\text{silica\_c-ps}} \cdot \int_0^{\infty} F_{\text{silica}}(q) \cdot \Psi(r_{\text{silica}}) \mathrm{d}r_{\text{silica}} \cdot S(q), \quad (6.4)$$

where $\phi_{\text{silica\_c-ps}}$ is the volume fraction of the silica nanoparticles within the core-particulate shell particles, and $F_{\text{silica}}(q)$ is the form factor of the silica nanoparticles, which is written as,

$$F_{\text{silica}}(q) = \left[(\xi_{\text{silica}} - \xi_{\text{med}}) \cdot A_{\text{s}}(q, r_{\text{silica}}) \cdot V_{\text{s}}(r_{\text{silica}}) \right]^2, \quad (6.5)$$

where ξ_{silica} is the scattering length density of the silica nanoparticles and $r_{\text{c\_c-ps}}$ is the radius of the silica nanoparticles. $\Psi(r_{\text{silica}})$ is the polydispersity distribution of the radius of the silica nanoparticles. S(q) is the structure factor. Particularly, the hard sphere Percus-Yevick structure factor is suitable for modelling the silica interparticle interactions within the particulate shell.[14]

The scattering intensity of the non-absorbed silica nanoparticles in medium phase (eq 6.1) is given as,

$$I_{\text{silica\_med}}(q) = \phi_{\text{silica\_med}} \cdot \int_0^{\infty} F_{\text{silica}}(q) \cdot \Psi(r_{\text{silica}}) \mathrm{d}r_{\text{silica}}, \quad (6.6)$$

where $\phi_{\text{silica\_med}}$ is the volume fraction of the non-absorbed silica nanoparticles in medium phase. This c-ps&silica model (eq 6.1) without free (non-absorbed) silica in the medium has been validated and the SAXS modelling results successfully reproduced SAXS patterns of core-particulate shell particles simulated by Monte Carlo simulations[14].

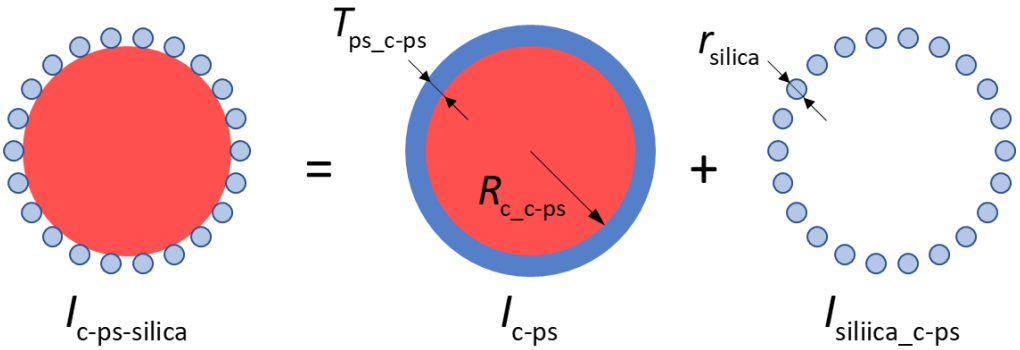

Figure 6.4 Schematic representation of the core-particulate shell with absorbed silica nanoparticles within the particle shell SAXS model. The intensity contributed by the core-particulate shell with absorbed silica nanoparticles within the particle shell, $I_{\text{c-ps-silica}}$, can be described as the sum of the intensity contributed by the core-particulate shell model, $I_{\text{c-ps}}$, and the intensity contributed by the absorbed silica nanoparticles within the particle shell model, $I_{\text{silica\_c-ps}}$. For the core-particulate shell model, the radius of the core is $R_{\text{c\_c-ps}}$, and the particulate shell thickness is $T_{\text{ps\_c-ps}}$. For the absorbed silica nanoparticles within the particle shell model, the radius of silica nanoparticles is r_{silica}.

6.4.2 Raspberry Model with Mass Balance

Adapting the raspberry model[15], the total intensity of the polymer/silica nanocomposite particles, I_{tot_rasp}, could be given as,

$$I_{tot\_rasp}(q) = I_{rasp}(q) + I_{silica\_med}(q) + I_{bg}, \tag{6.7}$$

where the intensity of the polymer/silica nanocomposite particles described by the raspberry model, I_{rasp}, could be written as,

$$I_{rasp}(q) = \phi_{rasp} \cdot \int_0^\infty \int_0^\infty F_{rasp}(q) \cdot \Psi(r_{c\_c\text{-}sp}) \cdot \Psi(r_{silica}) \mathrm{d}r_{silica} \mathrm{d}r_{c\_c\text{-}sp}, \tag{6.8}$$

where ϕ_{rasp} is the volume fraction of the core-particulate shell particles, and $F_{rasp}(q)$ is the form factor of the raspberry particle model. The form factor of the original raspberry model is given as,

$$\begin{aligned} F_{rasp}(q) = {} & (\xi_{c\_c\text{-}sp} - \xi_{med})^2 \cdot A_s^2(q, r_{c\_c\text{-}sp}) \cdot V_s^2(r_{c\_c\text{-}sp}) \\ & + 2n_{silica}^2 \cdot (\xi_{c\_c\text{-}sp} - \xi_{med})(\xi_{silica} - \xi_{med}) \cdot A_s(q, r_{c\_c\text{-}sp}) \cdot A_s(q, r_{silica}) \cdot \frac{\sin q(r_{c\_c\text{-}sp} + \alpha_{silica} r_{silica})}{q(r_{c\_c\text{-}sp} + \alpha_{silica} r_{silica})}, \\ & + n_{silica}(n_{silica} - 1) \cdot (\xi_{silica} - \xi_{med})^2 \cdot \left[A_s(q, r_{silica}) \cdot \frac{\sin q(r_{c\_c\text{-}sp} + \alpha_{silica} r_{silica})}{q(r_{c\_c\text{-}sp} + \alpha_{silica} r_{silica})} \right]^2 \\ & + n_{silica} \cdot (\xi_{silica} - \xi_{med})^2 \cdot A_s^2(q, r_{silica}) \cdot V_s^2(r_{silica}) \end{aligned} \tag{6.9}$$

where n_{silica} is the number of the silica nanoparticles within the particulate shell, α_{silica} is the fraction of the penetration depth of the silica nanoparticles in the polymer cores. However, this original raspberry form factor has not considered the silica interparticle interactions within the particulate shell for the final term of eq 6.9. Therefore, eq 6.9 should be rewritten as,

$$\begin{aligned} F_{rasp\_sf}(q) = {} & (\xi_{c\_c\text{-}sp} - \xi_{med})^2 \cdot A_s^2(q, r_{c\_c\text{-}sp}) \cdot V_s^2(r_{c\_c\text{-}sp}) \\ & + 2n_{silica}^2 \cdot (\xi_{c\_c\text{-}sp} - \xi_{med})(\xi_{silica} - \xi_{med}) \cdot A_s(q, r_{c\_c\text{-}sp}) \cdot A_s(q, r_{silica}) \cdot \frac{\sin q(r_{c\_c\text{-}sp} + \alpha_{silica} r_{silica})}{q(r_{c\_c\text{-}sp} + \alpha_{silica} r_{silica})}, \\ & + n_{silica}(n_{silica} - 1) \cdot (\xi_{silica} - \xi_{med})^2 \cdot \left[A_s(q, r_{silica}) \cdot \frac{\sin q(r_{c\_c\text{-}sp} + \alpha_{silica} r_{silica})}{q(r_{c\_c\text{-}sp} + \alpha_{silica} r_{silica})} \right]^2 \\ & + n_{silica} \cdot (\xi_{silica} - \xi_{med})^2 \cdot A_s^2(q, r_{silica}) \cdot V_s^2(r_{silica}) \cdot S(q) \end{aligned} \tag{6.10}$$

and this modified raspberry model form factor (eq 6.10) rather than the original raspberry form factor (eq 6.9)[15]. Nevertheless, this raspberry model has not been previously validated, and thus, the validation of the raspberry model and the comparisons between the core-particulate shell model with the raspberry model will be produced here. The Monte Carlo simulations of the core-particulate shell SAXS patterns were performed for various silica particle distributions which were described by the packing efficiency and interaction parameters of the silica particles within the particulate shell. Therefore, before the validations of the raspberry model, the geometrical restriction analysis is necessary in order

to check reliability and physical meaning of the structural parameters describing the polymer/silica nanocomposite particles.

6.4.3 Geometrical Constraints

The main features describing the silica nanoparticles on the polymer cores could include polydispersity of the silica nanoparticles, the number of silica nanoparticles on the polymer cores, and the packing structures.

The polydispersity of the silica nanoparticles could be directly measured by DLS or SAXS from experiment. For the Monte Carlo simulations[14], it can be assumed that the polydispersity of the silica nanoparticles obeyed the Gaussian distribution as $r_{silica} \sim N(R_{silica}, \sigma_{silica})$, where R_{silica} and σ_{silica} are the mean radius and its standard deviation of the silica nanoparticles. The polydispersity of the silica nanoparticles contributed to the raggedness of the particulate shell for c-ps&silica SAXS model, which cannot be described as the ideal particulate shell, even though considering the polydispersity of the particulate shell. Also, the raspberry model cannot replicate the raggedness of the silica nanoparticles on the polymer cores surface, because the equations 6.8 and 6.10 are derived only for the case where silica nanoparticles with the same radius, without counting particle dispersity, form the polymer/silica nanocomposite particle. Thus, a relatively narrow distribution of the silica nanoparticle radius was used for SAXS modelling and analysis. Practically, with $\sigma_{silica} / R_{silica} \leq 0.1$, the SAXS model fitting parameters were reasonable to reproduce simulated structures of the silica nanoparticles on the polymer cores.[14]

The number of the silica nanoparticles on the polymer cores also suffers from the polydispersities of the polymer cores and the silica nanoparticles. To resolve this problem, the superficial packing efficiency, η_{p_sur}, and the volume packing efficiency, η_{p_vol}, are introduced to represent the coverage and occupation of the polymer/silica composite particles by the silica nanoparticles, respectively.

The superficial packing efficiency were widely used to define the number silica nanoparticles within the particulate shell for c-ps&silica SAXS model.[14, 26] This superficial packing efficiency is calculated as,[27, 28]

$$\eta_{p\_sur} = \frac{n_{silica} \cdot A_{s\text{-}cap}}{A_{s\text{-}co}} = \frac{n_{silica} \cdot 2\pi r_{c\_c\text{-}sp}^2 \left(1 - \frac{\sqrt{\left(r_{silica} + r_{c\_c\text{-}sp}\right)^2 - r_{silica}^2}}{\left(r_{silica} + r_{c\_c\text{-}sp}\right)} \right)}{4\pi r_{c\_c\text{-}sp}^2}, \quad = \frac{n_{silica}}{2} \left(1 - \frac{\sqrt{\left(r_{silica} + r_{c\_c\text{-}sp}\right)^2 - r_{silica}^2}}{\left(r_{silica} + r_{c\_c\text{-}sp}\right)} \right) \tag{6.11}$$

where $A_{s\text{-}cap}$ is the spherical cap area coverage by one silica particle on the polymer cores

surface, and $A_{s\text{-}co}$ is the total area of the polymer core surface. Instead of giving the number of the silica nanoparticles within the particulate shell, the Monte Carlo simulations produced the superficial packing efficiency, and then using polydispersities of the radii of the polymer cores and the silica nanoparticles, the numbers of silica nanoparticles were calculated for particular conditions. However, there is no trivial relationship between the number of the silica nanoparticles on the polymer cores and the superficial packing efficiency for c-ps&silica SAXS model (eq 6.1). For the raspberry model, because only the number of the silica nanoparticles is the unknown fixed parameter in its form factor (eq 6.10), the superficial packing efficiency is suitable. To overcome the difficulties for c-ps&silica SAXS model, the average volume packing efficiency is introduced as,

$$\eta_{\text{p\_vol\_avg}} = \frac{\phi_{\text{silica\_c-sp}}}{\phi_{\text{silica\_c-sp}} + \phi_{\text{med\_c-sp}}}, \tag{6.12}$$

where $\phi_{\text{med\_c-ps}}$ is the volume fraction of the medium molecules within the particulate shell. Also, for a relative narrow distribution of nanoparticle radius, it may be meaningless to count the packing efficiency for each nanoparticle. To simplify the polydispersity issue of the polymer cores and the silica nanoparticles, and the distribution of the silica nanoparticles on the polymer cores, the ratio between the total volume of the particulate shell, $\int_0^\infty\int_0^\infty\left[V_s\left(r_{\text{c\_c-sp}}+t_{\text{sp\_c-sp}}\right)-V_s\left(r_{\text{c\_c-sp}}\right)\right]\cdot\Psi\left(r_{\text{c\_c-sp}}\right)\cdot\Psi\left(t_{\text{sp\_c-sp}}\right)dr_{\text{c\_c-sp}}dt_{\text{sp\_c-sp}}$, and the total volume of the polymer cores, $\int_0^\infty V_s\left(r_{\text{c\_c-sp}}\right)\cdot\Psi\left(r_{\text{c\_c-sp}}\right)dr_{\text{c\_c-sp}}$, was approximated by the ratio between the average volume of the particulate shell, $V_s(R_{\text{c\_c-ps}}+T_{\text{ps\_c-ps}})$-$V_s(R_{\text{c\_c-ps}})$, and the average volume of the polymer cores, $V_s(R_{\text{c\_c-ps}})$, as

$$\begin{aligned}&\frac{\int_0^\infty\int_0^\infty\left[V_s\left(r_{\text{c\_c-sp}}+t_{\text{sp\_c-sp}}\right)-V_s\left(r_{\text{c\_c-sp}}\right)\right]\cdot\Psi\left(r_{\text{c\_c-sp}}\right)\cdot\Psi\left(t_{\text{sp\_c-sp}}\right)dr_{\text{c\_c-sp}}dt_{\text{sp\_c-sp}}}{\int_0^\infty V_s\left(r_{\text{c\_c-sp}}\right)\cdot\Psi\left(r_{\text{c\_c-sp}}\right)dr_{\text{c\_c-sp}}}\\ &=\frac{V_s\left(R_{\text{c\_c-sp}}+T_{\text{sp\_c-sp}}\right)-V_s\left(R_{\text{c\_c-sp}}\right)}{V_s\left(R_{\text{c\_c-sp}}\right)}\end{aligned} \tag{6.13}$$

Meanwhile, the ratio between the total volume of the particulate shell and the total volume of the polymer cores was assumed to be equal to the ratio between the sum of volume fractions of the silica nanoparticles and the medium molecules within the particulate shell and the volume fraction of the polymer cores,

$$\begin{aligned}&\frac{\int_0^\infty\int_0^\infty\left[V_s\left(r_{\text{c\_c-sp}}+t_{\text{sp\_c-sp}}\right)-V_s\left(r_{\text{c\_c-sp}}\right)\right]\cdot\Psi\left(r_{\text{c\_c-sp}}\right)\cdot\Psi\left(t_{\text{sp\_c-sp}}\right)dr_{\text{c\_c-sp}}dt_{\text{sp\_c-sp}}}{\int_0^\infty V_s\left(r_{\text{c\_c-sp}}\right)\cdot\Psi\left(r_{\text{c\_c-sp}}\right)dr_{\text{c\_c-sp}}}\\ &=\frac{\phi_{\text{silica\_c-sp}}+\phi_{\text{med\_c-sp}}}{\phi_{\text{c-sp}}-\left(\phi_{\text{silica\_c-sp}}+\phi_{\text{med\_c-sp}}\right)}\end{aligned} \tag{6.14}$$

The ratio between the average volume of the particulate shell and the average volume of the

polymer cores could also be written as,

$$\frac{V_s\left(R_{c\_c\text{-}sp}+T_{sp\_c\text{-}sp}\right)-V_s\left(R_{c\_c\text{-}sp}\right)}{V_s\left(R_{c\_c\text{-}sp}\right)}=\frac{\left(R_{c\_c\text{-}sp}+T_{sp\_c\text{-}sp}\right)^3}{R_{c\_c\text{-}sp}^3}-1. \tag{6.15}$$

As the result, using equations 6.12, 6.14, and 6.15 with the approximation described by eq 6.13 the average thickness of the particulate shell could be expressed as,

$$T_{sp\_c\text{-}sp}=R_{c\_c\text{-}sp}\left(\sqrt[3]{\frac{\phi_{silica\_c\text{-}sp}}{\eta_{p\_vol\_avg}\phi_{c\text{-}sp}-\phi_{silica\_c\text{-}sp}}+1}-1\right). \tag{6.16}$$

Also, when assuming that the ratio between the total volume of the particulate shell and the total volume of the polymer cores is approximately equal to the ratio between the average volume of the particulate shell and the average volume of the polymer cores, the mean number of the silica nanoparticles on the polymer cores, N_{silica}, rather than the number of the silica nanoparticles on the individual polymer cores, could be more significant and representative for the whole system to describe the silica nanoparticles packing. Herein, N_{silica} is defined by the total number of the silica nanoparticles (defined as the volume fraction of the silica nanoparticles divided by the average volume of the single silica particle) divided by the total number of the polymer cores (defined as the volume fraction of the polymer cores divided by the average volume of the single polymer cores),

$$N_{silica}=\frac{\dfrac{\phi_{silica\_c\text{-}sp}}{\frac{4}{3}\pi R_{silica}^3}}{\dfrac{\phi_{c\text{-}sp}-\dfrac{\phi_{silica\_c\text{-}sp}}{\eta_{p\_vol\_avg}}}{\frac{4}{3}\pi R_{c\_c\text{-}sp}^3}}=\frac{\eta_{p\_vol\_avg}\cdot\phi_{silica\_c\text{-}sp}}{\eta_{p\_vol\_avg}\cdot\phi_{c\text{-}sp}-\phi_{silica\_c\text{-}sp}}\frac{R_{c\_c\text{-}sp}^3}{R_{silica}^3}. \tag{6.17}$$

Combined with eq 6.16, eq 6.17 could be rewritten as the

$$N_{silica}=\eta_{p\_vol\_avg}\cdot\frac{\left(R_{c\_c\text{-}sp}+T_{sp\_c\text{-}sp}\right)^3-R_{c\_c\text{-}sp}^3}{R_{silica}^3}. \tag{6.18}$$

Therefore, by defining the average superficial packing efficiency as,

$$\eta_{p\_sur\_avg}=\frac{N_{silica}}{2}\left(1-\frac{\sqrt{\left(R_{silica}+R_{c\_c\text{-}sp}\right)^2-R_{silica}^2}}{\left(R_{silica}+R_{c\_c\text{-}sp}\right)}\right), \tag{6.19}$$

the two packing efficiencies could eventually relate to each other as,

$$\eta_{\text{p\_sur\_avg}} = \frac{\left(R_{\text{c\_c-sp}} + T_{\text{sp\_c-sp}}\right)^3 - R_{\text{c\_c-sp}}^3}{2R_{\text{silica}}^3} \cdot \left(1 - \frac{\sqrt{\left(R_{\text{silica}} + R_{\text{c\_c-sp}}\right)^2 - R_{\text{silica}}^2}}{\left(R_{\text{silica}} + R_{\text{c\_c-sp}}\right)}\right) \cdot \eta_{\text{p\_vol\_avg}} \quad (6.20)$$

The packing structures represent how the silica nanoparticles organise on the polymer cores surface, which are based on the interactions between silica nanoparticles. Notably, in the previous Monte Carlo simulation study[14], only monolayer of the silica nanoparticles were considered, and thus, those simulations are suitable for both cores-particulate shell model and raspberry model. In addition, the raspberry model here could only describe the monolayer structure of the silica nanoparticles on the polymer cores because it only produces the centres of the silica nanoparticles at the certain distance, $\alpha_{\text{silica}}r_{\text{silica}}$, to the surface of the polymer cores. Moreover, the advantage of the c-ps&silica SAXS model is that it could potentially describe a multilayer structure of the silica nanoparticles on the polymer cores, because it translates the silica nanoparticles packing structures to the whole particulate shell structure without specifying the structure layout of the silica nanoparticles on the polymer cores. In addition, it is unnecessary to use the superficial packing efficiency for the multilayer structure of the silica nanoparticles on the polymer cores because its definition is clearly based on the fact that the silica nanoparticles all touch the polymer core surface, while for the multilayer structure, starting from the second layer, the silica nanoparticles are all out of touch with the polymer cores. However, the monolayer of the silica nanoparticles on the polymer cores is mainly targeted in this work.

Three types of the silica nanoparticle arrangements such as random particle packing, change-dependent repulsive particle interactions and Lennard-Jones particle interactions were considered in previous Monte Carlo simulations[14]. To describe and model these various types interparticle interactions, in previous research[14], hard-sphere structure factor solved with the Percus-Yevick closure relation (called for the sake of simplicity as hard-sphere Percus-Yevick structure factor) has been demonstrated to be an acceptable structure factor for three types of the interparticle interactions. However, the quantitative information derived from the hard-sphere Percus-Yevick structure factor has not been well interpreted. Herein, by describing the ideal unit cell of the silica nanoparticle packing structures (Figure 6.5), it is possible to reveal the physical meanings of quantitative information derived from the structure factor for the c-ps&silica model and the raspberry model.

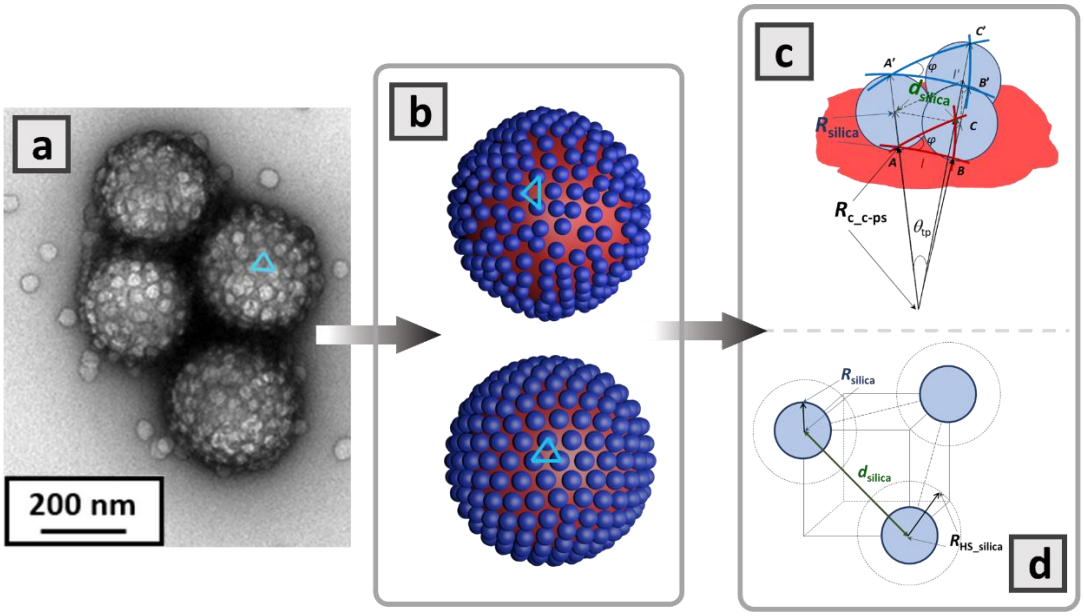

Figure 6.5 According to the TEM results of the final product of PTFEMA/silica nanocomposite particle (Figure 6.2), selected three closest silica nanoparticles could create an ideal unit cell of the silica nanoparticle packing structure (a). For the randomly distributed silica nanoparticles on the polymer cores (top b), such ideal unit cell is not well-defined, but for the regular packing structure (bottom b), such ideal unit cell is obvious. Such ideal unit cell is defined as the frustum *ABCA'B'C'* of a regular triangular pyramid with the length of three equal sides (*AB*, *BC*, *CA*) of *l* at the bottom (red lines) and with the length of three equal sides (*A'B'*, *B'C'*, *C'A'*) of *l'* at the top (blue lines) (c), and all angles of the bottom and top triangles are φ. The distance between the silica nanoparticle centres (d_{silica}) could be determined by the radius of the silica nanoparticles (R_{silica}) and the radius of polymer cores ($R_{c\_c\text{-}ps}$). For the estimation of the effective volume fraction of the hard-sphere Percus-Yevick structure factor of the silica nanoparticles, these three selected silica nanoparticles are the remained particles at the vertices of the primitive cubic (*cP*) with all distances between these three silica nanoparticle centres as the diagonals of the cube faces as d_{silica} (d).

Considering the centres of the silica nanoparticles on the polymer cores averagely located at vertices of a regular polyhedron, the ideal unit cell is defined as the frustum *ABCA'B'C'* of a regular triangular pyramid within three silica nanoparticles depicted as that the three slant heights are the diameter of the silica nanoparticles ($2R_{silica}$), the bottom is the spherical triangle (ΔABC) with three vertices as the contact points of the silica nanoparticles and the polymer cores, and the top is the spherical triangle ($\Delta A'B'C'$) with three vertices on the three silica nanoparticles (Figure 6.5 (c)). Since the polymer core and silica nanoparticle radii have a narrow standard deviation, herein, it is assumed that the radii of the polymer cores are the same and equal to $R_{c\_c\text{-}ps}$, and the radii of the silica nanoparticles also are the same and equal to R_{silica}. Therefore, it could be trivial to consider that the particulate shell thickness is $T_{ps\_c\text{-}ps}$ and equal to $2R_{silica}$ for the cores-particulate shell model. Herein, the ideal unit cell volume packing efficiency is given as,

$$\eta_{\text{p\_vol\_cell}} = \frac{\frac{1}{2}\cdot\frac{4}{3}\pi R_{\text{silica}}^3}{E\cdot\frac{\left(2R_{\text{silica}}+R_{\text{c\_c-sp}}\right)^3 - R_{\text{c\_c-sp}}{}^3}{3}} = \frac{2\pi R_{\text{silica}}{}^3}{E\left[\left(2R_{\text{silica}}+R_{\text{c\_c-sp}}\right)^3 - R_{\text{c\_c-sp}}{}^3\right]} \quad (6.21)$$

where E is spherical excess of the top or the bottom spherical triangle of the ideal unit cell, which is calculated as,

$$\begin{aligned} E &= 4\tan^{-1}\left[\sqrt{\tan\left(\frac{3}{4}\theta_{\text{tp}}\right)\tan^3\left(\frac{1}{4}\theta_{\text{tp}}\right)}\right] \\ &= 4\tan^{-1}\left\{\sqrt{\tan\left[\frac{3}{4}\cos^{-1}\left(1-\frac{d_{\text{silica}}^2}{2\left(R_{\text{silica}}+R_{\text{c\_c-sp}}\right)^2}\right)\right]\tan^3\left[\frac{1}{4}\cos^{-1}\left(1-\frac{d_{\text{silica}}^2}{2\left(R_{\text{silica}}+R_{\text{c\_c-sp}}\right)^2}\right)\right]}\right\} \end{aligned} \quad (6.22)$$

where θ_{tp} is the angle between two vectors of from polymer core centre to the attached points of two silica nanoparticle on the polymer core centre, and two nearest silica particles locating at a distance of d_{silica}. The number of the silica nanoparticles on the polymer cores under the ideal unit cell situation could be calculated *via* the number of the ideal unit cell, which could be given as the ratio between the area of the polymer cores and the area of the bottom spherical triangle, as,

$$N_{\text{silica\_cell}} = \frac{1}{2}\cdot\frac{4\pi R_{\text{c\_c-sp}}^2}{E\cdot R_{\text{c\_c-sp}}^2} = \frac{2\pi}{E}\cdot \quad (6.23)$$

Thus, $N_{\text{silica\_cell}}$ could be rewritten with eq 6.21 as,

$$N_{\text{silica\_cell}} = \frac{\eta_{\text{p\_sur\_cell}}}{2}\frac{\left(2R_{\text{silica}}+R_{\text{c\_c-sp}}\right)^3 - R_{\text{c\_c-sp}}{}^3}{R_{\text{silica}}{}^3}\cdot \quad (6.24)$$

For each ideal unit cell, it could provide its own volume packing efficiency. Assuming that all the polymer/silica nanocomposite particles are the same, the ideal unit cell volume packing efficiency should be equal to the average volume fraction efficiency. This means eq 6.24 should be equal to eq 6.18, and the only difference between eq 6.18 and eq 6.24 is that under the assumption of narrow particle dispersity $T_{\text{ps\_c-ps}}$ is replaced by $2R_{\text{silica}}$. Thus, the physical meaning of the particulate shell thickness could be the average diameter of the silica nanoparticles.

Assuming that the size polydispersities of the polymer cores and silica particles are narrow and the silica particles are averagely distributed on the polymer cores, the packing structures of the silica nanoparticles on the polymer cores could be considered as Figure 6.5 (d) illustrated. The silica nanoparticles form the monolayer structure on the polymer cores. Such monolayer of the silica nanoparticles is within the surface of the triangles with the sides equal to the diagonals of the cubic faces, and the silica nanoparticles are located on the vertices of such triangle (Figure 6.5 (d)). Because the silica nanoparticles at these vertices are the closest silica nanoparticles on the polymer cores, the length of the diagonals of the faces

of the cubic is d_{silica}. Since the silica interparticle interactions were described as the hard-sphere model for the SAXS analysis, the effective volume fraction of the hard-sphere Percus-Yevick structure factor could be given as the volume of the hard sphere particles divided by the volume of the unit cell as,

$$\phi_{HS\_silica} = \frac{\left(3 \cdot \frac{1}{8}\right) \cdot \frac{4}{3} \pi R_{HS\_silica}{}^{3}}{\left(\frac{d_{silica}}{\sqrt{2}}\right)^{3}} = \frac{\sqrt{2} \pi R_{HS\_silica}{}^{3}}{d_{silica}^{3}}, \quad (6.25)$$

where R_{HS_silica} is effective radius of the hard sphere for silica particle. By equations 6.20, 6.22, 6.23, and 6.24, d_{silica} is determined by the superficial packing efficiency, but R_{HS_silica} mainly has to be measured by SAXS modelling when giving the silica nanoparticles with the supposed interparticle interactions because it cannot be described by hard-sphere Percus-Yevick structure factor, even though it practically produced good fitting results.[14] Particularly, for random silica nanoparticles distribution condition when silica nanoparticles are considered as truly hard spheres, R_{HS_silica} could be approximately equal but not smaller than R_{silica}.

6.4.4 Validation of attempted SAXS models by Monte Carlo simulations and the following analysis for the monolayer silica nanoparticle packing structure

The validations by Monte Carlo simulations of the attempted structural models to describe polymer/silica nanocomposite particles depend on the goodness of fit to the SAXS patterns, and the following analysis includes the qualities and the physical meanings of the fitting variants results.

The validations by Monte Carlo simulations of c-ps&silica SAXS model have been presented,[14] and thus, these SAXS modelling results will be reviewed and discussed herein. The radii and their polydispersity of the polymer cores and the silica nanoparticles for Monte Carlo simulations of the SAXS patterns of the polymer/silica nanocomposite particles were set as 100 (±5) nm and 11(±1) nm, respectively. For various η_{p_sur}, different silica interparticle interaction were given. For η_{p_sur} = 0.09, 0.18 and 0.45, the interactions were considered as random distribution and charge-dependent repulsive interactions. For η_{p_sur} = 0.73, the interactions were considered as charge-dependent repulsive interactions and size-dependent Lennard-Jones interactions.

The reason when the condition of η_{p_sur} = 0.73 cannot be applied to random distribution of the silica interparticle interactions is because the η_{p_sur} of the particular shell saturation is approximately equal to 0.45. To explain the reason, the random sequential adsorption (RSA) model[29] could be the one of the references. The monolayer of the silica nanoparticles packing on the polymer cores could be described as the spherical cap on a two-dimensional surface. The maximum occupation of the one-dimensional random filling problem could be given as Rényi's parking constants[30] as 0.748. And because in the ideal unit cell of the silica

nanoparticles on the polymer cores with the spherical triangle bottom, the silica nanoparticles pack as the triangular lattice structure. The maximum silica nanoparticle packing density could be estimated as the product of the ratio of the area of the spherical cap and its circumscribed hexagon and the two-dimensional maximum packing density of Rényi's packing situation for the triangular packing structure, as $\frac{\sqrt{3}\pi}{6} \cdot \left[0.748^2 \cdot \sin\left(\frac{\pi}{3}\right)\right]$, which is equal to 0.439. This maximum packing density is close to the η_{p_sur} of the particular shell saturation, and because the silica nanoparticles packed on the polymer cores, the *c* of the particular shell saturation could be slightly larger than the estimated maximum silica nanoparticle packing density. Under these restrictions of the radii and their polydispersities of the polymer cores and the silica nanoparticles and various η_{p_sur}, the mass between the polymer cores and the silica nanoparticles are set. Therefore, the validation of c-ps&silica model and raspberry model not only include whether the models could interpret the morphologies of the particles but also involve whether the mass balance relationship between the polymer cores and the silica nanoparticles stands. For validation, the scattering length densities of polymer core (ξ_{core}), silica nanoparticle (ξ_{silica}), and medium as water (ξ_{med}) are 9.581 × 10^{10} cm^{-2}, 18.56 × 10^{10} cm^{-2}, and 9.42 × 10^{10} cm^{-2}, respectively. Therefore, $\xi_{c\_c\text{-}ps}$ in eq 6.3 is equal to ξ_{core}. And with eq 6.20, $\xi_{ps\_c\text{-}ps}$ in eq 6.3 is equal to $\eta_{p\_vol\_avg} \cdot \xi_{silica}$ + (1-$\eta_{p\_vol\_avg}$)·ξ_{med}. Though the scattering length densities between ξ_{core} and ξ_{med} are relatively closed, SAXS patterns (Figure 6.6) indicated polymer cores could be observed and distinguished from water background.

The polymer core radius, the silica nanoparticle radius and the superficial packing efficiencies can be used to estimate N_{silica_cell} (eq 6.24), $\eta_{p\_vol\_cell}$ (equations 6.21 and 6.22) and $\phi_{HS\_silica\_est}$ (equations 6.22, 6.23 and 6.25). These results could be compared with the results obtained from the c-ps&silica model fitting of the SAXS patterns calculated for the Monte Carlo simulated polymer/silica nanocomposite particles (Table 6.1). The estimated N_{silica_cell}, $\eta_{p\_vol\_cell}$, and $\phi_{HS\_silica\_est}$ were all reasonably matched the corresponding c-ps&silica SAXS fitting results. However, , the overrated or underrated N_{silica}, as discussed in the previous research[14], may break the mass balance relation between polymer cores and silica nanoparticles, which may limit the quantitative analysis of the polymer/silica structure. Also, when η_{p_sur} = 0.73, the modelling results of R_{HS_silica} were smaller than R_{silica}, and the maxima of the structure factor for the silica nanoparticles of the corresponding fitting obviously moved to high *q* position, which also indicated that the modelling results of R_{HS_silica} was not satisfactory (Figure 6.6). These two problems are connected to each other due to principally incorrect structure factor model, even though it practically produced reasonably good fitting results and good corresponding relations to the geometrical restrictions.

Table 6.1. The estimated number of the silica nanoparticles on the polymer cores under the ideal unit cell situation (N_{silica_cell}), the estimated closest distance between silica nanoparticles (d_{silica}), the estimated ideal unit cell volume packing efficiency ($\eta_{p\_vol\_cell}$) based on SAXS modelling result of R_{HS_silica}, and the estimated effective volume of the hard-sphere Percus-Yevick structure factor (ϕ_{HS_silica}) compared to the c-ps&silica SAXS modelling results of to the mean number of the silica nanoparticles on the polymer cores (N_{silica}), the effective radius of the

hard sphere for silica particle (R_{HS_silica}), the average volume packing efficiency ($\eta_{p\_vol\_cell}$), and the effective volume of the hard-sphere Percus-Yevick structure factor ($\phi_{HS\_silica\_m}$) from the Monto Carlo simulation SAXS patterns with different silica interparticle interactions at different superficial packing efficiencies (η_{p_sur})[14]. Notably, the R_{HS_silica} for estimated $\phi_{HS\_silica\_est}$ at random situations were set as 11 nm.

silica interpaticle interaction	η_{p_sur}	estimated N_{silica_cell}	model result N_{silica}	estimated $d_{silica}/2$ (Å)	model result R_{HS_silica} (Å)	R_{HS_silica} (Å) for estimation of ϕ_{HS_silica}	estimated $\eta_{p\_vol\_cell}$	model result $\eta_{p\_vol\_avg}$	estimated $\phi_{HS\_silica\_est}$	model result $\phi_{HS\_silica\_m}$
repulsion	0.09	37	32	345	289	289	5.97%	6.02%	32.69%	35.00%
random	0.18	73	67	245	122	110	11.93%	11.38%	5.00%	5.20%
repulsion			69		214	214		11.38%	36.84%	39.20%
random	0.45	183	208	155	111	110	29.83%	29.21%	19.83%	20.00%
repulsion			199		130	130		29.21%	32.74%	35.00%
repulsion	0.73	297	292	122	104	110	48.39%	47.92%	41.03%	35.00%
L J			314		106	110		47.92%	41.03%	41.00%

Compared with c-ps&silica model, n_{silica} of the form factor of raspberry model (eq 6.10) is given by eq 6.11 with various η_{p_sur} of Monte Carlo simulations. To valid the raspberry model, only the standard deviation of the silica nanoparticles, σ_{silica}, the effective radii, R_{HS_silica}, and the effective volume fraction of hard-sphere Percus-Yevick structure factor, ϕ_{HS_silica}, were variables in the raspberry modelling. The published patterns[14] do not include case corresponding to η_{p_sur} = 0.09, and therefore, the discussion is focused on the remaining cases (Table 6.2) with their fittings (Figure 6.6). The fittings by the raspberry model were reasonably acceptable except the random distribution of the silica nanoparticles on the polymer cores which also cannot be fitted well by the c-ps&silica SAXS model. It may be because discontinuous structures formed at low packing efficiency of silica particles, $\eta_{p\_sur} \leq$ 0.18, cannot be reproduced by the normal integral process involved in the form factor calculation. The standard deviations of the silica nanoparticles were always slightly larger than the given conditions of the silica nanoparticles and the effective radii of hard-sphere Percus-Yevick structure factor were always larger than the average radius of the silica nanoparticles. The effective volume fractions of hard-sphere Percus-Yevick structure factor were also larger than the results by the c-ps&silica model. Also, the peak intensity corresponding to the silica structure factor were overrated compared to the Monte Carlo simulated SAXS patterns and the fittings from c-ps&silica SAXS model. This is because the hard-sphere Percus-Yevick structure factor could not fully describe the silica interparticle interactions on the polymer cores. Even though it produced reasonably good fittings for the cores-particulate shell model, the number of the silica nanoparticles on the polymer cores may be overrated or underrated during the fitting process. For the raspberry model, because the number of the silica nanoparticles on the polymer cores was directly given by the initial conditions, the overrated intensities of the first peak originating from the hard-sphere Percus-Yevick structure factor may affect the quantification of the mass balance condition between the polymer and silica nanoparticles. The cases of the higher η_{p_sur} and the repulsive interactions between the silica nanoparticles enhance the overrated effects of the raspberry model (Figure 6.6).

Table 6.2. The standard deviation of the silica nanoparticles (σ_{silica}), the effective radii (R_{HS_silica}), and the effective volume fraction of hard-sphere Percus-Yevick structure factor ($\phi_{HS\_silica\_m}$) results of modified raspberry model fitting to the calculated SAXS patterns of Monto Carlo simulated polymer/silica nanoparticles with different silica interparticle interactions at different superficial packing efficiencies (η_{p_sur})[14]. The $\phi_{HS\_silica\_est}$ estimated by R_{HS_silica} (equations 6.22, 6.23 and 6.25) as the references compared with $\phi_{HS\_silica\_m}$. Notably, the R_{HS_silica} for estimated $\phi_{HS\_silica\_est}$ at random situations were set as 11 nm.

silica interpaticle interaction	η_{p_sur}	σ_{silica} (Å)	model result R_{HS_silica} (Å)	R_{HS_silica} (Å) for estimation of $\phi_{HS\_silica\_est}$	estimated $\phi_{HS\_silica\_est}$	model result $\phi_{HS\_silica\_m}$
random	0.18	10.55	128	110	5.00%	9.49%
repulsion		10.58	217	217	38.34%	40.87%
random	0.45	11.69	113	110	19.83%	25.86%
repulsion		10.20	137	138	38.84%	41.32%
repulsion	0.73	13.60	113	113	44.95%	45.72%
L J		15.57	116	116	47.62%	51.37%

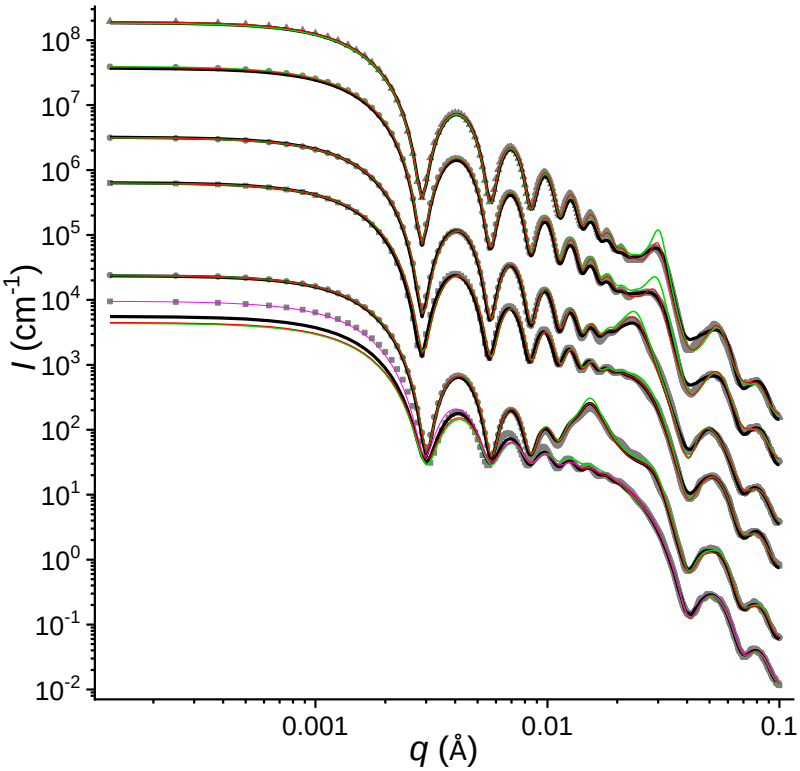

Figure 6.6. SAXS patterns of the polymer/silica nanocomposite particles simulated by Monte Carlo[14] (grey dots) presented from the bottom to the top of the graph for the following cases of silica nanoparticle distributions in the particulate shell: random distribution on the polymer cores with η_{p_sur} = 0.18, repulsive interactions on the polymer

cores with η_{p_sur} = 0.18, random distribution on the polymer cores with η_{p_sur} = 0.45, repulsive interactions on the polymer cores with η_{p_sur} = 0.45, repulsive interactions on the polymer cores with η_{p_sur} = 0.73, and the Lennard-Jones interactions on the polymer cores with η_{p_sur} = 0.73, respectively. Corresponding c-ps&silica SAXS modelling[14] (blacks), modified raspberry model (eq 6.10) (greens), the raspberry model with the correction by Boltzmann sigmoid equation for the silica nanoparticle structure factor (eq 6.27) (reds), the raspberry model with the corrections by Boltzmann sigmoid equations for the silica nanoparticle scattering amplitude and the silica nanoparticle structure factor (eq 6.28) (pinks), respectively. To avoid overlapping, the SAXS patterns have been shifted upwards using the same arbitrary multiplication factors as in the published literature[14].

To minimise the negative effects from failures of the structure factors, herein, a potential strategy is raised. The reason for such strategy is because SAXS modelling for the c-ps&silica SAXS model and raspberry model are relatively sensitive and the physical meanings after SAXS modelling are still critical for polymer/silica nanoparticles analysis. Because the overrated intensities of the structure factor located at the *q* region smaller than the maximum given by the structure factor, a coefficient, k_{sf}, could be introduced to reduce the effect overrated by the hard-sphere Percus-Yevick structure factor. To correct pattern of the overrated region by hard-sphere Percus-Yevick structure factor, the Boltzmann sigmoidal equation as[31],

$$BS_{sf} = k_{sf} + \frac{1-k_{sf}}{1+e^{\frac{qR_{HS\_silica}-3.97}{dq_{HS}}}}, \tag{6.26}$$

might be a simply option for the form factor (eq 6.10), where dq_{HS} is a fitting parameter, and the number 3.97 is given by the qR_{HS_silica} value where the hard-sphere Percus-Yevick structure factor reaches the first maximum. Therefore, the modified raspberry model form factor, eq 6.10, can be rewritten as,

$$\begin{aligned} F_{rasp\_BS}(q) = {} & \left(\xi_{c\_c\text{-}sp} - \xi_{med}\right)^2 \cdot A_s^2\left(q, r_{c\_c\text{-}sp}\right) \cdot V_s^2\left(r_{c\_c\text{-}sp}\right) \\ & + 2n_{silica}^2 \cdot \left(\xi_{c\_c\text{-}sp} - \xi_{med}\right)\left(\xi_{silica} - \xi_{med}\right) \cdot A_s\left(q, r_{c\_c\text{-}sp}\right) \cdot A_s\left(q, r_{silica}\right) \cdot \frac{\sin q\left(r_{c\_c\text{-}sp} + \alpha_{silica} r_{silica}\right)}{q\left(r_{c\_c\text{-}sp} + \alpha_{silica} r_{silica}\right)} \\ & + n_{silica}\left(n_{silica} - 1\right) \cdot \left(\xi_{silica} - \xi_{med}\right)^2 \cdot \left[A_s\left(q, r_{silica}\right) \cdot \frac{\sin q\left(r_{c\_c\text{-}sp} + \alpha_{silica} r_{silica}\right)}{q\left(r_{c\_c\text{-}sp} + \alpha_{silica} r_{silica}\right)}\right]^2 \\ & + \left(k_{sf} + \frac{1-k_{sf}}{1+e^{\frac{qR_{HS\_silica}-3.97}{dq}}}\right) \cdot n_{silica} \cdot \left(\xi_{silica} - \xi_{med}\right)^2 \cdot A_s^2\left(q, r_{silica}\right) \cdot V_s^2\left(r_{silica}\right) \cdot S(q) \end{aligned} \tag{6.27}$$

Therefore, the fitting variables here include k_{sf}, dq_{HS}, the standard deviation of the silica nanoparticles, the effective radius and the effective volume fraction of hard-sphere Percus-Yevick structure factor. The updated raspberry model produced more accurate fittings to the Monte Carlo simulated SAXS patterns, but the physical meaning of the effective volume fractions of the hard-sphere Percus-Yevick structure factor was still uncertain. Herein, the reduced effective volume fractions of the hard-sphere Percus-Yevick structure factor might be estimated by the procedure described below (Figure 6.7). The maximums of the value of

the hard-sphere Percus-Yevick structure factor at various ϕ_{HS_silica} could be measured and fitted by a polynomial equation as, $\left[S_{\mathrm{hs}}\left(\phi_{\mathrm{HS_{silica}}}\right)\right]_{\max} = 803{\phi_{\mathrm{HS_{silica}}}}^{6} - 1042{\phi_{\mathrm{HS_{silica}}}}^{5} + 550{\phi_{\mathrm{HS_{silica}}}}^{4} - 130{\phi_{\mathrm{HS_{silica}}}}^{3} + 16{\phi_{\mathrm{HS_{silica}}}}^{2} - 0.25\phi_{\mathrm{HS_{silica}}} + 1$, and when giving a measured ϕ_{HS_silica} by SAXS modelling, the corrected effective volume fraction, $\phi_{HS\_silica\_cor}$, could be given by $[S_{hs}(\phi_{HS\_silica})]_{max}$ when $[S_{hs}(\phi_{HS\_silica})]_{max}$ is equal to the reduced value of the structure factor as $[(1+k_{sf})\cdot[S_{hs}(\phi_{HS\_silica})]_{max}]/2$ (Table 6.3). These estimated effective volume fractions of hard-sphere Percus-Yevick structure factor for the given raspberry model were close to the results obtained by c-ps&silica SAXS modelling and the ideal monolayer structure prediction, which suggested that this empirical normalisation of the effective volume fraction of hard-sphere Percus-Yevick structure factor procedure could be applied to the further analysis, even though it lacks a theoretical derivation. When η_{p_sur} = 0.18 with random distributed silica nanoparticles, a large deviation between ϕ_{HS_silica} and $\phi_{HS\_silica\_cor}$ indicated that this correction by a polynomial equation was not suitable for such condition. For η_{p_sur} = 0.18 with silica nanoparticles of charge-dependent repulsive interactions and η_{p_sur} = 0.45 with both random distributed silica nanoparticles and silica nanoparticles of charge-dependent repulsive interactions, such correction was relatively successful to reduce the values of ϕ_{HS_silica} to $\phi_{HS\_silica\_cor}$ which were matched $\phi_{HS\_silica\_est}$. However, when η_{p_sur} = 0.73 with both random distributed silica nanoparticles and silica nanoparticles of charge-dependent repulsive interactions, ϕ_{HS_silica} were already matched $\phi_{HS\_silica\_est}$, and therefore, the correction by a polynomial equation was still not successful for these conditions. Thus, such correction by a polynomial equation could by applied to η_{p_sur} = 0.18 with silica nanoparticles of charge-dependent repulsive interactions and η_{p_sur} = 0.45 with both random distributed silica nanoparticles and silica nanoparticles of charge-dependent repulsive interactions. However, it was doubtful for the rest conditions. Even though ϕ_{HS_silica} could not actually provide accurate physical meanings for the structural information of the polymer/silica nanocomposite particles, the SAXS fittings of the raspberry model corrected by Boltzmann sigmoid equation (eq 6.27) could be still useful for SAXS modelling.

Table 6.3. The results of fitting of the raspberry model corrected by Boltzmann sigmoid equation (eq 6.27) to calculated SAXS patterns of Monto Carlo simulated polymer/silica nanoparticle with different silica interparticle interactions at different superficial packing efficiencies (η_{p_sur})[14]. Notably, the R_{HS_silica} for estimated $\phi_{HS\_silica\_est}$ at random situations were set as 11 nm.

silica interpaticle interaction	η_{p_sur}	σ_{silica} (Å)	R_{HS_silica} (Å)	R_{HS_silica} (Å) for estimation of ϕ_{HS_silica}	ϕ_{HS_silica}	k_{hs}	dp_{HS}	$\phi_{HS\_silica\_cor}$	$\phi_{HS\_silica\_est}$
random	0.18	10.42	128	110	5.32%	0.94	0.05	0.87%	5.00%
repulsion		10.57	217	217	40.87%	0.79	3.19	37.83%	38.34%
random	0.45	11.53	114	110	24.65%	0.83	0.21	17.88%	19.83%
repulsion		10.23	138	138	40.40%	0.79	0.56	37.28%	38.84%
repulsion	0.73	13.77	115	115	45.15%	0.57	0.21	39.40%	46.89%
LJ		15.08	116	116	50.27%	0.54	0.27	45.55%	48.12%

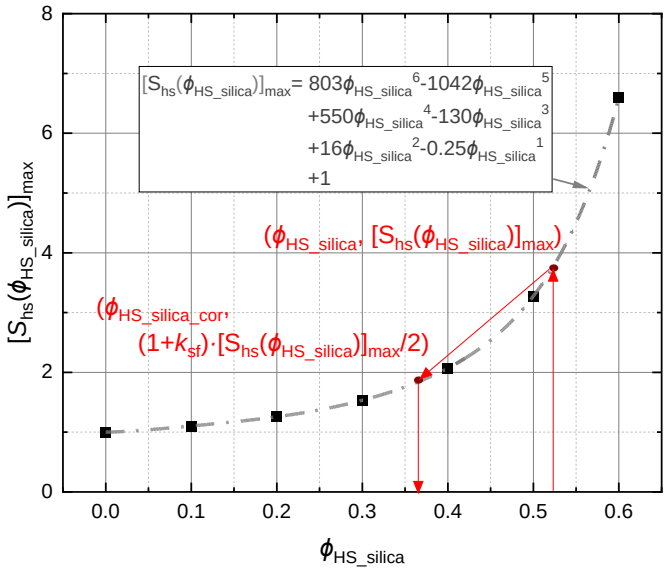

Figure 6.7. Dependence of the silica particle hard-sphere Percus-Yevick structure factor peak intensity, $[S_{hs}(\phi_{HS\_silica})]_{max}$, on the effective volume fractions, ϕ_{HS_silica}, (black squares) and a polynomial equation fitted to the data (grey line). After SAXS fitting of the raspberry model corrected by Boltzmann sigmoid equation (eq 6.27), the SAXS modelling results of effective volume fraction hard-sphere Percus-Yevick structure factor was given as ϕ_{HS_silica}. With the effective volume fraction correction by the polynomial equation, the peak intensity of polynomial equation is given as $[S_{hs}(\phi_{HS\_silica})]_{max}$ when the effective volume fraction is equal to ϕ_{HS_silica}. Then, $\phi_{HS\_silica\_cor}$ is given by the polynomial equation when $[S_{hs}(\phi_{HS\_silica\_cor})]_{max}$ is equal to $(1 + k_{sf})\cdot[S_{hs}(\phi_{HS\_silica})]_{max}$ /2.

An empirical approach could also be exploited to overcome uncertainty of fitting obtained for the low-density randomly distributed silica nanoparticles using eq 6.27. This equation can be modified as,

$$
\begin{aligned}
F_{\text{rasp\_dBS}}(q) = & \left(\xi_{\text{c\_c-sp}} - \xi_{\text{med}}\right)^2 \cdot A_s^2\left(q, r_{\text{c\_c-sp}}\right) \cdot V_s^2\left(r_{\text{c\_c-sp}}\right) \\
& + 2n_{\text{silica}}^2 \cdot \left(\xi_{\text{c\_c-sp}} - \xi_{\text{med}}\right)\left(\xi_{\text{silica}} - \xi_{\text{med}}\right) \cdot A_s\left(q, r_{\text{c\_c-sp}}\right) \cdot A_s\left(q, r_{\text{silica}}\right) \cdot BS_{\text{sp\_c-sp}} \cdot \frac{\sin q\left(r_{\text{c\_c-sp}} + \alpha_{\text{silica}} r_{\text{silica}}\right)}{q\left(r_{\text{c\_c-sp}} + \alpha_{\text{silica}} r_{\text{silica}}\right)} \cdot \\
& + n_{\text{silica}}\left(n_{\text{silica}} - 1\right) \cdot \left(\xi_{\text{silica}} - \xi_{\text{med}}\right)^2 \cdot \left[A_s\left(q, r_{\text{silica}}\right) \cdot BS_{\text{sp\_c-sp}} \cdot \frac{\sin q\left(r_{\text{c\_c-sp}} + \alpha_{\text{silica}} r_{\text{silica}}\right)}{q\left(r_{\text{c\_c-sp}} + \alpha_{\text{silica}} r_{\text{silica}}\right)} \right]^2 \\
& + BS_{\text{sf}} \cdot n_{\text{silica}} \cdot \left(\xi_{\text{silica}} - \xi_{\text{med}}\right)^2 \cdot A_s^2\left(q, r_{\text{silica}}\right) \cdot V_s^2\left(r_{\text{silica}}\right) \cdot S(q)
\end{aligned}
\tag{6.28}
$$

where $BS_{\text{sp\_c-ps}}$ is the Boltzmann sigmoid equation[31],

$$
BS_{\text{sp\_c-sp}} = k_{\text{sp\_c-sp}} + \frac{1 - k_{\text{sp\_c-sp}}}{1 + e^{\frac{q\left(r_{\text{c\_c-sp}} + r_{\text{silica}}\right) - 4.49}{dq_{\text{c\_c-sp}}}}},
\tag{6.29}
$$

where $k_{\text{sp\_c-ps}}$ and $dq_{\text{sp\_c-ps}}$ are the coefficients, and the number 4.49 is given by the $q(r_{\text{c\_c-ps}}+r_{\text{silica}})$ value where sphere form factor reaches the first minimum. The fitting performed using the corrected raspberry model form factor (eq 6.28) (Figure 6.6) with $k_{\text{sp\_c-ps}}$ = 1.52 and $dq_{\text{sp\_c-ps}}$ = 1.16 provided good fit to the randomly distributed silica nanoparticles at $\eta_{\text{p\_sur}}$ = 0.18 (Figure 6.4). Therefore, the Boltzmann sigmoid equation correction is relatively successful to correct the structure factor of the SAXS modelling. Even though it lacks clear interpretation of physical meanings, this method of Boltzmann sigmoid equation correction is relatively simple for correction of SAXS fitting process.

To conclude, these two SAXS models have no significant difference between each other, and both perform reasonable SAXS modelling results corresponding to the Monte Carlo simulation SAXS patterns. Therefore, either model could possibly describe the structural morphologies formed during PTFEMA/silica nanocomposite particle synthesis.

6.4.5 The c-ps&silica model for the *in situ* SAXS studies of the synthesis of the PTFEMA/silica nanocomposite particles

Since both models produced reasonably good fits to the simulated SAXS patterns of the polymer/silica nanocomposite particles with various silica nanoparticle monolayer packing structure, for the sake of simplicity, only c-ps&silica model was used for analysing time-resolved SAXS patterns collected during synthesis of the PTFEMA/silica nanocomposite particles. In this SAXS model, the volume fractions of the core-particulate shell particles, the absorbed silica nanoparticles, and the non-absorbed silica nanoparticles should rigorously follow the mass balance of components available in the reagent system. This imposes constrains on the variables of c-ps&silica SAXS model. The initial masses of the TFEMA monomer, the silica nanoparticles, and the water medium are $m_{\text{TFEMA\_ini}}$, m_{silica}, and m_{water}, respectively, and thus, the initial volumes of the TFEMA, the silica nanoparticles, and the water are given as $v_{\text{TFEMA\_ini}} = m_{\text{TFEMA\_ini}}/\rho_{\text{TFEMA}}$, $v_{\text{silica}} = m_{\text{silica}}/\rho_{\text{silica}}$, and $v_{\text{water}} = m_{\text{water}}/\rho_{\text{water}}$, respectively, where ρ_{TFEMA}, ρ_{silica}, and ρ_{water} are the densities of the TFEMA, the silica nanoparticles, and the water, respectively. Therefore, during the synthesis, the TFEMA monomers convert to the PTFEMA, and thus, the volume of PTFEMA is given as v_{PTFEMA} =

$conv_{TFEMA} \cdot m_{TFEMA\_ini}/\rho_{PTFEMA}$, where $conv_{TFEMA}$ is the TFEMA monomer mass conversion, and ρ_{PTFEMA} is the density of the PTFEMA. Meanwhile, the TFEMA volume during the synthesis is given as $v_{TFEMA} = (1 - conv_{TFEMA}) \cdot m_{TFEMA\_ini}/\rho_{TFEMA}$. As a result, the volume fractions of the PTFEMA, ϕ_{PTFEMA}, TFEMA, ϕ_{TFEMA}, and silica nanoparticles, ϕ_{silica}, are given as $v_{PTFEMA}/(v_{PTFEMA}+v_{TFEMA}+v_{silica}+v_{water})$, $v_{TFEMA}/(v_{PTFEMA}+v_{TFEMA}+v_{silica}+v_{water})$, $v_{silica}/(v_{PTFEMA}+v_{TFEMA}+v_{silica}+v_{water})$, respevtively. After the compounds form PTFEMA/silica nanocomposite particles, it is assumed that all the PTFEMA polymers form the cores of the nanocomposite particles, part of TFEMA monomer may be dissolved in the cores, and part of the silica nanoparticles comprises the PTFEMA/silica nanocomposite particles. Thus, the synthesised nanocomposite particle volume fraction can be expressed as,

$$\phi_{P/Snp} = \frac{\phi_{PTFEMA}}{1 - xmon} + A_{e\_silica} \cdot \phi_{silica}, \tag{6.30}$$

where *xmon* is the volume fraction of the TFEMA monomer in the polymer cores of the nanocomposite particles, A_{e_silica} is the silica nanoparticle packing efficiency on the PTFEMA polymer cores. Consequently, $\phi_{c\text{-}ps}$ in eq 6.2 is equal to $\phi_{P/Snp}$, $\phi_{silica\_c\text{-}ps}$ in eq 6.4 is equal to $A_{e\_silica} \cdot \phi_{silica}$, and ϕ_{silica_med} in eq 6.6 is equal to $(1 - A_{e\_silica}) \cdot \phi_{silica}$.

To further confine the fitting variables in c-ps&silica SAXS model, the scattering length density of the shell could be given as the function of the average volume packing efficiency,

$$\xi_{ps\_c\text{-}ps} = \eta_{p\_vol\_avg} \cdot \xi_{silica} + \left(1 - \eta_{p\_vol\_avg}\right) \cdot \xi_{med}, \tag{6.31}$$

where ξ_{silica} is the scattering length density of silica nanoparticle within the shell, and ξ_{med} is the scattering length density of the medium molecules within the shell. Also, the shell thickness of c-ps&silica SAXS model is restricted by eq 6.16. the scattering length density of the PTFEMA/silica nanocomposite particle core is given as:

$$\xi_{ps\_c\text{-}ps} = xmon \cdot \xi_{TFEMA} + \left(1 - xmon\right) \cdot \xi_{PTFEMA}, \tag{6.32}$$

where ξ_{TFEMA} and ξ_{PTFEMA} are scattering length densities of TFEMA and PTFEMA, respectively.

The densities of TFEMA, ρ_{TFEMA}, and H_2O, ρ_{med}, at the reaction temperature, 60 °C, were 0.983 g·cm^{-3} and 1.113 g·cm^{-3}, respectively. The density of PTFEMA, ρ_{TFEMA}, at 60 °C was estimated to be 1.456 g·cm^{-3} using a helium picnometer measurement on a dry powder at room temperature and assuming that the PTFEMA has the same thermal expansion coefficient as poly(methyl methacrylate)[32]. The density of silica, ρ_{silica}, at 60 °C was estimated to be 2.092 g·cm^{-3} using a helium pycnometer measurement on a dry powder at 20 °C and assuming that the relatively low linear thermal expansion coefficient of fused silica is 5.5×10^{-7} K^{-1}.[33] This value was assumed to be valid at the polymerisation temperature. Scattering length densities of TFEMA (ξ_{TFEMA}), PTFEMA (ξ_{PTFEMA}), silica nanoparticle (ξ_{silica}), and water (ξ_{med}) at 90 °C used for SAXS analysis are 9.669×10^{10} cm^{-2}, 1.265×10^{11} cm^{-2}, 1.775×10^{11} cm^{-2} and 9.271×10^{10} cm^{-2}, respectively.[34]

6.5 Results and Discussion

The TEM results suggested that it was highly likely that the silica nanoparticles formed a packed monolayer structure on the polymer cores. Thus, the validated c-ps&silica model (eq 6.1) could be applied for the modelling of the SAXS patterns (Figure 6.8 and Figure 6.9). These SAXS patterns collected during the PTFEMA/silica nanocomposite particle synthesis indicated relatively high size polydispersity indicated by only the first minimum at around q = 0.003 Å^{-1} and the second minimum around q = 0.006 Å^{-1} clearly observed via the SAXS patterns. According to Guinier law for SAXS analysis[35], these two first minimums of the SAXS patterns could reveal the total size of nanocomposite particles. Therefore, because of the relatively high polydispersity of the polymer/silica nanocomposite particles, the polydispersity of the polymer core and the polydispersity of the particulate shell cannot be estimated by SAXS modelling at the same time. The polydispersity of the particulate shell could be estimated by the polydispersity of the silica nanoparticles. This meant that the polydispersity of the polymer core radius in the core-particulate shell was required to be considered during the SAXS modelling. And even though ϕ_{silica} and ϕ_{TFEMA} were given by the initial reagent composition used for the synthesis, these two volume fractions were still required the validation. To clarify the fitting variables for the polymer/silica nanocomposite particles by c-ps&silica SAXS model, eq 6.1 could be presented by these potential fitting variables as,

$$I_{\text{c-sp\&silica}}(q) = I_{\text{c-sp\&silica}}\begin{pmatrix} \phi_{\text{silica}}, \phi_{\text{TFEMA}}, \\ conv_{\text{TFEMA}}, xmon, A_{\text{e}}, \eta_{\text{p\_vol\_avg}}, \\ R_{\text{c\_c-ps}}, \sigma_{\text{c\_c-ps}}, R_{\text{silica}}, \sigma_{\text{silica}}, R_{\text{HS\_silica}}, \phi_{\text{HS\_silica}} \end{pmatrix}. \quad (6.33)$$

For the SAXS analysis of this emulsion polymerisation, it is required to demonstrate the condition of TFEMA monomer, because it might be obtained in SAXS patterns and affect SAXS modelling. For such monomer, the solubility of TFEMA monomer in water is 0.906 g·dm^{-3} at 20 °C[36], and the density of TFEMA monomer is 1.181 g·cm^{-3} at 25 °C[20]. Therefore, the solubility of TFEMA monomer in water could be also estimated as 7.67 × 10^{-4} v/v at 20 °C. This indicated that TFEMA monomer might remain in monomer droplets or be hidden in the polymer cores during the polymerisation, because of the extremely poor TFEMA monomer solubility. Also, optical microscopy provided the evidence of monomer droplets at 0, 10, 20, 30, 40, 50 min of this polymerisation (Figure 6.10). Clearly, from 0 min to 50 min of the synthesis, the number and the size of TFEMA monomer droplet both decreased. At 0 min, the compressed large monomer droplets were also observed by the optical microscopy. And at 50 min of the synthesis, a small amount of μm-size TFEMA monomer droplets still remained in the medium. Also, nm-size TFEMA monomer droplets might exist in the system, but optical microscopy cannot observe nm-size TFEMA monomer droplet. Meanwhile, from the time-resolved SAXS patterns of polymerisation of the PTFEMA/silica nanocomposite

particles (Figure 6.11), no relatively large particles were observed at low *q* region. One of the possible reasons was that the size and the volume fraction of the TFEMA monomer droplets both decreased during the polymerisation. Therefore, potentially existed TFEMA monomer droplets might be hidden by the relatively strong scattering intensities of silica nanoparticles and the PTFEMA/silica nanocomposite.

According to the optical microscopy results, at 0 min of the synthesis, TFEMA monomer droplets appeared in the system. However, the first SAXS pattern (Figure 6.8) collected at 0 min suggested that there was no obvious structure factor required for this SAXS pattern. This meant that the c-ps&silica model was still suitable for this first SAXS pattern, because there is no extra structure factor for the scattering intensity of the non-absorbed silica nanoparticles in medium phase (eq 6.1). Thus, ϕ_{silica} was determined by the c-ps&silica modelling using only single population of the non-absorbed silica particles,

$$I_{\text{c-sp\&silica\_first}}(q) = I_{\text{c-sp\&silica}}\left(R_{\text{silica}}, \sigma_{\text{silica}}, \phi_{\text{silica}}\right), \tag{6.34}$$

which suggested that ϕ_{silica} was 1.20% v/v, which was 18.3% lower than the initial volume fraction of the silica nanoparticles calculated by the initial mass of the silica nanoparticles. Meanwhile, it also determined R_{silica} with σ_{silica} as 9.75 (± 2.14) nm, and these structural parameters of the silica nanoparticles were fixed during the synthesis. This R_{silica} with σ_{silica} was consistent with the silica nanoparticle diameter given from the company, Nouryon, and DLS results (Figure 6.3 (a)).

The final SAXS pattern at 210 min (Figure 6.9) can be used to determine ϕ_{TFEMA}. According to NMR results obtained for the final product of the reaction the TFEMA monomer conversion was 96%. of It was known, with the NMR results of 96% monomer conversion. Thus, ϕ_{TFEMA} was determined by c-ps&silica SAXS model fitting to the last SAXS frame without using $conv_{\text{TFEMA}}$ variable,

$$I_{\text{c-sp\&silica\_final}}(q) = I_{\text{c-sp\&silica}}\begin{pmatrix} \phi_{\text{TFEMA}}, \\ xmon, A_{\text{e}}, \eta_{\text{p\_vol\_avg}}, \\ R_{\text{c\_c-ps}}, \sigma_{\text{c\_c-ps}}, R_{\text{HS\_silica}}, \phi_{\text{HS\_silica}} \end{pmatrix}, \tag{6.35}$$

which suggested that ϕ_{TFEMA} was 2.96% v/v, which was 55.5% lower than the initial volume fraction of the monomer calculated by the initial mass of the monomer. Both ϕ_{silica} and ϕ_{TFEMA} were surprisingly lower than the expected initial volume fractions. The likely reason for the inconsistencies of relatively low ϕ_{silica} and ϕ_{TFEMA} observed by SAXS that the reaction mixture was heterogeneous in the stirrable reactor cell and penetration of the reagents into the narrow gap adjacent to the Kapton film windows transparent for X-rays was limited resulting in reduced local amount of the reaction components in comparison with the amount loaded in the cell. This means that the SAXS modelling results could not be fully comparable to the common laboratory results. However, relative volume fractions of the components can be used for the analysis. Thus, the following discussion focus on whether the SAXS modelling results could be justified by themselves rather than comparing with the possible laboratory-scale synthesis products characterised by DLS and TEM. The After the determination of ϕ_{silica}

and ϕ_{TFEMA} the other time-resolved SAXS patterns (Figure 6.11) could be fitted by

$$I_{\text{c-sp\&silica\_rest}}(q) = I_{\text{c-sp\&silica}}\left(\begin{matrix} conv_{\text{TFEMA}}, xmon, A_{\text{e}}, \eta_{\text{p\_vol\_avg}}, \\ R_{\text{c\_c-sp}}, \sigma_{\text{c\_c-sp}}, R_{\text{HS\_silica}}, \phi_{\text{HS\_silica}} \end{matrix}\right). \quad (6.36)$$

Considering the DLS results indicating that the polymer/silica nanocomposite particles were formed after 20 min of the synthesis, c-ps&silica SAXS model could be used for the SAXS pattern analysis after this point of the PTFEMA/silica nanocomposite particle synthesis (Table 6.4).

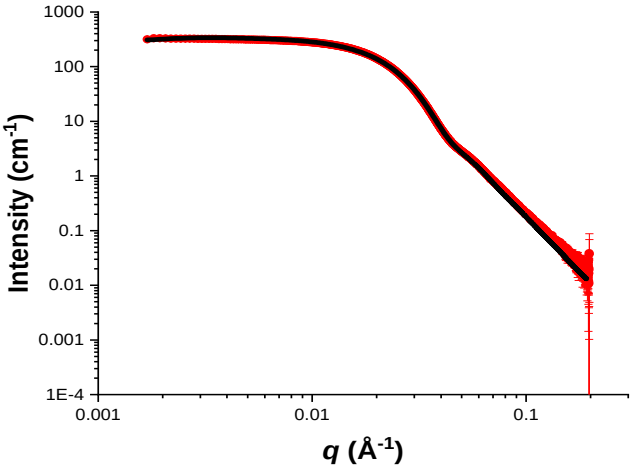

Figure 6.8. The first SAXS pattern recorded during the PTFEMA/silica nanocomposite particle synthesis (red circles) fitted by the SAXS model represented by eq 6.34 (black line).

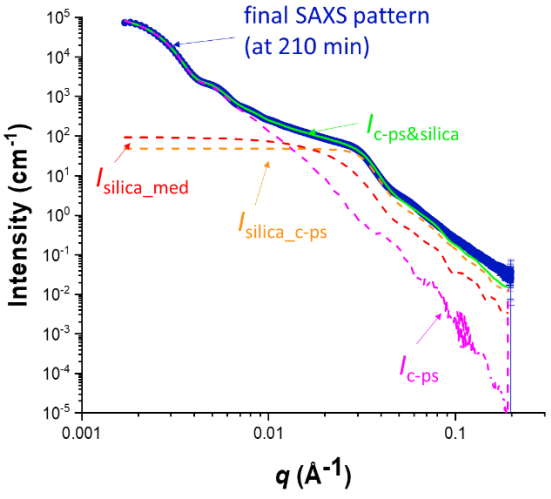

Figure 6.9. The final SAXS pattern recorded during the PTFEMA/silica nanocomposite particle synthesis (blue circles) fitted by the SAXS model represented by eq 6.35 (green line) with sub-intensities of the polymer/silica cores-particulate shell structure, $I_{c\text{-}ps}$ (pink), the self-correlation intensity of the silica nanoparticles absorbed within the particulate shell, $I_{silica\_c\text{-}ps}$ (orange), and the non-absorbed silica nanoparticles in medium phase, I_{silica_med} (red).

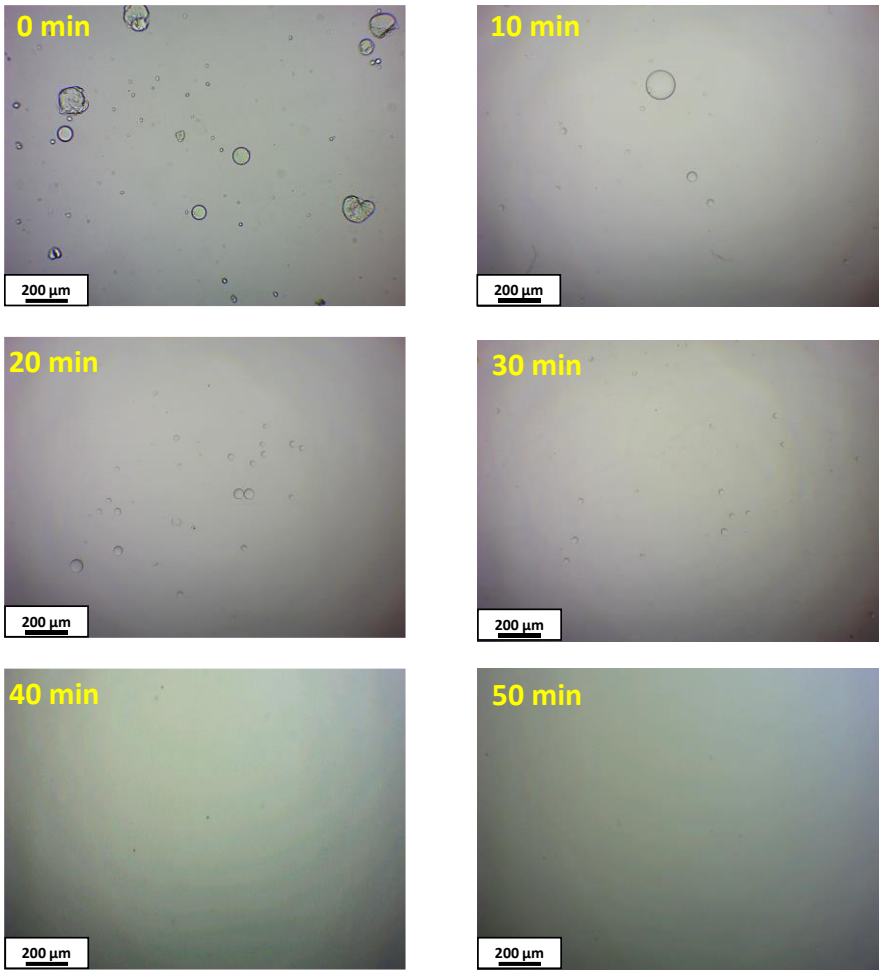

Figure 6.10. Optical microscopy images recorded at 0, 10, 20, 30, 40, 50 min during the laboratory-based synthesis of PTFEMA/silica nanocomposite particles via aqueous emulsion polymerization of TFEMA at 60 °C when targeting 10% w/w solids.

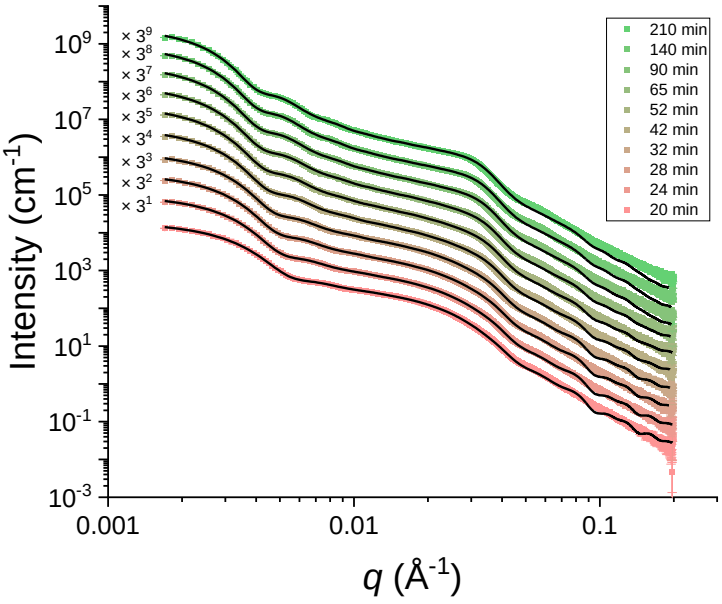

Figure 6.11. The selected SAXS patterns recorded at 20, 24, 28, 32, 42, 52, 65, 90, 140, and 210 min (final frame) of the PTFEMA/silica nanocomposite particle synthesis (gradient) fitted by the SAXS model represented by equations 6.35 and 6.36 (black line). The scattering patterns are shifted upward (the multiplication factors are indicated on the plots) to avoid overlap.

Table 6.4. Results of c-ps&silica SAXS model fitting to the SAXS patterns recorded during the PTFEMA/silica nanocomposite particle synthesis. The Excel® colour scales are used to enhance the presentations of the parameter tendency. The fitting variables, the variables dependent on the fitting variables, and the estimated variables are labelled in blue, yellow, and green, respectively. The cells with the maximum value are fully filled by the corresponding colours, and the cells with the minimum value are left blank. The c-ps&silica SAXS model fitting results included TFEMA monomer conversion ($conv_{TFEMA}$), the volume fraction of TFEMA monomer in the PTFEMA polymer cores (*xmon*), the silica nanoparticle packing efficiency on the PTFEMA polymer cores (A_{e_silica}), the average volume packing efficiency ($\eta_{p\_sur\_avg}$), the average radius of the polymer core ($R_{c\_c\text{-}ps}$), the polydispersity index of the radius of the polymer core (PDI = $\sigma_{c\_c\text{-}ps}$ / $R_{c\_c\text{-}ps}$), the average thickness of the particulate shell ($T_{ps\_c\text{-}ps}$), the effective radius of the hard sphere for silica particle (R_{HS_silica}), the effective volume of the hard-sphere Percus-Yevick structure factor (ϕ_{HS_silica}), and the average number of the silica nanoparticles within the particulate shell (N_{silica}). And the references including the distance between the silica nanoparticle centres (d_{silica}), the estimated effective volume of the hard-sphere Percus-Yevick structure factor by equations 6.22, 6.23 and 6.25 ($\phi_{HS\_silica\_est}$), and the average volume packing efficiency by equations 6.21 and 6.22 ($\eta_{p\_sur\_avg\_est}$) also presented to interpret SAXS modelling results.

time	$conv_{TFEMA}$	xmon	A_{e_silica}	model result $\eta_{p\_vol\_avg}$	$R_{c\_c\text{-}ps}$	PDI	$T_{ps\_c\text{-}ps}$	$R_{c\_c\text{-}ps}+T_{ps\_c\text{-}ps}$	model result R_{HS_silica}	model result ϕ_{HS_silica}	model result N_{silica}	estimated $d_{silica}/2$	$\phi_{HS\_silica\_est}$	$\eta_{p\_sur\_avg\_est}$
min					nm		nm	nm	nm			nm		
20	15.3%	0.00	21.3%	67%	56.62	0.23	15.83	72.45	7.76	32.3%	143.66	9.15	33.8%	78.0%
22	20.7%	0.00	25.8%	65%	61.13	0.23	16.13	77.26	7.87	31.1%	162.27	9.33	33.3%	77.2%
24	25.4%	0.00	29.4%	63%	64.31	0.22	16.30	80.60	7.94	30.3%	175.79	9.44	33.0%	76.6%
26	31.0%	0.08	33.3%	61%	66.97	0.22	15.36	82.33	7.89	28.8%	170.32	9.59	30.9%	69.1%
28	34.6%	0.08	36.0%	60%	68.76	0.22	15.51	84.28	7.93	28.4%	176.43	9.71	30.2%	68.3%
30	37.8%	0.09	38.3%	59%	70.34	0.22	15.66	86.00	7.99	28.0%	182.32	9.81	30.0%	67.8%
32	41.2%	0.10	40.8%	58%	71.80	0.21	15.76	87.56	8.03	27.3%	187.58	9.89	29.7%	67.3%
37	50.6%	0.14	47.0%	55%	75.09	0.21	15.78	90.87	8.10	26.3%	193.13	10.16	28.1%	64.0%
42	58.3%	0.14	53.2%	53%	77.74	0.21	16.07	93.81	8.21	25.8%	203.85	10.32	28.0%	63.5%
47	66.3%	0.16	56.3%	51%	79.84	0.21	16.13	95.96	8.28	25.2%	207.08	10.51	27.2%	61.5%
52	73.1%	0.18	60.4%	49%	81.37	0.21	16.23	97.60	8.33	24.5%	207.89	10.71	26.1%	59.7%
65	82.0%	0.17	66.3%	48%	83.57	0.21	17.00	100.57	8.50	24.0%	222.87	10.90	26.3%	61.0%
90	90.4%	0.12	71.2%	47%	85.91	0.21	18.31	104.22	8.71	23.7%	249.94	11.03	27.4%	65.1%
105	93.8%	0.08	72.7%	47%	86.97	0.20	18.99	105.96	8.84	23.8%	267.64	11.02	28.7%	68.2%
140	94.8%	0.07	74.3%	47%	87.11	0.21	19.42	106.53	8.87	23.4%	275.46	11.03	28.9%	70.0%
165	95.2%	0.06	75.2%	46%	87.21	0.21	19.73	106.94	8.90	23.1%	280.33	11.05	29.0%	71.1%
190	95.6%	0.06	75.8%	46%	87.39	0.20	19.95	107.34	8.91	23.0%	284.51	11.06	29.1%	71.9%
210	96.0%	0.05	76.0%	46%	87.61	0.20	20.05	107.66	8.95	22.9%	287.96	11.05	29.5%	72.4%

The SAXS modelling suggested that the polymer cores of the PTFEMA/silica nanocomposite particles continuously grew during the synthesis (Table 6.4). The final product radius measured by SAXS was 87.61 nm, which was consistent to TEM results (Figure 6.2). Meanwhile, PDI, given as $\sigma_{c\_c\text{-}ps}$ / $R_{c\_c\text{-}ps}$, of these polymer cores gradually reduced. Unlike polymer spherical micelles during PISA synthesis with the potential for both an intense copolymer chain exchange and fusion effects, the number density of the PTFEMA/silica nanocomposite particles of this aqueous emulsion polymerisation, $N_{P/Snp}$, given by a least square fitting, $\mathrm{MIN}\left\{\frac{1}{n_{frame}-6}\sqrt{\sum_{h=7}^{n_{frame}}\left[\phi_{PTFEMA}\left(t_{frame(h)}\right)-N_{P/Snp}\cdot V_s\left[R_{c\_c\text{-}ps}\left(t_{frame(h)}\right)\right]\right]^2}\right\}$,

where n_{frame} is the total number of recorded frames. $N_{P/Snp}$ remained relatively constant as 9×10^{12} cm^{-3} during the synthesis, which was within a typical range of the number density for emulsion polymerisation[37] (Figure 6.12).

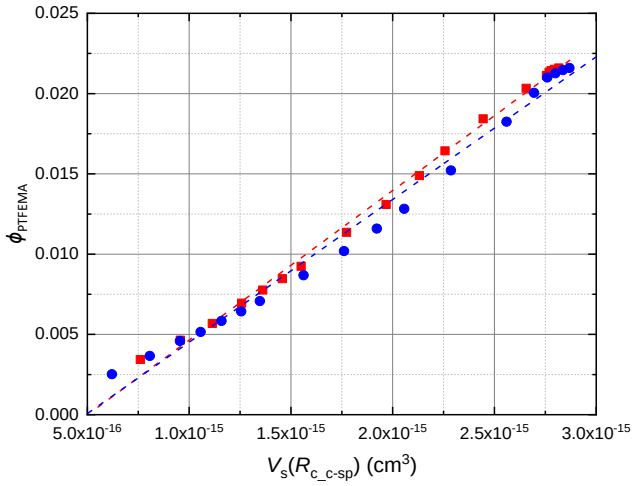

Figure 6.12. A relationship between the volume faction of PTFEMA, ϕ_{PTFEMA}, and the average volume of the

PTFEMA core of the PTFEMA/silica nanocomposite particles, $V_s(R_{c\_c\text{-}sp})$ obtained from the SAXS fitting results using equations 6.35 and 6.36 (red squares) and equations 6.39 and 6.40 (blue circles). Both set of data can be fitted by linear relationships (red and blue dashed lines, respectively).

Because R_{silica} measured by c-ps&silica SAXS model (eq 6.34) was 9.75 nm, the particulate shell thickness results by c-ps&silica SAXS modelling were relatively low, smaller than $2R_{silica}$ (= 19.50 nm), before 140 min of the synthesis. However, during the whole synthesis, $\eta_{p\_vol\_avg}$ measured by c-ps&silica SAXS model and the following $\eta_{p\_sur\_avg\_est}$ were both higher than 30% and 45%, which cannot be considered as the failure of c-ps&silica SAXS model at the situation of low silica nanoparticles packing density ($\eta_{p\_sur\_avg}$ = 0.09). One of the possible reasons could be that the silica nanoparticles may slightly penetrated into the PTFEMA cores. However, there was no evidence to support this proposal. Even though this surprising low particulate shell thickness by c-ps&silica SAXS modelling cannot be fully interpreted, the structure information of the silica nanoparticles packing structures were consistent measured by $\eta_{p\_vol\_avg}$, R_{HS_silica} and ϕ_{HS_silica}. These three parameters indicated that the packing density of silica nanoparticle on the polymer core was reducing during the polymerisation. Even though the silica nanoparticle density on the polymer cores was reducing during the synthesis, the silica nanoparticle packing efficiency was continuously increasing and reached 76.0% at the end of the synthesis. This rising silica nanoparticle packing efficiency is also indicated by the increasing N_{silica} calculated by eq 6.18 at a relatively constant number density of the PTFEMA/silica nanocomposite particles. Because $\eta_{p\_vol\_avg}$ was continuously decreasing during the polymerisation, the rising d_{silica} estimated by equations 6.22 and 6.23 along the polymerisation also revealed the gradual decrease of the number density of the silica nanoparticles on the polymer cores, although d_{silica} were under 9.75 nm for the first 30 min of the synthesis. The $\phi_{HS\_silica\_est}$ estimated by eq 6.25 was reasonably matched by ϕ_{HS_silica} produced by c-ps&silica SAXS model fitting results. c-ps&silica SAXS modelling of the final pattern of the synthesis provided $\eta_{p\_sur\_avg\_est}$ = 72.4%. According to the SAXS modelling results of ϕ_{HS_silica} and $\eta_{p\_sur\_avg}$ by c-ps&silica SAXS model validated by the SAXS patterns provided by Monte Carlo simulated polymer/silica nanocomposite particles (Table 6.1), if $\eta_{p\_sur\_avg}$ is over 45%, the interactions between silica nanoparticles on the polymer cores could be charge-dependent repulsive interaction or size-dependent Lennard-Jones interaction. And it is hardly considered that silica nanoparticles are random distributed on the polymer cores. And because the silica nanoparticles were modified and carried negative charges, with the c-ps&silica SAXS modelling results of $\eta_{p\_sur\_avg\_est}$ = 72.4%, the silica nanoparticles on the polymer cores still carried negative charged at the end of polymerisation. Also, because the silica nanoparticles were still charged on the PTFEMA cores, the silica nanoparticles soluble in the water may be expelled by the silica nanoparticles on the PTFEMA cores, which may be the reason why the silica packing efficiency continuously decreased after the polymer particle nucleation.

The conventional rate of the polymerisation (eq 1.8) was not suitable for assessing the

kinetics of the studied emulsion polymerisation as there was no relationship established between the monomer concentration in the core and the polymerisation rate. Instead, by measuring the relation between the estimated rate of the polymerisation at time $t+\Delta t/2$, $R_{p\_TFEMA}(t+\Delta t/2)$, defined as $[conv_{TFEMA}(t+\Delta t)-conv_{TFEMA}(t)]/\Delta t$, where Δt is the time gap between two selected modelled SAXS patterns, and the estimated remained volume fraction of the TFEMA at time $t+\Delta t/2$, $\phi_{TFEMA}(t+\Delta t/2)$, defined as $[\phi_{TFEMA}(t+\Delta t)+\phi_{TFEMA}(t)]/2$, it was found that the rate of the polymerisation of the PTFEMA/silica nanocomposite particles was approximately proportional to the remained TFEMA concentration in the whole system, which suggested that such polymerisation could be a diffusion-controlled reaction (Figure 6.13).

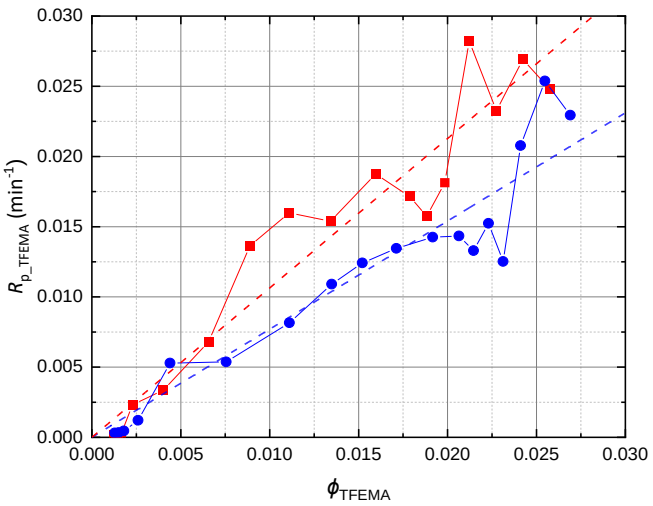

Figure 6.13. A relationship between the estimated rate of the polymerisation, R_{p_TFEMA}, and the estimated remained volume fraction of the TFEMA, ϕ_{TFEMA}, obtained from both the SAXS fitting results using equations 6.35 and 6.36 (red squares), and equations 6.39 and 6.40 (blue circles). Both set of data are fitted by linear relationships (red and blue dashed lines, respectively).

Therefore, the TFEMA monomer mass transfer during the potential diffusion-controlled polymerisation could be described by Fick's first law as,

$$J_{TFEMA}(t) = D_{TFEMA}\frac{\Delta\phi_{TFEMA}(t)}{\Delta x_{TFEMA}(t)}, \tag{6.37}$$

where D_{TFEMA} is the diffusion coefficient for TFEMA at reaction temperature, $\Delta\phi_{TFEMA}(t)$ is the difference of ϕ_{TFEMA} at times $t+\Delta t$ and t, and $\Delta x_{TFEMA}(t)$ is given as $\sqrt{\frac{3v_{TFEMA}(t)}{4\pi R_{c\_c\text{-}ps}(t)}}$ at t. $J_{TFEMA}(t)$ is the diffusion flux of the TFEMA at t, defined as

$$J_{\mathrm{TFEMA}}(t)=\frac{\Delta v_{\mathrm{TFEMA}}(t)}{A_{\mathrm{c\_c\text{-}ps}}(t)\cdot\Delta t}, \tag{6.38}$$

where $\Delta v_{\mathrm{TFEMA}}$ is the TFEMA volume difference between times $t+\Delta t$ and t, defined as $v_{\mathrm{TFEMA}}(t+\Delta t)-v_{\mathrm{TFEMA}}(t)$, and $A_{\mathrm{c\_c\text{-}ps}}(t)$ is the total surface area of the polymer cores of the PTFEMA/silica nanocomposite particles, defined as $\frac{3v_{\mathrm{TFEMA}}(t)}{4R_{\mathrm{c\_c\text{-}ps}}(t)}$. By this method, the D_{TFEMA} could be given by a least square fitting was applied to minimize the difference between $J_{\mathrm{TFEMA}}(t)$ and $\Delta\phi_{\mathrm{TFEMA}}(t)/\Delta x_{\mathrm{TFEMA}}(t)$, $\mathrm{MIN}\left\{\frac{1}{n_{\mathrm{frame}}-h+1}\sqrt{\sum_{h}^{n_{\mathrm{frame}}}\left[J_{\mathrm{TFEMA}}\left(t_{\mathrm{frame}(h)}\right)-D_{\mathrm{TFEMA}}\frac{\Delta\phi_{\mathrm{TFEMA}}\left(t_{\mathrm{frame}(h)}\right)}{\Delta x_{\mathrm{TFEMA}}\left(t_{\mathrm{frame}(h)}\right)}\right]^2}\right\}$, where n_{frame} is the total number of recorded frames, and h is the starting frame, which is equal to 1 in this case. And the least square fitting method provided as a result of D_{TFEMA} as 1.15×10^{-9} $m^2\cdot s^{-1}$. The estimation of the diffusion coefficient, $D_{\mathrm{TFEMA\_est}}$, could be given as $(k_B T_{\mathrm{TFEMA}})/(6\pi\cdot\eta_{\mathrm{water}}\cdot R_{\mathrm{TFEMA}})$, where T_{TFEMA} is the reaction temperature, 60 °C, η_{water} is the viscosity of water at the reaction temperature and R_{TFEMA} is the hydrodynamic radius of the TFEMA molecule. R_{TFEMA} is estimated by $[(3M_{\mathrm{TFEMA}})/(4\pi\cdot\rho_{\mathrm{TFEMA}})]^{1/3}$, which is 3.84×10^{-10} m. Therefore, $D_{\mathrm{TFEMA\_est}}$ is given as 1.22×10^{-9} $m^2\cdot s^{-1}$, which is close to D_{TFEMA} calculated by linear regression fitting of the $J_{\mathrm{TFEMA}}(t)$ and $\Delta\phi_{\mathrm{TFEMA}}(t)/\Delta x_{\mathrm{TFEMA}}(t)$ relationship (Figure 6.11).

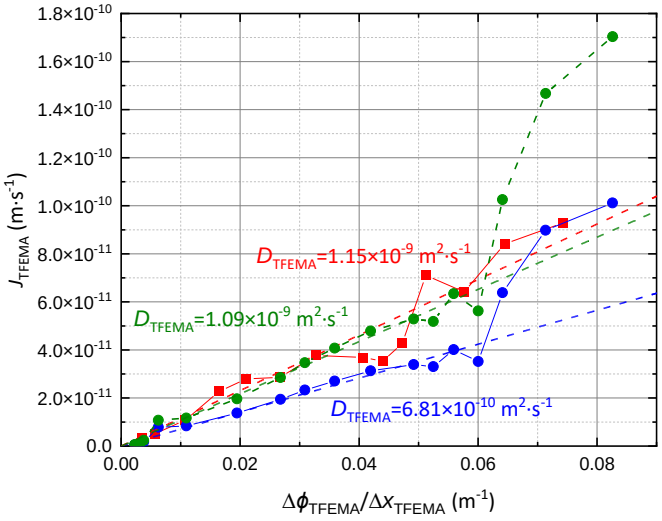

Figure 6.14. A relationship between the diffusion flux of the TFEMA at t, $J_{\mathrm{TFEMA}}(t)$, and the $\Delta\phi_{\mathrm{TFEMA}}(t)/\Delta x_{\mathrm{TFEMA}}(t)$ obtained from both the SAXS fitting results using equations 6.35 and 6.36 (red squares), and equations 6.39 and 6.40 (blue circles). Both set of data fitted by linear relationships (red and blue dashed lines, respectively) gave the diffusion coefficients of the TFEMA in water at 60 °C as 1.15×10^{-9} $m^2\cdot s^{-1}$ and 6.81×10^{-10} $m^2\cdot s^{-1}$, respectively. With correction of total surface area of the polymer cores of the PTFEMA/silica nanocomposite particles, the relationship between the diffusion flux of the TFEMA at t, $J_{\mathrm{TFEMA}}(t)$, and the $\Delta\phi_{\mathrm{TFEMA}}(t)/\Delta x_{\mathrm{TFEMA}}(t)$ obtained from both the SAXS fitting results using equations 6.39 and 6.40 (green circles) provided diffusion coefficients of the TFEMA in water at 60 °C as 1.09×10^{-9} $m^2\cdot s^{-1}$.

However, the SAXS modelling by c-ps&silica SAXS model provided an increasing shell thickness. The validation by the SAXS patterns calculated for the Monte Carlo simulated polymer/silica nanocomposite particles only confirms that c-ps&silica SAXS model is suitable for monolayer structure of silica nanoparticles on the polymer cores. Therefore, if the SAXS modelling results of the particulate shell thickness was over $2R_{silica}$, it may confuse other fitted variables during SAXS modelling. And therefore, when there was no controlled particulate shell thickness as $2R_{silica}$ in c-ps&silica SAXS modelling, other fitted variables might not produce reasonable results. Thus, the assumption of the particulate shell as constant as $2R_{silica}$ is required. Herein, by assuming the particulate shell as constant as $2R_{silica}$, the final pattern was fitted by

$$I_{\text{c-sp\&silica\_final\_T}}(q) = I_{\text{c-sp\&silica}}\begin{pmatrix} \phi_{\text{TFEMA}}, \\ xmon, A_{\text{e}}, \\ R_{\text{c\_c-ps}}, \sigma_{\text{c\_c-ps}}, R_{\text{HS\_silica}}, \phi_{\text{HS\_silica}} \end{pmatrix}, \tag{6.39}$$

and the rest patterns were fitted by

$$I_{\text{c-sp\&silica\_rest\_T}}(q) = I_{\text{c-sp\&silica}}\begin{pmatrix} conv_{\text{TFEMA}}, xmon, A_{\text{e}}, \eta_{\text{p\_vol\_avg}}, \\ R_{\text{c\_c-ps}}, \sigma_{\text{c\_c-ps}}, R_{\text{HS\_silica}}, \phi_{\text{HS\_silica}} \end{pmatrix}, \tag{6.40}$$

updating the SAXS modelling results (Table 6.5). The volume fraction of the TFEMA remained the same under the assumption and equations 6.39 and 6.40. This modified approach for SAXS analysis using constant particulate shell thickness produced results indicating a similar tendency for the PTFEMA core radius and its standard deviation, the silica nanoparticles packing efficiency on the polymer cores and slightly slower rate of polymerization (compare Tables 6.4 and 6.5). The SAXS analysis has also shown that *xmon* remained at low level during the SAXS data collection. Under this assumption of the particulate shell as constant as $2R_{silica}$, $\phi_{HS\_silica\_est}$ and $\eta_{p\_sur\_avg\_est}$ continuously decreased, while the estimated d_{silica} continuously increased. This indicated that the packing density of silica nanoparticles on the polymer cores became looser during the polymerisation. However, before 28 min of the synthesis, $\eta_{p\_sur\_avg\_est}$ was larger than 90.69 % which was the theoretical maximum of the $\eta_{p\_sur\_avg}$ [14, 26-28]. Meanwhile, the estimated d_{silica} was smaller than R_{silica} before 28 min of the synthesis. These SAXS modelling results indicated that c-ps&silica SAXS model may not be suitable for modelling the SAXS pattern before 28 min. One of the possible reasons was that the morphologies before 28 min were not well-defined core-particulate shell structure. Meanwhile, estimated ϕ_{HS_silica} under the assumption of the particulate shell as constant as $2R_{silica}$ was not matched the ϕ_{HS_silica} by SAXS modelling with constant particulate shell thickness. One of the possible reasons might be the defect of the hard-sphere Percus-Yevick structure factor without correction by eq 6.26. This might be improved for further structural analysis. The number density of the PTFEMA/silica nanocomposite particles of this aqueous emulsion polymerisation, $N_{P/Snp}$, still

remained around 9×10^{12} cm^{-3} (Figure 6.12) under the assumption of the particulate shell as constant as $2R_{silica}$. This $N_{P/Snp}$ was consistent with the result of $N_{P/Snp}$ without the assumption of the particulate shell as constant as $2R_{silica}$. Likewise, the relation between the monomer concentration in the polymer core and the rate of the polymerisation as well as the diffusion estimation could be processed after 28 min of the polymerisation, which indicated the slower rate of polymerisation (Figure 6.13) and the diffusion coefficient of the TFEMA in water which was estimated as 6.81×10^{-10} $m^2 \cdot s^{-1}$ by $\mathrm{MIN}\left\{\frac{1}{n_{frame}-h+1}\sqrt{\sum_{h}^{n_{frame}}\left[J_{TFEMA}\left(t_{frame(h)}\right)-D_{TFEMA}\frac{\Delta\phi_{TFEMA}\left(t_{frame(h)}\right)}{\Delta x_{TFEMA}\left(t_{frame(h)}\right)}\right]^2}\right\}$ when h = 5 (Figure 6.14). This condition of h = 5 is because after 28 min of the reaction, the SAXS modelling results can be interpreted in physical meanings. Compared with D_{TFEMA_est} as 1.22×10^{-9} $m^2 \cdot s^{-1}$ in water estimated by Stokes-Einstein equation and D_{TFEMA} as 1.15×10^{-9} $m^2 \cdot s^{-1}$ without the assumption of the particulate shell as constant as $2R_{silica}$, the diffusion coefficient of the TFEMA in water under the assumption of the particulate shell as constant as $2R_{silica}$ was relatively smaller than the expected D_{TFEMA_est} result. This relatively smaller D_{TFEMA} might indicate an extra repulsion of TFEMA monomer provided by PTFEMA/silica nanocomposite particles. One of the possible reasons could be that silica nanoparticles on the PTFEMA cores might reduce rate of TFEMA monomer transportation from the medium to the PTFEMA cores. To estimate the effect of silica nanoparticle by avoiding TFEMA fluently transported into the PTFEMA cores, $A_{c\_c\text{-}ps}$ now has to be corrected. Because the TFEMA monomers are transported through the gaps between silica nanoparticles on the PTFEMA cores (Figure 6.15), the total surface area of the polymer cores of the PTFEMA/silica nanocomposite particles is estimated by $\eta_{p\_vol\_avg} \cdot A_{c\_c\text{-}ps}$. Therefore, the diffusion coefficient of the TFEMA in water under assumption of the particulate shell thickness was over $2R_{silica}$ with modification of $A_{c\_c\text{-}ps}$ was estimated as 1.09×10^{-9} $m^2 \cdot s^{-1}$ by $\mathrm{MIN}\left\{\frac{1}{n_{frame}-h+1}\sqrt{\sum_{h}^{n_{frame}}\left[J_{TFEMA}\left(t_{frame(h)}\right)-D_{TFEMA}\frac{\Delta\phi_{TFEMA}\left(t_{frame(h)}\right)}{\Delta x_{TFEMA}\left(t_{frame(h)}\right)}\right]^2}\right\}$ when h = 5 (Figure 6.14). This result was close to D_{TFEMA_est} as 1.22×10^{-9} $m^2 \cdot s^{-1}$. Also, these results also indicated that before 28 min of the reaction, the morphologies of the particles cannot be simply described as silica nanoparticles absorbed on the PTFEMA polymer cores. Therefore, more assumptions and models are required for further analysis, similar with discussion in Chapter 4.

Table 6.5. Results of c-ps&silica SAXS model fitting to the SAXS patterns recorded during the PTFEMA/silica nanocomposite particle synthesis. It was assumed that the particle shell thickness is constant and equal to mean diameter of the silica particles ($2R_{silica}$) (equations 6.39 and 6.40). The Excel® colour scales are used to enhance the presentations of the parameter tendency in the same way as in Table 6.4. The fitting variables, the variables dependent on the fitting variables, and the estimated variables are labelled in blue, yellow, and green, respectively. The cells with the maximum value are fully filled by the corresponding colours, and the cells with the minimum value are left blank.

time	$conv_{TFEMA}$	$xmon$	A_{e_silica}	model result $\eta_{p\_vol\_avg}$	$R_{c\_c\text{-}ps}$	PDI	$T_{ps\_c\text{-}ps}$	$R_{c\_c\text{-}ps}+T_{ps\_c\text{-}ps}$	model result R_{HS_silica}	model result ϕ_{HS_silica}	model result N_{silica}	estimated $d_{silica}/2$	$\phi_{HS\_silica\_est}$	$\eta_{p\_sur\_avg\_est}$
min					nm		nm	nm	nm			nm		
20	11.3%	0.00	22.1%	65%	52.91	0.23	19.51	72.42	7.46	27.0%	161.60	9.30	64.0%	98.5%
22	16.3%	0.00	26.9%	63%	57.76	0.23	19.51	77.26	7.60	26.4%	180.96	9.48	60.5%	94.9%
24	20.5%	0.00	30.8%	61%	61.10	0.22	19.51	80.60	7.68	25.9%	195.23	9.58	58.6%	93.0%
26	23.0%	0.00	33.6%	61%	63.19	0.22	19.51	82.70	7.74	25.3%	205.26	9.63	57.8%	92.2%
28	26.1%	0.00	36.0%	60%	65.17	0.22	19.51	84.67	7.81	25.4%	213.20	9.70	56.4%	90.7%
30	28.7%	0.00	38.0%	59%	66.93	0.22	19.51	86.44	7.91	25.6%	221.15	9.75	55.5%	89.8%
32	31.6%	0.00	40.2%	59%	68.52	0.21	19.51	88.03	7.97	25.4%	228.28	9.80	54.7%	89.0%
37	38.7%	0.00	45.0%	57%	71.98	0.21	19.51	91.49	8.14	25.6%	241.87	9.95	52.3%	86.4%
42	45.4%	0.00	49.2%	56%	74.91	0.21	19.51	94.42	8.28	25.6%	253.88	10.06	50.6%	84.5%
47	51.7%	0.00	52.9%	55%	77.13	0.21	19.51	96.64	8.40	25.7%	261.69	10.17	49.0%	82.7%
52	57.1%	0.00	55.6%	54%	78.89	0.21	19.51	98.40	8.50	25.8%	266.36	10.29	47.3%	80.9%
65	67.7%	0.02	62.1%	51%	81.72	0.21	19.51	101.23	8.62	25.0%	270.64	10.53	44.1%	77.1%
90	81.2%	0.03	69.6%	48%	84.86	0.21	19.51	104.37	8.76	24.0%	273.31	10.84	40.5%	72.8%
105	89.1%	0.05	74.0%	47%	86.33	0.20	19.51	105.83	8.81	23.2%	272.66	11.02	38.5%	70.4%
140	93.3%	0.05	75.8%	46%	87.01	0.21	19.51	106.52	8.82	22.7%	272.71	11.10	37.7%	69.5%
165	94.5%	0.06	75.4%	46%	87.43	0.21	19.51	106.94	8.89	23.1%	276.30	11.08	37.9%	69.8%
190	95.3%	0.03	75.1%	46%	87.82	0.20	19.51	107.33	8.95	23.4%	279.33	11.06	38.1%	70.0%
210	96.0%	0.03	74.9%	47%	88.14	0.20	19.51	107.65	9.00	23.5%	282.40	11.04	38.3%	70.3%

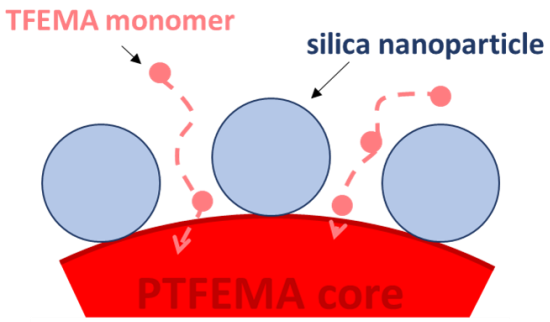

Figure 6.15. Schematic presentation of TFEMA monomer (pink circle) transported into PTFEMA core (red substrate) via the gaps between silica nanoparticles (blue circles) along the tracks (pink dash lines).

The constant particulate shell thickness assumption for c-ps&silica SAXS model (equations 6.38 and 6.39) did not significantly change the SAXS results obtained for the synthesis process of the PTFEMA/silica nanocomposite particles. Possibly, the relatively broad polydispersity of the PTFEMA cores of the nanoparticles has partially screened this effect on the SAXS analysis results and did not allow more details of the particulate shell structure to be produced. Both c-ps&silica SAXS modelling results under two different assumptions revealed the expected increasing of PTFEMA polymer core size and A_{e_silica} were observed during polymerisation process, after PTFEMA polymer cores were potentially all covered by the silica nanoparticles. Meanwhile, the silica nanoparticles packing structure surprisingly became looser, and finally the silica nanoparticles packing density reached the maximum of the lower limit of the uniform spheres ultimate packing density. It was possibly because negative charges still remained on the silica nanoparticles attached polymer core surfaces. Nevertheless, the modelling restrictions did not strongly affect the interpretation of the mechanism of this PTFEMA/silica nanocomposite particles emulsion polymerisation indicating a diffusion-controlled reaction

mechanism. No relationship between the amount of the TFEMA monomer in the PTFEMA polymer cores and the rate of polymerisation was observed but instead a strong relationship between the TFEMA monomer quantity remained in the reaction system and the rate of polymerisation was found from SAXS analysis. Compared with the mass transfer model in Chapter 3 and Chapter 5, which gives $\Delta x_{dri} = 2.26 \times 10^{-3}$ m and $\Delta x_{dri}(t) = 8.09 \times 10^{-2}$ m, here no $\Delta x_{dri}(t)$ involved because the mass transfer model with chemical potential effect is not invited here. However, considering that the TFEMA monomers are insoluble in water, the travelling distance affected by chemical potential in this case can be considered to be closed to $\Delta x_{TFEMA}(t)$, which was between 0.6 m and 1.2 m during the polymerisation. In Chapter 3, BzMA monomer was soluble in mineral oil, and in Chapter 4, though BzMA monomer was soluble in ethanol, the solubility was reduced by adding water in the system[38, 39]. Here, TFEMA was not soluble in water. These results indicate that the travelling distance affected by chemical potential will be longer when monomers are in the poorer solvents. This may be because the poorer solvents could press the monomers towards the polymer cores, and on the contrary, the monomers mainly remained Brownian motion in the better solvents.

6.6 Conclusion

For further investigate the polymerisation of PTFEMA/silica nanocomposite particles, SAXS technique was introduced to record such in-situ synthesis process. DLS and TEM results provide evident of polymer/silica nanocomposite particle nucleation process between 5 min and 20 min, and at 20 min of reaction, PTFEMA/silica nanocomposite particles were formed. After the previews from DLS and TEM, such PTFEMA/silica nanocomposite particles can be possibly described by c-ps&silica SAXS and the raspberry model. Meanwhile, geometric restrictions combined with the fitting variables attempt to fulfil the physical interpretations of these two models. Under such geometric restrictions, the previous validations and modelling results by the SAXS patterns calculated for the Monte Carlo simulated polymer/silica nanocomposite particles can be further explained. Superficial packing efficiency and volume packing efficiency, and effective volume fraction of hard-sphere Percus-Yevick structure factor now are available to demonstrate silica nanoparticle packing structure on polymer core surfaces. A further correction of hard-sphere Percus-Yevick structure factor for raspberry model provided more accurate SAXS fittings for those SAXS patterns. After the validations of two SAXS models, c-ps&silica SAXS model was chosen to model the in-situ SAXS patterns of the synthesis of the PTFEMA/silica nanocomposite particles with mass balance confinement. This c-ps&silica SAXS model with mass balance confinement provided relatively good SAXS fittings of the SAXS patterns of the PTFEMA/silica nanocomposite particles synthesis. The PTFEMA core of PTFEMA/silica nanocomposite particles grew during the synthesis, and the silica nanoparticles continuously attached on these PTFEMA cores. Meanwhile, the packing density of the silica nanoparticles on PTFEMA cores became looser during synthesis. With the validation of the c-ps&silica SAXS model, the

silica nanoparticles on PTFEMA cores might still carry with negative charges. However, the particulate shell thickness was increasing during the polymerisation. The number density of PTFEMA/silica nanocomposite particles nearly remained the same during the reaction. No relationship between *xmon* and rate of polymerisation was observed during the synthesis, and mass transfer model of TFEMA monomer from medium to PTFEMA cores was applied to this system. With estimated D_{TFEMA} in water by Stokes-Einstein equation, the diffusion coefficient of TFEMA in water measured by mass transfer model of TFEMA monomer was similar to estimated D_{TFEMA}. Nevertheless, the particular shell thickness provided by c-ps&silica SAXS model was not constant and equal to $2R_{silica}$. An assumption of the particular shell thickness as $2R_{silica}$ was applied to renew the c-ps&silica SAXS modelling of the synthesis of the PTFEMA/silica nanocomposite particles. Under this assumption of the particular shell thickness as $2R_{silica}$, relatively slower polymerisation was revealed. The packing density of the silica nanoparticles on PTFEMA cores still became looser during synthesis. The number density of PTFEMA/silica nanocomposite particles was the same as c-ps&silica SAXS modelling result without assumption of the particular shell thickness as $2R_{silica}$. However, the measured diffusion coefficient of TFEMA in water was significantly smaller than estimated D_{TFEMA}. This might indicate that silica nanoparticles on PTFEMA cores hindered the TFEMA transportation, and further correction to estimate diffusion coefficient of TFEMA transportation has confirmed this statement. These strong advantages of in-situ SAXS data collection and the modelling with analysis not only just support the post-mortem characteristic techniques but also emphases the understanding of the whole synthesis process of the polymer/silica nanocomposite particles, which could provide advice and inspire the design of synthesis process and the structures of the polymer/silica nanocomposite particles in the further.

6.7 References

1. Srivastava, A.; Mishra, V.; Singh, P.; Srivastava, A.; Kumar, R., Comparative study of thermal degradation behavior of graft copolymers of polysaccharides and vinyl monomers. *Journal of thermal analysis and calorimetry* **2012,** *107* (1), 211-223.

2. Srivastava, A.; Mishra, V.; Singh, S. K.; Kumar, R., One pot synthesis and characterization of industrially important graft copolymer (GOH-g-ACM) by using peroxymonosulphate/mercaptosuccinic acid redox pair. *e-Polymers* **2009,** *9* (1).

3. Srivastava, A.; Mishra, V.; Singh, S. K.; Kumar, R., Vanadium (V)/mandelic acid initiated graft copolymerization of acrylamide onto guar gum in an aqueous medium. *Journal of applied polymer science* **2010,** *115* (4), 2375-2385.

4. Balmer, J. A.; Schmid, A.; Armes, S. P., Colloidal nanocomposite particles: quo vadis? *Journal of Materials Chemistry* **2008,** *18* (47), 5722-5730.

5. Azioune, A.; Ben Slimane, A.; Ait Hamou, L.; Pleuvy, A.; Chehimi, M. M.; Perruchot, C.; Armes, S. P., Synthesis and characterization of active ester-functionalized polypyrrole− silica

nanoparticles: application to the covalent attachment of proteins. *Langmuir* **2004,** *20* (8), 3350-3356.

6. Gill, M.; Mykytiuk, J.; Armes, S. P.; Edwards, J. L.; Yeates, T.; Moreland, P. J.; Mollett, C., Novel colloidal polyaniline–silica composites. *Journal of the Chemical Society, Chemical Communications* **1992,** (2), 108-109.

7. Barthet, C.; Hickey, A. J.; Cairns, D. B.; Armes, S. P., Synthesis of novel polymer ‐ silica colloidal nanocomposites via free ‐ radical polymerization of vinyl monomers. *Advanced Materials* **1999,** *11* (5), 408-410.

8. Percy, M.; Barthet, C.; Lobb, J.; Khan, M.; Lascelles, S.; Vamvakaki, M.; Armes, S., Synthesis and characterization of vinyl polymer− silica colloidal nanocomposites. *Langmuir* **2000,** *16* (17), 6913-6920.

9. Tiarks, F.; Landfester, K.; Antonietti, M., Silica nanoparticles as surfactants and fillers for latexes made by miniemulsion polymerization. *Langmuir* **2001,** *17* (19), 5775-5780.

10. Schmid, A.; Armes, S. P.; Leite, C. A. P.; Galembeck, F., Efficient Preparation of Polystyrene/Silica Colloidal Nanocomposite Particles by Emulsion Polymerization Using a Glycerol-Functionalized Silica Sol. *Langmuir* **2009,** *25* (4), 2486-2494.

11. Schmid, A.; Fujii, S.; Armes, S. P.; Leite, C. A. P.; Galembeck, F.; Minami, H.; Saito, N.; Okubo, M., Polystyrene−Silica Colloidal Nanocomposite Particles Prepared by Alcoholic Dispersion Polymerization. *Chemistry of Materials* **2007,** *19* (10), 2435-2445.

12. Colard, C. A. L.; Teixeira, R. F. A.; Bon, S. A. F., Unraveling Mechanistic Events in Solids-Stabilized Emulsion Polymerization by Monitoring the Concentration of Nanoparticles in the Water Phase. *Langmuir* **2010,** *26* (11), 7915-7921.

13. Cornel, E. J.; van Meurs, S.; Smith, T.; O'Hora, P. S.; Armes, S. P., In Situ Spectroscopic Studies of Highly Transparent Nanoparticle Dispersions Enable Assessment of Trithiocarbonate Chain-End Fidelity during RAFT Dispersion Polymerization in Nonpolar Media. *Journal of the American Chemical Society* **2018,** *140* (40), 12980-12988.

14. Balmer, J. A.; Mykhaylyk, O. O.; Schmid, A.; Armes, S. P.; Fairclough, J. P. A.; Ryan, A. J., Characterization of polymer-silica nanocomposite particles with core–shell morphologies using Monte Carlo simulations and small angle X-ray scattering. *Langmuir* **2011,** *27* (13), 8075-8089.

15. Larson-Smith, K.; Jackson, A.; Pozzo, D. C., Small angle scattering model for Pickering emulsions and raspberry particles. *Journal of Colloid and Interface Science* **2010,** *343* (1), 36-41.

16. Cracowski, J.-M.; Montembault, V.; Améduri, B., Free-radical copolymerization of 2,2,2-trifluoroethyl methacrylate and 2,2,2-trichloroethyl α-fluoroacrylate: Synthesis, kinetics of copolymerization, and characterization. *Journal of Polymer Science Part A: Polymer Chemistry* **2010,** *48* (10), 2154-2161.

17. Chen, Y.; Chen, D.; Ma, Y.; Yang, W., Radical Polymerization of TFEMA and Relationship Between Surface Hydrophobicity and Molecular Weight of Poly-TFEMA. *Journal of Macromolecular Science, Part A* **2014,** *51* (3), 263-270.

18. Yokota, M.; Miwa, Y.; Ajiro, H.; Akashi, M., The systematic study of the microstructure of crosslinked copolymers from siloxane macromonomers and methacrylates by changes in composition and components. *Polymer Journal* **2012,** *44* (4), 301-305.

19. György, C.; Derry, M. J.; Cornel, E. J.; Armes, S. P., Synthesis of Highly Transparent

Diblock Copolymer Vesicles via RAFT Dispersion Polymerization of 2,2,2-Trifluoroethyl Methacrylate in n-Alkanes. *Macromolecules* **2021,** *54* (3), 1159-1169.

20. Czajka, A.; Armes, S. P., Time-Resolved Small-Angle X-ray Scattering Studies during Aqueous Emulsion Polymerization. *Journal of the American Chemical Society* **2021,** *143* (3), 1474-1484.

21. Brotherton, E. E.; Hatton, F. L.; Cockram, A. A.; Derry, M. J.; Czajka, A.; Cornel, E. J.; Topham, P. D.; Mykhaylyk, O. O.; Armes, S. P., In Situ Small-Angle X-ray Scattering Studies During Reversible Addition–Fragmentation Chain Transfer Aqueous Emulsion Polymerization. *Journal of the American Chemical Society* **2019,** *141* (34), 13664-13675.

22. Basham, M.; Filik, J.; Wharmby, M. T.; Chang, P. C.; El Kassaby, B.; Gerring, M.; Aishima, J.; Levik, K.; Pulford, B. C.; Sikharulidze, I., Data analysis workbench (DAWN). *Journal of synchrotron radiation* **2015,** *22* (3), 853-858.

23. Ilavsky, J.; Jemian, P. R., Irena: tool suite for modeling and analysis of small-angle scattering. *Journal of Applied Crystallography* **2009,** *42* (2), 347-353.

24. Fitzgerald, D., Technical Assessment of the Anton Paar DMA5000 density meter. *H&D Fitzgerald Ltd* **2000**.

25. Shaw, R., Dynamic Light Scattering Training. *Malvern Instruments Ltd* **2014**.

26. Balmer, J. A.; Mykhaylyk, O. O.; Fairclough, J. P. A.; Ryan, A. J.; Armes, S. P.; Murray, M. W.; Murray, K. A.; Williams, N. S. J., Unexpected Facile Redistribution of Adsorbed Silica Nanoparticles Between Latexes. *Journal of the American Chemical Society* **2010,** *132* (7), 2166-2168.

27. Mackay, A. L.; Finney, J. L.; Gotoh, K., The closest packing of equal spheres on a spherical surface. *Acta Crystallographica Section A* **1977,** *33* (1), 98-100.

28. Tarnai, T.; Gáspár, Z., Multi-symmetric close packings of equal spheres on the spherical surface. *Acta Crystallographica Section A* **1987,** *43* (5), 612-616.

29. Evans, J. W., Random and cooperative sequential adsorption. *Reviews of Modern Physics* **1993,** *65* (4), 1281-1329.

30. Rényi, A., On a one-dimensional problem concerning random space-filling problem. *Publ. Math. Inst. Hungar. Acad. Sci* **1958,** *3*, 109-127.

31. Velten, K., *Mathematical Modeling and Simulation: Introduction for Scientists and Engineers*. Wiley: 2009.

32. Mark, J. E., *Physical Properties of Polymers Handbook*. Springer New York: 2007.

33. Birch, F.; Clark, S. P.; Schairer, J. F.; Spicer, H. C., *Handbook of Physical Constants*. Geological Society of America: 2018.

34. Derry, M. J.; Fielding, L. A.; Warren, N. J.; Mable, C. J.; Smith, A. J.; Mykhaylyk, O. O.; Armes, S. P., In situ small-angle X-ray scattering studies of sterically-stabilized diblock copolymer nanoparticles formed during polymerization-induced self-assembly in non-polar media. *Chemical Science* **2016,** *7* (8), 5078-5090.

35. Zemb, T.; Lindner, P., *Neutron, X-Rays and Light. Scattering Methods Applied to Soft Condensed Matter*. Elsevier Science: 2002.

36. Sigma-Aldrich 2, 2-Trifluoroethyl methacrylate Product Page https://www.sigmaaldrich.com/SG/en/product/aldrich/373761 (accessed 2022-02-01).

37. Lovell, P. A.; El-Aasser, M. S., *Emulsion Polymerization and Emulsion Polymers*. John Wiley and Sons: Chichester, 1997.

38. Jones, E. R.; Semsarilar, M.; Wyman, P.; Boerakker, M.; Armes, S. P., Addition of water to an alcoholic RAFT PISA formulation leads to faster kinetics but limits the evolution of copolymer morphology. *Polymer Chemistry* **2016,** *7* (4), 851-859.
39. Jones, E. R.; Semsarilar, M.; Blanazs, A.; Armes, S. P., Efficient Synthesis of Amine-Functional Diblock Copolymer Nanoparticles via RAFT Dispersion Polymerization of Benzyl Methacrylate in Alcoholic Media. *Macromolecules* **2012,** *45* (12), 5091-5098.

Chapter 7: Conclusions

Chapter 7

Conclusions

According to the literature on RAFT-mediated polymerisation-induced self-assembly, this process can be subdivided into the following five stages: preparation of the reaction mixture (stage 1), initiation of the polymerization (stage 2), onset of copolymer self-assembly or micellar nucleation (stage 3), particle growth via monomer diffusion into micelle cores (stage 4) and termination (stage 5). In this Thesis, appropriate structural models and equations have been developed to describe the X-ray scattering of the system at each stage. These SAXS models are combined with the principle of mass balance for the various reagents and products to analyse both the kinetics of the polymerisation and the self-assembly process using time-resolved SAXS patterns recorded during such syntheses. In particular, three formulations are studied: RAFT dispersion polymerisation in a non-polar solvent (Chapters 3 and 4), RAFT emulsion polymerisation in a binary mixture of two polar solvents (Chapter 5) and the preparation of vinyl polymer-silica nanocomposite particles via traditional free radical aqueous emulsion polymerisation (Chapter 6).

For the case of RAFT dispersion polymerisation in a non-polar solvent, the synthesis of $PSMA_{31}$–$PBzMA_{2000}$ diblock copolymer nano-objects in mineral oil was studied. Block copolymer self-assembly to form spherical micelles occurs within the first few minutes, although the BzMA polymerisation was allowed to proceed for nearly 3 h. SAXS models that accounted for the mass balance of the reagents enabled not only the spherical micelle core radius and the radius of gyration of the solvophilic PSMA blocks to be determined but also the unreacted monomer and solvent volume fractions within the growing spherical micelle cores. These data, together with the volume fractions of mineral oil and BzMA monomer within the continuous phase calculated from the X-ray scattering length density, provided an opportunity to monitor the kinetics of this RAFT dispersion polymerisation including the BzMA monomer conversion. SAXS analysis revealed that, after micellar nucleation, the rate of polymerisation was proportional to the concentration of BzMA monomer within the micelle cores, which is consistent with theoretical predictions. A power law scaling relationship between the spherical micelle core radius and the PBzMA DP indicated that particle growth could be subdivided into three distinct time intervals, depending on the monomer supply from the continuous phase to the micelle cores. For the first interval, which occurs immediately after micellar nucleation, the solvophobic PBzMA chains remain partially stretched within the micelle cores. During the second interval, when the solvent is gradually displaced from the micelle cores by the incoming BzMA monomer, the increase in the micelle core volume is proportional to the volume occupied by the PBzMA chains. The most likely scenario for particle growth during this interval is that the particle volume increases by taking up monomer from the surrounding medium, followed by conversion of this imbibed BzMA into PBzMA chains. The third interval coincides with a reduction in the rate of mass transport of BzMA monomer into the growing particles. Although micelle swelling by monomer should lead to an increase in the particle volume, concomitant conversion of

monomer into polymer necessarily leads to densification and hence to an overall reduction in the particle volume. It was also demonstrated that Flory-Huggins parameters for pairs of the components in this system could be calculated from the SAXS data. Although, the mass transfer of the reaction components could be used to monitor the rate of supply of monomer during the BzMA polymerisation, the χ parameters calculated from this mass transfer model differed from χ parameters calculated from Hansen solubility parameters. This inconsistency requires further independent verification of the SAXS models using other chemical reactions such as free radical polymerisation.

For the case of RAFT emulsion polymerisation in polar media, the synthesis of $PDMA_{43}$–$PBzMA_{200}$ diblock copolymer nano-objects in 80/20 w/w ethanol/water was studied. This binary solvent mixture complicated the SAXS analysis because the solvent composition that penetrated the micelle cores is likely to differ from that in the continuous phase as ethanol is a less bad solvent for the growing PBzMA chains compared to water. Unfortunately, increasing the number of variables to account for this likely variation in the solvent composition led to unstable fits to the SAXS patterns. In order to stabilise such SAXS model fittings, two assumptions were considered: (i) the solvent composition within the spherical micelle cores is precisely the same as that in the continuous phase (i.e. 80/20 w/w ethanol/water) or (ii) only ethanol can penetrate into the micelle cores. A structural model based on the first assumption was implemented to identify all four stages of the PISA process (stages 2-5) during RAFT synthesis of $PDMA_{43}$–$PBzMA_{200}$ diblock copolymer nano-objects: initiation of the polymerization when the reaction mixture comprised only $PDMA_{43}$ chains, BzMA monomer and the binary solvent mixture (stage 2); the onset of micellar nucleation when the system comprised two populations of scattering objects, i.e. dissolved copolymer chains and spherical copolymer micelles (stage 3), completion of the copolymer self-assembly when only a single population of spherical micelles could be detected in the system (stage 4) and termination of the BzMA polymerisation (stage 5). However, when making the first assumption, the BzMA monomer concentration within the PDMA-PBzMA micelle cores calculated during stage 4 was not linearly proportional to the rate of polymerisation (as observed for the RAFT dispersion polymerisation conducted in a non-polar medium). This suggested that the assumption of an identical solvent composition for both the continuous phase and within the micelle cores is most likely not valid, thus leading to a discrepancy between the experimental data and theoretical expectations. A structural model based on the second assumption indicated that, during stages 4 and 5, the concentration of BzMA monomer present within the micelle cores was close to zero. This suggested that the overall rate of polymerisation should be controlled solely by the rate of diffusion of BzMA monomer from the BzMA emulsion particles through the continuous phase (solvent) to the spherical micelles. In this case, the monomer supply is constrained by its solubility in the 80/20 w/w ethanol/water binary mixture used for the synthesis. This makes the RAFT dispersion polymerisation of BzMA in such a binary mixture of polar solvents differ significantly from the RAFT dispersion polymerisation of BzMA in non-polar media (e.g. mineral oil). In the case of the dispersion polymerisation, supply of the BzMA monomer, abundant in the continuous phase, to the reaction point (inside of the micelles) is virtually unrestricted and as a result a high (peak) concentration of the monomer in the micelles is reached during this synthesis. In the case of the emulsion polymerisation, supply of the BzMA monomer to the reaction point

is hindered by the monomer transfer through the continuous phase and as a result the monomer concentration in the micelles is low and as soon as a monomer molecule reaches a micelle it will be consumed by the reaction. This conclusion makes the second assumption as a more likely scenario for the micelle core formation. However, this assumption did not provide satisfactory fits to the experimental SAXS patterns corresponding to the initial stages of the synthesis. This result may suggest that just after the spherical micelle formation (stages 2 and 3) the micelle core contains high concentration of water which is excluded from the core only at a later stage (stage 4). Thus, a further improvement of the SAXS model based on the second assumption would be required in order to obtain satisfactory results for the initial stages of the RAFT emulsion polymerisation.

In addition to the PISA process via RAFT synthesis of diblock copolymers in polar and non-polar medium, the approach developed for SAXS analysis incorporating mass balance of the reaction components were applied to the formation of PTFEMA/silica nanocomposite particles via traditional free radical aqueous emulsion polymerisation. Since the structure of these PTFEMA/silica nanocomposite particles differed from that of the spherical micelles, the previously published core-particulate shell and raspberry models were considered for SAXS analysis. The core-particulate shell model was found to be more suitable for SAXS analysis of the synthesis of PTFEMA/silica nanocomposite particles. The traditional rate of polymerisation was not appropriate for assessing the kinetics of emulsion polymerisation. In addition, no a relationship between the monomer concentration within the particle cores and the polymerisation rate was established during analysis. Instead, by determining the relationship between the calculated rate of TFEMA polymerisation and the estimated remaining volume fraction of TFEMA monomer, the rate of formation of the PTFEMA/silica nanocomposite particles was found to be approximately proportional to the remaining TFEMA concentration in the whole system. This suggested that this polymerisation was a diffusion-controlled reaction. Moreover, this approach yielded a diffusion coefficient for TFEMA monomer in water comparable to that reported in the literature. Time-resolved SAXS measurements indicated that particle nucleation occurred within 10-15 min of the onset of polymerization. Once nucleation has occurred, nascent core-shell particles can be observed by TEM and SAXS patterns can be satisfactorily fitted using a three-population scattering model for the synthesised core-shell particles. The model incorporates a population balance of silica particles to account their redistribution between the particulate silica shell of the formed core-shell particles and the non-adsorbed silica nanoparticles that remain within the aqueous continuous phase. This approach enabled the nanocomposite particle diameter, silica shell thickness, mean number of silica particles within the shell, silica aggregation efficiency and packing density within the silica shell to be monitored during the TFEMA polymerization. A final silica shell thickness of 20 nm was calculated, which is consistent with coverage of the PTFEMA latex cores by a monolayer of adsorbed silica nanoparticles. SAXS analysis also indicated that the silica aggregation efficiency was approximately 75%, which was consistent with *postmortem* DLS, TEM and TGA studies.

SAXS analysis using appropriate structural models that account for mass balance between the various reaction components provided not only a deeper understanding of the various structural and morphological transformations that occur during the free radical emulsion

polymerisation but also enabled exploration of the more complex self-assembly of diblock copolymer chains during the early stages of RAFT dispersion polymerisation (Chapter 4). Although pair distance distribution function analysis of the time-resolved SAXS patterns recorded during the first 14 min of the synthesis of $PSMA_{31}$–$PBzMA_{2000}$ spherical nanoparticles indicated that the copolymer chains could self-assemble to form particle dimers, SAXS analysis based on structural models incorporating the dimers of particles including copolymers did not support this PDDF analysis. Instead, SAXS suggests that, at the initial stage of the synthesis of such $PSMA_{31}$–$PBzMA_{2000}$ nanoparticles, the reaction components and products form several populations, which subsequently transform into a single population comprising spherical micelles. SAXS analysis suggests that the pre-micellar reaction mixture comprises ill-defined spherical particles formed by relatively short copolymer chains, with both solvent (mineral oil) and BzMA monomer being located within the particle cores. The initial stage of the synthesis of $PSMA_{31}$–$PBzMA_{2000}$ nanoparticles comprises three steps: the initially soluble PSMA-PBzMA chains first form ill-defined nascent particles (step 1), which are then transformed into well-defined spherical micelles by releasing some copolymer chains, and/or possible fission of these relatively large ill-defined nascent particles to form dimers (step 2) followed by the formation of a single population of monomer-swollen growing micelles/nanoparticles until the end of the polymerisation (step 3). Analysis of structural parameters confirmed that the polymerisation kinetics and monomer diffusion from the continuous phase to the growing micelle cores are set at the onset of micelle nucleation and hold through the reaction course until it slows down by a complete consumption of BzMA monomer.

Although the SAXS models developed in this study provide unprecedented details regarding the polymerisation kinetics and the rate of mass transport of the monomer and solvent, there are several limitations to implementing this approach. Such time-resolved SAXS experiments require access to large-scale synchrotron facilities, auxiliary measurements of the background scattering of various reagent mixtures over a range of concentrations and determination of the scattering length density of each reaction component at the synthesis temperature. Moreover, various assumptions, restrictions and confinements are required to facilitate SAXS analysis. A large number of fitting parameters increases the computer time required to fit scattering equations to experimental SAXS patterns and further time is required to ensure that the data analysis remains as physically realistic as possible. Thus, judicious combination of time-resolved SAXS measurements with other *in situ* techniques that provide additional independent information regarding the reaction kinetics (e.g. vibrational spectroscopy) would be highly desirable for the further study of such heterogeneous polymerisations.

As SAXS modelling with mass balance confinement has brought deep analysis of PISA synthesis in non-polar and polar system and conventional emulsion polymerisation, further work is required. Since this Thesis mainly focuses on the time-resolved SAXS modelling and analysis of spherical micelle (Chapter 3 and 5) and spherical particle (Chapter 4 and 6), deeper understanding of the morphological transitions from spherical micelle to worm-like micelle and from worm-like micelle to vesicle are emerged for SAXS analysis. Also, particle behaviours, for instance particle growth via Ostwald ripening, can be observed by SAXS and then analysed by SAXS modelling with mass balance. The monomer supply and the potential solvent

expelling process should be discussed further. And since SAXS and the following modelling can reveal the stabiliser efficiency for the conventional emulsion in Chapter 6, this method can be introduced to improve the efficiency of industrial emulsion polymerisation. Also, this method can be used to track other absorption processes, for instance, proteins absorbed on polymer cores, and reveal their mechanisms. SAXS model coding is also required to be improved. In additional, this SAXS modelling with mass balance can be possibly applied to WAXS analysis.

For SAXS modelling in Igor Pro, the code and the main panel setting can be access on https://github.com/gliao2sheffield/Thesis_SAXS_Example/blob/main/PSMA-PBzMA%20example.pxp, which is one but not perfect example for the SAXS modelling of the PSMA-PBzMA PISA synthesis discussed in Chapter 3. For the users who tend to apply SAXS modelling with mass balance for further analysis, this SAXS modelling example should be further modified case-by-case.